University of Sheffield

Process and Formulation Optimization of a Continuous Microfluidic-Based Platform for High-Quality mRNA-LNP Production

Zidi Yang

Supervised by

Dr Zoltán Kis & Dr Adam J Brown

A thesis submitted in partial fulfilment of the requirements for the degree of Doctor of Philosophy

The University of Sheffield

Chemical, Materials and Biological Engineering

April 28, 2025

Table of Contexts

Acknowledgements

At this point in writing, I look up from The Diamond and realize that I have already stepped into the 28th spring of my life. In late April 2025, on the eve of my birthday, I pen the final words of my thesis acknowledgements here in Sheffield, UK.

My PhD journey began in the aftermath of the COVID-19 pandemic. I am deeply grateful to the University of Sheffield and my supervisor, Dr. Zoltán Kis, for providing me with this invaluable opportunity and platform to engage in such exciting research. Being able to work at the forefront of such a dynamic field gave me tremendous motivation, and under Dr. Kis's guidance and support, I was able to carry out research focusing on mRNA vaccines, one of the hottest topics of our time.

I would also like to sincerely thank all the members of our research group for their guidance and assistance throughout my studies. It has been a true honor and privilege to work alongside you.

My heartfelt gratitude goes to my family. Despite the long distance that separates us, your unwavering support, encouragement, and care have been the strongest driving force behind my perseverance.

I am also sincerely thankful to my friends: Kewen, Yifei, Xingjian, Mincen, Ziwei, Lingxiao, Bill and Chona, Jixin and Bella. Your companionship and support have brought warmth and strength to this journey. Remember don't look back in anger.

Many literary works conclude with a reference to "tomorrow," so allow me to end my PhD journey the same way—with a quote inspired by Hermann Hesse: "What will tomorrow become? It may become a bouquet of flowers, a falling star, a wish; it may become a promise, a blessing. Tomorrow will become the first day of the rest of your life."

Finally, thank you to everyone I have met along the way, and to all the kindness and goodwill I have received.

Abstract

Messenger RNA (mRNA) has emerged as a transformative platform for vaccines and targeted therapies due to its capacity for precise and rapid gene expression. The COVID-19 pandemic underscored both its promise and the challenges of large-scale production. In response, continuous flow manufacturing—guided by Quality by Design (QbD) principles and enabled by automation and digital technologies—offers a scalable, consistent, and efficient alternative to traditional batch production.

This thesis begins with an overview of vaccine evolution, comparing conventional and mRNA vaccine technologies, and highlighting lipid nanoparticles (LNPs) as key delivery vehicles. It outlines their composition, biological function, and critical quality attributes (CQAs), while introducing modern manufacturing methods, including microfluidics and tangential flow filtration (TFF).

A comprehensive experimental framework was developed for mRNA-LNP production, covering in vitro transcription (IVT), formulation, purification, and characterization. Microfluidic mixer types, formulation parameters, and purification techniques were systematically optimized. Key process parameters (CPPs) were refined using univariate and response surface methodology (RSM), establishing robust process windows that enhanced encapsulation efficiency and size control while minimizing variability.

Further investigations into lipid composition revealed an optimized formulation (ALC-0315/DOPE/ALC-0159/Cholesterol) with superior particle uniformity, stability, and transfection efficiency. Finally, an integrated continuous manufacturing platform was established, incorporating real-time size and PDI monitoring and single-pass TFF. This system achieved high encapsulation efficiency, low residual ethanol, and maintained mRNA integrity, meeting regulatory standards.

Overall, this study provides a scalable, GMP-compatible approach to mRNA-LNP production and a framework for future innovations in formulation, real-time monitoring, and continuous biomanufacturing.

Key Words: mRNA-Lipid Nanoparticle, Continuous mRNA-LNP manufacturing, Quality by Design (QbD) process optimization, Real-time size-PDI monitoring

Schematics Summary

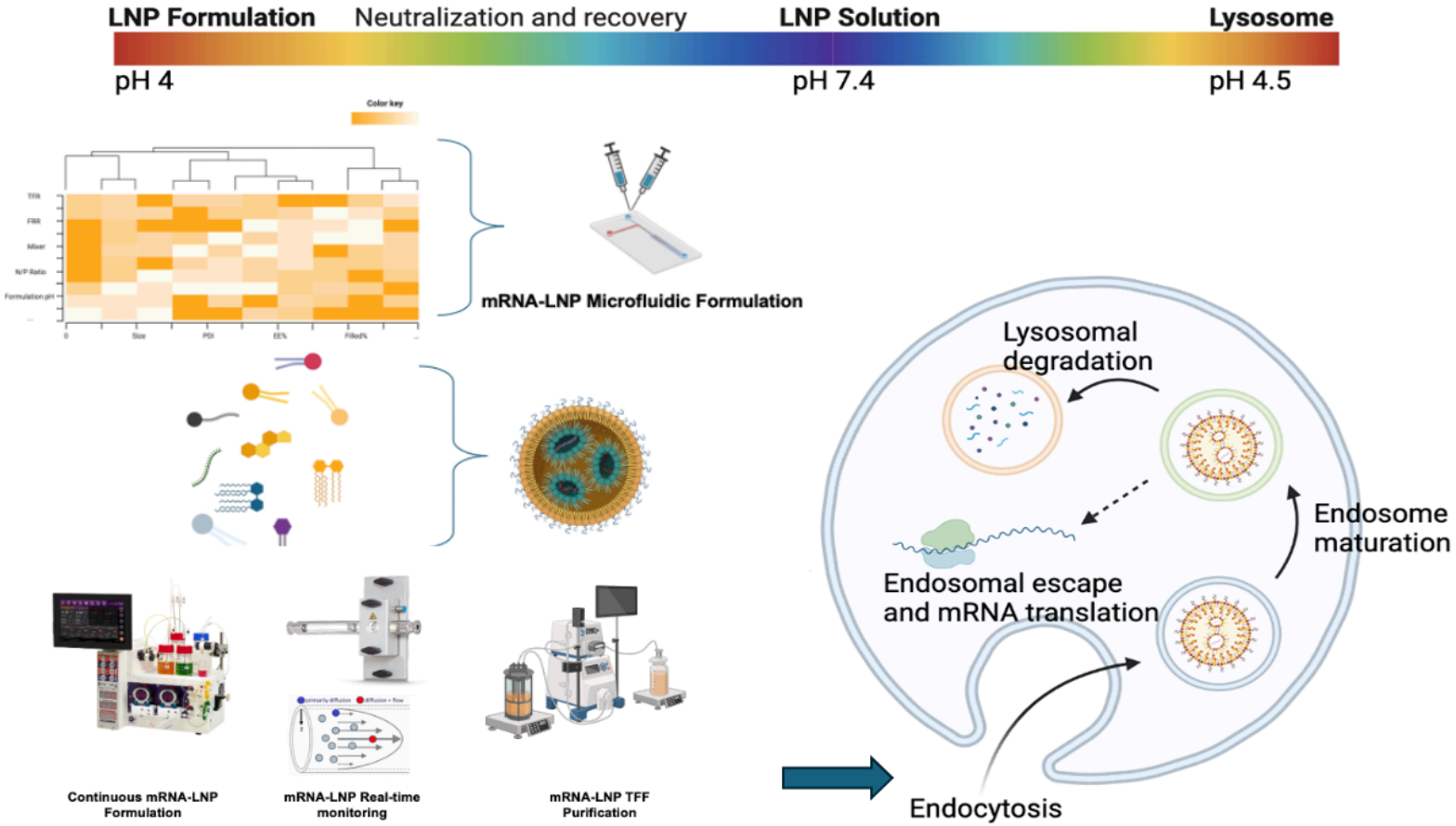

List of Abbreviations, Symbols, and Units

Abbreviations:

LNP (Lipid Nanoparticle)
mRNA (Messenger RNA)
QbD (Quality by Design)
PDI (Polydispersity Index)
ICH (International Council for Harmonization)
CPP (Critical Process Parameters)
CQA (Critical Quality Attributes)
DoE (Design of Experiment)
EE% (Encapsulation Efficiency)
TFR (Total Flow Rate)
FRR (Flow Rate Ratio)
TFF (Tangential Flow Filtration)
SP-TFF (Single-Pass Tangential Flow Filtration)
RSM (Response Surface Methodology)
DLS (Dynamic Light Scattering)
NFS (Nano Flow Sizer)
NanoFCM (Nano Flow Cytometry)
N/P Ratio (Nitrogen-to-Phosphate Ratio)
DSPC (1,2-Distearoyl-sn-glycero-3-phosphocholine)
DOPE (1,2-Dioleoyl-sn-glycero-3-phosphoethanolamine)
PEG (Polyethylene Glycol)
DOTAP (1,2-dioleoyl-3-trimethylammonium-propane)
DOPC (1,2-dioleoyl-sn-glycero-3-phosphocholine)
IVT (In Vitro Transcription)
DMEM (Dulbecco's Modified Eagle Medium)
PBS (Phosphate Buffered Saline)
DTT (Dithiothreitol)
HEPES (4-(2-hydroxyethyl)-1-piperazineethanesulfonic acid)
T7 (T7 RNA Polymerase)
ATP (Adenosine Triphosphate)
CTP (Cytidine Triphosphate)
GTP (Guanosine Triphosphate)

UTP (Uridine Triphosphate)

IPP (Inorganic Pyrophosphatase)

HEPES (4-(2-Hydroxyethyl)-1-piperazineethanesulfonic)

Tris-Cl (Tris(hydroxymethyl)aminomethane hydrochloride

TMP (Transmembrane Pressure)

ABV (Automatic Backpressure Valve)

PCC (Process Chromatography Columns)

Symbols and Units:

nm (Nanometer)

µg (Microgram)

µL (Microliter)

mL/min (Milliliter per minute)

kDa (Kilodalton)

mol% (Mole Percent)

Re (Reynolds Number)

kPa (Kilopascal)

N/m² (Newton per Square Meter)

1. INTRODUCTION

The development of vaccines epitomizes humanity's sustained scientific progress in combating pathogenic microorganisms. This technological evolution can be traced back to the empirical application of cowpox inoculation in the 18th century, which marked a paradigm shift from observational immunity to systematic scientific investigation. The synergistic advancement of microbial isolation techniques and immunological theories has driven transformative innovations in vaccine design. In the 19th century, vaccines based on pathogen inactivation or attenuation strategies achieved a balance between immunogenicity and safety through physicochemical methods [1, 2]. The 20th century witnessed the advent of recombinant DNA technology, which enabled the expression of specific antigenic epitopes [2]. This advancement gave rise to subunit vaccines that circumvented the risks associated with whole-pathogen approaches. In the 21st century, the emergence of mRNA–lipid nanoparticle (mRNA-LNP) platforms has redefined the logic of vaccine production. By coupling in vitro transcription with lipid-based delivery systems, development timelines have been compressed from years of biological cultivation to mere weeks of molecular engineering [3, 4]. This transformation demonstrates the interdisciplinary convergence of synthetic biology and nanomedicine. Iterative advancements in manufacturing have significantly improved vaccine accessibility and standardization. For instance, mammalian cell culture systems have replaced traditional egg-based processes, ensuring greater product homogeneity [5]. Microfluidic mixing enables precise hydrodynamic control over nanocarriers, while continuous manufacturing enhances cost-efficiency through the use of process analytical technology (PAT) and modular integration [5, 6]. Vaccine safety management has transitioned from empirical risk assessment to rational molecular design. This shift is exemplified by the use of modified nucleotides to regulate the innate immunogenicity of mRNA, and by chromatographic purification techniques that remove residual host cell proteins [7, 8]. Contemporary vaccinology is entering a computation-driven era, where CRISPR-mediated epitope prediction and formulation screening powered by machine learning are playing increasingly vital roles in accelerating vaccine development [9-11], and the adaptability of modular mRNA platforms

collectively establish a multidimensional defense matrix against emerging infectious diseases [12].

1.1. Vaccines

Coronaviruses are a class of enveloped, positive-sense single-stranded RNA viruses that can cause a wide range of respiratory infections, from mild colds to severe pneumonia. Since the outbreak of COVID-19, there has been an unprecedented global focus on coronavirus research, catalyzing rapid advances in vaccine technologies, antiviral drug development, and public health strategies [13]. Various types of vaccines have been developed globally, and they can be broadly categorized into five main types based on their preparation techniques: inactivated vaccines/live attenuated vaccines, viral vector vaccines, protein subunit vaccines, and mRNA vaccines [14, 15]. Vaccine development constitutes a highly structured scientific process necessitating rigorous multi-phase validation and iterative optimization. The standardized pipeline encompasses: (1) pathogenicity mechanism deconvolution, (2) antigenic epitope screening and molecular engineering, (3) preclinical safety and efficacy evaluations, followed by (4) GMP-compliant process development and manufacturing. Subsequent stages involve phased clinical trials (Phase I-III), regulatory review and approval, alongside post-marketing surveillance incorporating real-world effectiveness assessments and manufacturing comparability studies.

However, the development of a vaccine is only the first step toward its large-scale application. Factors such as storage requirements (e.g., mRNA vaccines requiring ultra-low temperatures), the management of adverse effects (such as rare cases of blood clotting), and immune durability (e.g., the need for booster doses) all play crucial roles in determining a vaccine's practicality and in shaping global vaccination strategies. These factors not only affect the vaccine's effectiveness but also have a profound impact on the distribution and vaccination strategies worldwide [16, 17].

1.1.1. Inactivated Vaccines/Live Attenuated Vaccines

Inactivated vaccines are a type of vaccine produced by rendering pathogens (viruses or bacteria) non-infectious through physical methods (e.g., heat or radiation) or chemical agents (e.g., formaldehyde or β-propiolactone) [18]. This process (Figure 1) renders pathogens non-replicative while preserving their immunogenicity. The primary advantages of inactivated vaccines include a high safety profile—due to the absence of infectious risk—and strong production stability, making them particularly suitable for the control of high-risk pathogens [19].

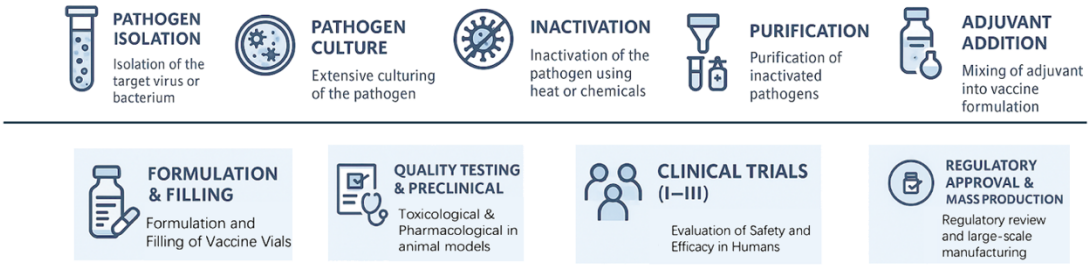

Figure 1. Inactivated Vaccine Production

While inactivated vaccines often exhibit constrained immunological efficacy due to transient humoral responses and insufficient cellular immunity, live attenuated vaccines (LAVs) have emerged to address these limitations. In contrast to the "complete inactivation" strategy of traditional vaccines, LAVs utilize precision attenuation methodologies to selectively disable pathogen virulence while preserving controlled replicative capacity. A representative example is the Edmonston-Zagreb measles vaccine strain, which demonstrates a 10,000-fold reduction in neurovirulence relative to its wild-type counterpart following over 80 serial passages in chicken embryo fibroblasts yet retains robust CD8+ T cell memory induction.

This "controlled pathogenesis mimicry" mechanism enables single-dose immunization to confer decades-long protective immunity, achieving population-level protection rates exceeding 95% in global poliomyelitis and yellow fever eradication initiatives. Crucially, LAV development requires meticulous equilibrium between immunogenic potency and genetic stability. The principal scientific challenge resides in engineering irreversible attenuation

pathways through targeted gene knockout or codon deoptimization strategies—an innovation frontier actively advanced by reverse genetics platforms and synthetic biology approaches.

The technology for inactivated vaccines dates back to the early 20th century, initially applied in rabies prevention. It was later widely used in preventing diseases like poliomyelitis and hepatitis A [20]. With advancements in manufacturing processes, the introduction of aluminum-based adjuvants (e.g., aluminum hydroxide) has significantly enhanced the immunogenicity of inactivated vaccines. In addition, techniques such as ultrafiltration and chromatography have improved antigen purity and reduced the incidence of adverse reactions—for example, adverse reaction rates for influenza vaccines are typically below 1% [21]. Additionally, the Vero cell culture system has enabled large-scale production.

During the COVID-19 pandemic, Chinese companies Sinovac (CoronaVac) and Sinopharm (BBIBP-CorV) employed β-propiolactone-based inactivation technology to develop some of the world's earliest inactivated vaccines, which were introduced in 2020 [22]. These vaccines have an annual production capacity exceeding 5 billion doses. Real-world data indicate that a two-dose regimen can reduce the incidence of severe cases by 80–90%, with over 2.5 billion doses administered primarily in developing countries [23].

The unique strengths of inactivated vaccines include a favorable safety profile (suitable for immunocompromised individuals), ease of storage and transportation (maintained at 2–8 °C), and broad antigen coverage (eliciting multi-epitope immune responses). However, several challenges remain, including relatively low immunogenicity (necessitating multiple doses or adjuvant enhancement), a 10–20-fold reduction in neutralizing antibody titers against variants such as Omicron, and reliance on high-level biosafety infrastructure (e.g., P3 laboratories), which contributes to extended production timelines (6–8 weeks) [24].

Nonetheless, with continued innovations in adjuvants (e.g., toll-like receptor agonists), the incorporation of multivalent antigens (e.g., Delta and Omicron

variants), and advancements in delivery systems such as nasal sprays, inactivated vaccines are poised to maintain their irreplaceable role in combating emerging infectious diseases [25].

1.1.2. Viral Vector Vaccines

Figure 2 shows a classic example: how Viral Vector Vaccines production process. Viral vector vaccines employ genetically engineered viruses as carriers to deliver antigen-encoding genes from target pathogens into human cells, thereby inducing an immune response [26, 27]. These vaccines mimic natural viral infections and effectively elicit both cellular and humoral immune responses [28]. The key advantages of viral vector vaccines include high immunogenicity (robust activation of both T and B cell responses), the elimination of in vitro protein expression (thereby avoiding complex protein production and purification), and the potential for long-lasting immunity. For example, certain vectors such as the measles virus can induce prolonged immune protection, whereas adenoviral vectors often require booster doses [29].

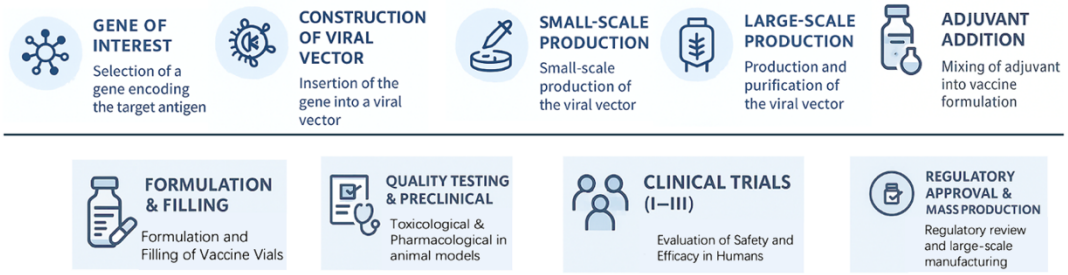

Figure 2. Viral Vector Vaccine Production

The development of viral vector vaccines dates back to the 1980s, initially for gene therapy and cancer immunotherapy, later expanding to infectious disease vaccines [30]. In 2019, Ervebo, an Ebola vaccine based on the vesicular stomatitis virus (VSV) vector, became the first commercially approved viral vector vaccine [31].

During the COVID-19 pandemic, several viral vector vaccines received emergency use authorization, including AstraZeneca (ChAdOx1-S), Janssen

(Ad26.COV2.S), and Sputnik V (Ad26/Ad5) [32, 33]. These vaccines commonly use adenoviruses as vectors to deliver the SARS-CoV-2 spike (S) protein gene, prompting the immune system to generate antibodies and T-cell responses against the spike protein [34]. Large-scale clinical trials and real-world data confirm their effectiveness in preventing severe COVID-19 cases and hospitalizations [35]. Notably, Janssen's single-dose vaccine demonstrated 66-85% protection against severe COVID-19, making it particularly useful for emergency vaccination campaigns [36].

Advantages of viral vector vaccines include strong immunogenicity (capable of eliciting both humoral and cellular immune responses), well-established production technology (as demonstrated in Ebola vaccine development), and favorable storage and transportation requirements (typically maintained at 2–8 °C). However, several challenges remain. These include pre-existing immunity to adenoviral vectors, which may diminish vaccine efficacy; reduced effectiveness against emerging variants (e.g., neutralizing antibody titers against Omicron BA.1 have been shown to decrease by 5–10-fold, with real-world protection against infection declining to 40–60%); and rare but serious adverse events, such as potential associations between the AstraZeneca and Janssen vaccines and thrombotic complications [37].

Nonetheless, ongoing efforts to optimize vector selection (e.g., employing rare serotype adenoviruses), enhance adjuvant formulations (to improve long-term immune responses), and explore alternative delivery routes (such as intranasal administration) ensure that viral vector vaccines will continue to play a pivotal role in future vaccine development and the control of emerging infectious diseases [38].

1.1.3. Protein Subunit Vaccines

Protein subunit vaccines are a type of vaccine that induces an immune response by using recombinant technology to produce and purify key antigenic proteins of a pathogen, such as spike proteins or toxins, rather than extracting them directly from the pathogen [39, 40]. As protein subunit vaccines do not contain the complete virus or bacterium, they offer a high safety profile, posing no risk of infection while enabling precise optimization of immunogenic regions

to enhance efficacy. Their immune response is primarily mediated by humoral immunity (i.e., B cell–mediated antibody production) and typically requires the use of adjuvants to augment immunogenicity [41].

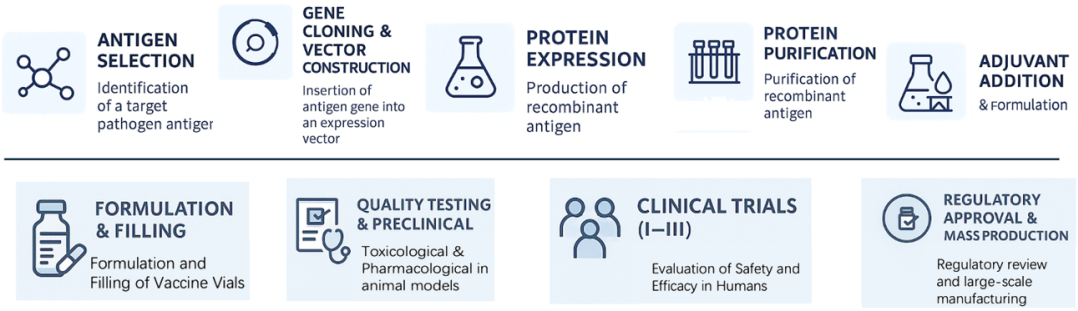

Figure 3. The process of developing a protein subunit vaccine.

The development of protein subunit vaccines (Figure 3) dates back to the mid-20th century, with early applications in vaccines against pertussis (Infanrix, GSK), hepatitis B (Heptavax-B, Merck), and influenza (Fluarix, GSK). Advances in recombinant protein technology have enabled the production of high-purity antigens using mammalian, yeast, or insect cell expression systems, which can be formulated with adjuvants such as AS03, MF59, or CpG oligonucleotides to enhance immunogenicity [42, 43]. During the COVID-19 pandemic, Novavax (NVX-CoV2373) developed one of the world's first protein subunit vaccines, incorporating a recombinant spike protein formulated with Matrix-M adjuvant to enhance immune responses [44]. Clinical trials demonstrated that two doses of the Novavax vaccine provided over 90% efficacy, significantly reducing severe disease. Additionally, Cuba's Abdala vaccine (RBD trimer) and India's Corbevax vaccine (RBD dimer) employed low-cost expression systems, with an annual production capacity of 100 million and 1 billion doses, respectively, significantly increasing vaccine availability in low- and middle-income countries [45]. Meanwhile, Sinovac (SCB-2019), Bharat Biotech (Corbevax), and Zhifei Longcom (ZF2001) have also introduced protein subunit vaccines, further expanding their presence in the global vaccine market [46, 47].

The primary advantages of protein subunit vaccines include high safety, as they do not contain a replicating virus, making them suitable for immunocompromised individuals. Additionally, they can precisely target key antigenic sites, ensuring a controlled immune response. The production process is relatively mature, allowing for scalable manufacturing [48].

Furthermore, these vaccines exhibit good storage stability, with most remaining stable at 2-8°C for at least six months (e.g., Novavax), while some require -20°C long-term storage [49]. Because they can leverage existing vaccine production platforms, protein subunit vaccines are highly accessible and play an essential role in long-term immunization programs. However, there are challenges associated with protein subunit vaccines. First, they have relatively lower immunogenicity, requiring multiple doses or adjuvants to enhance their effectiveness [50]. Second, the production cycle is longer, as antigen purification and protein folding optimization are complex processes that can slow down manufacturing [51]. Additionally, protein subunit vaccines may have reduced adaptability to new variants. For example, the emergence of Omicron led to a decline in neutralizing antibody titers, reducing the vaccine's protective efficacy [52]. Addressing these issues will require ongoing technological advancements to enhance the vaccine's responsiveness to emerging infectious diseases [53].

Despite these challenges, protein subunit vaccines will continue to play a crucial role in future vaccine development and infectious disease prevention. With advancements in adjuvant technology (e.g., TLR agonists), optimization of antigen expression platforms (e.g., plant-based systems), and the development of multivalent vaccines (e.g., Omicron + Delta bivalent vaccines), the efficacy of protein subunit vaccines is expected to improve [54]. By refining vaccine formulations to enhance adaptability to new variants and streamlining production to shorten manufacturing cycles, protein subunit vaccines will remain a key tool in global immunization strategies and the fight against emerging infectious diseases [48, 55].

1.1.4. mRNA Vaccine

mRNA vaccines are an innovative type of vaccine that utilizes messenger RNA (mRNA) technology to introduce the genetic code for a pathogen's key antigen into human cells, allowing them to produce the antigen protein and induce an immune response [10, 56]. This approach mimics natural viral infection, activating both cellular (T-cell) and humoral (B-cell) immunity, providing robust protection. Since mRNA does not integrate into the host genome and degrades

rapidly in the body, these vaccines offer notable safety, immunogenicity, and adaptability advantages [57].

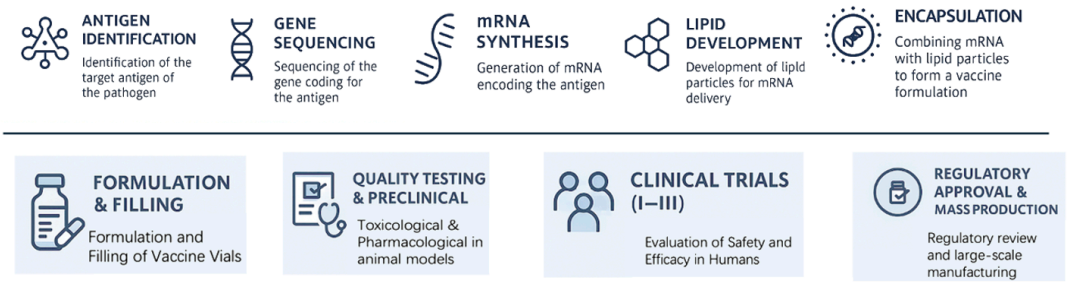

Figure 4. The process of developing a mRNA vaccine.

The development of mRNA vaccines dates back to the 1990s, but challenges such as mRNA instability, low delivery efficiency, and overly high reactogenicity or immunogenicity initially prevented widespread application. However, advancements in lipid nanoparticle (LNP) delivery systems, chemical modifications (e.g., pseudouridine modifications), and 5′ cap structure optimization have overcome these limitations, enabling efficient delivery, enhanced stability, and reduced reactogenicity [58]. During the COVID-19 pandemic, Pfizer-BioNTech (BNT162b2) and Moderna (mRNA-1273) pioneered the first-ever approved mRNA vaccines, receiving Emergency Use Authorization (EUA) in late 2020 [59, 60]. Large-scale clinical trials demonstrated that two doses of mRNA vaccines a two-dose regimen provided over 90% efficacy, significantly reducing severe disease and mortality. As mRNA vaccine technology matures, CureVac (CVnCoV), Sanofi-GSK, and Arcturus have been actively developing second-generation mRNA vaccines to improve tolerability and antigen design [61]. Additionally, mRNA vaccines are being explored for preventing influenza, rabies, and Zika virus and are showing great promise in personalized cancer vaccine applications [62].

The key advantages of mRNA vaccines include high immunogenicity, as they can simultaneously activate T-cell and B-cell immune responses to provide strong and long-lasting protection [63]. Furthermore, mRNA vaccines do not require traditional cell culture (e.g., Vero cells), avoiding biosafety risks associated with live-virus handling [64]. Their short production cycle, often

completed within weeks, makes them ideal for rapidly responding to emerging variants. The highly adaptable manufacturing platform allows for rapid vaccine design by simply modifying the mRNA sequence, ensuring broad applicability [65]. In terms of storage, next-generation mRNA vaccines are being developed with improved cold-chain requirements, with some novel formulations remaining stable for months at 2-8°C, reducing logistics costs and improving global accessibility.

However, mRNA vaccines still face challenges. Firstly, mRNA is highly unstable, requiring stringent storage conditions, with early mRNA vaccines (e.g., BNT162b2) necessitating ultra-cold storage at -70°C, limiting distribution in certain regions [66]. Secondly, rare adverse reactions such as myocarditis and pericarditis have been reported, primarily in young males, although most cases were mild and resolved without complications. Additionally, the protective efficacy against emerging variants has declined over time. For instance, after the emergence of the Omicron variant, first-generation mRNA vaccines showed reduced protection against infection but still provided high efficacy in preventing severe disease, prompting the development of bivalent mRNA vaccines (Omicron + original strain) [37].

Despite these challenges, mRNA vaccines will continue to play a pivotal role in vaccine development and global health strategies. Advancements in delivery systems (e.g., novel LNPs), improved mRNA stability (e.g., circular RNA or self-amplifying RNA, saRNA), and antigen design (e.g., multivalent mRNA vaccines) will help enhance immune durability and variant protection [67]. Furthermore, mRNA vaccine applications are expanding into personalized cancer immunotherapy and autoimmune disease treatments. With ongoing technological innovations, mRNA vaccines are expected to establish a strong presence in both global vaccine markets and precision medicine in the years to come [68, 69].

1.1.5. Comparison of vaccine production processes

The selection of vaccine production processes requires balancing speed, safety, cost, and accessibility. Among them, mRNA vaccines, utilizing in vitro transcription technology, can achieve rapid production within 2 to 3 weeks,

making them suitable for swiftly addressing viral variants [70]. However, their requirements for ultra-low temperature storage (-70°C) and the high costs associated with lipid nanoparticles (LNP) limit their global accessibility [71]. In terms of core differences, mRNA vaccines have the fastest production speed but also the highest costs, higher technical barriers, and relatively limited global accessibility. Future optimization directions include developing lyophilized formulations to enhance the accessibility of mRNA vaccines. Overall, mRNA vaccines, with their rapid production and flexible adjustment capabilities against variants, occupy a central position in the future vaccine technology landscape and are expected to further improve in stability and global reach through technological advancements [72].

The COVID-19 pandemic has been a turning point for RNA vaccine development. In 2020, the first two mRNA vaccines were approved, leading to significant investments in mRNA technology. By 2025, seven mRNA vaccines and three self-amplifying RNA (saRNA) vaccines have been licensed [73]. It is anticipated that in the coming years, more mRNA and saRNA vaccines will be approved for the treatment of infectious diseases and cancers [74]. Although current LNPs are effective for intramuscular injections, they may not be optimal for mucosal delivery [75]. For instance, respiratory delivery of RNA vaccines can enable non-invasive vaccination and potentially enhance local immune responses, capturing respiratory pathogens more effectively at the entry point [76]. However, mucus in the respiratory tract and pulmonary surfactants in the alveoli present physical barriers to RNA vaccines, potentially leading to instability of current RNA formulations and limiting their entry into target cells. Additionally, delivering mRNA vaccines to the respiratory tract faces formulation challenges, as it requires generating aerosols or dry powders suitable for inhalation, along with concerns about inducing respiratory inflammation [77]. To address these challenges, research into novel delivery systems with improved stability and efficacy in mucosal tissues is necessary.
After initial successes, RNA vaccines are now entering a consolidation phase. They have played a crucial role in mitigating the severity of the COVID-19 pandemic. Currently, researchers engaged in this platform are eager to see where it will lead in the future. And the Table 1 shows the compare of the these four types of vaccines.

Table 1. A Comprehensive Comparison of Inactivated Vaccines, Viral Vector Vaccines, Protein Subunit Vaccines and mRNA Vaccines.

	Inactivated Vaccines	Viral Vector Vaccines	Protein Subunit Vaccines	mRNA Vaccines
Key Raw Materials	1. Live virus (e.g., SARS-CoV-2) 2. Inactivating agent (β-propiolactone) 3. Aluminum adjuvant	1. Viral vector (adenovirus, VSV)[78] 2. Mammalian cells (HEK293, PER.C6) 3. Adjuvant	1. Recombinant protein antigen 2. Adjuvant (AS03, aluminum salts)	1. Plasmid DNA template 2. In vitro transcription enzymes 3. Lipid nanoparticles (LNP)
Production Process	1. Virus culture (Vero cells/egg-based) 2. Inactivation 3. Purification 4. Adjuvant mixing	1. Viral vector production (cell culture) 2. Virus purification (density gradient centrifugation) 3. Formulation	1. Antigen expression (CHO/yeast) 2. Protein purification (chromatography) 3. Adjuvant mixing	1. Plasmid amplification 2. mRNA transcription 3. LNP encapsulation 4. Purification (TFF)
Production Timeline	**Longest** (6–8 weeks)	**Moderate** (4–6 weeks)	**Moderate** (5–7 weeks)	**Shortest** (2–3 weeks)
Technical Challenges	1. High-containment facilities (BSL-3) [79] 2. Inactivation validation (residual live virus risk)	1. Cell culture contamination control 2. Pre-existing immunity (adenovirus vectors)[80] 3. Viral titer consistency	1. Protein folding and glycosylation control 2. Adjuvant-antigen compatibility 3. High-purity antigen production	1. mRNA stability 2. LNP encapsulation efficiency 3. Scalability and quality control [81]

Equipment Requirements	1. Large-scale cell culture tanks (Vero cells) 2. BSL-3 validation labs	1. Suspension cell culture systems 2. Ultracentrifuges (virus purification)	1. Mammalian/yeast fermentation tanks 2. Chromatography systems	1. Bioreactors (plasmid production) 2. Microfluidic devices (LNP encapsulation)
Cost	**Low** (mature traditional processes)	**Moderate** (high cell culture costs)	**Moderate** (high adjuvant/purification costs)	**High** (Lipids and 5' capping reagents)
Scalability	**Moderate** (dependent on virus culture scale)	**Low** (limited by cell culture capacity)	**High** (compatible with existing recombinant protein platforms)	**High** (rapid in vitro transcription scale-up)
Storage Conditions	**2–8°C** (aluminum adjuvant stability)	**2–8°C** (adenovirus vector stability)	**2–8°C** (some require -20°C for long-term storage)	**-70°C to -20°C** (LNP degradation risk)
Marketed	Sinovac (CoronaVac), Sinopharm (BBIBP-CorV)	AstraZeneca (ChAdOx1), CanSinoBio (Ad5-nCoV)	Novavax (NVX-CoV2373), Zhifei Biotech (ZF2001)	Pfizer-BioNTech (BNT162b2), Moderna (mRNA-1273)

1.2. Gene Delivery

Gene delivery therapy aims to introduce exogenous genes into patients to repair or replace defective genes or enhance cellular functions, thereby treating diseases or improving health conditions [82]. The main principles include gene replacement (e.g., CFTR gene replacement for treating cystic fibrosis), gene silencing (e.g., siRNA for reducing the expression of mutated genes), gene editing (e.g., CRISPR-Cas9 technology for correcting genetic mutations), and gene enhancement (e.g., VEGF gene for promoting angiogenesis) [83].

With the approval of COVID-19 mRNA vaccines, mRNA therapy has become a hot topic in the biomedical field. Before the large-scale rollout of mRNA vaccines, researchers had already explored the use of exogenous nucleic acids such as DNA, siRNA, and miRNA for gene regulation or gene therapy, investigating their applications in disease intervention [84, 85].

To date, various bio-derived and chemical-based delivery materials have been developed, some of which have shown promising delivery efficiency. Bio-derived vehicles, including exosomes and virus-like particles (VLPs, e.g., PEG10 VLPs), have demonstrated potential in specific applications. In terms of chemically synthesized delivery systems, polymers, inorganic nanoparticles, and lipid-based nanoparticles (LNPs) have been widely applied due to their high delivery efficiency and versatility.

1.2.1. Viral vector/Virus-Like Particle

Viral vector delivery was the first technology applied in gene delivery, leveraging the natural infection capabilities of viruses to introduce exogenous genes into target cells [86]. As early as the 1960s, scientists attempted to use retroviruses for gene transduction. The first successful human gene therapy trial involved the use of retroviruses to treat a patient with adenosine deaminase (ADA) deficiency [87]. During the COVID-19 pandemic, AstraZeneca's adenoviral vector vaccine was successfully developed and launched, further demonstrating the significant potential of viral vectors in vaccine development.

Different types of viral vectors are suitable for distinct applications. For example, adenoviruses (Ad) can infect both dividing and non-dividing cells and enable transient, high-efficiency gene expression, making them widely used in vaccine development [88]. Lentiviruses, modified from HIV, integrate into the host genome, allowing for long-term gene expression, which is particularly beneficial in CAR-T cell therapy. Additionally, retroviruses are also utilized in some gene delivery applications [89].

Compared to non-viral vectors (such as LNPs), viral vectors exhibit higher cellular uptake efficiency and enable robust gene expression. They are particularly advantageous in genetic and neurological disease therapies due to their ability to facilitate long-term gene expression [90]. However, viral vectors face several challenges. For instance, adenoviruses and adeno-associated viruses (AAVs) may be recognized and cleared by the immune system, reducing delivery efficiency [91]. Moreover, certain viral vectors pose risks of genome integration, potentially leading to genetic mutations. Another limitation is their restricted payload capacity (e.g., AAVs have a maximum payload of ~4.7kb), making it difficult to deliver large nucleic acid molecules. Additionally, viral vector production is complex and costly.

Future advancements will focus on optimizing viral vector design to enhance targeting and safety, developing hybrid delivery strategies (such as combining viral vectors with nanoparticles), exploring the integration of CRISPR gene editing technology with viral vectors, and promoting large-scale production to expand the clinical applications of viral vector therapies [92].

1.2.2. Polymeric materials

Polymeric nanoparticles have attracted significant interest in nucleic acid delivery due to their tunable properties and versatile design. Various polymeric materials, such as polyethyleneimine (PEI), poly(β-amino esters) (PBAEs), poly(lactic-co-glycolic acid) (PLGA), and chitosan, have been developed to encapsulate and protect nucleic acids from enzymatic degradation while facilitating cellular uptake [93]. These polymers can be chemically modified to improve their biocompatibility, stability, and transfection efficiency. Some polymeric nanoparticles employ cationic polymers to form electrostatic

complexes with negatively charged nucleic acids, enhancing cellular internalization [94]. Additionally, biodegradable polymers allow for controlled drug release, improving the therapeutic efficacy of gene delivery systems.
Polymeric nanoparticles offer several advantages, including structural flexibility, ease of large-scale production, and the ability to incorporate functional modifications such as targeting ligands or stimuli-responsive elements [95]. However, their clinical translation remains limited due to concerns about cytotoxicity, variability in transfection efficiency, and potential accumulation in tissues, which may lead to adverse effects. While polymeric nanoparticles have not yet emerged as the dominant nucleic acid delivery system, ongoing research in polymer engineering, such as the development of biodegradable and charge-altering polymers, may enhance their biocompatibility and expand their applications in gene therapy [96].

1.2.3. Inorganic Nanoparticles

Inorganic nanoparticles have gained attention in nucleic acid delivery due to their unique properties. Gold nanoparticles (AuNPs) can bind negatively charged nucleic acids (e.g., siRNA, plasmid DNA) via electrostatic interactions, and upon near-infrared (NIR) irradiation, they generate localized heating to enhance nucleic acid release and cell membrane permeability [97]. Similarly, magnetic nanoparticles (MNPs) made of Fe_3O_4 or Fe_3O_4@Au can be guided by an external magnetic field and release nucleic acids through heat under an alternating magnetic field. These nanoparticles offer high stability, resisting temperature, pH changes, and enzymatic degradation, making them suitable for long-term storage [98]. Their structure can be precisely controlled, and by conjugating ligands (e.g., antibodies, peptides, aptamers), they enable targeted gene delivery.

However, their clinical application is limited due to biocompatibility and toxicity concerns, relatively low delivery efficiency, and challenges in large-scale production. As a result, inorganic nanoparticles have not become a primary nucleic acid delivery method, though future innovations in degradability and smart response strategies may expand their potential in targeted therapies.

1.2.4. Liposome/Lipid Nanoparticle

LNPs played a pivotal role in controlling the COVID-19 pandemic and have continued to receive widespread attention in the post-pandemic era. With excellent biocompatibility and high cellular uptake efficiency, lipid nanoparticles have become a central platform for nucleic acid delivery [99]. LNPs encapsulate siRNA or mRNA within a lipid bilayer, where ionizable lipids remain neutral at physiological pH and become positively charged in the acidic endosomal environment, facilitating nucleic acid release and improving delivery efficiency [100]. And figure 5 shows the structure difference of liposome and lipid nanoparticle.

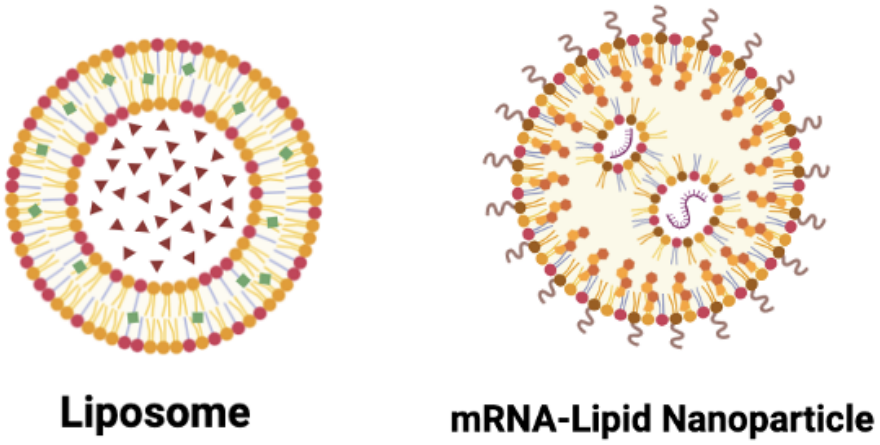

Figure 5. The structural difference between liposome and mRNA-lipid nanoparticles (mRNA-LNP). Liposomes can encapsulate water-soluble drugs (e.g. paclitaxel, doxorubicin liposomes).

LNP technology has achieved breakthroughs in gene silencing (e.g., Onpattro®) and mRNA vaccines (e.g., COVID-19 vaccines) [101]. However, several challenges remain, including temperature sensitivity, limited extrahepatic delivery efficiency, and potential immune responses. The success of COVID-19 vaccines has demonstrated the feasibility of LNPs as nucleic acid delivery carriers, yet there is still room for improvement in both manufacturing processes and formulation strategies. Current research focuses on (1) optimizing LNP formulations for targeted delivery to specific organs such as the lungs and brain, (2) developing lyophilization techniques to enhance storage stability and reduce reliance on cold chain logistics, and (3) adjusting lipid composition to minimize toxicity and off-target effects [102, 103].

As LNP technology advances, post-pandemic research is increasingly incorporating additional functionalities, enhancing delivery efficiency, targeting specificity, and other biological properties, leading to increasingly complex LNP structures and formulations [101, 104]. Therefore, establishing a standardized LNP formulation platform is crucial for optimizing manufacturing processes, improving reproducibility, and accelerating the development of next-generation nucleic acid therapeutics.

1.3. Lipid Nanoparticle in Gene Delivery

Lipid nanoparticles (LNPs) are a revolutionary gene delivery tool capable of safely and efficiently transporting therapeutic nucleic acids, such as mRNA, siRNA, or CRISPR components, into target cells. With their intelligent pH-responsive properties and exceptional delivery efficiency, LNPs have emerged as a key platform for gene therapy and vaccine development. Their application has not only accelerated the global rollout of COVID-19 mRNA vaccines but also paved the way for innovative treatment strategies for genetic disorders, cancer, and other major diseases. As LNP technology continues to advance, it is expected to drive breakthroughs in next-generation gene therapies, further expanding the clinical potential of nucleic acid-based medicines [105].

1.3.1. LNP Development and Application

Lipid nanoparticles (LNPs) have their origins in traditional liposomes technology and have evolved into highly efficient nucleic acid delivery platforms in a process of continuous optimization. Its evolution incorporates the needs of materials science, nanotechnology, and gene therapy. Early Liposomes technologies were mainly used for small molecule drug delivery, such as Doxil® (Adriamycin Liposome), to improve efficacy by increasing circulation time and reducing toxicity [106]. However, in the area of nucleic acid delivery, conventional liposomes face the bottleneck of inefficient escape from cellular endosomes - nucleic acids need to enter the cytoplasm to be effective, and liposomes lack an efficient escape mechanism [107].

To address this issue, researchers have developed cationic liposomes (e.g., DOTAP), hoping to take advantage of their positively charged properties to

enhance binding to negatively charged nucleic acids [108]. However, this strategy suffers from low encapsulation rates and a tendency to aggregate. In addition, the continued positive charge of cationic lipids at physiological pH conditions may lead to cell membrane damage, hemolysis and inflammation, limiting their use in gene delivery [109].

The introduction of Ionizable Lipids and the optimization of delivery efficiencies have been central breakthroughs in the development of LNPs. The revolutionary design of ionizable lipids truly laid the foundation for the success of LNP in nucleic acid delivery, and in 2018, Alnylam's development of Onpattro® (Patisiran) validated the value of LNP in the clinic as the first approved siRNA-LNP drug. Subsequently, the 2020 Covid outbreak and the global deployment of Pfizer/BioNTech and Moderna's mRNA-LNP vaccine further demonstrated the safety, efficacy and rapid production capacity of LNP [56, 62]. On this basis, LNP is expected to achieve breakthroughs in more disease areas, and more and more mRNA drugs are being developed, such as individualized tumor vaccines (e.g. BioNTech's BNT111), and CRISPR editing (in vivo knockdown of oncogenes) [110]. And the table 2 shows the previous and current application of lipid nanoparticle.

Table 2. The RNA therapy based on the LNP delivery.

Name	Drug Type	Indication	Approved Year	Stage
Doxil®[111]	Doxorubicin Liposome	Metastatic ovarian cancer	1995	Approved
Onpattro®	siRNA	Hereditary transthyretin-mediated amyloidosis with polyneuropathy	2018	Approved
Comirnaty®[112]	mRNA Vaccine	COVID-19 Prevention	2020	Approved
Spikevax®[112]	mRNA Vaccine	COVID-19 Prevention	2020	Approved
ARCT-810[113]	mRNA Therapeutic	Hepatitis B Virus Infection	TBD	Clinical Trial Phase
NTLA-2001[114]	CRISPR/Cas9 Gene Editing	Transthyretin Amyloidosis (ATTR)	TBD	Clinical Trial Phase

BNT111[68]	mRNA Vaccine	Cancer	Melanoma	TBD	Clinical Trial Phase

*Updated 11th July 2024 All clinical trials listed in this table are based on ClinicalTrials.gov and official announcements from pharmaceutical companies.

Unlike siRNA-LNP delivery, mRNA molecules are larger (~1000-4000 nt), more chemically complex, prone to degradation, and more difficult to encapsulate [115]. In addition, mRNA vaccines require intramuscular delivery and activation of the immune system, unlike siRNA-LNP, which is rapidly degraded in the liver. mRNA-LNP breaks through these technological barriers and is the world's first large-scale application of an mRNA drug.

In terms of manufacturing processes, mRNA vaccines need to be produced globally on a large scale, with batch-to-batch consistency, while meeting stringent sterility and quality control (QC) standards. However, there is still room for optimization: most LNPs are currently stored at -20°C to -70°C, resulting in high cold chain costs [116]. Lack of Precision Process Monitoring (PAT): Real-time monitoring of particle size, PDI and encapsulation rate through Dynamic Light Scattering (DLS) on-line testing improves quality control. Freeze-drying storage processes are also being explored, as well as end-to-end automation with microfluidic modules, on-line purification (Tangential Flow Filtration, TFF) and filling systems. The LNP production process has evolved from manual laboratory preparation to highly automated continuous flow production. In the future, with the development of material innovation, intelligent control and green manufacturing, the LNP industry will further push the boundaries of efficiency and safety. With the maturity of freeze-drying technology, AI design, and targeted modification, LNP is expected to reach a higher level in the industrialization of gene drugs [117].

1.3.2. The Composition and Self-assembly Mechanism

Lipid nanoparticles (LNPs) are composed of ionizable lipids, helper phospholipids, cholesterol, and PEG lipids, forming a core-shell structure that encapsulates nucleic acids. Their mechanism relies on the protonation of ionizable lipids in acidic endosomes, disrupting the membrane structure to release nucleic acids into the cytoplasm, achieving efficient drug delivery [99].

The spherical morphology of LNPs arises from the thermodynamic drive to minimize interfacial energy in aqueous environments, combined with the molecular geometry of lipid components that favors curved, closed structures. In microfluidic systems, the rapid mixing of lipid-containing organic and aqueous phases further accelerates this self-assembly process, enabling the spontaneous formation of uniform, spherical nanoparticles that efficiently encapsulate nucleic acids. And the mechanism of LNP formulated and the structure of mRNA-LNP is shown schematically in Figure 6.

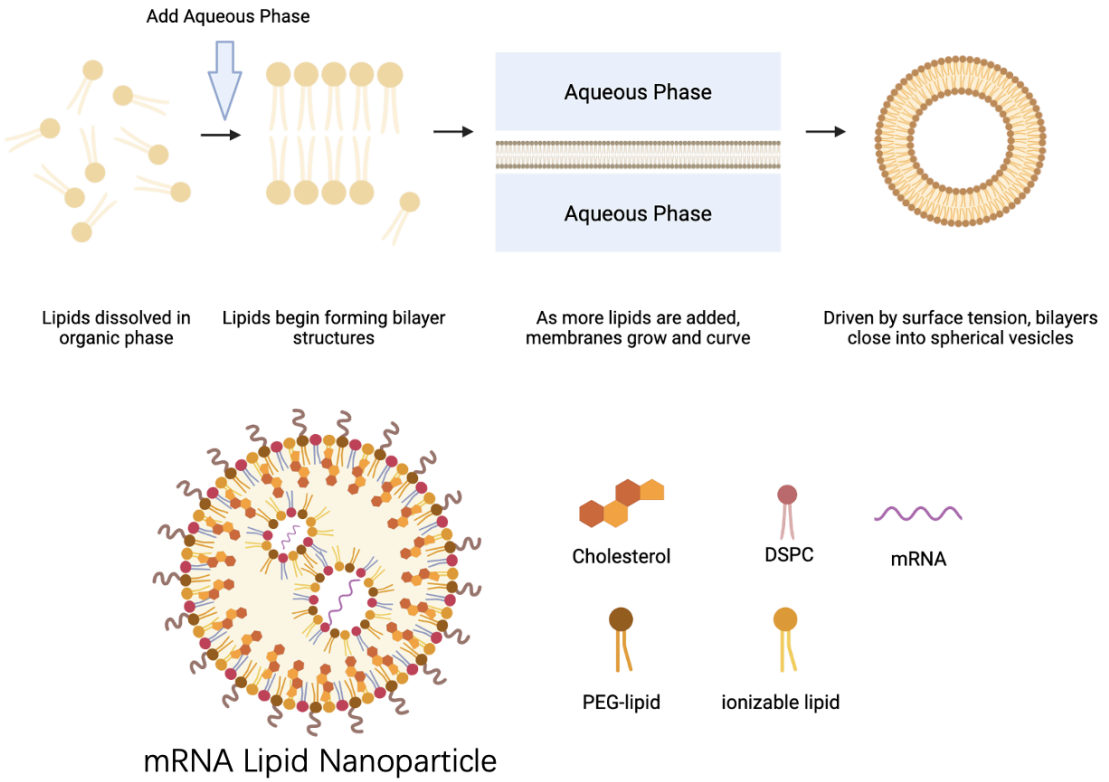

Figure 6. Structure and self-assembly mechanism of mRNA-LNP. Lipids dissolved in organic solvents rapidly self-assemble into bilayer structures upon mixing with an aqueous mRNA solution. Driven by hydrophobic forces and surface tension, these structures spontaneously curve and enclose the mRNA, forming spherical lipid nanoparticles for efficient encapsulation and delivery. And the mRNA is the active ingredient and ionizable lipid to bind electrostatically to the nucleic acid. Cholesterol stabilizes the nanoparticle structure and mediates cytokinesis via the low-density lipoprotein (LDL) receptor [118]. Helper lipid accelerates the structural transformation of LNP in cells and accelerates drug release. PEG-lipid improves the overall stability of LNP and prolongs the circulation time of LNP.

1.3.2.1. Ionizable/Cationic Lipids

Ionizable lipids are key and main components of lipid nanoparticle (40mol%-50mol%) delivery systems, with their acid dissociation constant (pKa) determining LNP ionization behavior and surface charge, thereby affecting stability, toxicity, and delivery efficiency. Early permanently charged cationic lipids, such as DOTAP (1,2-dioleoyl-3-trimethylammonium-propane), used for nucleic acid delivery, tended to interact with negatively charged serum proteins in the bloodstream, leading to LNP aggregation and rapid clearance by the mononuclear phagocyte system (MPS), thus reducing circulation half-life. Additionally, these lipids exhibited high hemolytic activity, potentially disrupting red blood cell membranes, causing hemoglobin release, and increasing toxicity risks [119]. This limitation also contributed to the failure of gene therapy formulations based on DOTAP/DOTMA in clinical trials during the last century.

To overcome these challenges, researchers developed ionizable cationic lipids with pKa values between 6.0 and 7.0, which exhibit environmental responsiveness. These lipids remain positively charged in acidic environments (e.g., pH 4.0), enhancing nucleic acid encapsulation efficiency, while they become nearly neutral at physiological pH (7.4), reducing toxicity during circulation. Once inside the endosome/lysosome, where pH drops below the lipid's pKa, they regain positive charge, facilitating endosomal escape and effective nucleic acid release into the cytoplasm [120]. Current research also suggests that pKa plays a role in LNP targeting, with studies indicating that LNPs with pKa values of 6.2–6.5 are optimal for hepatic siRNA delivery, whereas those with pKa values of 6.6–6.9 are better suited for intramuscular administration of mRNA vaccines [121].

Ionizable lipids generally consist of three key components: the amino head group, which determines the lipid's pKa and charge state; the hydrophobic tail, which influences membrane fusion, stability, and degradation rate; and the internal linker that connects the two. Through combinatorial chemistry, researchers can fine-tune the tail structure to further optimize LNP performance. Pfizer's ALC-0315, used in COVID-19 vaccines, employs a four-branched tail design, demonstrating that increasing lipid tail branching (e.g., methyl or ethyl branches) enhances membrane fusion capability and improves endosomal

escape efficiency [122]. Moderna's SM-102 incorporates hydrolyzable groups such as ester and carbonate bonds, allowing metabolic breakdown into non-toxic products, thereby reducing long-term accumulation risks [123]. In terms of production processes, the development of coatings such as polysarcosine or polysorbate as alternatives to PEG lipids is being explored to mitigate PEG lipid-induced allergic reactions [124].

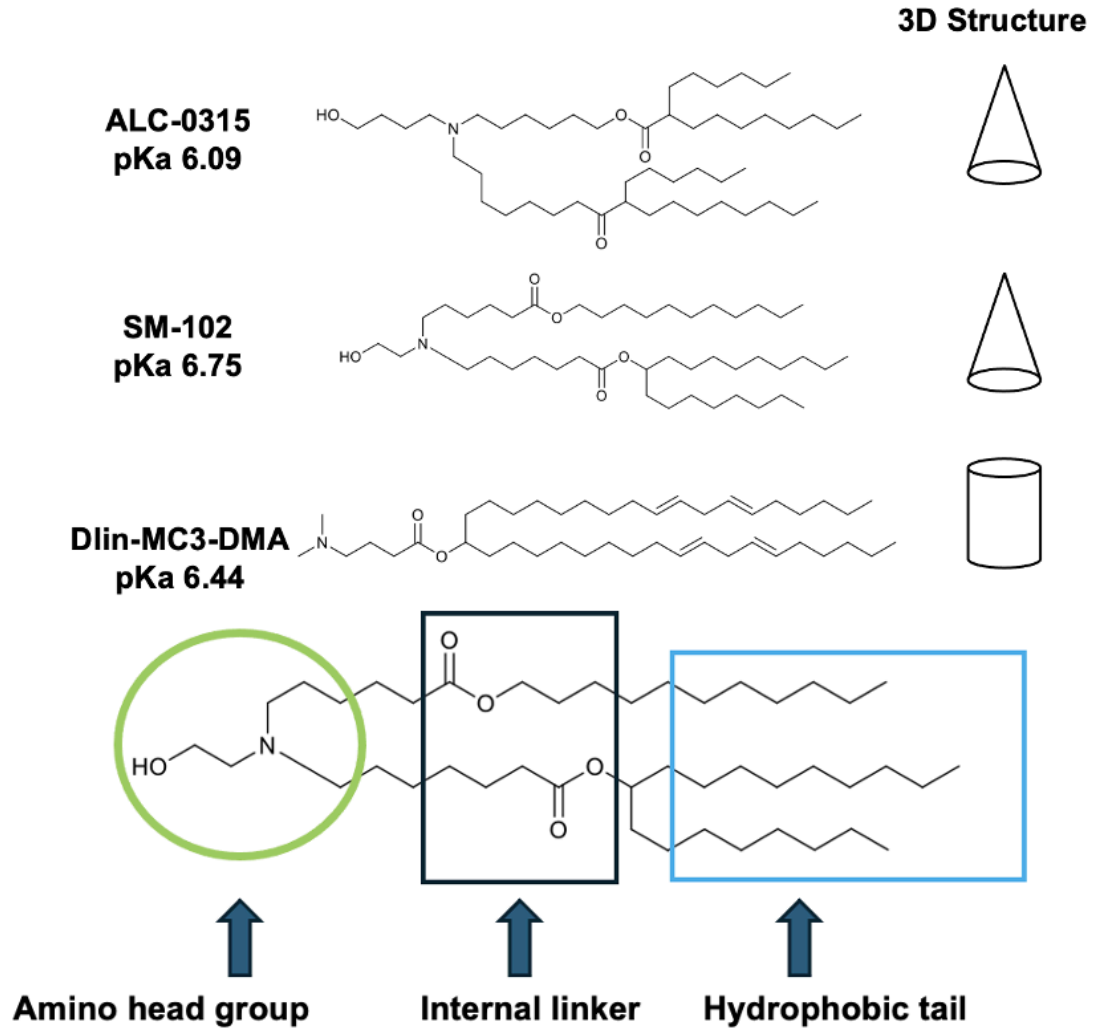

Figure 7. This is the structural diagram of the ionizable lipid SM-102 (used in Moderna's Spikevax®). It consists of three main components: the amino head group, internal linker, and hydrophobic tail, and is the main component in LNP formulations. The amino head group is highlighted with a green circle, the internal linker is marked with a black box, and the hydrophobic tail is indicated by a blue box.

Currently, high-throughput screening (HTS) techniques play a crucial role in optimizing ionizable lipids. Researchers typically employ in vitro and in vivo HTS to identify optimal lipid structures from hundreds of candidates, selecting LNP formulations with high delivery efficiency and low toxicity [125].

Furthermore, AI-driven computational design is advancing the field by predicting structure-activity relationships (SAR) and guiding rational chemical modifications of lipid structures [126]. Regarding LNP targeting, the currently approved ionizable lipids are primarily used for hepatic LNP delivery, such as in siRNA therapeutics, while mRNA vaccines have relatively low targeting requirements. However, increasing research efforts are directed toward LNP delivery to specific tissues such as the lungs, bone marrow, spleen, and T cells. Lung-targeted delivery holds potential for gene therapy, while bone marrow and spleen-targeted LNPs could enable immune cell delivery for cancer treatment. LNP-mediated RNA delivery to T cells could enhance CAR-T cell therapy [127]. Additionally, LNP formulations designed to overcome the blood-brain barrier (BBB) are showing promise for gene therapy applications in central nervous system disorders [128].

In terms of manufacturing processes, it is essential to consider the impact of newly designed ionizable lipids. Highly branched lipids may require a reduction in cholesterol content to prevent excessive rigidity. Differences in lipid solubility may necessitate adjustments in ethanol-to-aqueous phase flow ratios or temperature settings to ensure optimal formulation and production efficiency [129].

1.3.2.2. Phospholipids (Helper Lipids)

Phospholipids, a class of helper lipids, play a crucial role in the formation of lipid nanoparticles (LNPs) and in facilitating endosomal escape, typically accounting for approximately 10 mol% of LNP formulations. In both preclinical and clinical applications, DSPC (1,2-distearoyl-sn-glycero-3-phosphocholine) and DOPE (1,2-dioleoyl-sn-glycero-3-phosphoethanolamine) have been widely used for many years. Given their established roles, studying the structure-activity relationships (SAR) of phospholipids and optimizing their chemical structures to enhance the physical and biological properties of LNPs holds significant importance [130].

Traditional phospholipids have inherent limitations, such as high structural rigidity and difficulty in chemical modification. To address these challenges, Liu et al. developed hundreds of ionizable phospholipids (iPhos), among which

9A1P9, featuring a zwitterionic head group and three alkyl tails [131]. The unique structure of iPhos lipids allows them to adopt a cone shape more readily within endosomes, ultimately enhancing membrane destabilization and cargo release. Furthermore, iPhos-based LNPs have shown potential for targeted delivery to the liver, spleen, and lungs, making them highly promising for organ-specific delivery in mRNA therapeutics and CRISPR-Cas9 gene editing systems.

Unlike cholesterol and ionizable lipids, phospholipids currently do not follow a fixed design paradigm; both phosphoethanolamine (PE) and phosphocholine (PC) head groups have been successfully incorporated into LNP formulations for nucleic acid delivery [132]. However, their impact on LNP formulation and manufacturing processes differs, highlighting the need for further optimization in lipid composition to improve formulation stability and delivery performance. Developing a better understanding of phospholipid roles in LNP assembly and refining their integration into formulations remains a key research focus. DOPE, characterized by its conical molecular geometry due to unsaturated oleoyl chains, inherently adopts an inverse hexagonal phase under physiological conditions rather than a lamellar bilayer, precluding self-assembly into closed liposomal structures. Although cholesterol modulates membrane fluidity, it fails to suppress DOPE's intrinsic non-lamellar phase propensity, leading to bilayer destabilization. In contrast, DSPC's saturated linear chains stabilize the lamellar phase, synergizing with cholesterol to enhance membrane rigidity and thereby enabling robust liposome formation.

Overall, phospholipids play a critical role in mRNA-LNP delivery, and ongoing studies continue to validate their potential for enhancing delivery efficiency, organ targeting, and endosomal escape mechanisms. These advancements pave the way for the future development of mRNA therapeutics and gene editing technologies, providing novel insights for improving LNP-based drug delivery platforms.

1.3.2.3. Cholesterol

Cholesterol, as a key auxiliary component in lipid nanoparticles (LNPs), accounts for approximately 40 mol% of the lipid phase composition and plays a crucial role in LNP stability, membrane fusion, delivery efficiency, and targeting capability. Consequently, optimizing cholesterol focuses on functional modifications, alternative lipid development, and formulation synergy, which not only enhance LNP performance but also introduce new challenges in manufacturing processes [133].

Current research on cholesterol optimization is primarily directed toward two key aspects. The first is imparting pH responsiveness and cell targeting properties. For instance, cholesteryl oleate incorporated into LNPs enables preferential targeting of hepatic endothelial cells, while 20α-hydroxycholesterol (20α-OH) significantly enhances mRNA delivery to endothelial cells within the liver [134]. The second approach explores natural cholesterol alternatives, with Iravani et al. screening various plant-derived cholesterol analogs and discovering that β-sitosterol-modified LNPs (eLNPs) not only significantly improve transfection efficiency but also reduce immune risks associated with animal-derived components [135]. Additionally, synthetic sterol-cholesterol complexes improve water solubility, facilitating the pre-mixed lipid formulation of LNPs for large-scale manufacturing.

In LNP manufacturing, cholesterol modifications also introduce new technical challenges. Certain cholesterol derivatives, such as CHEMS, may increase solution viscosity, impacting microfluidic mixing efficiency, necessitating adjustments in chip channel design and flow rate ratios. Moreover, the inclusion of functionalized cholesterol may disrupt the balance of other lipid components, such as ionizable lipids, requiring design of experiments (DoE) to optimize LNP formulations for a balance of delivery efficiency, stability, and manufacturability.

Overall, the role of cholesterol in LNP systems is shifting from passive structural support to active functional regulation. Through chemical modifications, alternative lipid development, and synergistic formulation design, cholesterol can enhance LNP targeting specificity and safety, expanding its potential applications in gene delivery [136]. However, these improvements also

increase the complexity and cost of manufacturing, necessitating modular design, continuous-flow production, and AI-driven optimization to enable scalability and cost-effectiveness. Looking ahead, functionalized cholesterol may play a pivotal role in overcoming LNP liver-targeting limitations and broadening gene therapy applications to new indications.

1.3.2.4. PEGylated Lipids

PEGylated lipids are incorporated at the lowest proportion in LNP formulations, typically around 1–2 mol%, primarily to reduce nanoparticle aggregation, prolong circulation time, and evade clearance by the mononuclear phagocyte system (MPS) [137], In most clinical LNP formulations, PEG-lipids with polyethylene glycol chain lengths of ~2 kDa (PEG2000) are typically used, striking a balance between circulation time extension and efficient cellular uptake. In most LNP formulations, PEG2000 is commonly used to balance circulation time and cellular uptake. Shorter PEG chains (e.g., PEG1000) enable faster shedding and improved delivery, while longer chains (e.g., PEG5000) prolong blood circulation. The desorption rate also depends on the hydrophobic anchor length—shorter or unsaturated tails (e.g., C14) detach faster than saturated long tails (e.g., C18). Recent PEG-lipid designs incorporate cleavable linkers or responsive moieties to optimize in vivo behavior and reduce immunogenicity [71, 138]. However, due to their long-chain macromolecular nature, the PEG layer hinders LNP interactions with target cells, reducing endosomal escape efficiency and ultimately lowering transfection rates. Research on the desorption rates of PEGylated lipids with different alkyl chain lengths has revealed that shorter alkyl chains result in faster PEG detachment, which correlates with higher LNP delivery efficiency [138]. These findings emphasize that PEG lipid chain length and concentration significantly influence LNP pharmacokinetics, pharmacodynamics, and biodistribution [139].

Despite its advantages, PEGylation also introduces adverse effects, such as hypersensitivity reactions (via complement system activation), the accelerated blood clearance (ABC) phenomenon, and systemic reactogenicity due to anti-PEG antibodies upon repeated administration [140]. To address these

challenges, researchers are developing PEG alternatives, including poly(glycerol) and poly (amino acids), which offer potential improvements in LNP delivery efficiency and safety.

Due to its low proportion in LNP compositions, PEGylated lipids have a minimal impact on the manufacturing process. However, PEG lipid optimization is shifting from a simple stealth function toward dynamic, responsive, and multifunctional designs, aiming to overcome immunogenicity limitations and enhance delivery efficiency.

1.3.2.5. Lipid nanoparticle Mechanism of Transfection

During lipid nanoparticle formulation process, ionizable lipids, helper phospholipids, cholesterol, and PEGylated lipids self-assemble with nucleic acids through rapid precipitation, forming a core-shell structured lipid nanoparticle (LNP). The LNP shell effectively protects nucleic acids from RNase degradation in circulation, maintaining stability and ensuring efficient delivery.

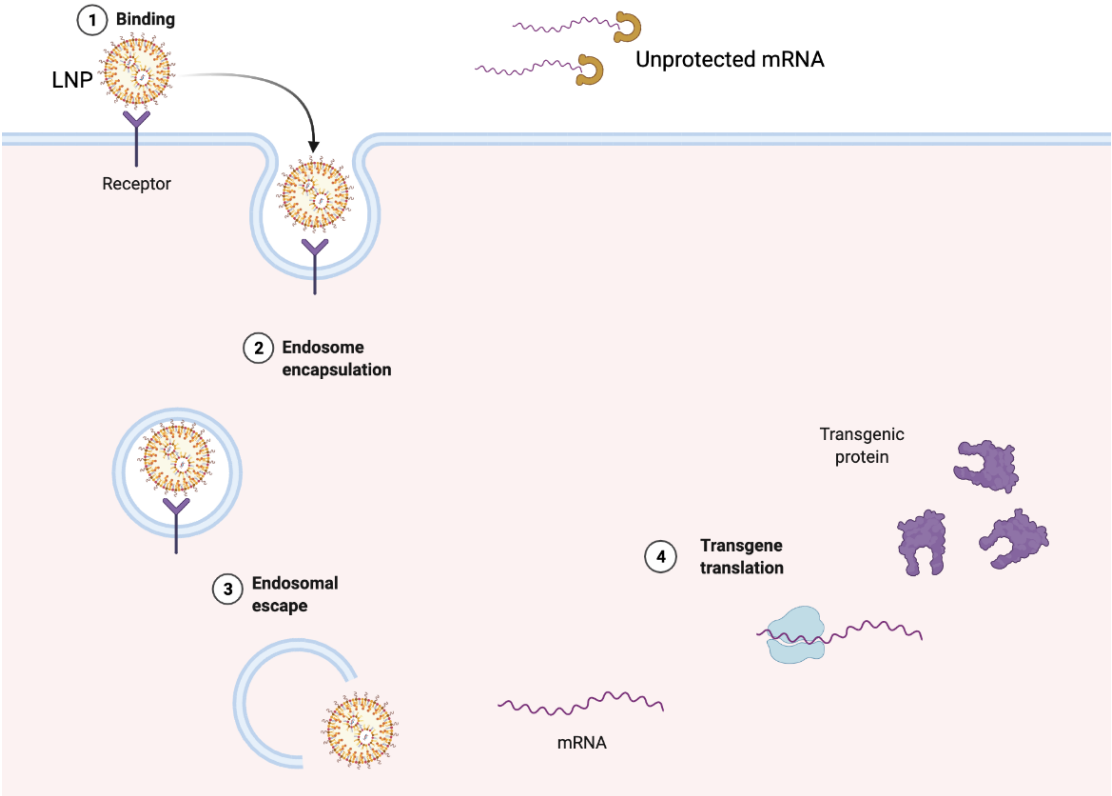

Figure 8. The mechanism of action of mRNA-LNP. Compared to unprotected mRNAs, they can be better captured by cells with the help of LNPs. LNPs are taken up

by the cell and then preserved in the endosome. The pH within endosomes progressively decreases (from ~6.5 to 4.5–5.0), a process that reprotonates ionizable lipids, conferring them a positive charge. This facilitates electrostatic interactions with negatively charged phospholipids in the endosomal membrane, thereby inducing membrane fusion or disruption to enable endosomal escape. Upon reaching the neutral cytoplasmic environment (pH ≈7.4), lipid deprotonation destabilizes the nanoparticle structure, leading to gradual mRNA release from the lipid matrix. The liberated mRNA is subsequently captured by free ribosomes to initiate translation. The mRNA is expressed and does not enter the nucleus and no gene conservation occurs.

After systemic administration, lipid nanoparticles (LNPs) are taken up by cells primarily via non-specific endocytosis, a process facilitated by their nanoscale size (~80–100 nm), neutral or slightly negative surface charge, and PEGylated coating, which also helps prolong circulation and reduce recognition by the mononuclear phagocyte system (MPS) [140, 141]. Once internalized, LNPs are encapsulated within early endosomes, which progressively acidify as they mature into late endosomes [109]. This pH drop (from ~6.5 to ~5.0) leads to the protonation of ionizable lipids within the LNP, converting them into positively charged species [88, 141]. These cationic lipids interact electrostatically with the negatively charged phospholipids in the endosomal membrane, disrupting membrane integrity through several mechanisms: (1) membrane fusion, where lipids merge with the endosomal bilayer to form transient pores; (2) non-lamellar phase transition, where structural rearrangement into an inverted hexagonal phase promotes membrane destabilization; (3) the proton sponge effect, where osmotic swelling due to proton accumulation induces endosomal rupture; and (4) charge-driven membrane perturbation, leading to leakage [141]. These mechanisms collectively enable the release of the encapsulated nucleic acids—such as mRNA—into the cytoplasm, where they can be translated by ribosomes. If the LNP fails to escape the endosome, its cargo is routed to lysosomes for enzymatic degradation, and the resulting waste may be removed from the cell via exocytosis [141]. Therefore, efficient endosomal escape is a major barrier to intracellular delivery and a key determinant of therapeutic efficacy. Its success is influenced by the physicochemical properties of the LNP, including the pKa and molecular geometry of ionizable lipids, the chain structure of helper lipids, the length and desorption rate of PEG-lipids, and the overall formulation design that governs the LNP's responsiveness to the endosomal environment [99].

As nucleic acids dissociate from the LNP core and enter the cytoplasm, they exert their respective functions [142]. For instance, mRNA is translated by ribosomes into functional proteins, typically without integrating into the host genome, allowing for transient expression. Meanwhile, LNP lipid components (such as ionizable lipids and cholesterol) are metabolized or excreted, while PEGylated lipids gradually detach during delivery. Eventually, the LNP particles are degraded by lysosomes. Through this sophisticated delivery mechanism, LNPs function as an "intelligent courier system" for nucleic acid therapeutics, balancing efficiency and safety, and significantly advancing the field of gene therapy [84].

1.3.3. LNP CQAs and Analysis Method

The Critical Quality Attributes (CQAs) of lipid nanoparticles (LNPs) are fundamental parameters that ensure safety, efficacy, and consistency, encompassing physical, chemical, biological, and stability aspects [143]. And Figure 9 shows general detection methods and equipment of LNP analysis.

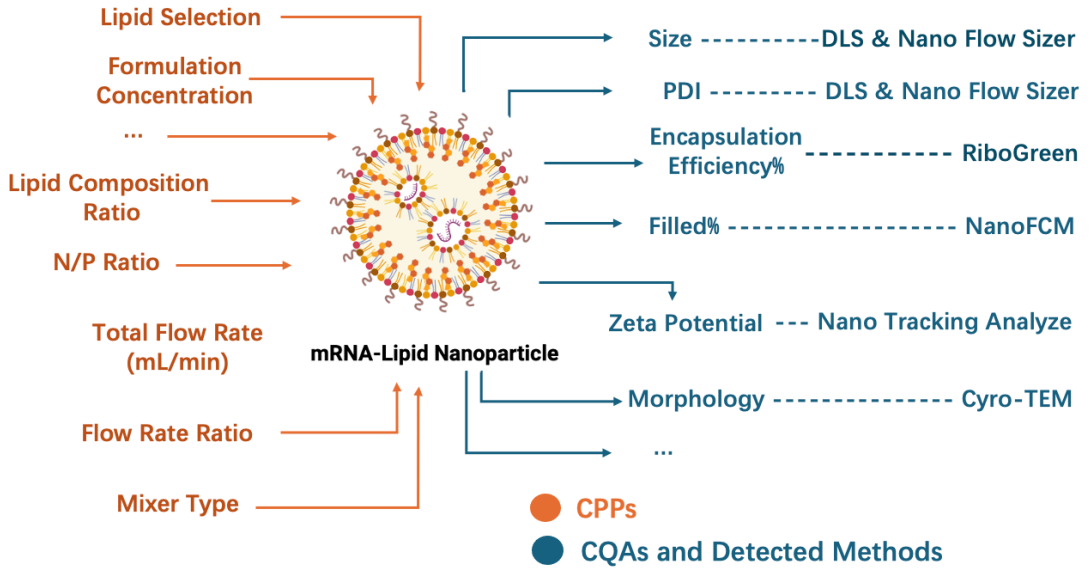

Figure 9. Analytical strategies and equipment methods for mRNA-LNP analysis. This figure demonstrates the effects of various key parameters during the preparation of mRNA-lipid nanoparticles (LNPs), including lipid ratios, flow rates, mRNA concentrations, and different mixer types. The figure also lists the various analytical methods used to characterise LNPs, such as particle size analysis, dynamic light scattering and NanoFCM, to help optimize the quality and properties of LNPs.

These attributes provide comprehensive quality control, covering LNP physicochemical properties and biological functionality, forming the foundation for the stability and therapeutic performance of gene delivery systems. During manufacturing, a Quality by Design (QbD) approach, combined with Process Analytical Technology (PAT), is essential for real-time monitoring and optimization, ensuring compliance with regulatory standards, enhancing clinical translation, and facilitating the industrialization of nucleic acid therapeutics. Table 3 summarizes the commonly used analytical techniques in lipid nanoparticle (LNP) manufacturing and quality control (QC) environments [143]. In early discovery and preclinical research stages, a broader range of techniques is typically employed—similar to those used for other nanoscale delivery systems—including physicochemical characterization, drug loading analysis, in vitro release studies, protein expression, immunogencity, and the stability evaluation. However, the listed methods reflect the current standard practices for routine QC and process monitoring during large-scale LNP production.

Table 3. CQAs for LNP and analytical methods and criteria [143, 46].

Critical Quality Attributes	Analytical Method	Unit	Acceptance Criteria
Size	dynamic light scattering	nm	20-200
PDI (Polydispersity Index)	dynamic light scattering	-	< 0.2
Zeta Potential (Surface charge)	dynamic light scattering	mV	>±20mV
Filled particles%	RiboGreen Assay/Nano Flow Cytometry	%	-
EE% (Encapsulation Efficiency) %	RiboGreen Assay	%	≥ 90%
Morphology	TEM/CryoEM	-	-

1.3.3.1. Particle Size and PDI (Polydispersity Index)

In nanoparticle preparation, particle size (nm) and polydispersity index (PDI) are critical parameters determining physical properties, biological behavior, and clinical potential. Size directly governs biodistribution and targeting particles of

80-150 nm (e.g., siRNA drug Onpattro®) efficiently penetrate liver sinusoidal endothelial gaps for hepatocyte targeting, while inhaled mRNA vaccines require sub-100 nm particles to reach deep alveoli, and sub-50 nm particles with cell-penetrating peptides can cross the blood-brain barrier [144]. PDI (ranging 0-1) reflects size uniformity, where high PDI (>0.3) causes delivery variability and dose inconsistency. Microfluidic technology achieves clinical-grade PDI (<0.1) through precise mixing. Notably, size and PDI regulation are decoupled—increasing cholesterol content improves PDI with minimal size effects, necessitating design of experiments (DoE) for lipid optimization [145]. The synergy between process innovation and formulation engineering is transforming passive delivery into precision medicine. Future integration of AI-driven modeling and interdisciplinary approaches will enable next-generation gene therapies through nanometer-scale precision control. During early formulation screening and method validation, complementary techniques including nanoparticle tracking analysis (NTA), nano-flow cytometry (NanoFCM), and cryo-electron microscopy (cryo-EM) were employed to validate size distribution and structural morphology, especially for complex or polydisperse systems [121]. While dynamic light scattering (DLS) remains the most widely used technique for measuring nanoparticle size and polydispersity index (PDI), recent advances have led to the development of refined platforms such as NanoFlowSizer (NFS), which enables real-time, in-process monitoring in manufacturing settings [146].

1.3.3.2. Zeta Potential

In nanoparticle systems, zeta potential (surface charge, mV) is a critical parameter characterizing colloidal stability, biodistribution, and cellular interactions. Measured via electrophoretic mobility, its value determines dispersion stability—near-neutral or slightly negative potentials (-10 to +10 mV) minimize nonspecific protein adsorption and prolong circulation, while highly positive potentials (>+20 mV) enhance cell membrane binding but trigger aggregation and immune clearance [146]. For LNPs, COVID-19 vaccines (e.g., Comirnaty®) maintain zeta potential at -2 to +2 mV through PEGylation, balancing immune evasion and hepatic targeting. In contrast, cationic liposomes (e.g., DOTAP-based vectors) exhibit zeta potentials >+30 mV, improving cellular uptake at the cost of toxicity [147]. Zeta potential must be

contextually optimized: brain-targeted LNPs require mild negativity (-5 to -10 mV) to bypass blood-brain barrier repulsion, while pH-responsive nanoparticles shift to positive charge in acidic tumor microenvironments to enhance uptake. Current strategies employ lipid composition tuning (e.g., ionizable lipid pKa design) and surface engineering (e.g., polysarcosine coatings) [148]. Future integration of stimuli-responsive materials and computational modeling will enable on-demand charge programming, ushering in an era of intelligent nanomedicine. For the measurement, Zeta potential was traditionally measured by electrophoretic light scattering (ELS) which still based on the DLS, but newer methods like phase analysis light scattering (PALS) offer higher sensitivity, especially for low-conductivity or viscous samples, improving accuracy in formulation development.

1.3.3.3. Filled Particles% and Encapsulation Efficiency (EE%)

In lipid nanoparticle (LNP) formulation development, Filled Particles% and Encapsulation Efficiency (EE%) serve as dual critical metrics, evaluating delivery system quality through "particle validity" and "payload economy" [149]. Filled Particles% reflects the proportion of nucleic acid-carrying particles (e.g., >95% in mRNA vaccines), minimizing empty particle competition for cellular uptake pathways. EE% quantifies the percentage of encapsulated nucleic acid relative to total input (e.g., >90%), directly determining material utilization and production costs. While both can be preliminarily screened via RiboGreen fluorescence assays, process optimization requires advanced strategies: tuning ionizable lipid/nucleic acid charge ratios promotes preferential encapsulation, and microfluidic turbulent mixing enhances uniformity, synergistically improving both metrics. The COVID-19 mRNA vaccine exemplifies this balance, achieving >90% in both parameters through precise lipid/mRNA ratio control [150]. Future integration of in-line fluorescence monitoring with microfluidic real-time feedback systems will enable dynamic parameter adjustment. Machine learning models analyzing historical process data to predict optimal N/P ratios and mixing conditions promise to revolutionize LNP manufacturing by reducing trial-and-error cycles and advancing intelligent precision production. Encapsulation efficiency (EE%) and filled particle percentage are commonly assessed using fluorescence-based assays or ultracentrifugation techniques. Recent advances, such as nano-flow cytometry

(NanoFCM) and single-particle imaging, now enable direct quantification at the individual particle level, offering higher resolution and improved accuracy for heterogenous populations [149].

1.3.3.4. Morphology

The morphology of lipid nanoparticles (LNPs) is a critical determinant of their delivery efficiency, stability, and biodistribution. Typically exhibiting a core-shell structure, LNPs compress nucleic acids within a lipid core surrounded by a stabilizing outer layer of phospholipids, cholesterol, and PEG lipids. Cryo-TEM reveals that COVID-19 vaccine LNPs (e.g., Comirnaty®) display a uniform core-shell morphology (50 nm core, 5-10 nm shell), essential for efficient delivery [151]. Advanced techniques like SAXS and AFM further decode lipid phase behavior and surface topology, linking smooth PEG-coated surfaces to prolonged circulation [152]. Morphology control strategies—such as branched ionizable lipids (e.g., ALC-0315) and microfluidic turbulence—enable spherical monodisperse particle. Emerging research explores stimuli-responsive morphologies (pH/light-triggered transformations) and AI-driven design to predict structure-function relationships. Challenges remain in maintaining morphological consistency during scale-up and addressing dynamic biological interactions. Understanding LNP morphology bridges nanoscale engineering to clinical efficacy, paving the way for intelligent delivery systems. Cryo-transmission electron microscopy (cryo-TEM) is particularly suitable for observing lipid nanoparticles (LNPs) because it allows visualization of particles in their near-native hydrated state without staining or drying. Compared to conventional TEM or SEM, cryo-TEM preserves the delicate lipid bilayer structure and internal morphology, providing nanometer-scale resolution of size, shape, lamellarity, and encapsulated content. This makes it ideal for validating LNP structural integrity and heterogeneity during formulation development.

1.3.3.5. Cell Experiment

In the development of lipid nanoparticles (LNPs), biological experiments serve as the cornerstone for validating delivery efficiency, safety, and functionality. Transfection efficiency testing is particularly critical, as it determines whether LNPs can effectively deliver nucleic acids to target cells and exert therapeutic

effects. Cytotoxicity assessment is essential to ensure biosafety, while for specific LNPs, targeting specificity validation is required to guarantee precise delivery. Looking ahead, integrating organoid models, single-cell sequencing, and computational modeling will further enhance the predictive power of biological testing, accelerating the translation of LNPs from bench to bedside.

1.3.4. LNP future strategy

The development of mRNA-LNP-based COVID-19 vaccines began with the genomic analysis of SARS-CoV-2 and the identification of the spike protein as a key antigenic target. Subsequently, mRNA encoding the antigen was synthesized via in vitro transcription and encapsulated within lipid nanoparticles (LNPs) to enhance in vivo stability and transfection efficiency. During the preclinical phase, the vaccine was systematically evaluated for immunogenicity and safety in vitro and in animal models, with further optimization of mRNA structure and lipid formulation to improve delivery performance. Clinical trials proceeded through Phase I (safety and tolerability), Phase II (immune response), and Phase III (protective efficacy). Under the urgency of the pandemic, regulatory authorities employed rolling review and Emergency Use Authorization (EUA) pathways to expedite approval. Following favorable Phase III outcomes, a New Drug Application (NDA) or Biologics License Application (BLA) was submitted, and upon approval, the vaccine was authorized for market release. Post-marketing surveillance through Phase IV trials continues to assess long-term safety and effectiveness.

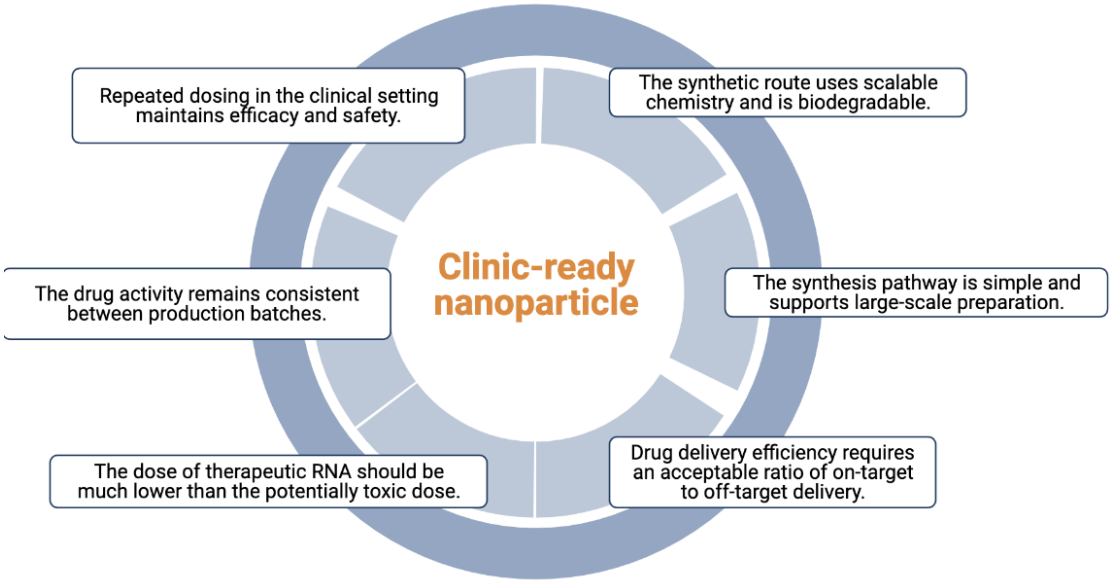

Figure 10.Six characteristics of successful nucleic acid-lipid nanoparticle drug delivery systems. The incorporation of ester bonds by ionizable lipids can improve the safety of LNPs. Targeted and off-target delivery needs to be measured using both biodistribution and functionalization metrics. In the case of RNA-LNP, for example, 95% of the RNA may be retained in endosomes and biodistribution does not predict functional delivery of RNA. Conditions permitting, toxicological studies should be carried out in non-human primates.

The future evolution of lipid nanoparticle (LNP) manufacturing will focus on technological integration and precision control: Microfluidic advancements with real-time sensors (e.g., NanoFlowSizer) enable dynamic parameter optimization (flow rate/temperature), while continuous-flow architectures—integrated with tangential flow filtration (TFF) systems—shorten nucleic acid drug production cycles to under 30 days. AI-driven platforms like MIT's LNP-OPT leverage generative AI to analyze historical data, predicting optimal N/P ratios and particle sizes (<5% error), while digital twins simulate lyophilization ice crystal effects to refine cryoprotectants [153]. Clinically, CureVac's Dry-Print technology unifies mixing-purification-lyophilization, and portable microfluidic devices (e.g., NanoGenerator®) empower point-of-care production of personalized neoantigen vaccines (e.g., BioNTech's CAR-T mRNA therapies) [154]. Ultimately, LNP manufacturing will converge continuous flow, AI design, green chemistry, and precision medicine into a closed-loop ecosystem bridging labs to clinics.

1.4. LNP Formulation and Manufacturing

Lipid-based nanoparticles (LNPs) have evolved from traditional liposome technologies, which have been studied as drug delivery systems for over half a century. While liposomes typically exhibit lamellar bilayer structures, LNPs used for nucleic acid delivery often display non-lamellar internal morphologies, such as inverted micelles or amorphous cores, tailored to enhance encapsulation efficiency and cellular uptake. Traditional liposome preparation techniques have been adapted and optimized to meet the specific demands of nucleic acid delivery, forming the foundation for current LNP production strategies. The following section reviews several conventional preparation methods, highlighting their mechanisms and limitations to inform future process optimization.

1.4.1. Thin-film hydration

The thin-film hydration method (also known as the Bangham method or hand-shaking technique), recognized as the pioneering liposome preparation technology, involves three fundamental steps: dissolving lipid components (cationic DOTAP, phospholipids, and cholesterol) in organic solvents like chloroform to form a homogeneous mixture, followed by solvent removal via rotary evaporation under vacuum to create a uniform lipid film on the flask wall—a rate-limiting step requiring hours of drying [155]. Subsequent hydration with nucleic acid-containing buffer (siRNA/mRNA) induces lipid film detachment and self-assembly into multilamellar vesicles, which are then processed through membrane extrusion or sonication to yield monodisperse nanoparticles. While valued for its minimal equipment requirements and low cost in laboratory-scale production, this method faces critical limitations including low nucleic acid encapsulation efficiency (<30%), broad size distribution (PDI>0.3), and organic solvent residue risks, driving its gradual replacement by modern microfluidic technologies in industrial applications [156].

1.4.2. Ethanol Injection

Ethanol Injection (EI) is a classical method for LNP preparation, which involves the dissolution of lipids in ethanol to form a homogeneous solution, followed by a rapid injection of nucleic acid-containing aqueous phase, which results in the self-assembly of lipids to form LNPs, and the eventual removal of the ethanol by dialysis or ultrafiltration to complete the purification [157]. The core mechanism of this method, proposed by Batzri and Korn in 1973, is based on the self-assembly behavior of lipids at the interface between ethanol and the aqueous phase, leading to the rapid formation of nanoparticles. The main advantage of this method is the mildness of the process, which avoids the risk of nucleic acid degradation at high temperatures, and has been used in the development of early siRNA-LNPs. However, its limitation is the difficulty in controlling ethanol residues, especially when ethanol forms azeotropes with water, and the difficulty in completely removing the solvent by conventional methods [158]. In addition, the method has a weak control of particle size homogeneity, which is significantly affected by the injection rate and tends to

lead to a high polydispersity index (PDI) (<0.25). To address these issues, the researchers proposed an improved strategy by using an aqueous phase injection of ethanol and removing the solvent by rotary evaporation to reduce the ethanol residue and optimize the particle size distribution. However, this method still has some limitations, such as the low solubility of some lipids in ethanol, and the possibility that ethanol may trigger the denaturation of some bioactive molecules, thus affecting its application.

1.4.3. Reverse Phase Evaporation

Reverse Phase Evaporation (REV) is a liposome preparation method, first proposed by Szoka and Papahadjopoulos in 1978, whose main feature is the formation of anticellular micelles or water-in-oil (w/o) emulsions during the preparation process, which significantly improves the encapsulation rate of water-soluble drugs [159]. Compared with the thin-film hydration and ethanol injection methods, this method can achieve up to 65% encapsulation of water-soluble drugs in low ionic strength media (e.g., 0.01 M NaCl), and it is one of the most effective ways to encapsulate hydrophilic drugs in conventional liposome preparation methods. The preparation process involves dissolving the lipids in an organic solvent, followed by addition of an aqueous phase and emulsification using intermittent ultrasound to form anticellulose micelles, and then placing the emulsion in a rotary evaporator for evaporation under reduced pressure to evaporate the organic solvent to form a viscous gel, after which the addition of an aqueous phase is continued and further evaporation is carried out until sufficient hydration is achieved, and the gel collapses and forms an aqueous suspension of the liposomes when enough of the organic solvent is removed. This method is more effective in retaining the aqueous phase and improving the drug-carrying capacity of hydrophilic drugs, but there are some limitations. It is not applicable to easily degradable molecules (e.g., peptides) because the water-soluble drug is directly dissolved in the aqueous phase and comes into direct contact with organic solvents during emulsification and evaporation, as well as being subject to sonication [160]. In addition, the method is prone to residual organic solvents during preparation, which may interact with lipids or drugs and affect the quality and safety of the final product.

1.4.4. Microfluidic Technology

Microfluidics Technology (Microfluidics) is a fluid manipulation technology based on micron-scale channels (10-100 μm), with its core principle lying in the precise design of microscale hydrodynamic behaviors (e.g., laminar flow, diffusion-dominated mixing, surface tension effects) to achieve high-precision control of picolitre- to nanoliter-scale fluids [161, 162]. The integration of 3D printing, nanomaterials, and intelligent sensing technologies in the early 21st century further expanded its application boundaries in organ-on-a-chip, single-cell sequencing, and drug delivery [163]. In recent years, microfluidics has gradually become the technological paradigm in the synthesis of lipid nanoparticles (LNPs), replacing traditional liposome preparation processes (e.g., ethanol injection, reverse evaporation) and providing revolutionary solutions for the clinical translation of nucleic acid drugs and mRNA vaccines, owing to its advantages in high throughput, reproducibility, and modularity [164].

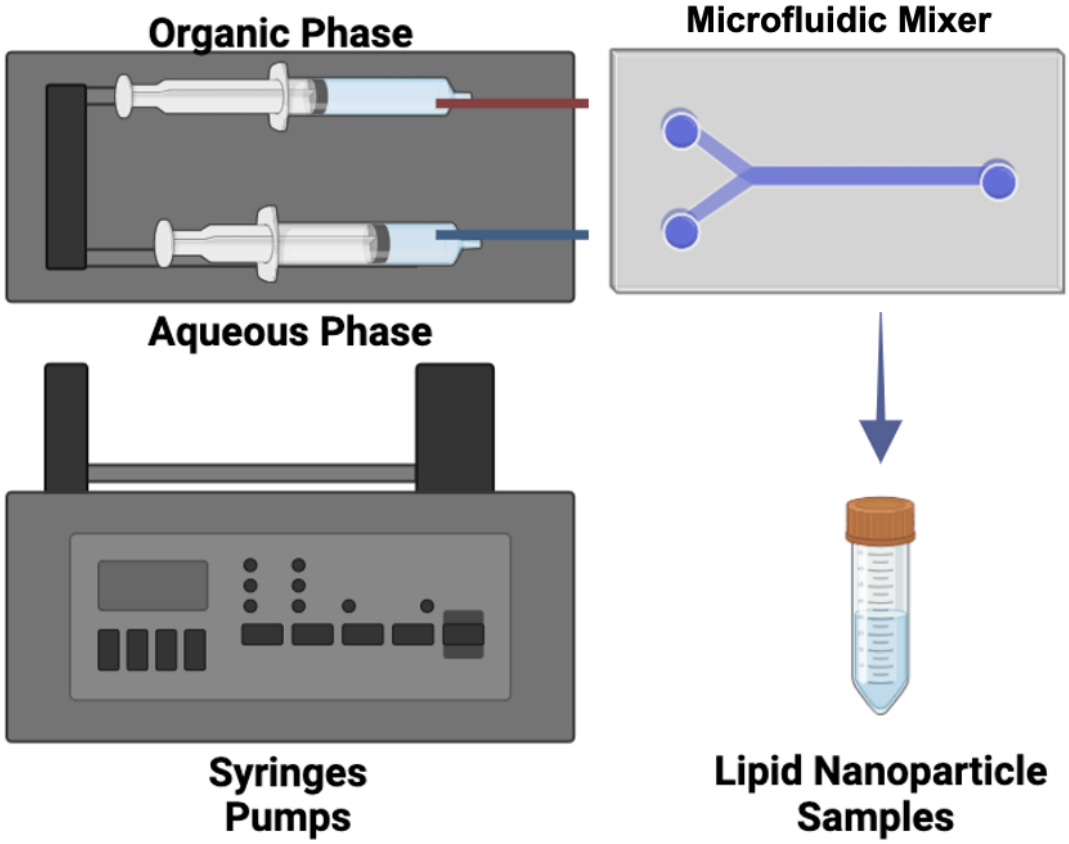

Figure 11. A basic microfluidic device and co-flowing junction. High flow rates can produce smaller sized lipid nanoparticles, however, when flow rates are too high, microfluidic devices inevitably have some problems. For example, the microfluidic chip is short-circuited and the pump is unable to inject the chip at the set rate due to resistance.

Microfluidic technology drives the rapid mixing of the lipid-containing organic phase and nucleic acid-containing aqueous phase within microchannels, where solvent polarity changes trigger rapid lipid precipitation and self-assembly, yielding monodisperse lipid nanoparticles [165]. Compared to conventional methods, microfluidics enables rapid homogeneous mixing of lipid-alcohol and aqueous buffer phases within milliseconds through precise fluid control in microchannels. Additionally, active mixing strategies (e.g., acoustic agitation, electroosmotic actuation) further enhance mixing uniformity for complex fluids, such as high-viscosity nucleic acid solutions. Studies confirm that microfluidically synthesized LNPs significantly improve nucleic acid cellular uptake efficiency and reduce immunogenicity due to their uniform coating structures and well-defined core-shell interfaces [166].

In industrial-scale applications, the scalability and process controllability of microfluidics have emerged as critical advantages. The microfluidic platforms adopted by BioNTech and Moderna for COVID-19 mRNA vaccine production integrate online dynamic light scattering (DLS) and Raman spectroscopy for real-time monitoring of particle size and encapsulation efficiency, enabling seamless scaling from laboratory to hectoliter reactors [167]. Currently, the technology is advancing toward intelligent manufacturing, where machine learning algorithms optimize fluid parameters (e.g., flow rate, mixing ratio) to adaptively regulate LNP targeting and drug release kinetics, laying the technical foundation for personalized precision medicine [168].

Laminar flow occurs when mixed fluid flows in parallel layers without forming a perpendicular or opposite flow to the main direction, and each molecule follows the path of the previous one. In contrast, turbulence occurs when the fluid undergoes irregular fluctuations, resulting in continuous mixing of size and direction. For tube flow, Reynolds numbers less than 2300 indicate laminar flow, 2300-4000 indicate transitional flow, and values greater than 4000 indicate turbulence dominated by inertial forces.

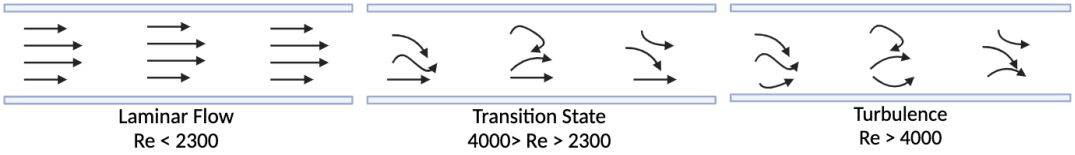

Figure 12. Schematic diagram of fluid flow as a function of Reynolds number

The type of flow is governed by viscous and inertial forces, usually measured by the Reynolds number. To characterize the flow properties, the Reynolds (Re) number was calculated using the following equation (1) below, where $\rho(kg/m^3)$ is the density of the fluid, $u(m/s)$ is the velocity of the fluid, $Dh(m)$ is the characteristic dimension (When the channel is circular, the Dh is diameter of the pipe), and $\mu(Pa \cdot S)$ is the viscosity of the fluid. $A(m^2)$ is the cross-sectional area of the fluid channel and $P_{wet}(m)$ is the wetted perimeter of the channel (i.e., the perimeter of the fluid contact). In addition, at low Reynolds numbers (less than 2300), fluid flow is primarily dominated by viscous forces, resulting in a laminar state.

The Péclet number (Pe) is a crucial parameter in microfluidic systems, describing the balance between convective transport and molecular diffusion, where $u(m/s)$ is the local velocity, $l(m)$ is the characteristic length, and $D(m^2/s)$ is the mass diffusion coefficient. A higher Péclet number implies that convective transport significantly surpasses diffusion, which helps minimize molecular exchange between the dispersed and continuous phases, thereby enhancing encapsulation efficiency. These calculations can precisely regulate the mixing speed and other parameters to ensure the stable synthesis of high-quality LNP, which provides a key process guarantee for the production of gene drugs and vaccines [169]

1.5. mRNA manufacturing and Purification

Less than a week after the outbreak of the COVID-19 pandemic, scientists swiftly released the complete genome sequence of the novel coronavirus (SARS-CoV-2). This rapid genomic analysis enabled researchers to commence

the design and development of mRNA vaccines based solely on the viral genetic information, without the need to obtain actual pathogen samples, thereby significantly reducing vaccine development timelines. Traditionally, vaccine development necessitates the isolation, cultivation, and inactivation of pathogens—a process that is both time-consuming and complex. In contrast, mRNA vaccine development requires only the known genetic sequence of the pathogen. Following the release of the SARS-CoV-2 sequence, Moderna developed its first batch of candidate vaccines in just 28 days, a response speed unprecedented in prior vaccine development efforts [170].

1.5.1. DNA Template Prepared

The construction and production of plasmid DNA predominantly utilize Escherichia coli expression systems, where target genes are inserted into specific plasmid vectors via molecular cloning, followed by restriction endonuclease digestion, ligase-mediated recombination, bacterial transformation, high-density fermentation, and chromatographic purification (e.g., anion-exchange chromatography) to obtain high-purity supercoiled plasmids. Linearization is achieved through restriction enzyme-specific cleavage or recombinase treatment to eliminate autonomous replication risks of circular DNA and enhance biosafety in mRNA in vitro transcription (IVT) and gene therapy. While this system offers advantages such as mature processes, cost-effectiveness, and scalability, limitations including endotoxin contamination, supercoiled structural heterogeneity, and byproduct interference from incomplete linearization require optimization of plasmid design (e.g., antibiotic marker-free backbones) and precise enzymatic reaction control to improve product quality and safety.

1.5.2. mRNA In vitro transcription reaction

In vitro transcription (IVT) of mRNA is a cell-free process that synthesizes primary mRNA using a linearized DNA template (containing T7/SP6 promoters and target sequences), RNA polymerase (e.g., T7 RNA polymerase), nucleotides (NTPs), and modified nucleosides (e.g., pseudouridine). This is followed by enzymatic or co-transcriptional addition of 5' cap structures and 3' Poly(A) tails to enhance stability and translational efficiency[171]. The final therapeutic-grade mRNA is purified via chromatography (e.g., oligo-dT affinity)

or tangential flow filtration to remove unreacted components and double-stranded RNA byproducts. While IVT offers rapid production (within days), adaptability (to pathogen mutations and personalized antigen design), and absence of genomic integration risks, challenges persist, including mRNA instability, potential immunogenicity, and high purification costs at scale. Furthermore, despite its accelerated workflow, optimizing reaction conditions and scaling up production require computational modeling (e.g., multiphysics simulations) and machine learning algorithms to enhance yield and batch consistency. Future advancements necessitate nucleotide modification (e.g., N1-methylpseudouridine), improved capping analogs (e.g., CleanCap®), and efficient purification strategies (e.g., CRISPR-based dsRNA removal) to ensure product quality and clinical safety [172].

1.5.3. mRNA Purification

Following in vitro transcription (IVT) of mRNA, industrial-scale purification constitutes a critical step to ensure product purity, safety, and functionality. Current methodologies predominantly employ chromatographic methods, precipitation techniques, and tangential flow filtration (TFF) for mRNA purification. In mRNA precipitation purification, most technologies operate via modulation of intermolecular electrostatic interactions among RNA molecules. High-concentration ammonium sulfate (1.8-2 M) disrupts electrostatic repulsion between RNA molecules, inducing aggregation and precipitation. However, this approach demonstrates limited efficiency in removing T7 RNA polymerase. TFF employs ultrafiltration membranes to separate substances by molecular weight, serving purposes such as concentration, buffer exchange, and removal of low-molecular-weight impurities. Nevertheless, TFF primarily functions as a pretreatment step prior to chromatography and final buffer formulation. Chromatographic methods remain central to industrial mRNA purification, utilizing poly(A) tail interactions with oligo(dT) ligands immobilized on chromatographic columns through AT base-pairing (hydrogen bonding). High-salt conditions suppress electrostatic repulsion to facilitate binding, followed by low-salt elution [173].

Exemplified by the ÄKTA Oligo(dT) chromatography system(figure 13 shows below), specifically engineered for PCC applications at process development

and manufacturing scales, this technology integrates upstream and downstream unit operations (e.g., continuous perfusion culture and inline inactivation), significantly reducing footprint, resin consumption, and overall process time[174]. With real-time monitoring (e.g., UV absorbance, conductivity feedback) and validated linear scale-up strategies, PCC stabilizes the purification of labile molecules (e.g., viral vectors or mRNA-protein complexes), maintaining >95% target product activity retention. Compared to batch chromatography, PCC enhances productivity by 30-50%, reduces buffer usage by over 60%, and decreases column volume to one-third of conventional processes [175].

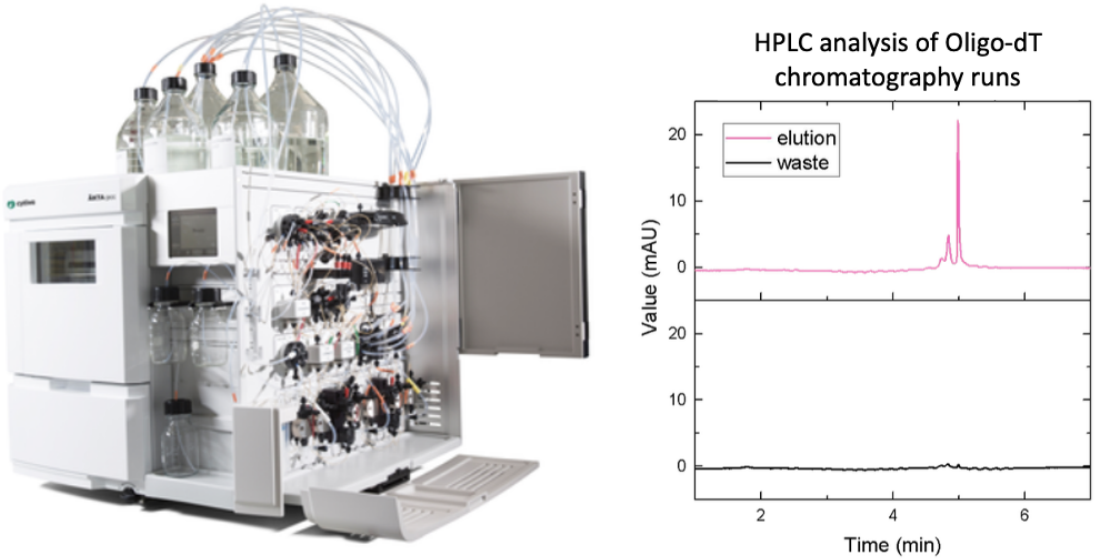

Figure 13. The AKTA PCC. An automated liquid chromatography system for Oligo-dT purification equipped with multiple fluid pathways and reservoir bottles for efficient nucleic acid separation. The results were analysed in high performance liquid chromatography (HPLC), indicating the successful elution of Oligo-dT.

Nevertheless, challenges such as complex valve-switching logic and dynamic equilibrium control require optimization through multivariate modeling (e.g., mass balance equations coupled with computational fluid dynamics) and AI-driven algorithms to address column efficiency decay and cross-contamination risks [176]. Future integration with modular bioreactors and adaptive control platforms will accelerate the industrialization of continuous biomanufacturing.

1.6. LNP Purification

The post-formulation purification of lipid nanoparticles (LNPs) is designed to remove unencapsulated nucleic acids (e.g., free mRNA/DNA), free lipids (unbound lipid molecules), and organic solvents (e.g., ethanol), while accomplishing buffer exchange to adapt to storage or administration conditions [81, 101]. This process achieves multiple objectives through selective separation techniques: eliminating unencapsulated nucleic acids reduces immunogenicity and off-target risks; removing free lipids prevents their self-assembly into heterogeneous particles or induction of in vivo toxicity; controlling residual organic solvents (e.g., ethanol ≤0.1%, compliant with ICH Q3C standards) ensures injection safety; and transitioning to an optimized buffer system (e.g., pH 7.4 PBS) maintains long-term colloidal stability of LNPs [177]. Current mainstream purification strategies rely on physical size-based separation mechanisms.

1.6.1. Dialysis

Dialysis, a classical purification technology based on semipermeable membrane diffusion, selectively removes small-molecule impurities while retaining lipid nanoparticles for solvent exchange and impurity clearance [178]. The core procedure involves loading crude LNPs into dialysis tubing (MWCO10-50 kDa) immersed in a target buffer (e.g., PBS or Tris-HCl), where ethanol and other small molecules passively diffuse out driven by concentration gradients, typically requiring multiple buffer changes to reduce residual ethanol. Dialysis offers notable advantages at lab scale: low equipment cost (no pumps or pressure control), operational simplicity, and near-zero shear stress to preserve LNP structural integrity [179]. However, limitations include prolonged processing time, low throughput (milliliter-scale), and inefficient removal of free lipid aggregates with sizes comparable to LNPs. Mitigation strategies include gradient dialysis, prefiltration (e.g., 0.22 μm filters for large particles), or hybrid workflows combining dialysis with tangential flow filtration (TFF). Although largely replaced by high-efficiency TFF in industrial production, dialysis retains value in small-scale research, early process development, and shear-sensitive formulations (e.g., mRNA-protein complexes) [180].

1.6.2. Ultra-filtration

Ultra-filtration (UF) is a membrane-based purification technology that selectively retains lipid nanoparticles (LNPs, 50-150 nm in diameter) using ultrafiltration membranes with controlled molecular weight cutoffs (MWCO 10-300 kDa), while removing small-molecule impurities such as free nucleic acids, organic solvents, and salts. The core procedure involves circulating crude LNPs under high-speed centrifugal force across the membrane surface, where permeate carries away impurities, and retentate is concentrated for buffer exchange to obtain high-purity LNPs. However, the high-speed centrifugal force imposes stringent equipment requirements, and shear forces during the process may induce particle rupture, leading to mRNA loss. Despite being gradually replaced by tangential flow filtration (TFF) in large-scale production, ultra-filtration remains widely utilized in small-scale laboratory settings and rapid buffer optimization studies due to its operational simplicity and high efficiency [181].

1.6.3. Tangential flow filtration

The inefficiency of dialysis and the structurally disruptive high shear forces inherent in ultrafiltration collectively drove the breakthrough development of tangential flow filtration (TFF) for lipid nanoparticle (LNP) purification [182]. TFF revolutionizes traditional filtration through crossflow design, where fluid flows parallel to ultrafiltration membranes, selectively retaining LNPs while removing unencapsulated nucleic acids, free lipids, and organic solvents, with continuous tangential scouring significantly reducing membrane fouling. By precisely regulating transmembrane pressure (TMP), tangential flow rate, and concentration factor, TFF achieves >90% LNP recovery while maintaining polydispersity index (PDI) and encapsulation efficiency [183]. Compared to ultracentrifugation and dialysis, TFF has become a cornerstone technology in industrial mRNA vaccine production due to its high throughput (hectoliter-scale batch processing), linear scalability (membrane area 0.1-10 m^2), and low-shear stress design [169].

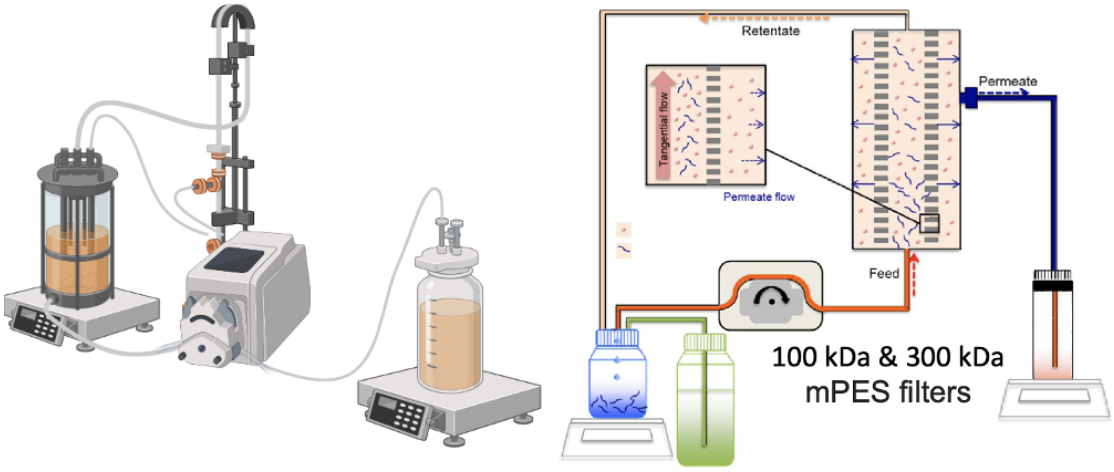

Figure 14. A tangential flow filtration (TFF) system, comprising a feed tank, pump, and filtration module, purifies and concentrates targets (e.g., LNPs or mRNA) by directing samples parallel to ultrafiltration membranes (selected by molecular weight cutoff). During recirculation, low-molecular-weight impurities (e.g., free nucleotides, solvents) exit as permeate, while targets are retained in the retentate. Its tangential flow mode and transmembrane pressure control minimize membrane fouling, making TFF vital for scalable biopharmaceutical manufacturing.

Challenges such as flux decline from membrane fouling and residual surfactant interference are addressed through membrane material modifications (e.g., hydrophilic PES coatings), inline turbidity monitoring, and periodic backflushing to enhance process robustness. Future integration with continuous manufacturing and artificial intelligence-driven dynamic parameter modulation (e.g., real-time TMP/flow rate optimization) will further elevate the production efficiency and quality consistency of gene therapies, advancing their transition toward cost-effective and compliance-ready therapeutics

1.7. Conclusion

This review systematically traces the evolution of vaccine development from empirical inoculation methods to the contemporary era of mRNA–lipid nanoparticle (mRNA-LNP) platforms, highlighting how technological convergence across microbiology, immunology, nanomedicine, and synthetic biology has revolutionized vaccine design and production. By categorizing vaccines into inactivated, viral vector, protein subunit, and mRNA types, the review compares their preparation techniques, production challenges, storage requirements, and global accessibility. Special attention is given to mRNA

vaccines, which, owing to their rapid production speed and high adaptability, have redefined vaccine manufacturing paradigms, despite challenges related to stability and distribution.

Expanding beyond vaccines, the review delves into gene delivery technologies, analyzing the advantages and limitations of viral vectors, polymeric nanoparticles, inorganic nanoparticles, and lipid-based systems. Among these, lipid nanoparticles (LNPs) are identified as the most promising carriers for nucleic acid therapeutics due to their superior biocompatibility, delivery efficiency, and modular design. Detailed discussions cover the composition of LNPs (ionizable lipids, helper lipids, cholesterol, PEG-lipids), their endosomal escape mechanisms, and critical quality attributes (CQAs) essential for ensuring product consistency and therapeutic performance. Furthermore, the review emphasizes the importance of process development in mRNA and LNP production, including the evolution from traditional liposome preparation methods to advanced microfluidic-based continuous manufacturing. Key manufacturing challenges, such as encapsulation efficiency, stability, and scalable purification via tangential flow filtration (TFF), are addressed, underscoring the integration of quality-by-design (QbD) principles and real-time process analytical technologies (PAT).

The comprehensive understanding established here lays a solid theoretical foundation for subsequent experimental studies. Specifically, it underscores the critical role of LNP formulation parameters (such as lipid composition, particle size, and encapsulation efficiency) and purification strategies (such as TFF and dialysis) in determining the biological performance of nucleic acid therapeutics. This insight will guide the optimization of LNP synthesis conditions, buffer systems for dialysis, and the implementation of scalable, reproducible, and GMP-compliant manufacturing processes. The detailed discussion on CQAs will also inform the design of robust analytical methodologies necessary for real-time monitoring and quality control in experimental setups, ultimately advancing the transition from laboratory research to clinical translation.

2. Experiments Sections and Materials, Reagent & Equipment

2.1. Materials and Reagent

2.1.1. mRNA In Vitro Reaction Reagent

Table 4. mRNA IVT reaction reagent and experiment concentration

Materials	Supplier	Catalogue/Lot Number	Stock Concentration
ATP	Roche	4980824103	10 mM
CTP	Roche	4980875103	10 mM
UTP	Roche	4979818103	10 mM
GTP	Roche	4980859103	10 mM
IPP	Roche	8140677103	0.05 U/μL
T7 polymerase	Roche	8140669103	246.1 U/μL
RNase inhibitor	Roche	09537589103	1 U/μL
HEPES	Gibco	15630080	1 M
Magnesium acetate	Sigma-Aldrich	M2545	2 M
DTT	Thermo Fisher	R0861	1 M
Spermidine	Sigma-Aldrich	S2626	6.4 M
eGFP DNA template		-	-

2.1.2. mRNA Lipid Nanoparticle Formulation & Analysis

Table 5. LNP microfluidic formulation reagent and materials

Materials	Supplier	Catalogue/Lot Number	Stock Concentration
Cholesterol	BOC Science	B21LN11182	N/A
ALC-0315	BOC Science	B23V12291	N/A
Dlin-MC3-DMA	AVT	1224606-06-7	N/A

SM102	BOC Science	BL-M000103	N/A
DSPC	BOC Science	BL-M000029	N/A
DOPE	BOC Science	B24V03292	N/A
PEG-2000-Mal	AVT	474922-22-0	N/A
ALC-0159	BOC Science	B22V04063	N/A
Ethanol	VWR	23C304006	N/A
Acetate buffer	Thermo Fisher	R0861	1 M
PBS buffer	Sigma-Aldrich	S2626	1 M
HEPES buffer	Sigma-Aldrich	83264	1 M
Tris Buffer	Thermo Fisher	A11379	1 M

2.1.3. E. coli and Cell Line Material

Table 6. E. coli Culture Reagent

Materials	Supplier	Catalogue/Lot Number	Stock Concentration
Tryptone	Sigma-Aldrich	T4532	N/A
Yeast Extract	Sigma-Aldrich	07533	N/A
NaCl	Thermo Fisher	J21618.36	N/A
Agar	Thermo Fisher	30391623	N/A
Kanamycin Sulfate	Thermo Fisher	15160054	100 X, 10 mg/mL
Plasmid Extract Kit	QIAGEN	27104	N/A

Table 7. HEK293 Cell Line Reagent

Materials	Supplier	Catalogue/Lot Number	Stock Concentration
DMEM	Sigma-Aldrich	D6429	1 x
FluoroBrite™ DMEM	Gibco	A1896701	1 x
Fetal Bovine Serum	Thermo Fisher	A5670701	1 x
Pen-Streptomycin	Thermo Fisher	15071163	5000 Unit/mL
Trypsin-EDTA	Thermo Fisher	15160054	0.25% phenol red

PBS buffer	Gibco	10010023	1 x
mRNA Trans-IT Kit	Mirus	MIR2225	N/A

2.2. mRNA Phase Prepare

2.2.1. DNA template prep and linearization

Enhanced Green Fluorescent Protein (eGFP) was selected as a model gene due to its high stability, strong fluorescence signal, and extensive use as a reporter in gene delivery and expression studies. The eGFP plasmid was initially amplified by transforming Escherichia coli DH5α competent cells via the heat shock method. Briefly, 5 µL of eGFP plasmid (10–100 ng) was added to 50 µL of chemically competent DH5α cells, incubated on ice for 30 minutes, heat-shocked at 42°C for 45 seconds, and then placed back on ice for 2 minutes. Subsequently, 500 µL of LB broth was added, and the mixture was incubated at 37°C with shaking at 200 rpm for 1 hour. The transformed cells were plated onto LB agar plates containing 100 µg/mL ampicillin and incubated overnight at 37°C. Single colonies were picked and inoculated into 5 mL of LB broth with ampicillin (100 µg/mL), and grown overnight (8–12 h) at 37°C, 200 rpm. The culture was then scaled up to 50–100 mL for high-yield plasmid extraction.

Plasmids were extracted using the QIAGEN Plasmid Miniprep Kit following the manufacturer's protocol. Lysis, neutralization, and binding to silica membranes were carried out under standard alkaline lysis conditions. The plasmid DNA was eluted in nuclease-free water or TE buffer. DNA concentration was measured using a NanoDrop 2000 spectrophotometer via the absorbance of the 260 nm wavelength UV light, while sample purity was evaluated by 260/280 and 260/230 absorbance ratios. Acceptable purity was defined as a 260/280 ratio of 1.8–2.0 and a 260/230 ratio >2.0. If the concentration of eluted plasmid was insufficient for downstream applications (typically <100 ng/µL), samples were further concentrated using a centrifugal DNA concentrator (e.g., Amicon Ultra-0.5, 30 kDa MWCO) at 14,000 × g for 10–15 minutes. To prepare for in vitro transcription (IVT), the plasmid was linearized using the restriction enzyme SfiI (New England BioLabs). The digestion was performed in a total volume of 50 µL containing 2–3 µg of plasmid DNA, 1× CutSmart buffer, and 1 µL of SfiI-HF

enzyme, and incubated at 50°C for 10–15 minutes. Complete linearization was verified by running 1–2 µL of the reaction mixture on a 1% agarose gel stained with GelRed or SYBR Safe dye. Linearized plasmids were then purified to remove enzymes and potential contaminants using phenol: chloroform (1:1 v/v) extraction. An equal volume of equilibrated phenol:chloroform was added to the digestion mixture, vortexed vigorously for 30 seconds, and centrifuged at 13,000 × g for 10 minutes at room temperature. The aqueous (top) phase was carefully collected and mixed with 2.5× volume of cold ethanol and 0.1 volume of 3 M sodium acetate (pH 5.2), followed by incubation at –20°C for 1 hour. DNA was pelleted by centrifugation at 14,000 × g for 15 minutes, washed with 70% ethanol, air-dried, and re-dissolved in nuclease-free water.

The final linearized, purified plasmid was quantified again via NanoDrop and stored at –20°C until use in the IVT reaction.

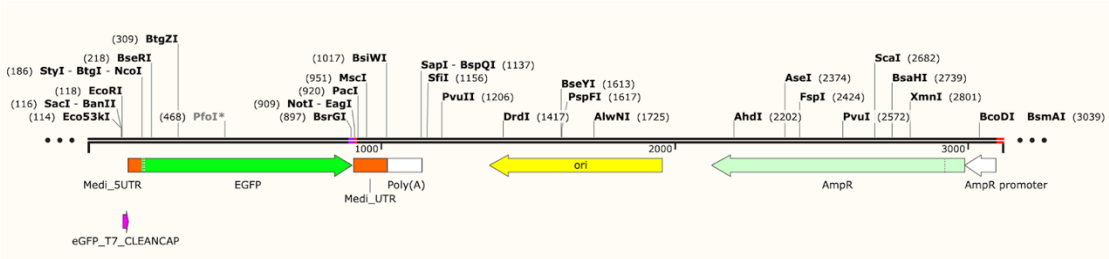

Figure 15. DNA plasmid after linearised process, ready for the in vitro transcription (IVT) reaction. The initial segment of the plasmid comprises the Medi_5'UTR, a non-translated region located upstream of the promoter. The EGFP (Enhanced Green Fluorescent Protein) gene serves as a reporter gene for investigating gene expression, encoding a fluorescent marker protein widely utilized for labeling, quantifying, or visualizing protein expression in cellular systems. The poly(A) sequence facilitates mRNA maturation and stability. The origin of replication (ori) governs plasmid replication, while the ampicillin resistance gene (AmpR) confers ampicillin resistance, enabling cell or E.coli growth in antibiotic-supplemented media. Restriction enzyme recognition sites—including EcoRI, BamHI, and PacI—are strategically positioned within the plasmid sequence to enable targeted DNA sequence insertion or deletion through enzymatic cleavage.

2.2.2. mRNA IVT Production

RNA replicons are synthesized through in vitro transcription (IVT) using linearized DNA templates. The T7 RNA polymerase binds to the T7 promoter of the DNA template, reads the sequence, and synthesizes the corresponding

RNA molecules. To optimize the IVT reaction, a custom buffer was used instead of a commercial one. For the batch mRNA IVT reaction, prepare the 10 X buffer reagents (10 mL each) can easy to start the IVT experiments. And keep it in the 4 degrees for the fresh. Table 8 shows the details for the IVT buffer reagents.

Table 8. 10 X IVT buffer reagents

Component	Stock concentration	Final Concentration	Volume Ratio
HEPES	1 M	400 mM	4.0 mL
Magnesium acetate	2 M	420 mM	2.1 mL
DTT	1 M	100 mM	1.0 mL
Spermidine	6.4 M	20 mM	0.031 mL
Triton X-100	-	0.01 % (v/v)	0.01 mL
Nuclease free water	-	Up to 10 mL	2.85 mL

A typical IVT reaction includes the following components: i) linearized plasmid DNA (pDNA) with a T7 promoter; ii) nucleoside triphosphates (NTPs) for the four bases (10mM each); iii) ribonuclease inhibitor to inactivate RNase; iv) pyrophosphatase to degrade accumulated pyrophosphate; v) magnesium ions as a cofactor for T7 polymerase. The reaction was carried out at 37°C for two hours and stored in the -80°C freezer for further use. And Figure 17 and table 9 shows the experiment regent details.

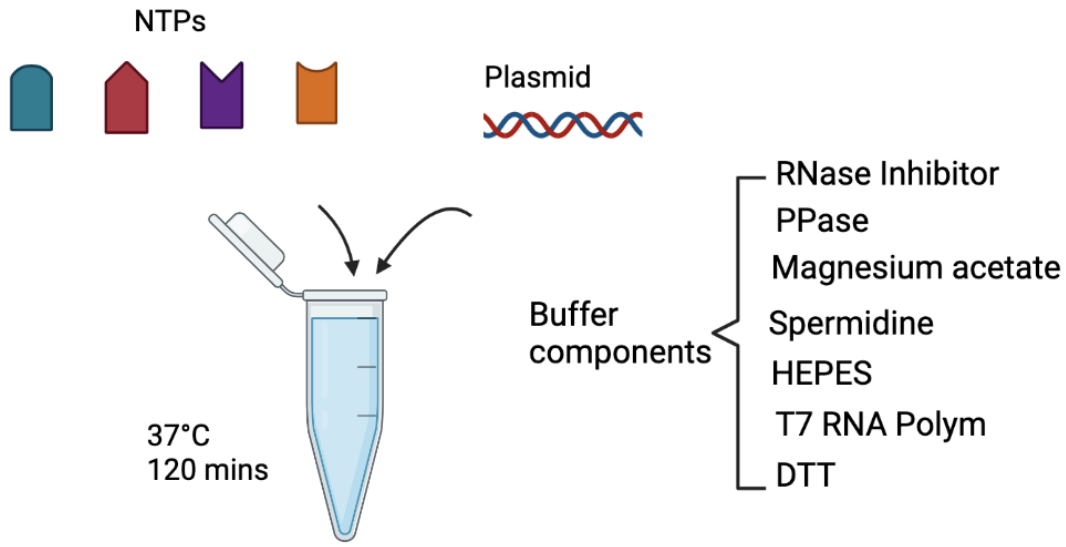

Figure 16. The process of in vitro transcription (IVT) for synthesizing RNA from a plasmid template. It shows the addition of various components like NTPs, RNase

inhibitor, magnesium acetate, and other buffer components, followed by incubation at 37°C for 120 minutes to produce the RNA. The reaction system incorporates RNase Inhibitor to prevent RNA degradation by ribonucleases during transcription, and Pyrophosphatase (PPase) to remove undesired pyrophosphate groups from mRNA. Magnesium acetate functions as a cofactor to activate the catalytic activity of T7 RNA polymerase in mRNA synthesis. Spermidine stabilizes RNA tertiary structures and prevents improper folding or instability during in vitro transcription. HEPES buffer maintains a stable pH environment to facilitate enzymatic activity, while T7 RNA polymerase directs mRNA synthesis according to the DNA template. Dithiothreitol (DTT), a reducing agent, protects T7 RNA polymerase from oxidative inactivation. The coordinated action of these components ensures high efficiency and stability in mRNA production.

Table 8. 1mL IVT composition

Name of reagent	Stock conc.	IVT conc.	Volume of reagent
ATP	100 mM	10 mM	0.1 mL
CTP	100 mM	10 mM	0.1 mL
GTP	100 mM	10 mM	0.1 mL
UTP/N1-Me-pseudo UTP	100 mM	10 mM	0.1 mL
m7G(5')ppp(5')(2'OMeA)pG (Capping reagent)	100 mM	10 mM	0.1 mL
T7 Polymerase	2461 U/ µL	246.1 U/ µL	0.1 mL
IPP	1 U/ µL	0.05 U/ µL	0.05 mL
RNase inhibitor	40 U/ µL	1 U/ µL	0.025 mL
DNA template (eGFP)	1 µg/ µL	0.05 µg/ µL	0.05 mL
IVT Buffer(10X)	10 X	1X	0.1 mL
RNase free water	-	-	0.175 mL
Total			1 mL

Determination of mRNA yield and concentration was performed after purification, and concentration measurements at this step were not meaningful due to the presence of magazines and trace losses during purification.

2.2.3. mRNA Purification

Following purification using the Monarch RNA Cleanup Kit, the mRNA concentration was measured using the NanoDrop One spectrophotometer. The

average post-purification concentration reached approximately 4,905 ng/µL. Taking into account the 2× dilution factor introduced during the purification step, the corrected yield of the crude IVT product was estimated to be around 9,810 ng/µL. This high recovery rate (>70%) confirmed the efficiency of the spin-column-based purification protocol and ensured that sufficient RNA was obtained for downstream applications.

To evaluate RNA quality and detect residual impurities, both crude and purified mRNA samples were analyzed by ion exchange chromatography (IEX-HPLC), in collaboration with a postdoctoral researcher in our group with expertise in analytical method development. The crude IVT sample was serially diluted (1:10, then 1:10, then 1:2), yielding a total dilution factor of 1:200 prior to injection. The Monarch-purified mRNA sample was diluted 1:50 followed by 1:2, resulting in a final dilution of 1:100, or effectively 1:200 when considering the initial dilution during the purification step. The chromatograms confirmed a significant reduction in unincorporated nucleotides and other byproducts after purification.

Residual nucleotide content was also evaluated through quantitative analysis. As expected, CTP was undetectable in all samples, suggesting its complete consumption during transcription, while ATP, UTP, and GTP remained at detectable levels, consistent with partial usage. The purified samples exhibited reduced free nucleotide signals, further supporting the efficacy of the cleanup. To assess RNA integrity and verify transcript size, fragment analysis and capillary electrophoresis were performed using the Agilent Bioanalyzer and Advanced Analytical Fragment Analyzer systems. These assays were conducted with the support of a postdoctoral colleague specializing in nucleic acid analytics. The electropherograms confirmed the presence of a sharp, single peak corresponding to the expected transcript length, with minimal degradation products, indicating high-quality RNA suitable for transfection and translation studies.

Overall, this multi-modal analytical strategy ensured the accuracy of mRNA quantification, the removal of synthesis-related impurities, and the integrity of the final product, providing a reliable basis for downstream functional assays.

2.3. Fabrication and Setup of Microfluidic Device

2.3.1. Introduction of T-mixer

The PEEK High Pressure Tee Assembly is precisely designed to withstand the environmental pressures in high-pressure regions of a system. Made from the inert material PEEK, it offers excellent chemical resistance. The assembly includes three F-300 Fingertight Fittings and is compatible with 1/16 OD stainless steel or PEEK tubing. It can withstand a maximum operating pressure of 3500 psi (241 bar). The swept volume is 0.57 µL, and the through hole has a diameter of 0.5 mm. And the Figure 17 shows organic phase (blue) and aqueous phase (red) flow and mix process in T-mixer. And after the formulation, the lipid nanoparticle (yellow) will flow through the output side.

Microfluidic System for Sample Flow of T-mixer

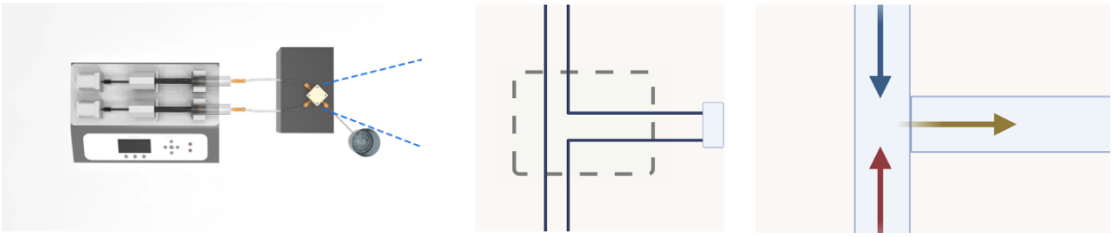

Figure 17. The Schematic of fluid flow in T-Mixer

In the context of LNP microfluidic production, this PEEK High Pressure Tee Assembly is essential for ensuring precise fluid control and stable performance under high-pressure conditions. Its ability to handle high pressures and provide reliable fluid mixing is critical for the accurate production of lipid nanoparticles, where consistent flow rates and mixing efficiency are key to optimizing the final product quality. The injection tubing is connected to the syringe via a Luer fitting, ensuring stable fluid delivery and sealing performance. The mixer should be thoroughly cleaned before and after use, and dried with compressed air. After LNP synthesis, anhydrous ethanol should be passed through to thoroughly flush out any residual organic and aqueous phases in the channels.

During formulation, lipid solutions in ethanol (organic phase) and aqueous buffer containing nucleic acids were loaded into separate syringes and

connected to the PEEK T-mixer inlets via Luer fittings. A dual-channel syringe pump was used to drive both phases simultaneously, with total flow rates (TFR) ranging from 4 to 24 mL/min, and flow rate ratios (FRR) of aqueous to organic phase systematically varied from 1:1 to 10:1 to evaluate their impact on LNP properties. The total volume processed per run was 4 mL, and approximately 3 mL of LNP suspension was collected at the outlet. Immediately after collection, the crude LNPs were diluted with 10 mM PBS buffer (pH 7.4) to a final volume of ~15 mL to ensure particle stabilization and prepare samples for downstream characterization and purification steps. All operations were performed under sterile conditions, and the microfluidic chip was flushed thoroughly with anhydrous ethanol after each run.

2.3.2. Introduction of Swirl Mixer

Various microfluidic chips can be selected depending on the preparation conditions. Dr. Jordan MacInnes designed four swirl mixers (SW 0.5*1, SW 0.5*2, SW 0.5*4, SW 0.25*1) for microfluidic preparation of different material systems [184]. Among them, microfluidic devices and chip mixers incorporating SW 0.5*2 and SW 0.5*4 structures were used for lipid nanoparticle (LNP) synthesis. The mixing tube has a cross-sectional area of 0.275 mm^3 and a hydraulic diameter (Dh) of 0.00065 m. And figure 18 shows the mixing details of two phase. Mixed streams of morphology present swirl.

Microfluidic System for Sample Flow of Swirl Mixer

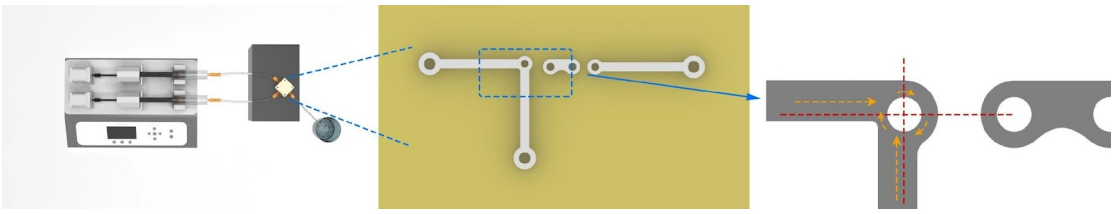

Figure 18. The Schematic of fluid flow in Swirl Mixer

The organic and aqueous phases are mixed at a predefined flow rate ratio, and the mixing process is optimized through precise control of syringe flow rate and injection volume, ensuring uniform mixing and improved LNP formation efficiency and stability. The injection tubing is connected to the syringe via a Luer fitting, ensuring stable fluid delivery and sealing performance. The mixer

should be thoroughly cleaned before and after use and dried with compressed air. After LNP synthesis, anhydrous ethanol should be passed through to thoroughly flush out any residual organic and aqueous phases in the channels.

For experiments using the Swirl Mixer, the operation procedure remained consistent with that of the T-mixer setup, while the total flow rate (TFR) was increased to a range of 28–240 mL/min to accommodate higher-throughput synthesis.

2.3.3. Introduction of Herringbone Mixer

The Herringbone Mixer was purchased from Darwin Microfluidics, and the Fluidic 1460 Herringbone Mixing Chip, designed by Microfluidic ChipShop, is intended to facilitate the rapid and efficient mixing of different liquids in microfluidic systems. This chip features herringbone-shaped channels, which enhance mixing efficiency by introducing chaotic advection, thereby reducing the required channel length for effective mixing. The chip includes two distinct channel designs (Structure A and B), providing greater experimental flexibility. In LNP microfluidic synthesis, Channel A was selected due to pump flow rate limitations. The channel has a depth of 200 μm, a width of 600 μm, and a mixing section height of 75 μm. This configuration ensures thorough mixing of the organic and aqueous phases within a short distance, improving the uniformity and stability of LNP formation. The injection tubing is connected to the syringe via a Luer fitting, ensuring stable fluid delivery and sealing performance. And the Figure 19 shows the herringbone mixer flow details. The two phases are mixed well under the mix of the bump.

Microfluidic System for Sample Flow of Herringbone Mixer

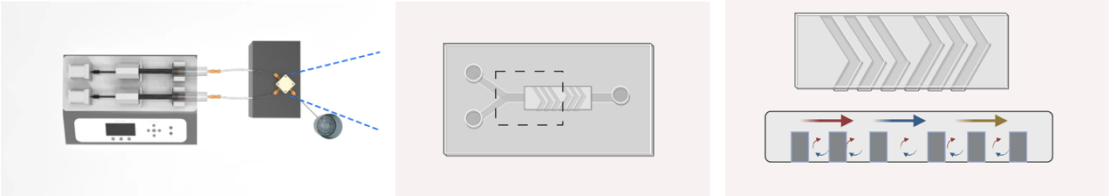

Figure 19. The Schematic of fluid flow in Herringbone Mixer

The chip is equipped with Mini Luer ports, allowing seamless and leak-free integration with other microfluidic components. The material of choice is polycarbonate (PC). Although lipids and certain plastics may exhibit compatibility issues to some extent, studies have shown that PC or cyclic olefin polymer (COP) has excellent chemical inertness and solvent resistance, posing no significant impact on LNP synthesis. Furthermore, these materials offer high optical clarity, making them suitable for fluorescence detection, microscopic observation, and other analytical applications, making them an ideal choice for LNP microfluidic production. The mixer should be thoroughly cleaned before and after use and dried with compressed air. After LNP synthesis, anhydrous ethanol should be passed through to thoroughly flush out any residual organic and aqueous phases in the channels. The Herringbone mixer follows the same procedure, with its TFR setting ranging from 1 mL/min to 6 mL/min.

2.3.4. Theoretical calculations and Compare of mixers design

In the LNP synthesis process, the Reynolds number (Re) is calculated based on the microfluidic chip's channel dimensions and input flow rate parameters to determine the fluid flow state. By adjusting the flow rate (u) and hydraulic diameter (D_h), the fluid can be maintained in the turbulent region (Re > 4000), enhancing the mixing efficiency between the two phases. Optimizing chip dimensions and fluid parameters improves mixing efficiency, ensuring uniform and stable LNP formation. And 3 microfluidic mixers details shows below (Table 9).

Table 9. Microfluidic Mixers details

Mixer	Mixed mechanism	Tubing Size	Swept Volume	Pressure drop Model (ΔP)	Materials
T-mixer	Molecular diffusion	0.275 mm^3	0.57 µL	Simplified Channel, Intersection Disturbance	PEEK plastic
Swirl Mixer	Centrifugal force-induced secondary flow, Dean vortex.	0.93 mm^3	2.05 µL	Helical path, rotating chamber	PEEK plastic

Herringbone mixer	Chaotic flow, periodic asymmetric structures disrupt laminar flow	0.12 mm^3	0.20 μL	Minimal structural disturbance, linear path	PEEK plastic

In microfluidic systems, pressure drop (ΔP) is a critical factor affecting flow stability and device compatibility. The T-mixer exhibits moderate pressure drop due to its simple straight-through geometry. In contrast, the Swirl Mixer introduces higher pressure drop resulting from its extended curved channels and vortex-inducing chamber, especially under elevated flow rates. The Herringbone Mixer maintains relatively low to moderate pressure drop by leveraging passive microstructures for mixing without significantly elongating the flow path. This balance makes it particularly suitable for applications requiring enhanced mixing with minimal backpressure.

2.3.5. Syringe Pumps Introduction

The Fusion 4000X is a motorized multi-channel syringe pump with dual independent drive channels, enabling pulsation-free and highly reproducible flow control. Its programmable multi-step flow mode allows users to input complex fluid delivery profiles, supporting programming via the device, making it ideal for LNP synthesis, microfluidic mixing, and pharmaceutical formulation research. This device was purchased from Chemyx and can be expanded to a four-syringe push-pull system, supporting syringe sizes from 0.5mL to 100mL, with a flow rate range of 1 mL/min to 170.5 mL/min. It features a touchscreen interface, USB, RS232, and TTL control, making it GMP and lab-compliant, easy to clean, and highly reliable. The precision-machined metal body and all-glass touchscreen enhance stability and user convenience.

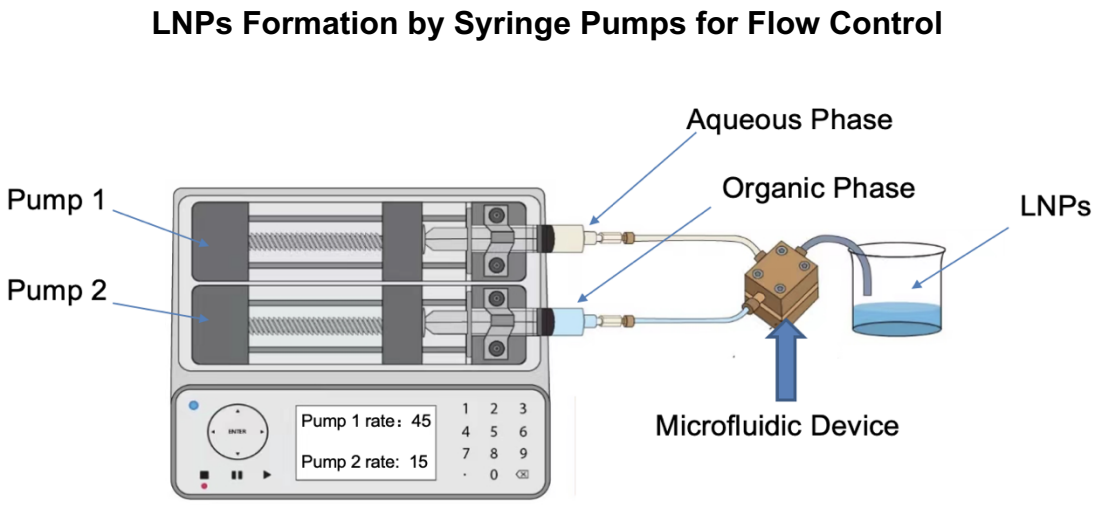

Figure 20. The LNP lab formulation process by syringe pumps and microfluidic mixer.

Figure 20 shows the lab formulation experiment. This is an ultra-high precision syringe pump offering ±<0.35% accuracy and ±<0.05% reproducibility. It boasts an extremely wide flow rate range, from 0.0001 μL/min to 170.5 mL/min, and possesses a powerful 85lb thrust to overcome high backpressure in microfluidic chips. The Fusion 4000X supports a wide range of experimental applications and lays the foundation for future transition to piston pumps, further improving stability and adaptability in fluid delivery processes.

2.3.6. Piston Pumps Introduction

The Vapourtec R-Series (Vapourtec's V-3 precision peristaltic pump) is a modular flow chemistry system, primarily utilizing its continuous production pump module in the continuous synthesis of lipid nanoparticles (LNPs). The pump in this series is a piston pump (plunger pump), in which a stepper motor drives a piston to move reciprocally within a precisely machined pump chamber, thereby directly propelling fluid flow. Since the linear displacement of the piston is strictly correlated with the step count of the motor, the system achieves high-precision flow rate control, making it well-suited for LNP synthesis, which requires precise proportional mixing. The pump operates within a flow rate range of 0.01–50 mL/min and pumping at 10 bar, generating smooth output flow across the full pressure range with an accuracy error of less than ±1%, enabling seamless scalability from milligram-scale laboratory synthesis to kilogram-scale industrial production. Additionally, the system offers high

expandability, allowing the integration of additional sensors to accommodate complex reaction conditions, such as photochemical reactions or high temperature/high-pressure environments. Consequently, the Vapourtec R-Series is not only applicable to laboratory-scale microfluidic synthesis of LNPs but also meets the requirements for continuous production of active pharmaceutical ingredients (APIs) under good manufacturing practice (GMP) conditions.

2.4. LNP preparation by Microfluidic

2.4.1. N/P Ratio Calculation

In mRNA-LNP formulations, the N/P ratio—defined as the molar ratio of ionizable nitrogen groups (from cationic lipids) to phosphate groups (on nucleic acids)—is a critical parameter influencing nanoparticle stability, size, and delivery efficiency. Electrostatic interactions between these oppositely charged components drive nanoparticle self-assembly. An imbalanced N/P ratio can lead to aggregation, poor encapsulation, or reduced transfection efficiency.

For calculation, an average molecular weight of 330 g/mol is commonly used for nucleotide monophosphates (AMP, GMP, CMP, UMP) to estimate the phosphate content across different mRNA sequences. For instance, at an mRNA concentration of 0.17 mg/mL (≈6.25 mmol/mL), using 1 mL of organic phase (Dlin-MC3-DMA) and 3 mL of aqueous phase, the N/P ratio can be accurately determined to guide formulation optimization.

$$mmolmol$$

$$N/P\ ratio=$$

$n_{Nucleic\ acid}$ is the amount of nucleic acid in moles and $M_{Nucleic\ acid}$ is the molar mass of nucleic acid.

Table 10. The different N/P Ratio Experiment Setting

N/P ratio	C(Mc3)		C(Nucleic Acid)	
1: 1	1.56 mmol/L	1 mg/ml	0.17 mg/ml	170 μg/ml
4: 1	6.25 mmol/L	4 mg/ml	0.17 mg/ml	170 μg/ml
6: 1	9.36 mmol/L	6 mg/ml	0.17 mg/ml	170 μg/ml
10: 1	15.6 mmol/L	10 mg/ml	0.17 mg/ml	170 μg/ml

The length of the nucleic acid is not specified in the calculations, and this is because the length of the nucleic acid does not affect the mass concentration used. Using the values obtained for single-stranded RNA and the above calculation, for example, the amount of substance of **P** required is also fixed at 1.545×10^{-6} mol, while keeping the N/P ratio and the amount of substance of **N** constant. The mass concentration of nucleic acid is related to the amount of substance of **P** as follows:

$\mathbf{n}_{\text{nucleic acid}}$ is the amount of substance (moles) of the nucleic acid and $\mathbf{M}_{\text{nucleic acid}}$ is the molar mass of the nucleic acid. For a 1000 nt RNA, one mRNA molecule has 1000 anions; whereas for a 2000 nt RNA, one mRNA molecule has 2000 anions and the amount of substance (moles) required is only half that of 1000 nt. Still, the corresponding the molar mass of the RNA is doubled (not taking into account the weight difference of the different bases). So, the final value does not change when the two are multiplied. Therefore, it is more convenient to convert mRNA to mass concentration for calculations when using mRNA.

2.4.2. Preparation of Lipid Nanoparticle

In liposome preparation, DSPC and cholesterol were combined at a 3:2 molar ratio to provide structural integrity—DSPC enhances membrane stability, while cholesterol improves fluidity and durability. For mRNA-LNP formulations, FDA-approved ionizable and PEGylated lipids were directly included to ensure biocompatibility and formulation consistency.

Orgacin Phase: The organic phase was prepared by dissolving the lipid mixture in anhydrous ethanol to form a clear, homogeneous solution. Ethanol was chosen for its ability to dissolve both polar and nonpolar lipids. Lipids were weighed into glass vials to avoid solvent-container interactions, and the solution

was sonicated in a sealed container to minimize ethanol evaporation and ensure reproducibility.

Use only anhydrous ethanol to prevent lipid aggregation due to water contamination. Protect light-sensitive lipids from light, and use the solution promptly to avoid concentration shifts or precipitation. Record all preparation details for traceability.

Aqueous Phase: In this step, 25 mM sodium acetate buffer (pH 4.0) was used as the aqueous phase for lipid nanoparticle (LNP) synthesis, without including nucleic acid cargo during formulation. This strategy was chosen due to the limited availability of mRNA and the need to optimize formulation and process parameters under controlled conditions. Although nucleic acids were not incorporated, the lipid self-assembly behavior—including particle size, polydispersity index (PDI), and morphology—can still be effectively simulated using PBS.

Using NaAc buffer as the aqueous phase allows reliable evaluation of key formulation variables such as flow rate ratio (FRR), total flow rate (TFR), lipid composition, and mixing performance. Since these parameters are primarily governed by lipid–aqueous interactions rather than the nucleic acid itself, "empty" LNPs provide a reproducible, cost-effective model for early-stage process development, ensuring robustness before scaling up or loading therapeutic payloads.

Formulation by Microfluidic: The prepared organic and aqueous phases were loaded into syringes and installed onto a dual-channel syringe pump system. Syringe brand and model were entered into the system interface to ensure accurate calibration of inner diameter and plunger stroke. Flow parameters—including separate flow rate (to set different flow rate ratio), and injection volume—were configured according to experimental design. After verifying secure syringe installation and channel assignment, the mixing process was initiated. To minimize errors from flow rate instability at the beginning and end of the run, only the central portion of the eluent was collected, while initial and terminal fractions were discarded. The collected sample was immediately diluted using an isotonic, pH-neutral buffer (e.g., 10mM PBS pH

7.4) to stabilize the nanoparticles for downstream characterization and purification procedures.

2.4.3. mRNA-LNP Formulation

Through a combination of spectrophotometry, ion exchange chromatography (IEX-HPLC), and capillary electrophoresis, the purification and analytical workflow provided comprehensive insights into mRNA quality. These analyses confirmed the RNA concentration and yield, removal of unincorporated nucleotides and reaction byproducts, and transcript integrity and size uniformity. Importantly, fragment analysis revealed minimal degradation and a dominant peak at the expected transcript length, supporting suitability for downstream applications such as transfection. In addition to purity and integrity, functional mRNA requires structural features such as a 5' cap and a 3' poly(A) tail. The 5' cap structure (typically added co-transcriptionally or enzymatically post-IVT) enhances stability and translation efficiency by protecting against exonuclease degradation and facilitating ribosome recognition. Meanwhile, the poly(A) tail improves mRNA stability and nuclear export, and prolongs translational activity in the cytoplasm. These elements are critical for ensuring efficient gene expression in both in vitro and in vivo applications.

Several of the analyses were conducted with the assistance of postdoctoral researchers in our group, whose support and technical expertise are gratefully acknowledged.

To prepare mRNA-lipid nanoparticles (mRNA-LNPs), a 25mM sodium acetate buffer (pH < 4.5) was selected as the aqueous phase solution. This acidic buffer facilitates electrostatic interactions between ionizable lipids and negatively charged plasmids. Under acidic conditions, ionizable lipids carry a positive charge, thereby enhancing their binding affinity with the plasmid. The mRNA concentration was adjusted according to the experimental design, and the concentration was calibrated using NanoDrop prior to synthesis. After calibration, the mRNA solution was transferred into a container, and air bubbles were expelled to ensure the accuracy and stability of subsequent operations. Once everything is prepared, the pump can be set according to the

experimental requirements to mix the two phases and obtain mRNA-LNPs. All process parameters, including total flow rate, flow rate ratio, concentration, and lipid-to-cholesterol ratio, are detailed in the accompanying figures. All experimental procedures were performed under room temperature conditions.

2.4.4. mRNA-LNP Purification

High ethanol content (~25%) in freshly prepared LNPs can significantly distort particle size measurements and promote nanoparticle fusion. To ensure accurate characterization and maintain product stability, immediate 5× dilution with buffer is recommended post-synthesis. If dialysis is used for purification, the sample should be transferred into the buffer promptly (within 5 minutes). Early dilution and purification are critical to prevent size deviation and ensure reproducible results. And figure 21 shows different purification process. An efficient purification process and buffer system are also crucial for maintaining LNP stability and enabling subsequent experiments.

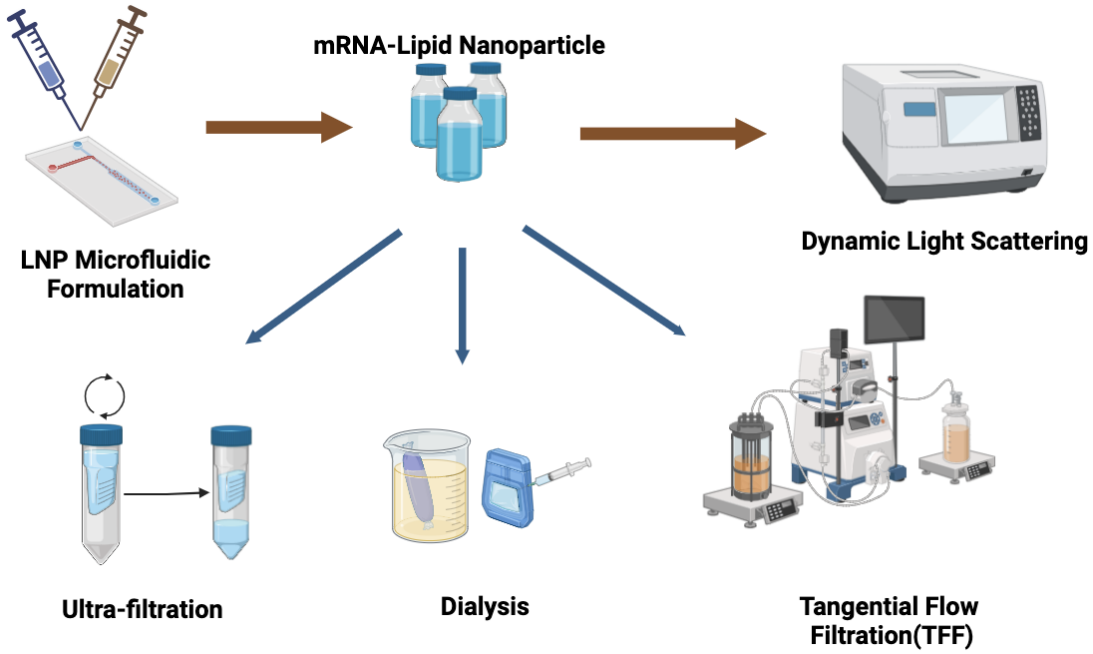

Figure 21. The different purification and characterization, schematic diagrams

Dialysis: Dialysis serves as the most fundamental purification method for nanoparticles, aiming to remove residual organic solvents, unencapsulated nucleic acids, and free lipids. The crude LNP suspension is placed within a dialysis bag or cassette featuring an appropriate molecular weight cut-off, immersed in a large volume of buffer solution (such as PBS). Under gentle

stirring at low temperatures, small molecules are progressively removed via passive diffusion whilst retaining the nanoparticles. Repeated exchange of the external buffer solution maintains the concentration gradient, enhancing both the purity and biocompatibility of the LNPs. Following dialysis, the LNPs may undergo concentration and filtration before being stored under suitable conditions for subsequent applications.

Ultrafiltration: After dialysis, ultrafiltration is used to further concentrate and purify the LNP suspension. The sample is diluted with cold PBS and transferred to a centrifugal filter unit (e.g., 30 kDa MWCO), then centrifuged at low temperature to reduce the volume. This concentration-dilution cycle can be repeated to remove remaining small molecules and adjust the buffer. Unlike dialysis, which relies on passive diffusion over time, ultrafiltration offers faster processing through pressure-driven separation and is suitable for volume adjustment, buffer exchange, or final concentration prior to storage. However, excessive centrifugal force or prolonged operation may risk nanoparticle aggregation or partial loss, especially for fragile formulations.

Tangential Flow Filtration: Tangential flow filtration was used for the purification of crude LNP suspensions, employing a hollow fiber membrane with appropriate molecular weight cutoff. The sample was diluted with a neutral buffer to reduce viscosity and minimize membrane fouling. During diafiltration, buffer was continuously added while permeate was removed to maintain a constant volume, enabling efficient removal of unencapsulated nucleic acids and residual solvents. After purification, the system was thoroughly cleaned and disinfected to ensure membrane integrity and sterility.

Compared to dialysis, TFF offers faster processing and greater scalability by actively driving buffer exchange under controlled flow and pressure. Unlike centrifugal ultrafiltration, TFF reduces shear-related damage and sample loss, making it more suitable for sensitive formulations. However, its operation requires more complex equipment and careful maintenance to prevent membrane fouling and ensure consistent performance.

In this research, dialysis was employed as an essential step for LNP purification. The TFF methodology and associated optimization experiments are presented exclusively in Chapter 5.

2.5. Characterization and analysis of mRNA-LNP

All values in this study were expressed as means ± SD (standard deviation). Experiments were independently repeated at least three times, with more than three experimental batches conducted per condition. For each experimental setup, three technical replicates were performed to ensure reproducibility. Differences among groups were analyzed using one-way analysis of variance (ANOVA) with GraphPad Prism 9.0 software. Statistical differences were considered significant at ****P < 0.0001; ***P < 0.001; **P < 0.01 and *P < 0.05.

2.5.1. Size &PDI

The particle size and polydispersity index (PDI) of lipid nanoparticles (LNPs) are measured by Dynamic Light Scattering (DLS) using the NanoBrook 90 plus Pals Particle size Analyzer (Brookhaven Instrument, NY, USA). Measurements were conducted under controlled laboratory conditions, with room temperature maintained at 25 °C, which was also set as the default measurement temperature. The viscosity and refractive index (RI) values were input based on the properties of the aqueous buffer used (e.g., 10 mM PBS, pH 7.4). To validate the parameter settings, a 100 nm polystyrene standard sample was used for calibration. The system settings were confirmed when the measurement error was within 1%. DLS detects particle size based on Brownian motion, with smaller particles moving faster, and the hydrodynamic diameter is determined by the particle’s diffusion coefficient. And the detect shows below in figure 22. To ensure optimal signal acquisition, the instrument's auto-attenuation function was employed to automatically adjust laser intensity and detector sensitivity based on sample turbidity. Each sample was measured with five replicates, with each run lasting 45 seconds.

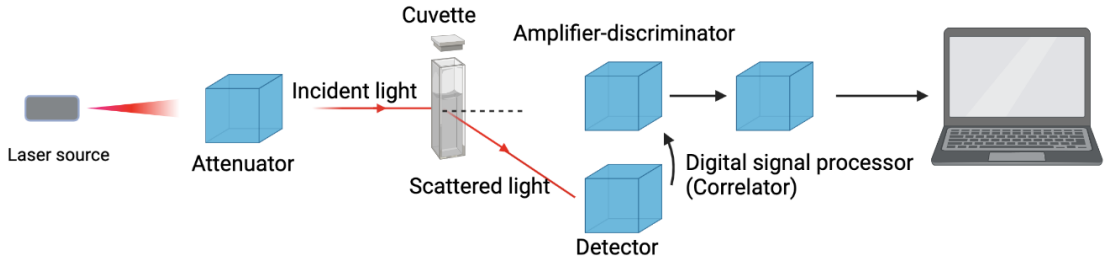

Figure 22. The mechanism of DLS detection.

The average hydrodynamic diameter was calculated from the correlation function using the Stokes–Einstein equation:

where **D** is the translational diffusion coefficient, $\mathbf{k_B}$ is the Boltzmann constant, **T** is the absolute temperature (in Kelvin),in the detection process is 25 °C (298.15 K) , **η** is the dynamic viscosity of the dispersant, during the experiments is 0.8872 mPa·s in water. and $\mathbf{d_H}$ is the hydrodynamic diameter. The instrument's software automatically computes $\mathbf{d_H}$ by fitting the autocorrelation function to a cumulant or distribution model based on the measured diffusion coefficient. And the Refractive Index (RI) is 1.330 in detection.

Nano Flow Sizer: Building on this, NanoFlowSizer (NFS) uses Spatially Resolved Dynamic Light Scattering (SR-DLS) technology with Near Infrared (NIR) light to detect the depth of scattered light, enhancing measurement accuracy (shows in figure 23), the same measurement parameters (temperature, viscosity, RI) were used to ensure consistency and comparability between methods. Autocorrelation curve from intensity fluctuations, reflecting Brownian motion of particles. NFS is particularly suitable for measuring high-turbidity samples, minimizing the effects of flow, and providing real-time, precise particle size monitoring. This gives NFS a distinct advantage in LNP production, ensuring size consistency, optimizing formulation and processes, and enhancing stability, encapsulation efficiency, and drug release properties. Compared to traditional DLS, NFS offers a more efficient and reliable solution for high-quality LNP production, with significant application potential.

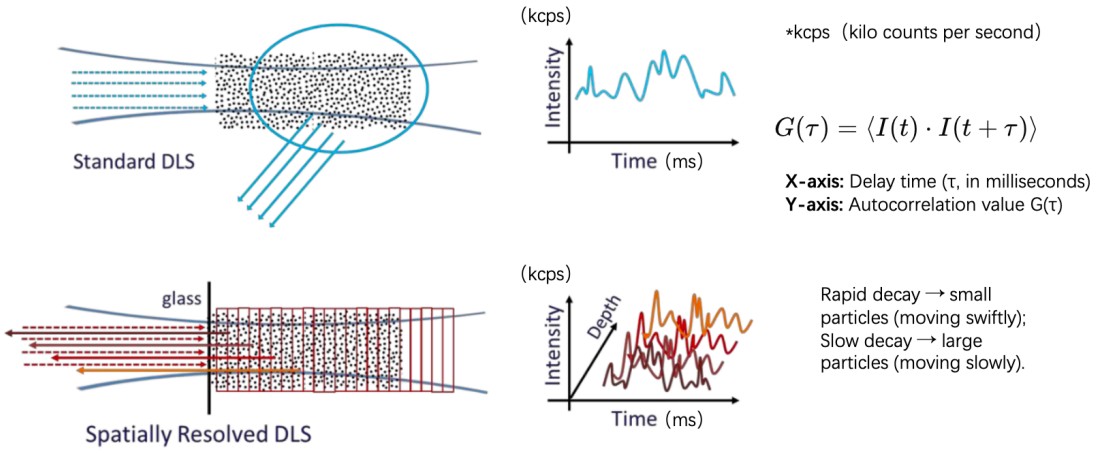

Figure 23. The detection details of Standard DLS and SR-DLS. In standard dynamic light scattering (DLS, top figure), the laser beam illuminates the entire sample volume, with scattered light collected as a global signal. In scattered-reflection dynamic light scattering (SR-DLS, bottom figure), the laser penetrates vertically through a transparent window (e.g., glass), collecting scattered signals at multiple depths within the flowing sample. The autocorrelation function on the right reflects the 'decay of correlation with time delay' in particle motion.

In addition to its high measurement accuracy and real-time monitoring capabilities, NFS offers a modular design, making it particularly suitable for the needs of LNP production. This modularity allows for the flexible replacement of components based on experimental requirements and the easy addition of extra sensors to measure parameters such as temperature and pressure. This feature enables NFS to provide continuous monitoring during LNP production, offering real-time feedback on changes in particle size, distribution, and other critical physical parameters. Such continuous monitoring helps optimize formulations and production processes, ensuring the consistency and quality of LNPs. Furthermore, NFS's adaptability allows it to handle high-concentration and high-turbidity samples, which is essential for complex systems in LNP production. With real-time data feedback, NFS effectively enhances the automation and control of LNP production, offering significant potential for a wide range of applications. In experimental measurements, all procedures should be strictly followed according to the Standard Operating Procedure (SOP) to ensure the accuracy and reproducibility of the experimental results. According to the SOP, the first step is to calibrate the instruments to ensure

their proper functioning. Before conducting measurements, the samples must be processed as per the prescribed procedure, such as dilution, dissolution, and pre-treatment, to remove any impurities or bubbles that might interfere with the measurements.

2.5.2. Encapsulation Efficiency%

Nano Flow Cytometry and RiboGreen assays were employed to evaluate the encapsulation efficiency of mRNA-LNPs. Nano Flow Cytometry was used to analyze individual LNP particles, enabling simultaneous detection of size and fluorescence-labeled RNA encapsulation on a per-particle basis. The samples were diluted and stained with fluorescent RNA-binding dye prior to measurement, and encapsulated vs unencapsulated particles were gated using control formulations. RiboGreen assay was used as a complementary method. mRNA concentrations were measured before and after RNase treatment to determine the proportion of protected (encapsulated) RNA. Fluorescence was recorded using a microplate reader, and encapsulation efficiency was calculated as the ratio of RNase-protected signal to total signal. Together, these methods provided both population-level and particle-level insights into mRNA encapsulation.

Ribogreen Assay: The Quant-iT RiboGreen® RNA Assay is a fluorescence-based method widely used for quantifying nucleic acids. In the context of mRNA-loaded lipid nanoparticles (mRNA-LNPs), this method enables the determination of encapsulation efficiency (EE%) by taking advantage of the dye's selective binding to free, unencapsulated RNA. Since intact LNPs shield the encapsulated RNA from dye access, only free RNA contributes to fluorescence signals prior to LNP disruption. To calculate encapsulation efficiency, the LNP sample is divided into two aliquots. One aliquot is analyzed directly to measure the free (unencapsulated) RNA. The second aliquot is treated with 1% Triton X-100, a non-ionic surfactant that disrupts the LNP structure and releases all encapsulated RNA, allowing measurement of the total RNA content.

The encapsulation efficiency is determined using the following equation: Encapsulation Efficiency (%) = (Total RNA − Free RNA) / Total RNA × 100

Standard curves were prepared using serial dilutions of RNA standards in TE buffer, and both pre- and post-lysis samples were incubated with RiboGreen dye. Fluorescence was recorded using a plate reader (Excitation: 480 nm; Emission: 520 nm), and RNA concentrations were interpolated from the standard curve. All measurements were performed in duplicates or triplicates to ensure data consistency. This approach offers a simple, sensitive, and high-throughput method for quantifying RNA encapsulation without requiring particle-level resolution. However, care must be taken to avoid surfactant-induced degradation or fluorescence quenching, and appropriate controls must be included to correct for background signals.

While Nano Flow Cytometry provides particle-resolved encapsulation information, RiboGreen is especially suitable for early-stage formulation screening and routine quality control, offering a cost-effective and efficient solution when total encapsulation levels are the primary concern.

The High Range and Low Range Curve Schematic

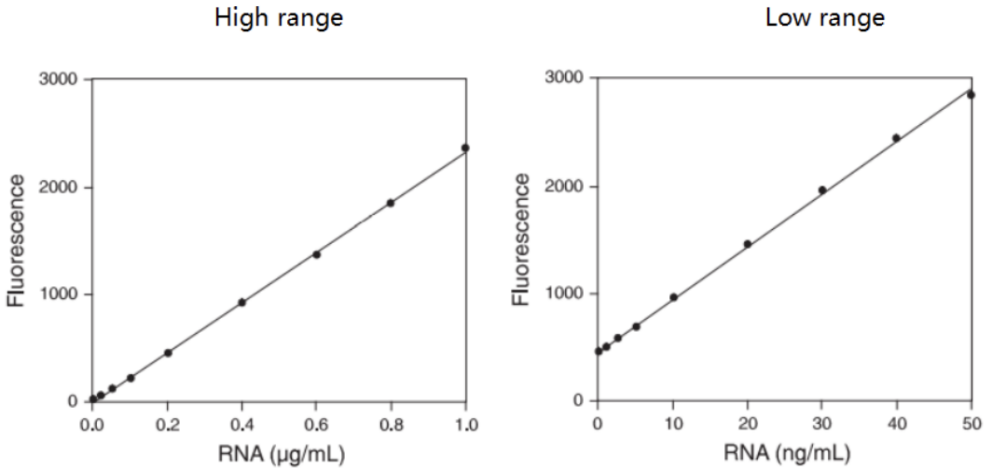

Figure 24. The high (left) and low (right) range standard curve line. By measuring the fluorescence intensity readings of the sample and comparing them against the concentration range of the standard curve, the mRNA concentration of the sample is determined, thereby enabling the calculation of the encapsulation efficiency.

Nano Flow Cytometry: In the experiment, SYTO RNA Select and other membrane-permeable nucleic acid dyes are used to label mRNA encapsulated within LNPs, effectively distinguishing between empty LNPs and drug-loaded LNPs. Empty LNPs, lacking nucleic acid content, only display scattering signals,

while drug-loaded LNPs simultaneously show both scattering and fluorescence signals.

SYTO 9 introduction: Alow-molecular-weight membrane-permeant green fluorescent dye, penetrates the phospholipid bilayer of lipid nanoparticles (LNPs) via its amphiphilic structure (hydrophobic aromatic rings and hydrophilic amino groups), enabling fluorescence emission upon binding to encapsulated nucleic acids (e.g., dsDNA or RNA). While the dense bilayer of intact LNPs partially restricts SYTO9 permeation efficiency, optimizing dye concentration, incubation time, and temperature enhances nucleic acid interaction, thereby quantitatively evaluating LNP encapsulation efficiency and structural integrity, which provides critical quality control data for gene delivery system development.

Experimental Steps: Nano flow cytometry (nFCM) was used to quantify LNP particle concentration and assess nucleic acid encapsulation efficiency. SYTO 9, a membrane-permeable nucleic acid dye, was employed to stain encapsulated RNA. For LNPs above 2×10^{10} particles/mL, samples were first diluted and stained with 10× SYTO 9, followed by a 30-minute incubation at room temperature in the dark. Lower-concentration samples were stained directly without pre-dilution, adjusting dye concentration proportionally. All stained samples were further diluted (100–200×) prior to analysis, aiming for a particle flow rate of 2,000–12,000 particles/min. Data were analyzed using standard nFCM software to evaluate particle count, fluorescence positivity, and size distribution.

2.6. Cell line and E. coli Culture work

2.6.1. E. coli culture

The Escherichia coli strain (DH5α) containing the target plasmid (pVAX1) was inoculated under sterile conditions into LB liquid medium containing an appropriate concentration of kanamycin. After inoculation, the culture bottle was placed in a 37°C incubator with shaking at 200 rpm to ensure adequate oxygen supply. The culture was incubated for 12-16 hours until the bacterial culture reached the log phase. After incubation, the cells were collected by

centrifugation, and plasmid DNA was extracted using the QIAGEN® Plasmid Kit, strictly following the QIAGEN protocol to ensure high purity and yield. The extracted plasmid was verified by gel electrophoresis for integrity and quantified using NanoDrop to ensure it was suitable for subsequent experiments.

2.6.2. Cell Line Experiment

HEK293 cells (ATCC, CRL-1573) were selected for their robust growth and high transfection efficiency, making them widely applicable in gene expression and delivery studies. Cells were maintained under standard culture conditions using DMEM supplemented with fetal bovine serum and antibiotics. Cell viability and density were routinely monitored to ensure consistent physiological status for downstream applications. When cells reached optimal confluence, they were passaged and reseeded in multi-well plates to prepare for transfection. Cells were plated approximately 18–24 hours prior to transfection to ensure adherence and uniform growth. Cell density was adjusted according to cell type and experimental requirements to achieve $\geqslant$80% confluency at the time of transfection.

2.6.3. Transfection Experiment

Plasmid transfection was conducted using Lipofectamine™ 3000, which served as a positive control for evaluating LNP-based delivery efficiency due to its high transfection efficacy and well-characterized mechanism. For naked mRNA transfection, the Trans-IT mRNA kit was employed, providing efficient cytoplasmic delivery and stabilization of mRNA under optimized conditions. To ensure comparability, all mRNA used across different transfection approaches (LNP-based or reagent-based) originated from the same batch, eliminating variability associated with material differences. eGFP-mRNA-loaded LNPs were used to evaluate transfection efficiency under varying concentrations. The LNPs were filtered and diluted in culture medium to generate a concentration gradient for dose–response analysis. Transfection was performed by adding defined volumes of LNP solution to the culture wells, followed by incubation under standard conditions. Fluorescence expression was monitored to assess delivery performance across different concentrations.

2.6.4. Principal Component Analysis

Principal Component Analysis (PCA) was applied to the Design of Experiments (DoE) dataset to identify the major sources of variation linking critical process parameters (CPPs) with critical quality attributes (CQAs). Input variables included total flow rate (TFR), flow rate ratio (FRR), lipid concentration, DSPC-to-cholesterol molar ratio, and PEG-lipid percentage. Output variables were particle size (nm) and polydispersity index (PDI). Prior to analysis, all variables were mean-centered and scaled to unit variance. PCA was performed using JMP software (version X), and the results were visualized through a scree plot of explained variance, a biplot combining loadings and scores, and a correlation-based heatmap. The first two principal components captured the majority of the variance (>70%), highlighting strong negative correlations between flow-related parameters (TFR, FRR) and particle size, consistent with the heatmap analysis. The biplot further illustrated clustering of experimental runs according to flow settings, confirming that high flow rates and higher FRRs consistently resulted in smaller, more monodisperse LNPs. These PCA findings were interpreted alongside DoE and heatmap results, serving primarily as an exploratory validation tool rather than a central analytical method in this study.

3. The impact of Critical Process Parameters (CPPs) on Critical Quality Attributes (CQAs) in mRNA-LNP microfluidic Manufacturing

Microfluidic technology offers a stable and precise platform for the production of mRNA-loaded lipid nanoparticles (mRNA-LNPs), allowing for the flexible adjustment of critical process parameters (CPPs), such as total flow rate (TFR), flow rate ratio (FRR), and lipid concentration. These parameters directly influence critical quality attributes (CQAs), including particle size, polydispersity index (PDI), and encapsulation efficiency (EE%). A comprehensive understanding of the relationship between CPPs and CQAs is essential for achieving high-quality and reproducible LNP formulations. The implementation of the Quality by Design (QbD) approach further enhances this process by embedding quality into both products and manufacturing workflows through systematic design and process understanding [143].

From a cost-effectiveness perspective, the Quality by Design (QbD) approach emphasizes the optimization of critical process parameters (CPPs) to minimize material waste. For example, improving encapsulation efficiency (EE%) can reduce the consumption of costly mRNA, while optimizing mixing parameters can maximize the utilization of solvents and lipids, thereby lowering overall production costs. Moreover, continuous manufacturing significantly reduces batch-to-batch variability, thereby minimizing rework and compliance risks. By integrating QbD principles, a continuous mRNA-LNP production platform can strengthen the relationship between CPPs and critical quality attributes (CQAs), simultaneously improving product quality and enabling economic scalability [186]. This approach provides robust data to support large-scale mRNA therapeutics production and establishes a foundation for meeting stringent regulatory requirements.

Looking ahead, a microfluidic-based continuous production platform holds great promise for improving the global accessibility of mRNA-based

therapeutics, paving the way for the commercialization of gene and nucleic acid medicines. In this study, several widely used microfluidic mixers will be systematically investigated through experimental evaluation and comparative analysis. The study aims to explore their effects on critical quality attributes (CQAs) and further optimize key performance indicators (KPIs), thereby providing both theoretical support and practical guidance for the continuous manufacturing of lipid nanoparticles [187]. In the DoE study conducted using JMP software, five input factors were evaluated: total flow rate (TFR), flow rate ratio (FRR), total lipid concentration, DSPC-to-cholesterol molar ratio, and the percentage of PEG-lipid. The output responses included particle size, polydispersity index (PDI), and encapsulation efficiency (EE%). A full-factorial or custom design matrix was generated to systematically explore the interactions between formulation and process parameters.

3.1. T-mixer

The simple linear geometry of the T-mixer ensures minimal variation in flow conditions, which makes it easy to predict and optimize operating parameters based on the Reynolds number. Increasing the flow rate will increase the Reynolds number and thus shorten the mixing time, but may affect the homogeneity of lipid precipitation.

3.1.1. The Essential Calculation and flow rates screened

By calculating the Reynolds number, the flow characteristics of the T-mixer can be quantitatively evaluated. This helps to optimize the flow rates and flow ratios, thereby increasing the mixing efficiency and consequently enhancing the critical quality attributes (CQAs) of the LNP. Table 11 shows the liposome formulation results and Re number, total pressure drops (bar), mixing time change.

Table 11. Process of Preparing Liposome Parameters by T-Mixers

Total flow rate (mL/min)	**Aqueous : solvent (EtOH) ratio = 3/1**

	Re	Total pressure drops (bar)	Mixing time (ms)	Size (nm)	PDI
4	509.3	2.8	13.3	276.9±13.3	0.316±0.032
6	763.9	4.2	8.8	293.7±10.4	0.285±0.035
8	1018.6	5.6	6.3	241.8±9.3	0.241±0.024
10	1273.2	7.0	5.3	195.8±7.6	0.254±0.017
12	1527.9	8.5	4.4	127.1±6.2	0.207±0.016
16	2237.2	11.3	3.3	79.3±4.2	0.145±0.010
20	2546.5	14.1	2.4	70.9±5.6	0.157±0.011
24	3155.8	16.9	2.1	67.8±4.6	0.149±0.013
28	3565.7	19.7	1.8	58.3±5.9	0.160±0.01

*Calculations of Reynolds number, total pressure drop and mixing time were generated according to the mixer channel. Considering the actual length of the tubing, the waste volume per experiment was approximately 1.46 mL. The organic phase was composed of DSPC and cholesterol in a 3:2 composition ratio (as for mRNA-LNP) dissolved in anhydrous ethanol at a total concentration of 16 mg/mL. Aqueous phase is 25mM NaAc Buffer, pH 4.0. Same as formulation buffer. Size and PDI were measured by DLS assay. Three independent replicate experiments were performed to assess the stability and reproducibility of the results. Formulation has been previously tested with water and does not leak at the flow rates shown in the chart. The syringe pump used for the experiment was also calibrated.

As the total flow rate increased, both the Reynolds number and total pressure drop rose markedly, while the corresponding mixing time decreased from 13.3 ms to 1.8 ms. These changes reflect a substantial enhancement in microfluidic mixing efficiency under high-Re conditions. Experimental results demonstrated that increasing the flow rate led to a pronounced reduction in the particle size of lipid nanoparticles (LNPs), from 276.9 nm at 4 mL/min to 58.3 nm at 28 mL/min. Concurrently, the polydispersity index (PDI) exhibited a consistent downward trend, reaching a minimum of 0.145, suggesting improved nanoparticle uniformity.

These findings indicate that elevated flow rates in T-mixer systems promote more efficient nanoprecipitation and self-assembly of LNPs, resulting in smaller and more homogeneous particles. However, at excessively high flow rates (e.g., ≥24 mL/min), slight fluctuations in particle size and PDI were observed, possibly due to shear-induced instabilities or reduced residence time. This suggests the

existence of an optimal flow rate range balancing mixing efficiency and formulation stability.

The synthesis of blank lipid nanoparticles further validated the strong correlation between Reynolds number–based predictions and experimental outcomes, offering deeper insights into the mixing characteristics of the T-mixer system. These findings provide a robust theoretical and experimental foundation for optimizing mixing parameters, refining mRNA-LNP formulation processes, and supporting scalable manufacturing and performance evaluation.

3.1.2. Effect of Flow Setting (TFR, FRR & Lipid Concentration)

As a simple and commonly used microfluidic mixer, the design features and operational flexibility of the T-mixer make it an ideal modelling tool for analyzing the effects of Critical Process Parameters (CPPs) on Critical Quality Attributes (CQAs). The effects of three critical parameters, Total Flow Rate, Flow Rate Ratio and Lipid Concentration, on particle size (Size), polydispersity index (PDI) and encapsulation efficiency (EE%) are analyzed below. Choosing NanoFlowSizer to measure size and PDI, and the EE% measured by Ribogreen.

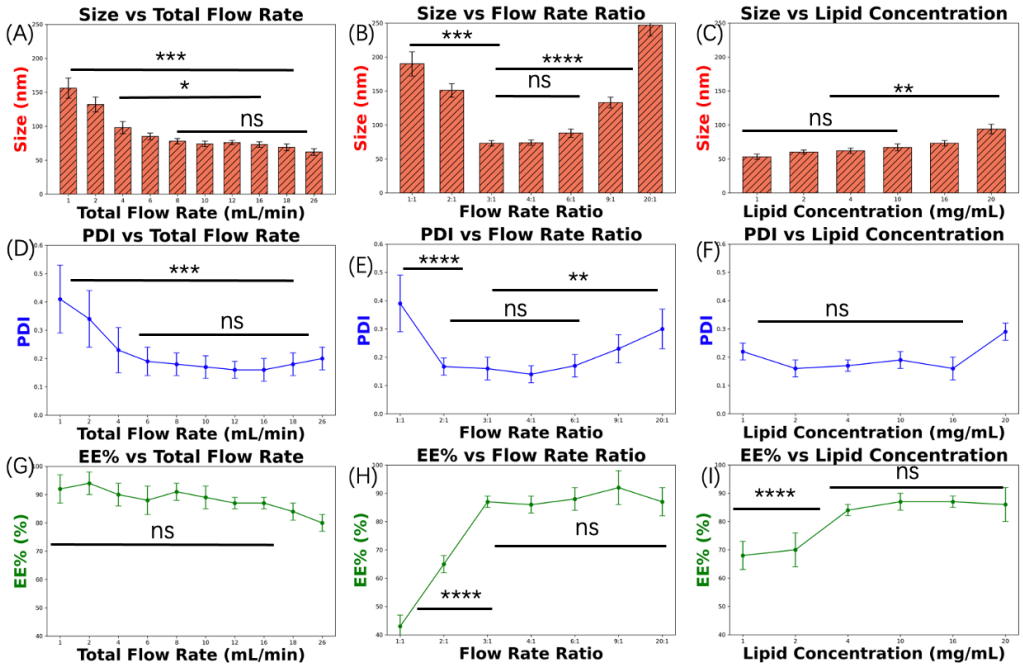

Figure 25. The schematic of the variation of size (A-C), PDI (D-F) and encapsulation efficiency (G-I) with total flow rate (mL/min), flow rate ratio and lipid concentration (mg/mL) of T-mixer. The effect of Flow Rate Setting (T-mixer):

Based on Reynolds number systematic experiments and analyses were conducted to investigate the effects of total flow rate (TFR, 1–26 mL/min) and flow rate ratio (FRR, 1:1–20:1). Considering the actual length of the tubing, the waste volume per experiment was approximately 1.46 mL. The composition of the mRNA-lipid nanoparticles included ALC-0315: DOPE: Chol: ALC-0159, with total lipid concentrations shown in the figures. eGFP was selected as the mRNA component, with an approximate length of 3039 nucleotides (nts). The lipids were dissolved in anhydrous ethanol, and the mRNA was dissolved in 25 mM sodium acetate buffer at pH 4.0. And the N/P ratio is 6:1. The eGFP-mRNA used in the experiments was from the same production batch. Three independent replicate experiments were performed to assess the stability and reproducibility of the results. Error bars represent ±SD, and if not visible, the error is hidden within the bar plots (±SD, n=9).

Experimental data demonstrate significant regulatory effects of total flow rate, flow rate ratio, and lipid concentration on the size, uniformity, and encapsulation efficiency of lipid nanoparticles (LNPs) (Figures 25 A-C). When maintaining a fixed flow ratio (3:1) and lipid concentration (16 mg), increasing the total flow rate from 1 mL/min to 26 mL/min reduced particle size linearly from 156 ± 15 nm to 62 ± 5 nm (60.3% reduction), while the polydispersity index (PDI) decreased from 0.41 ± 0.12 to 0.20 ± 0.04 (Figures 25 A,D). These results indicate that enhanced fluid mixing efficiency at higher flow rates suppresses excessive particle growth and improves size uniformity. However, when exceeding 16 mL/min, encapsulation efficiency (EE%) dropped significantly from 92% to 80% (Figure 25 G), likely due to insufficient mixing time for complete drug-lipid integration.

At fixed total flow rate (16 mL/min) and lipid concentration (16 mg), variations in flow rate ratio (aqueous:organic phase) exhibited nonlinear effects (Figures 25 B,E,H). Optimal performance occurred at 3:1 ratio, yielding minimal particle size (73 ± 4 nm) and lowest PDI (0.16 ± 0.04). Extreme ratios (1:1 or 20:1) increased size to 190 ± 18 nm and 257 ± 16 nm, respectively, with PDI rising to 0.30 ± 0.07. This pattern correlates with phase mixing homogeneity—the 3:1 ratio likely represents a balance point for solvent diffusion, while extreme ratios induce phase separation that compromises uniformity. Notably, EE% peaked at 92 ± 6% under 9:1 ratio (Figure 25 H), suggesting moderate organic phase dilution promotes ordered lipid alignment.

Lipid concentration displayed threshold-dependent behavior (Figure 25 C,F,I). Gradual size increase from 53 ± 4 nm to 73 ± 4 nm and stable PDI (0.16-0.19) were observed at concentrations ≤16 mg. Beyond this threshold, size surged to 94 ± 7 nm with PDI elevation to 0.29 ± 0.03, indicating structural reorganization of lipid molecules into complex multilayered arrangements. EE% plateaued above 87% at concentrations ≥10 mg ($p = 0.62$), demonstrating saturation of drug-loading capacity at moderate concentrations.

Interactions between critical process parameters (CPPs) significantly influence product quality. The synergistic combination of total flow rate (16 mL/min) and flow ratio (3:1) achieved balanced mixing efficiency and interfacial behavior, optimizing particle size (73 nm), PDI (0.16), and EE% (87%) simultaneously. However, at extreme flow ratios (20:1), increasing lipid concentration to 20 mg only partially restored EE% (43% → 86%) while worsening PDI by 72% (0.14 → 0.30), revealing limitations in parameter compensation strategies.

Based on these findings, we recommend a core operational window: total flow rate 16 mL/min, flow ratio 3:1, and lipid concentration 16 mg/mL. Within this range, particle size remains <75 nm, PDI <0.2, and EE% >87%. For industrial translation, three control priorities emerge: 1) Avoid insufficient mixing at low flow rates (<12 mL/min); 2) Prevent phase separation at extreme ratios (>6:1); 3) Limit lipid concentration to ≤16 mg to avert structural transitions. Future studies should employ real-time monitoring (e.g., Nano Flow Sizer) to track nucleation dynamics and computational fluid dynamics to optimize mixer design, thereby advancing scalable LNP production.

3.1.3. Effect of Different Lipid Nanoparticle Composition

The flow rate optimization experiments conducted with the T-mixer have identified an operational window for achieving efficient mixing under various flow conditions, providing a solid foundation for further exploration of mRNA-LNP formulation optimization. Building upon this, the present study will systematically investigate key formulation parameters (CPPs), including PEG-lipid content (1.5%-25%), lipid-to-cholesterol ratio (1:1-9:1), and N/P ratio (1:1-10:1), to evaluate their effects on critical quality attributes (CQAs) such as

particle size, polydispersity index (PDI), encapsulation efficiency (EE%), and stability. PEG-lipid content is a critical factor in determining the stability and biodistribution of LNPs; however, excessive proportions may increase particle size and affect PDI. The lipid-to-cholesterol ratio directly impacts the membrane fluidity and structural stability of the nanoparticles. Meanwhile, the N/P ratio serves as a core parameter for nucleic acid drug delivery efficiency, where optimization is essential for enhancing mRNA encapsulation efficiency and biological activity. By studying the combined effects of these variables, this research aims to comprehensively understand their interactive influence on LNP performance.

The objective of this study is to use experimental data to optimize mRNA-LNP formulation parameters, achieving precise control over particle size, reduced polydispersity index, and improved encapsulation efficiency. Ultimately, these findings will provide theoretical and experimental support for the production of stable, reproducible, and application-specific LNPs. Choosing NanoFlowSizer to measure size and PDI, and the EE% measured by Ribogreen.

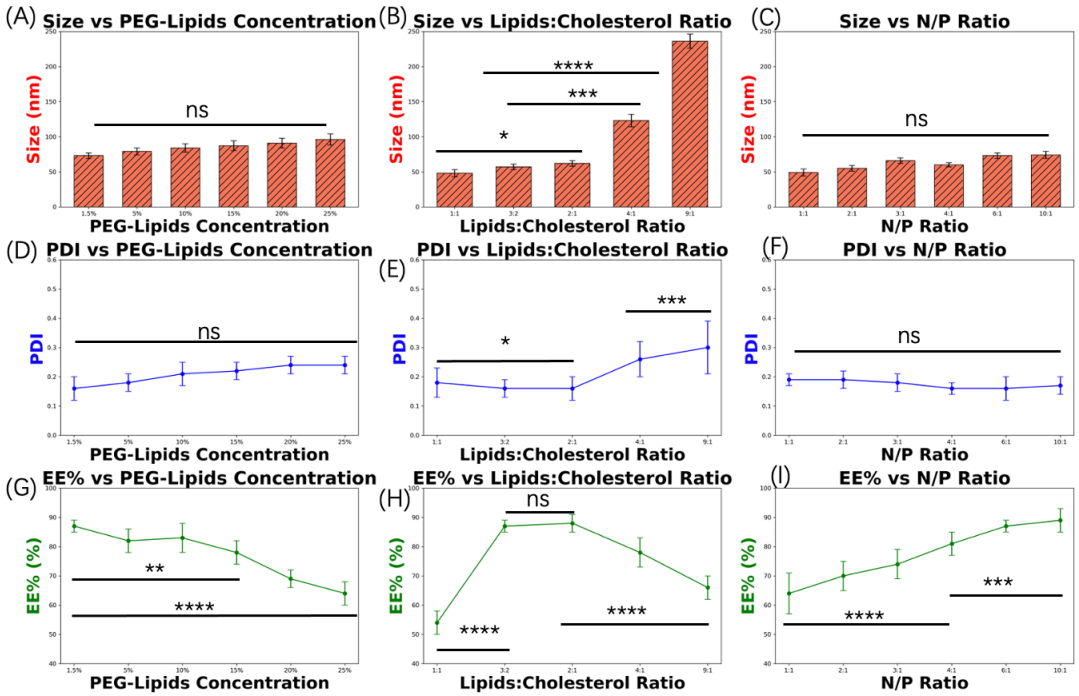

Figure 26. The schematic of the variation of size (A-C), PDI (D-F) and encapsulation efficiency (G-I) with PEG-lipid ratio, Lipids: Cholesterol ratio and N/P ratio of T-mixer. The effect of Organic Phase Compositions (T-mixer): The PEG-Lipid content (1.5mol%-20mol%), the lipid to cholesterol ratio (1:1-9:1), and different N/P ratios (1:1-10:1) were determined separately. The most stable TFR :16 mL/min and

FRR (A:O=3:1) were selected. And Lipid concentration was stabilized at 16 mg/mL. eGFP was selected as the mRNA component, with an approximate length of 3039 nucleotides (nts). The lipids were dissolved in anhydrous ethanol, and the mRNA was dissolved in 25 mM sodium acetate buffer at pH 4.0. The eGFP-mRNA used in the experiments was from the same production batch. Three independent replicate experiments were performed to assess the stability and reproducibility of the results. Error bars represent ±SD, and if not visible, the error is hidden within the bar plots (±SD, n=9).

As shown in Figure 26 (A, D, G), increasing the PEG-lipid ratio from 1.5% to 25% (with fixed lipid: cholesterol ratio 3:2 and N/P ratio 6:1) significantly altered nanoparticle properties. Particle size increased linearly from 73 ± 4 nm (1.5%) to 96 ± 8 nm (25%) (31.5% growth), while polydispersity index (PDI) rose from 0.16 ± 0.04 to 0.24 ± 0.03 (Figure 26 D). This suggests that elevated PEG content may retard lipid self-assembly through steric hindrance, prolonging particle growth. Encapsulation efficiency (EE%) decreased from 87 ± 2% to 64 ± 4% (26.4% reduction), indicating excessive PEGylation likely disrupts lipid-drug interactions.

Under fixed PEG-lipid (1.5%) and N/P ratio (6:1), lipid: cholesterol ratio exhibited nonlinear effects (Figure 26 B,E,H). Adjusting the ratio from 1:1 to 3:2 increased size from 48 ± 5 nm to 57 ± 4 nm, reduced PDI from 0.18 ± 0.05 to 0.16 ± 0.03, and enhanced EE% from 54 ± 4% to 87 ± 2%. However, further increasing the ratio to 9:1 caused drastic size expansion (236 ± 10 nm, +314%), elevated PDI (0.30 ± 0.09), and reduced EE% (66 ± 4%), emphasizing the need for moderate cholesterol content (3:2–4:1) to prevent structural instability.

At fixed PEG-lipid (1.5%) and lipid: cholesterol ratio (3:2), increasing N/P ratio (nucleic acid: lipid charge ratio) from 1:1 to 10:1 progressively improved EE% from 64 ± 7% to 89 ± 4% (+38.4%) (Figure 26 C,F,I). Notably, the smallest particle size (60 ± 3 nm) and lowest PDI (0.16 ± 0.02) occurred at N/P 4:1, suggesting balanced charge-mediated assembly dynamics.

Multivariate analysis identified 1.5% PEG-lipid, 3:2 lipid: cholesterol ratio, and 6:1 N/P ratio as optimal for balancing size (73 ± 4 nm), PDI (0.16 ± 0.04), and EE% (87 ± 2%). Deviations (e.g., PEG-lipid >10% or lipid: cholesterol ratio beyond 3:2–4:1) significantly compromised uniformity and drug loading.

Recommended screening priorities include PEG-lipid ≤5%, lipid: cholesterol ratio 3:2–4:1, and N/P ratio 6:1–10:1 to ensure stability and encapsulation performance.

The T-mixer demonstrates superior performance in lipid nanoparticle (LNP) synthesis by enabling precise control over hydrodynamic parameters (total flow rate, flow ratio) and formulation variables (lipid concentration, PEGylation, lipid: cholesterol ratio, N/P ratio), allowing tailored optimization of particle size (48–257 nm), monodispersity (PDI 0.08–0.41), and encapsulation efficiency (54–94%). Unlike conventional methods, its microfluidic design ensures robust nanoparticle production across broad operational ranges (1–26 mL/min) and reveals previously unrecognized parameter interdependencies. Notably, extreme dilution conditions (20:1 flow ratio) can be partially mitigated by lipid concentration adjustment (43%→86% EE%), while strategic parameter offsets (e.g., increasing N/P ratio from 6:1 to 10:1 at 6:1 flow ratio) enhance EE% (87%→89%) without significantly compromising PDI (0.16→0.17). These findings uncover a nonlinear synergy between hydrodynamic and compositional factors, challenging traditional empirical thresholds and advancing rational formulation design for complex nanosystems.

3.2. Swirl Mixer

The complex curved channels and integrated mixing elements (such as spiral structures) of the Swirl Mixer significantly enhance fluid mixing efficiency. Its unique geometric design allows for effective mixing across a wider range of Reynolds numbers. As flow rate increases, the Swirl Mixer utilizes vortices and secondary flows to further improve mixing efficiency and reduce mixing time. This design maintains excellent mixing performance even at high flow rates, optimizing nanoparticle uniformity and critical quality attributes (CQAs) [188]. While the Swirl Mixer excels in efficient mixing, its more complex flow effects may require finer parameter adjustments to ensure stability.

3.2.1. The Essential Calculation and flow rates screened

The Swirl Mixer's complex curved channel design and integrated mixing elements (spiral structures & layered configurations) enhance mixing efficiency

through vortex flow and secondary flows, achieving efficient mixing across a broader range of Reynolds numbers [189]. Its mixing performance is more stable and less dependent on extreme flow rate conditions [190]. The Swirl Mixer effectively breaks the limitations of traditional diffusion mixing by introducing swirling flow in the channel, making it suitable for a wider range of flow rates. Its turbulent characteristics allow it to maintain good mixing performance at high flow rates. Table 12 shows the liposome formulation results and Re number, total pressure drops (bar), mixing time change.

Table 12. Process of Preparing Liposome Parameters by Swirl Mixers

Total flow rate (mL/min)	**Aqueous: solvent (EtOH) ratio = 3/1**				
	Re	Total pressure drops (bar)	Mixing time (ms)	Size (nm)	PDI
28	1069.5	0.2	1.311	67.9±6.3	0.134±0.017
40	1527.9	0.3	0.918	63.5±5.7	0.103±0.014
60	2291.8	0.9	0.612	60.7±3.4	0.085±0.005
80	3055.7	1.6	0.459	58.5±2.5	0.071±0.006
100	3819.7	2.3	0.367	57.5±2.0	0.067±0.004
120	4583.6	3.5	0.306	55.3±1.6	0.060±0.004
140	5347.6	4.8	0.262	54.9±2.2	0.075±0.007
160	6111.5	6.2	0.229	53.6±2.5	0.089±0.010
180	6875.5	7.9	0.204	54.4±2.8	0.083±0.011
200	7660.8	9.7	0.188	52.2±2.6	0.071±0.008
240	9167.3	14.0	0.153	50.2±3.1	0.094±0.014

*Calculations of Reynolds number, total pressure drop and mixing time were generated according to the Swirl mixer channel. Considering the actual length of the tubing, the waste volume per experiment was approximately 2.08 mL. The organic phase was composed of DSPC and cholesterol in a 3:2 composition ratio (as for mRNA-LNP) dissolved in anhydrous ethanol at a total concentration of 16 mg/mL. Aqueous phase is 25mM NaAc Buffer, pH 4.0. Same as formulation buffer. Size and PDI were measured by DLS assay. Three independent replicate experiments were performed to assess the stability and reproducibility of the results. Formulation has been previously tested with water and does not leak at the flow rates shown in the chart. The syringe pump used for the experiment was also calibrated.

As the flow rate increases from 28 mL/min to 240 mL/min, the Reynolds number rises significantly, indicating intensified turbulence unique to the Swirl Mixer design. This enhanced turbulence contributes to the steady decrease in mixing time from 1.311 ms to 0.153 ms, showcasing the mixer's capability to rapidly achieve uniform mixing, even at high flow rates.

Compared to other mixers, the Swirl Mixer consistently produces smaller nanoparticles (size reduced from 67.9 nm to 50.2 nm) with a narrower distribution (PDI from 0.134 to 0.060), particularly at higher flow speeds. This highlights its advantage in generating more homogeneous lipid nanoparticles, a critical requirement for precision in mRNA-LNP formulations.

The distinct characteristics of the Swirl Mixer make it particularly suited for high-speed, high-throughput processes, enabling rapid and efficient LNP production with superior quality and scalability.

3.2.2. Effect of Flow Setting (TFR, FRR & Lipid Concentration)

As an advanced microfluidic mixer, the Swirl Mixer, with its complex curved channel design and integrated mixing elements, offers superior mixing efficiency and flexibility. Its design makes it particularly suitable for analyzing the effects of Critical Process Parameters (CPPs) on Critical Quality Attributes (CQAs). Below, the impact of parameters such as TFR, FRR, and Lipid Concentration on particle size (Size), polydispersity index (PDI), and encapsulation efficiency (EE%) is evaluated. Choosing NanoFlowSizer to measure size and PDI, and the EE% measured by Ribogreen.

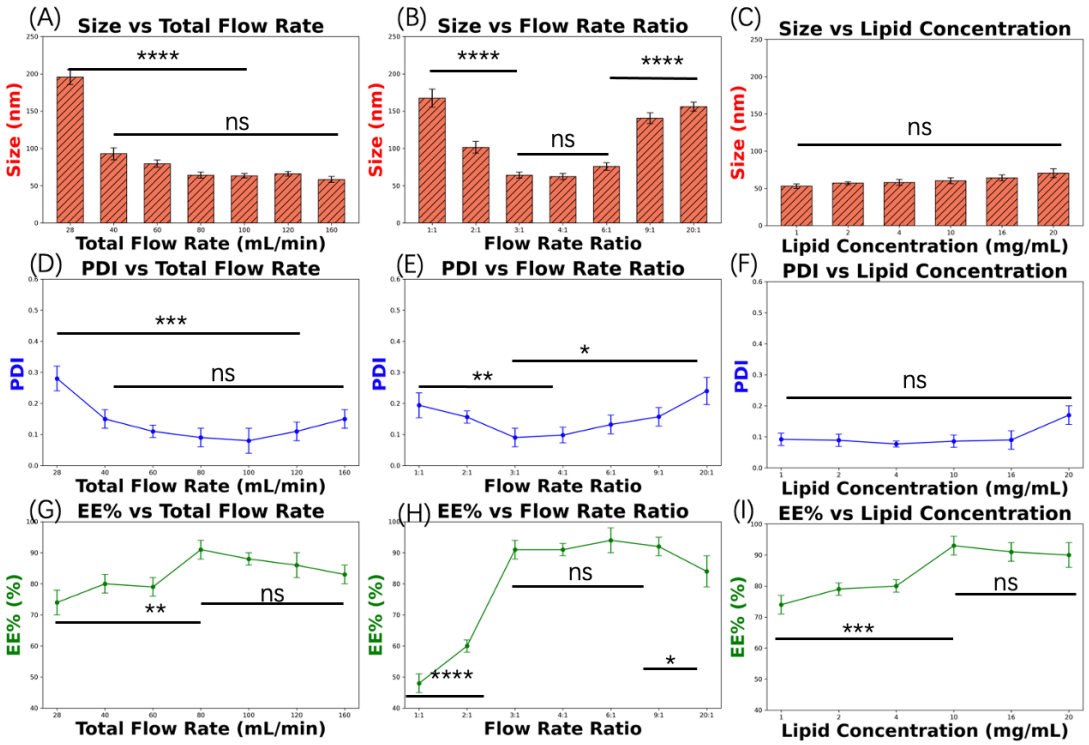

Figure 27. The schematic of the variation of size (A-C), PDI (D-F) and encapsulation efficiency (G-I) with total flow rate (mL/min), flow rate ratio and lipid concentration (mg/mL) of Swirl Mixer. The effect of Flow Rate Setting (Swirl-mixer): Based on Reynolds number calculations and the specific design of the T-mixer, systematic experiments and analyses were conducted to investigate the effects of total flow rate (TFR, 28–160 mL/min) and flow rate ratio (FRR, 1:1–20:1). Considering the actual length of the tubing, the waste volume per experiment was approximately 2.08 mL. The composition of the mRNA-lipid nanoparticles included ALC-0315: DOPE: Chol: ALC-0159 (48.5: 12.5: 38.5: 1.5, mol%), with total lipid concentrations shown in the figures. And the N/P ratio is 6:1. eGFP was selected as the mRNA component, with an approximate length of 3039 nucleotides (nts). The lipids were dissolved in anhydrous ethanol, and the mRNA was dissolved in 25 mM sodium acetate buffer at pH 4.0. The eGFP-mRNA used in the experiments was from the same production batch. Three independent replicate experiments were performed to assess the stability and reproducibility of the results. Error bars represent ±SD, and if not visible, the error is hidden within the bar plots (±SD, n=9).

Under fixed flow ratio (3:1) and lipid concentration (16 mg), increasing the total flow rate from 28 mL/min to 160 mL/min (Figure 27 A) in the Swirl Mixer reduced particle size from 195.6 ± 10 nm to 58.4 ± 4 nm (70.1% reduction), with polydispersity index (PDI) decreasing from 0.28 ± 0.04 to 0.08 ± 0.04 (minimum at 100 mL/min) (Figure 27 D). Encapsulation efficiency (Figure 26G) peaked at 91 ± 3% (80 mL/min) before slightly declining to 83 ± 3% at 160 mL/min,

indicating an optimal mixing intensity window (80–100 mL/min). Compared to T-mixer, Swirl Mixer achieved smaller particles (<65 nm) and lower PDI (<0.1) at higher flow rates (>60 mL/min).

At fixed 80 mL/min flow rate, varying the flow ratio (1:1→20:1) revealed nonlinear effects: minimal size (62.3–64.1 nm) and PDI (0.09–0.098) occurred at 3:1–4:1 ratios, while EE% peaked at 94 ± 4% under 6:1 ratio (Figure 27 H). Lipid concentration (Figure 27 C,F,I) exhibited threshold behavior: EE% increased from 74 ± 3% (1 mg) to 93 ± 3% (10 mg) then stabilized (90 ± 4% at 16–20 mg), whereas PDI reached its lowest value (0.077 ± 0.01) at 4 mg before rising to 0.17 ± 0.03 beyond 16 mg.

Swirl Mixer outperforms T-mixer in two key aspects, the first is High-Flow Compatibility: Maintains smaller particles (58.4 nm vs. T-mixer's 62 nm) at 160 mL/min, favoring scalable production; And the other is Dilution Resilience: Retains 84 ± 5% EE% at 20:1 flow ratio (vs. T-mixer's 87 ± 5%) under extreme dilution. However, Swirl Mixer shows greater sensitivity to lipid concentration variations: PDI increases by 120% beyond 16 mg (vs. 81% for T-mixer), demanding stricter material balance control during lipid assembly.

3.2.3. Effect of different Lipid Nanoparticle compositions

Building upon the flow rate optimization studies, similar experiments were conducted using the Swirl Mixer to systematically investigate key formulation parameters (CPPs), including PEG-lipid content (1.5%-25%), lipid-to-cholesterol ratio (1:1-9:1), and N/P ratio (1:1-10:1). The objective of this study was to evaluate their impact on critical quality attributes (CQAs), such as particle size, polydispersity index (PDI), encapsulation efficiency (EE%), and stability, thereby providing insights into the optimization of mRNA-LNP formulations. Choosing NanoFlowSizer to measure size and PDI, and the EE% measured by Ribogreen.

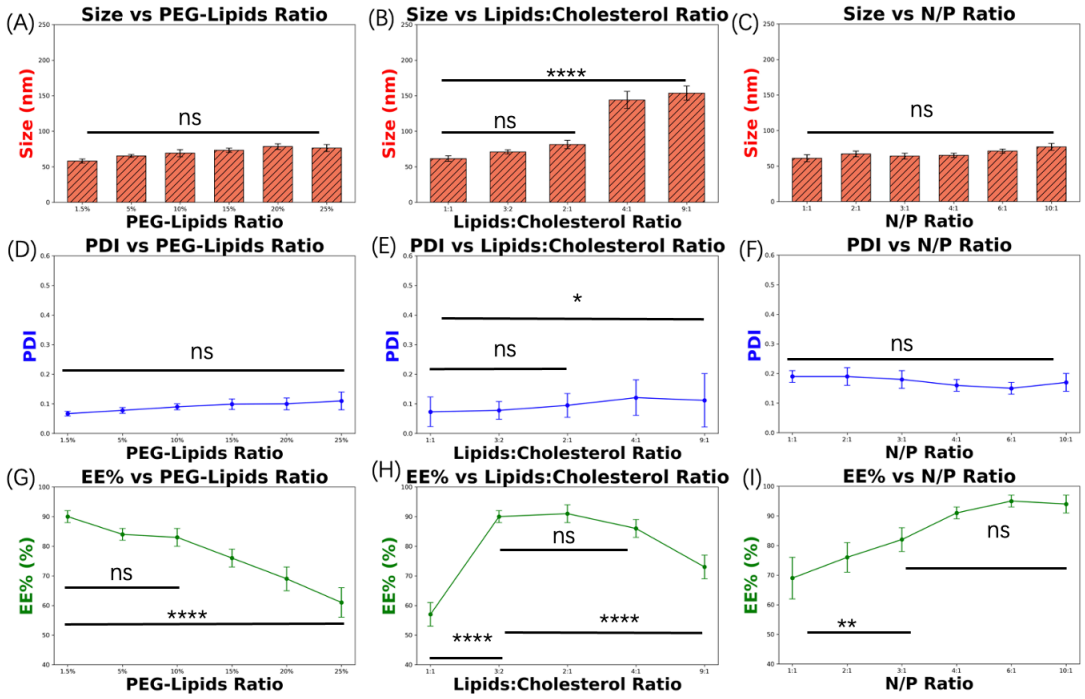

Figure 28. The schematic of the variation of size (A-C), PDI (D-F) and encapsulation efficiency (G-I) with PEG-lipid ratio, Lipids: Cholesterol ratio and N/P ratio of Swirl Mixer. The effect of Organic Phase Compositions (Swirl mixer): The PEG-Lipid content (1.5mol%-20mol%), the lipid to cholesterol ratio (1:1-9:1), and different N/P ratios (1:1-10:1) were determined separately. The most stable TFR :80 mL/min and FRR (A:O=3:1) were selected. And Lipid concentration was stabilized at 16 mg/mL. eGFP was selected as the mRNA component, with an approximate length of 3039 nucleotides (nts). The lipids were dissolved in anhydrous ethanol, and the mRNA was dissolved in 25 mM sodium acetate buffer at pH 4.0. The eGFP-mRNA used in the experiments was from the same production batch. Three independent replicate experiments were performed to assess the stability and reproducibility of the results. Error bars represent ±SD, and if not visible, the error is hidden within the bar plots (±SD, n=9).

Swirl Mixer demonstrates core trends similar to T-mixer in formulation parameter responses, yet its performance variations reveal unique mixing mechanism characteristics. As shown in Figure 28 (A, D, G), increasing the PEG-lipid ratio from 1.5% to 25% enlarges particle size from 58 ± 3 nm to 76.3 ± 5 nm (+31.5%), elevates PDI from 0.067 ± 0.008 to 0.11 ± 0.03, and reduces EE% from 90 ± 2% to 61 ± 5%. Compared to T-mixer (73→96 nm, PDI 0.16→0.24), Swirl Mixer exhibits superior size control and uniformity at equivalent PEG ratios. Figure 28 (B,E,H) further illustrates that adjusting the lipid: cholesterol ratio from 1:1 to 9:1 drastically increases particle size from

61.4 ± 4 nm to 153.5 ± 10 nm (+150%), while EE% peaks at 91 ± 3% (2:1 ratio), outperforming T-mixer's 87 ± 2% (3:2 ratio). This suggests vortex-enhanced mixing improves cholesterol distribution homogeneity, though extreme ratios (>4:1) still induce lipid aggregation.

Results in Figure 28 (C, F, I) show that increasing the N/P ratio from 1:1 to 10:1 enhances EE% from 69 ± 7% to 94 ± 3%, peaking at 95 ± 2% (6:1 ratio), superior to T-mixer's 87 ± 2%. Swirl Mixer achieves minimal size (65 ± 3 nm) and lowest PDI (0.16 ± 0.02) at N/P=4:1, whereas T-mixer under the same conditions yields larger particles (73 ± 4 nm) and higher PDI (0.16 ± 0.04), confirming that vortex-driven charge balancing effectively suppresses particle aggregation. Unlike T-mixer, which relies on laminar/turbulent shear, Swirl Mixer employs 3D vortices to enhance local mixing efficiency, enabling stable production at 160 mL/min. However, it shows greater sensitivity to lipid concentration variations (120% PDI increase vs. T-mixer's 81%), necessitating compensation through N/P ratio optimization (e.g., 95% EE% at 6:1). Subsequent experiments will compare performance with Herringbone Mixer.

3.3. Herringbone Mixer

The herringbone-shaped channel design of the Herringbone Mixer effectively introduces secondary flows and remix, significantly improving mixing efficiency. Compared to the T-mixer, the Herringbone Mixer demonstrates stronger fluid mixing capabilities under low flow rate conditions. Its design minimizes variations in flow conditions, making it more straightforward to optimize operational parameters based on the Reynolds number [191]. As the flow rate increases, the Herringbone Mixer efficiently shortens mixing time while maintaining high control over fluid properties [192]. Its unique fluid dynamics make it an ideal solution for achieving high nanoparticle uniformity and structural stability.

3.3.1. The Essential Calculation and flow rates screened

The Herringbone Mixer’s unique herringbone-patterned channel design enhances mixing efficiency by introducing secondary flows and chaotic

advection, enabling superior mixing across a wider range of Reynolds numbers. Compared to conventional linear channels, the herringbone structure disrupts laminar flow and promotes more uniform mixing, even at low flow rates [193]. This design overcomes the limitations of purely diffusive mixing by inducing transverse fluid motion, making it ideal for low-to-moderate flow rates. The Herringbone Mixer exhibits robust performance in ensuring homogeneity and precise control of nanoparticle size distribution, offering excellent adaptability to a range of flow conditions. Table 13 shows the liposome formulation results and Re number, total pressure drops (bar), mixing time change.

Table 13. Process of Preparing Liposome Parameters by Herringbone Mixers

Total flow rate(mL/min)	**Aqueous : solvent (EtOH) ratio = 3/1**				
	Re	Total pressure drops (bar)	Mixing time (ms)	Size (nm)	PDI
1	421.87	0.3	24.0	366.9±17.4	0.416±0.12
2	843.74	0.6	12.0	293.7±14.3	0.385±0.07
4	1689.38	1.7	8.0	241.8±8.7	0.241±0.06
6	2544.96	3.5	4.8	195.8±9.7	0.254±0.05
8	3378.44	6.2	3.9	127.1±8.2	0.237±0.04
10	4098.61	8.5	2.1	121.4±7.6	0.251±0.05

*Calculations of Reynolds number, total pressure drop and mixing time were generated according to the Herringbone mixer channel. Considering the actual length of the tubing, the waste volume per experiment was approximately 0.78 mL. The organic phase was composed of DSPC and cholesterol in a 3:2 composition ratio (as for mRNA-LNP) dissolved in anhydrous ethanol at a total concentration of 16 mg/mL. Aqueous phase is 25mM NaAc Buffer, pH 4.0. Same as formulation buffer. Size and PDI were measured by DLS assay. Three independent replicate experiments were performed to assess the stability and reproducibility of the results. Formulation has been previously tested with water and does not leak at the flow rates shown in the chart. The syringe pump used for the experiment was also calibrated.

As the total flow rate increased from 1 mL/min to 10 mL/min, the Reynolds number rose significantly, indicating enhanced turbulent mixing, while the total pressure drop also increased, reflecting greater fluid resistance at higher flow rates. Mixing time was dramatically reduced from tens of milliseconds to just a

few milliseconds, demonstrating the high mixing efficiency of the Herringbone Mixer under high-flow conditions. With increasing flow rates, the particle size of LNPs decreased notably, accompanied by a reduction in the polydispersity index (PDI), indicating the production of smaller and more uniformly distributed nanoparticles. The Herringbone Mixer is suitable for producing larger and broader-distribution LNPs under low-flow conditions, while its excellent uniformity and particle size control make it particularly effective under high-flow conditions.

3.3.2. Effect of Flow Setting (TFR, FRR & Lipid Concentration)

Choosing NanoFlowSizer to measure size and PDI, and the EE% measured by Ribogreen.

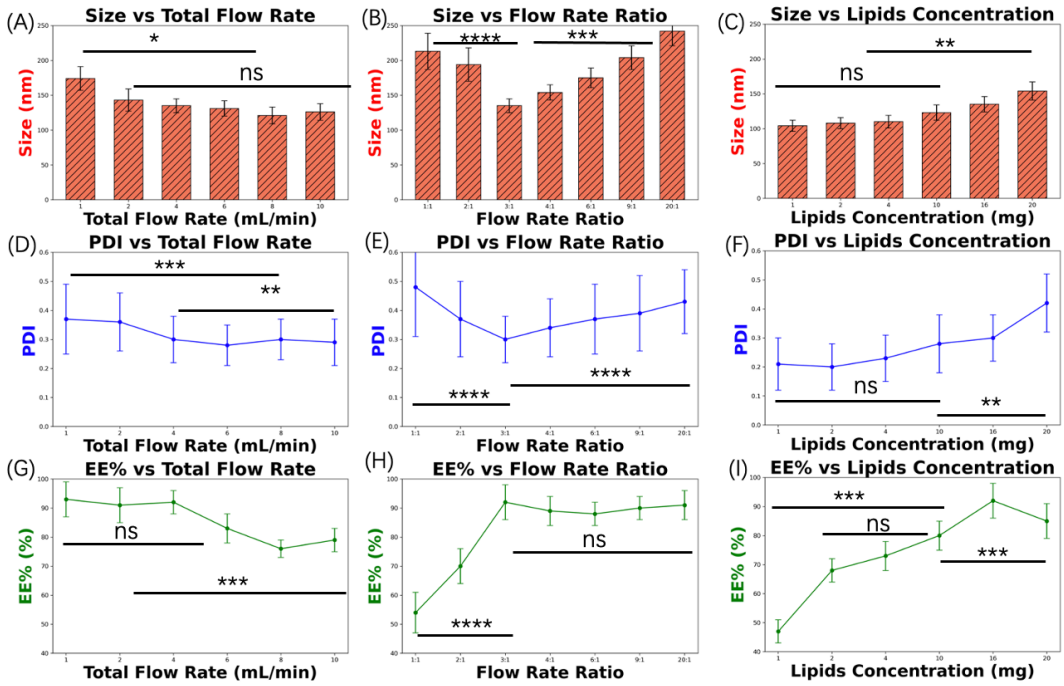

Figure 29. The schematic of the variation of size (A-C), PDI (D-F) and encapsulation efficiency (G-I) with total flow rate (mL/min), flow rate ratio and lipid concentration (mg/mL) of Herringbone Mixer. The effect of Flow Rate Setting (Herringbone Mixer): Based on Reynolds number calculations and the specific design of the T-mixer, systematic experiments and analyses were conducted to investigate the effects of total flow rate (TFR, 28–160 mL/min) and flow rate ratio (FRR, 1:1–20:1). Considering the actual length of the tubing, the waste volume per experiment was approximately 0.78 mL. The composition of the mRNA-lipid nanoparticles included ALC-0315: DOPE: Chol: ALC-0159 (48.5: 12.5: 38.5: 1.5, mol%), with total lipid concentrations shown in the figures. And the N/P ratio is 6:1. eGFP was selected as the mRNA component, with an approximate length of 3039 nucleotides (nts). The lipids

were dissolved in anhydrous ethanol, and the mRNA was dissolved in 25 mM sodium acetate buffer at pH 4.0. The eGFP-mRNA used in the experiments was from the same production batch. Three independent replicate experiments were performed to assess the stability and reproducibility of the results. Error bars represent ±SD, and if not visible, the error is hidden within the bar plots (±SD, n=9).

The Herringbone Mixer demonstrates fundamentally distinct mixing mechanisms compared to T-mixer and Swirl mixer, with data characteristics revealing unique performance constraints. As shown in Figure 29 A, increasing the total flow rate (1→10 mL/min) reduces particle size from 174 ± 17 nm to 126 ± 12 nm, but the polydispersity index (PDI) remains above 0.28 (Figure 29D), accompanied by size rebound (131→126 nm) beyond 6 mL/min. This indicates that its herringbone-patterned periodic turbulence induces flow recirculation at higher rates, compromising mixing homogeneity. Figure 29B illustrates that adjusting the flow ratio (1:1→20:1) yields minimal size (135 ± 10 nm) at 3:1 ratio, while extreme ratios (20:1) cause abrupt size expansion to 242 ± 21 nm (+79%) with PDI elevation to 0.43 ± 0.11, significantly exceeding Swirl mixer's performance (156.1 ± 6 nm, PDI 0.24 ± 0.044) under equivalent conditions. Furthermore, Figure 29C/F/I demonstrates that lipid concentration variations (1→20 mg) result in low encapsulation efficiency (EE% 47 ± 4% at 1 mg), improving to 92 ± 6% at 16 mg but accompanied by PDI degradation from 0.21 ± 0.09 to 0.30 ± 0.08, confirming heightened sensitivity to material equilibrium.

Diverging from T-mixer's laminar shear and Swirl mixer's vortex-driven mixing, Herringbone mixer relies on herringbone-induced periodic turbulence, which introduces two critical flaws: 1) Poor flow rate compatibility, with a maximum effective rate of 10 mL/min (vs. 26 mL/min for T-mixer and 160 mL/min for Swirl mixer) and size rebound at high flow rates; 2) Elevated data variability, evidenced by larger standard deviations (e.g., size SD=17 nm at 1 mL/min vs. Swirl mixer's 10 nm), reflecting unstable mixing reproducibility. Due to these limitations and anomalous trends (e.g., abnormal EE% increase to 91 ± 5% at 20:1 flow ratio, contradicting conventional dilution effects), Herringbone mixer was excluded from subsequent formulation optimization studies.

3.4. Comprehensive Comparative Analysis of T-Mixer, Swirl Mixer, and Herringbone Mixer: Stability, Response Surface Analysis, and CPP-CQA Correlations

This study focuses on the T-mixer, Swirl Mixer, and Herringbone Mixer, three foundational microfluidic devices widely used in liquid-liquid phase mixing. While these mixers share a common application in facilitating rapid mixing, their mixing principles and fluid dynamics differ significantly. The T-mixer, based on simple diffusion mixing, features the simplest structure and is suitable for small-scale trials. The Swirl Mixer enhances mixing efficiency through vortex flow and secondary flow, excelling under high flow rates [194]. Meanwhile, the Herringbone Mixer leverages chaotic advection to promote mixing, demonstrating exceptional uniformity and distribution control within specific conditions.

The objective of this study is to conduct a comprehensive analysis and comparison of the performance of these three mixers, focusing on the effects of key process parameters (CPPs) on critical quality attributes (CQAs), such as particle size (Size), polydispersity index (PDI), and encapsulation efficiency (EE%). Furthermore, this study explores their applicability in scale-up and continuous production processes. By comparing the advantages and limitations of these designs, the research aims to identify which mixer design better meets the key performance indicators (KPIs) required for mRNA-LNP production, providing theoretical and experimental insights for efficient large-scale manufacturing.

3.4.1. Mixers Stability Analysis

This study begins with a preliminary stability analysis of mRNA-LNPs synthesized using the T-mixer, Swirl Mixer, and Herringbone Mixer. Given that the storage and transportation of LNPs remain significant challenges in the development of gene therapies, conducting foundational stability evaluations is essential [195]. By comparing the stability of LNPs produced by different mixers,

this research seeks to uncover the influence of mixing methods on the final product's performance.

It is important to note that the stability of LNPs is not only determined by their intrinsic formulation and physical characteristics but is also closely linked to the purification process. Therefore, this section focuses on analyzing how different mixing strategies impact LNP stability, providing critical insights for optimizing production processes. This analysis aims to reveal how mixing efficiency, particle size uniformity, and polydispersity index (PDI) relate to LNP stability over time, offering robust data support for the end-to-end workflow from production to storage and transportation. Figure 30 are results of stability.

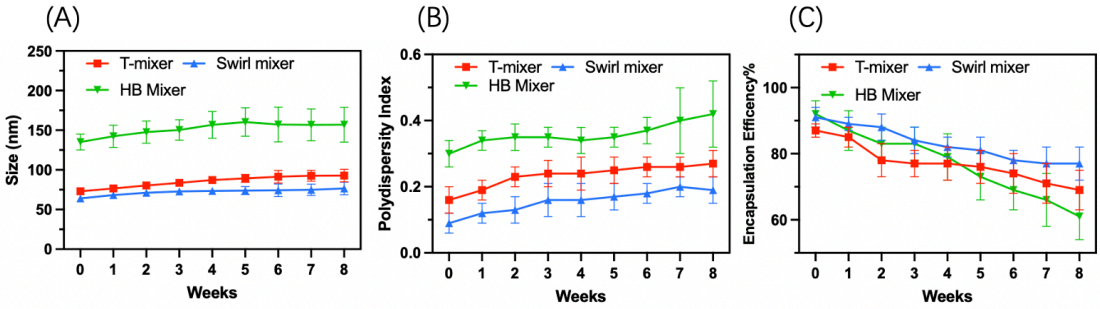

Figure 30. The three mixer stability experiments. The samples were diluted with PBS buffer pH 7.4 following a consistent protocol after synthesis and stored in glass containers at 4°C under light-protected conditions. And the formulation and dilution interval within 30 seconds to avoid the high organic phase effect. Due to variations in chip designs, it was challenging to produce LNPs with identical characteristics, but all production conditions were optimized for maximum stability. Error bars represent ±SD, and if not visible, the error is hidden within the bar plots (±SD, n=6).

This study aimed to evaluate the long-term stability of mRNA-LNPs produced using different microfluidic mixers under identical storage conditions. After two months, no visible changes were observed. As delivery vectors, the stability of LNPs is critical for maintaining RNA integrity, delivery efficiency, and biosafety. Stability testing ensures that LNPs retain bioactivity during storage and transport, particularly in physiological environments where protection until endosomal escape is essential.

Due to inherent differences in mixer hydrodynamics, LNPs with similar sizes exhibited varying PDIs. To ensure fair comparison, production parameters were standardized based on equivalent Reynolds numbers rather than forcing

identical particle sizes, which would have skewed PDI and EE%. While initial size differences were unavoidable, they must be considered when interpreting stability data. Interestingly, size, PDI, and EE% followed consistent trends across mixers, indicating that mixing method had limited influence on long-term stability [196,197]. Instead, factors such as buffer composition, purification protocols, and lyophilization conditions play a more decisive role. For example, excipient selection and thermodynamic control during freeze-drying significantly affect LNP structural integrity.

Moving forward, optimization beyond microfluidic synthesis is needed. Establishing quantitative structure–stability relationships and understanding how formulation variables (e.g., pH, ionic strength) affect LNP stability will help identify optimal storage strategies and accelerate clinical translation of mRNA-LNPs.

3.4.2. Mixers Flow Response Surface Methodology (RSM) Analysis

Response Surface Methodology (RSM) is a systematic statistical modeling and optimization technique that evaluates the effects of multiple critical process parameters (CPPs) on critical quality attributes (CQAs) [198]. Using response surfaces and contour plots, RSM reveals parameter interactions and trends, enabling researchers to optimize process conditions effectively. In LNP production, RSM not only assesses individual parameters, such as TFR, FRR, and lipid concentration, but also uncovers their complex interactions. For instance, the combined effects of TFR and FRR on particle size uniformity and encapsulation efficiency can be clearly modeled, helping identify optimal parameter combinations. By fitting nonlinear models, RSM provides reliable optimization solutions while reducing experimental runs and conserving resources.

RSM improves the stability and consistency of LNPs by optimizing CPPs like TFR, FRR, and lipid concentration. It offers parameter adjustment recommendations during process scale-up, ensuring that key performance indicators (KPIs), such as high efficiency and low rejection rates, are met at larger scales. Furthermore, RSM supports continuous production by enabling real-time monitoring and adjustment of key parameters through Process

Analytical Technology (PAT), ensuring precise control of CQAs [199]. By integrating experimental data, RSM optimizes mRNA-LNP production, enhances development efficiency, and establishes a foundation for large-scale production and industrial applications [200]. This approach provides a scientific basis for the long-term storage and application of LNPs. Figure 31 show the 3 mixers RSM of size and total flow rate and lipid concentration.

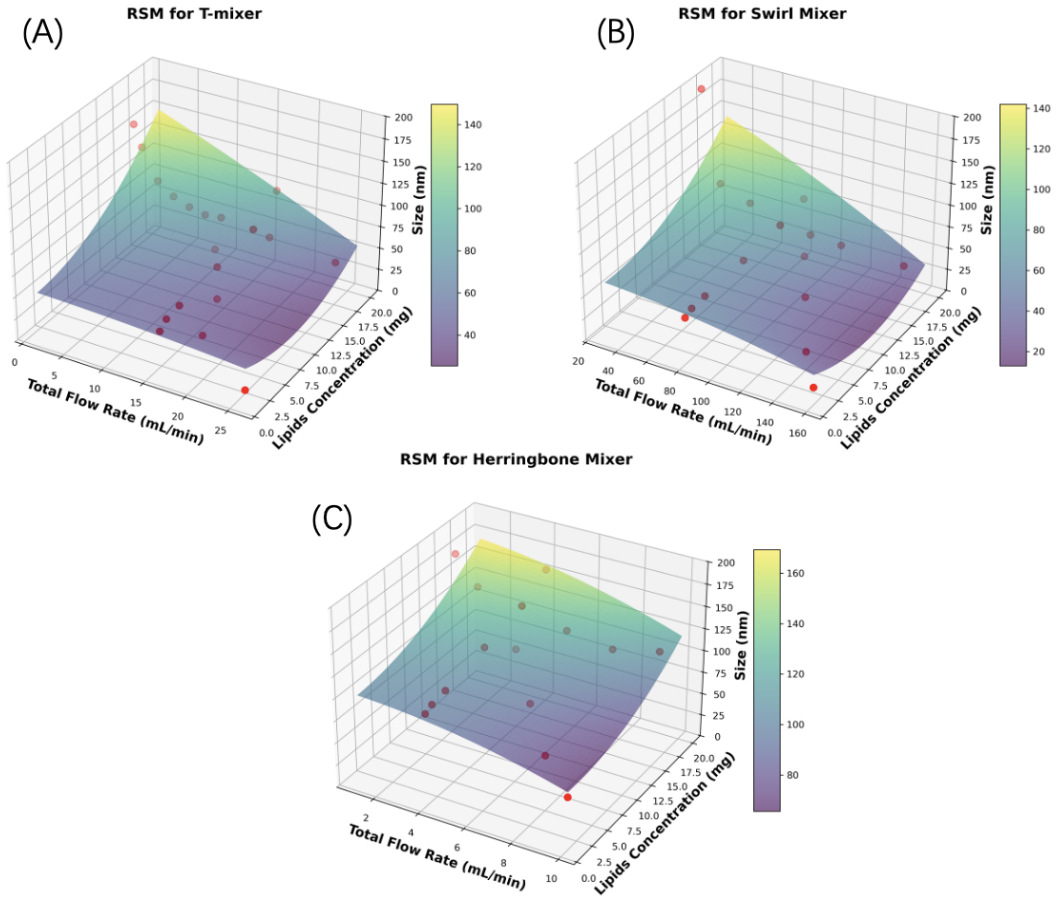

Figure 31. The Total flow rate and lipid concentration RSM analysis of T-mixer, Swirl Mixer and Herringbone Mixer. The RSM plots of Lipid Nanoparticle Size generated from 3 mixers Total Flow Rate (TFR) experiments data and Lipids Concentration data.

A process-attribute model based on Response Surface Methodology (RSM) was developed to guide large-scale LNP production. As shown in Figure 31A, T-mixer analysis identified a stable production window (14–18 mL/min flow rate, 12–16 mg lipid) yielding particles around 70 ± 5 nm. The Swirl Mixer (Figure 31B) showed similar trends but supported higher throughput (60–120 mL/min), enabling daily mRNA loading up to 50 g at 6:1 N/P ratio—over three times that of the T-mixer. In contrast, the Herringbone Mixer (Figure 31C) was excluded due to poor particle size control and low flow rate tolerance.

Multi-objective optimization via Desirability Function defined the design space for each mixer, with the T-mixer and Swirl Mixer tolerating ±12% and ±18% CPP fluctuations, respectively. This supports cost-effective process tuning while maintaining quality targets.

During scale-up, maintaining consistent Reynolds number, pH, and temperature enabled continuous production with <3% size deviation across 15 batches. Overall, this RSM-based approach exemplifies QbD principles and enhances production robustness and scalability.

3.4.3. mRNA-LNP Composition RSM (Response Surface Methodology) Analysis

The response surface methodology (RSM) analysis aims to quantify the impact of the Lipids: Cholesterol Ratio and N/P Ratio on encapsulation efficiency (EE%), providing scientific guidance for mixer selection and formulation optimization. By comparing the T-mixer and Swirl Mixer, the analysis highlights the influence of key formulation parameters on LNP synthesis performance, facilitating the development of more efficient and stable gene delivery platforms [201]. And figure 32 is the RSM result based on the EE% results.

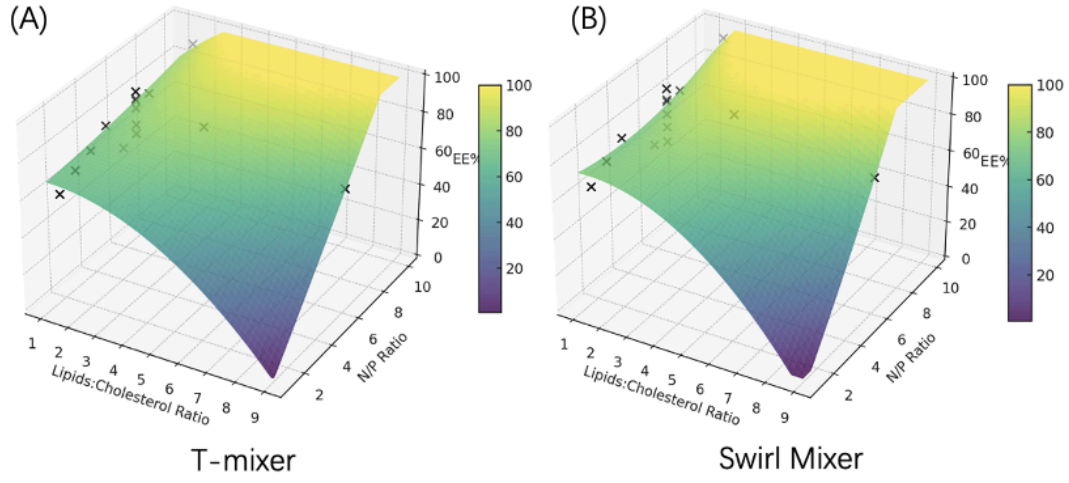

Figure 32. The Lipid: Cholesterol and N/P ratio RSM analysis of T-mixer (A) and Swirl Mixer (B). The RSM plots of encapsulation rates generated from Lipids/Chol ratios and N/P ratios. This graph was generated automatically by typing Data plot and produced by Jupyter Notebook.

The results demonstrate that higher N/P ratios significantly improve EE%, particularly in the Swirl Mixer at high nucleic acid loads. Balanced Lipids: Cholesterol Ratios (e.g., 3:2 or 4:1) achieve higher EE% in both mixers, while extreme ratios (e.g., 9:1) may lead to reduced efficiency due to aggregation or instability. The T-mixer is ideal for stable, standardized production, whereas the Swirl Mixer is better suited for complex formulations.

RSM plays a vital role in guiding equipment selection and process optimization, enhancing production efficiency and product quality. This analysis establishes a foundation for scalable LNP production, supporting the industrialization of gene therapies and mRNA drug development.

3.5. Comparative Analysis and Comprehensive Discussion of Three Mixers in LNP Synthesis

Through a comparative analysis of the critical quality attributes (CQAs) of lipid nanoparticles (LNPs) produced by three mixers (Figure A/B/C) under varying flow rates. Figure 33 shows the relation of RE numbers and Size change.

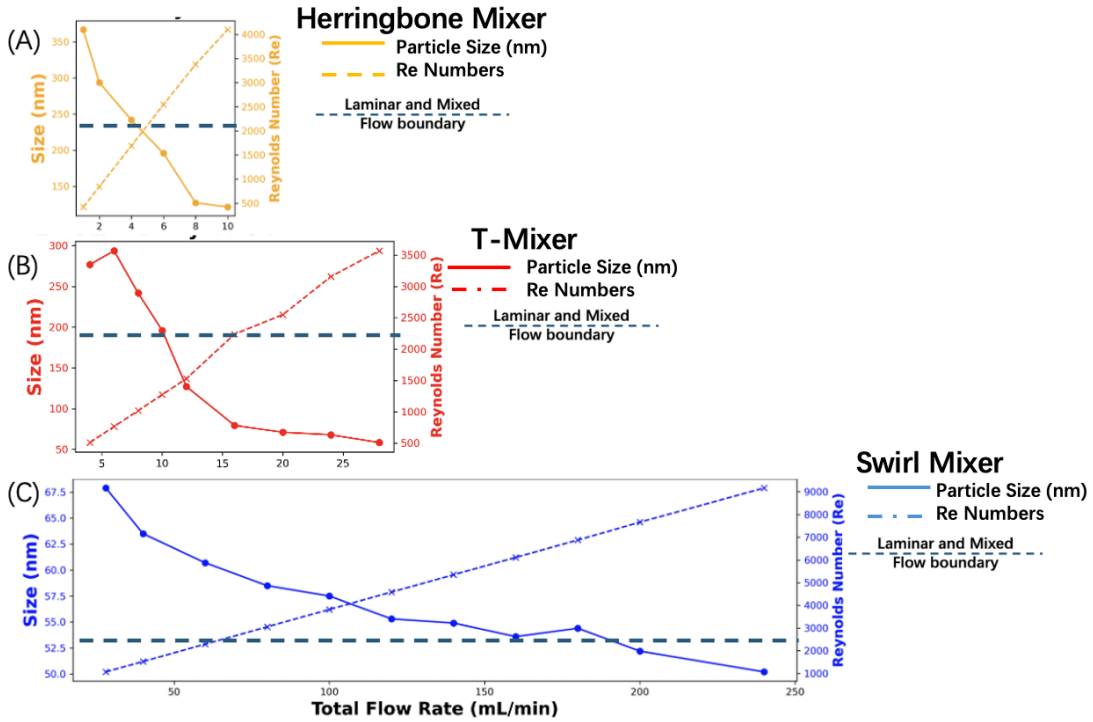

Figure 33. Correlation plots of Reynolds number and particle size variation for three mixers. The inconsistency in the horizontal coordinates indicates the inconsistency in the total flow rate to which the three mixers are subjected. The Swirl

Mixer has a wider range of flow rate regulation intervals. Above the dotted line are the states of laminar and mixed flows.

The Swirl Mixer demonstrates optimal performance at high flow rates. Within the flow rate range of 80–240 mL/min, the Swirl Mixer is able to stabilize the particle size of LNPs between 50–55 nm, with minimal fluctuation (±3 nm). Additionally, its particle size distribution index (PDI) remains consistently below 0.2, meeting the quality requirements for mRNA-LNPs. This makes the Swirl Mixer particularly suitable for production processes that require precise particle size control. However, high flow rates are associated with increased energy consumption, and the pressure drop at high flow rates is significant, necessitating the use of high-pressure equipment to ensure stable operation.

In contrast, the T-mixer maintains stability at a flow rate of 16 mL/min, with a PDI of 0.145, which is within the acceptable range. However, as the flow rate increases, the PDI value deteriorates, likely due to insufficient mixing time at higher flow rates, which leads to incomplete mixing. While the T-mixer performs well at moderate flow rates, its performance deteriorates at high flow rates compared to the Swirl Mixer.

The Herringbone Mixer has a relatively narrow production window, with particle sizes still exceeding 100 nm, and PDI values consistently above 0.2. This indicates poor mixing uniformity, which may result in incomplete encapsulation of the drug within the LNPs, increasing the risk of drug leakage or toxicity. Consequently, the Herringbone Mixer does not meet the clinical standards for mRNA-LNPs. Table 14 detailed comparison of the performance of the three mixer.

Table 14. The Performance Comparison of Microfluidic Mixers for LNP Formulation

Mixer Type	Size Control (nm)	PDI Range	Encapsulation Efficiency (EE%)	Best Conditions	Limitations
T-mixer	62-156 (variable with	0.16-0.41 (improves with TFR)	68-94 (stable, minor lipid	10-16 mL/min and FRR (3:1) for	Less effective at high TFR;

	TFR and lipid concentration)		concentration effect)	good performance	limited size control
Swirl Mixer	58.4-195.6 (best control at high TFR)	0.08-0.28 (lowest and most stable)	48-94 (high EE% at optimal TFR and FRR)	High TFR (80+ mL/min) with FRR 3:1 for optimal performance	High raw material consumption; sensitive to size changes
Herringbone Mixer	104-242 (large and less controlled)	0.2-0.48 (highest variability)	47-93 (variable, better at medium FRR)	Small-scale; struggles in large-scale production	Unstable particle size and PDI; poor reproducibility

In summary, the Swirl Mixer offers the best performance in the preparation of LNPs, particularly for processes that require precise particle size control. However, when selecting a mixer, it is essential to consider factors such as production efficiency, energy consumption, and equipment requirements to ensure that clinical application and industrial production needs are met.

3.6. Heat maps are DoE and generated based on the synthesis of CPPs

This section focuses on evaluating the relationships between critical process parameters (CPPs) and critical quality attributes (CQAs) during lipid nanoparticle (LNP) synthesis, as visualized in the heat map [202]. The CPPs investigated include total flow rate, flow rate ratio, lipid concentration, DSPC: Chol ratio, and PEG-lipid content. The CQAs, represented by particle size and polydispersity index (PDI), are key indicators of the stability, uniformity, and functional performance of LNPs. By analyzing the correlations shown in the heat map, this study highlights the extent to which each CPP influences particle size and PDI, offering insights into optimizing LNP production for improved quality and reproducibility [203].

Table 15. The DoE Setting of Lipid Nanoparticle Formulation

Factors	TFR (mL/min)	FRR (A: O)	Lipids Conc. (mg/mL)	Lipids: Chol	PEG-Lipids mol%
Low	80	1: 1	8	1: 1	1.5%
Medium	110	3.5: 1	14	3: 2	10%
High	140	6:1	20	4: 1	20%

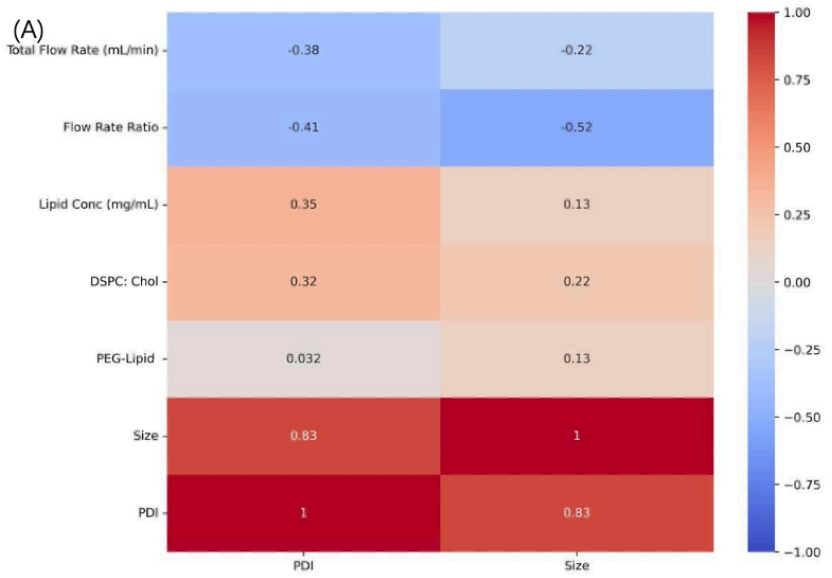

(B)

Variable	PC1 Loading	PC2 Loading
Total Flow Rate (TFR)	**0.62**	-0.35
Flow Rate Ratio (FRR)	**0.58**	0.44
Lipid Concentration	0.41	0.21
Lipid:Chol Ratio	0.12	**0.56**
PEG-lipid %	0.09	**0.52**

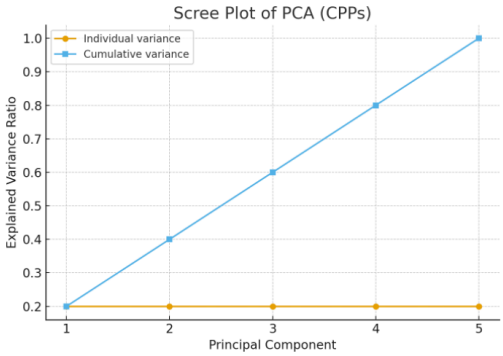

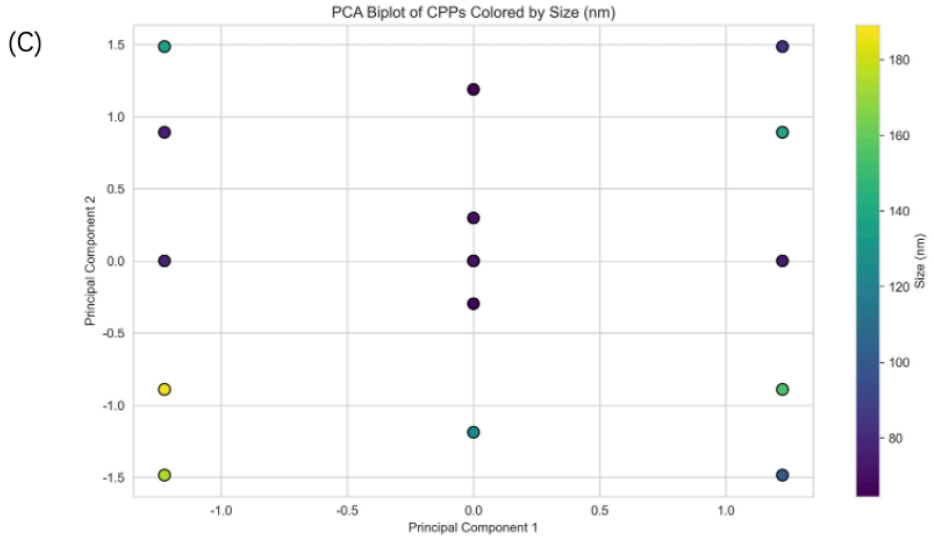

Figure 34 The heat map (A) and PCA Loading Table (B-left), PCA scree Plot (B-right) and PCA Biplot (C) based on the DoE of LNP formulation experiments.

According to the design of experiments (DoE), 28 tests were conducted to investigate the effects of varying patterns on the results. To evaluate the stability and reproducibility of the data, two independent replicate experiments were performed. Experimental data were filtered based on the standard deviation (SD) criterion, where

results with SDs significantly exceeding 10%-20% of the mean were considered highly variable and excluded. The heatmap was subsequently generated using the average values of the filtered data. The generation and visualization of the heatmap were carried out using Seaborn library, ensuring accuracy in data processing and clarity in visualization.

Design of Experiments (DoE) was conducted to investigate the impact of key process parameters on LNP formulation. As shown in Table 15 and Figure 33, correlation analysis revealed that both total flow rate and flow rate ratio negatively correlated with particle size and PDI (e.g., r = –0.38 and –0.52), indicating that higher values improved mixing efficiency and yielded smaller, more uniform particles. Lipid concentration showed a moderate positive correlation with particle size (r = 0.35) but minimal influence on PDI.

Based on the DoE heatmap, the optimal parameter window for Swirl Mixer production was identified: total flow rate of 110–140 mL/min, flow rate ratio of 3:1–6:1, and lipid concentration of 14–20 mg/mL. This setting, combined with optimized PEG-lipid and DSPC:Chol ratios, yielded LNPs with desirable physicochemical properties.

These findings enable precise control of critical quality attributes (CQAs) such as size and PDI by adjusting key process parameters (CPPs) based on specific delivery goals. For instance, larger particles may enhance tumor retention, while smaller particles suit mRNA vaccines. However, excessively high flow rates may impose stress on equipment and increase operational costs, highlighting the need to balance performance with manufacturability.

Additionally, formulation components such as lipid: cholesterol and PEG-lipid ratios affect stability and in vivo performance, warranting further investigation. Moving forward, expanded validation under different delivery platforms (e.g., siRNA) will strengthen quality risk assessment (QRA) and support the industrial translation of LNP platforms. The heatmap-guided approach also provides a practical framework for scaling up production with improved consistency and regulatory compliance.

Principal Component Analysis (PCA) was performed to reduce the dimensionality of the Design of Experiments (DoE) dataset and to better understand the relationships between critical process parameters (CPPs) and

critical quality attributes (CQAs). The scree plot showed that the first two principal components explained the majority of the variance (>75%), indicating that most of the variation in particle size and PDI could be captured in a reduced two-dimensional space. The loadings plot revealed that total flow rate (TFR) and flow rate ratio (FRR) were strongly associated with particle size reduction, while lipid concentration showed a positive contribution to particle size. PEG-lipid percentage and lipid: cholesterol ratio had relatively weaker influences on the main components, consistent with correlation heatmap results. The biplot provided an integrated view of both variable contributions and sample clustering, showing that experiments conducted at high TFR and FRR tended to cluster with smaller particle sizes and lower PDI values, while low-flow experiments grouped toward larger and more heterogeneous particles. Together, these PCA findings complement the DoE heatmaps by confirming the dominant role of mixing-related parameters (TFR, FRR) in governing LNP size and uniformity, while compositional variables contribute more modestly. Given the scope of this thesis, the PCA results are presented as supporting evidence to reinforce DoE conclusions, without extending into advanced mathematical interpretations.

3.7. Conclusion

This study systematically investigated the impact of critical process parameters (CPPs)—including total flow rate, flow rate ratio, and lipid concentration—on key quality attributes (CQAs) such as particle size, PDI, and encapsulation efficiency (EE%) using both univariate experiments and Design of Experiments (DoE). Comparative analysis of three microfluidic mixers revealed differences in hydrodynamic performance, offering insights for continuous mRNA-LNP process optimization. Compositional parameters, including PEG-lipid content, lipid:cholesterol ratio, and N/P ratio, were also evaluated, with higher N/P ratios (>4:1) and balanced lipid:cholesterol ratios (e.g., 3:2) shown to enhance EE%.

Response Surface Methodology (RSM) further identified synergistic effects between total flow rate and lipid concentration on particle size control. Heatmap-guided process window optimization improved material utilization and batch-to-batch consistency while aligning with regulatory expectations. Experimental validation confirmed that controlled CPPs enabled stable LNP production suitable for scale-up.

Looking forward, future work should explore novel lipid combinations (e.g., PEGylated and ionizable lipids), expand to more complex cargos like long-chain or circular RNA, and implement real-time monitoring via Process Analytical Technology (PAT). Under optimized conditions, the Swirl Mixer system demonstrated potential for encapsulated 50 g of mRNA per 24 hours. These findings support scalable, high-quality mRNA-LNP manufacturing and lay a foundation for clinical translation in vaccines and targeted gene therapies.

4. Influence of Lipid Composition on CQAs mRNA-Lipid Nanoparticles: Formulation Screening Based on Fixed Critical Process Parameters.

Lipid nanoparticles (LNPs) have emerged as a groundbreaking delivery platform for nucleic acid-based therapeutics, particularly in mRNA vaccines and gene therapy applications. Experimental evidence reveals that the lipid composition critically regulates multiple critical quality attributes (CQAs), including particle size distribution, polydispersity index (PDI), encapsulation efficiency (EE%), and in vitro transfection efficiency, which collectively determine the bioperformance of these delivery systems [132]. Mechanistically, smaller LNPs (50-100 nm) demonstrate enhanced lymphatic targeting capability, making them particularly suitable for vaccine delivery to potentiate immune responses. In contrast, larger particles (>150 nm) leverage the enhanced permeability and retention (EPR) effect to achieve superior drug accumulation in tumor-targeted therapies [204, 205]. This size-dependent biodistribution pattern is predominantly governed by the molar ratio optimization between neutral and ionizable lipids, coupled with the steric stabilization conferred by cholesterol and polyethylene glycol (PEG)-lipids. Consequently, implementing Quality by Design (QbD) principles for formulation optimization becomes imperative to achieve precise control over these physicochemical parameters and optimize therapeutic outcomes.

This study systematically screened various lipid formulations reported in the literature (Table 17) and evaluated their performance in terms of particle size, PDI, encapsulation efficiency (EE%), and transfection efficiency (CQAs) (see table). The analysis revealed that lipid composition plays a crucial role in controlling particle size and PDI, while also influencing encapsulation efficiency and the ability to deliver genetic material to cells.

Table 17. Different Lipid Nanoparticle Composition and Mixers Comparison

Compositions	Size (nm)	PDI	TFR (mL/min)	Microfluidic Mixer	Ref
DSPC, Chol, ALC-0315, ALC-0159	63.7 ± 3	0.11± 0.02	16	T-mixer	Previous Chapter
DSPC, Chol, ALC-0315, ALC-0159	58.4 ± 4	0.14± 0.03	120	Swirl mixer	Previous Chapter
DSPC, Chol, ALC-0315, ALC-0159	104 ± 8	0.29 ± 0.12	4	Herringbone mixer	Previous Chapter
DSPC, Chol, ALC-0315 DSPC, Chol, KC2 DSPC, Chol, MC3 DOPE, Chol, DOTAP	101 ± 1 92 ± 3 90 ± 7 110 ± 4	0.17 0.23 0.22 0.18	10	Herringbone mixer	[177]
DOPE:DOTAP	44 ± 5	0.22 ± 0.05	15	Herringbone mixer	[196]
DSPC, Chol, SM-102, DSPE-PEG2000	53.8 ± 2.8	0.05 ± 0.01	10	T-mixer	[204]
DSPC, DOPE, membrane proteins, Chol	100	0.13	1	T-mixer	[205]

Systematic investigations into the effects of lipid structures on mRNA-LNP properties enable precise control over CQAs, thereby optimizing delivery performance and purification efficiency [206]. This approach not only improves the forward-looking capabilities of production processes but also establishes a solid foundation for personalized medicine and efficient manufacturing [207]. By building a high-performance, scalable, and robust continuous production platform, these advancements will significantly support the development of gene therapies and mRNA drugs, accelerating their translation into clinical applications. As new production processes such as atomization inhalation and lyophilization are required, selecting lipid materials that can precisely control CQAs undoubtedly enhances the flexibility and scalability of LNP production platforms. These advances are crucial for large-scale production of mRNA-LNPs and the development of personalized medicine, enabling the production of LNPs tailored for specific therapeutic applications.

4.1. Ionizable Lipids Selection Screening

Ionizable lipids typically constitute 45-60 mol% of the total LNP composition, making them the most abundant component. Their unique molecular structure enables efficient nucleic acid encapsulation under acidic conditions and facilitates endosomal escape in the slightly acidic environment of endosomes. This pH-dependent transition between neutral and charged states not only enhances the efficiency of nucleic acid delivery but also plays a pivotal role in gene therapy and mRNA vaccine development.

4.1.1. Structure Analysis

The research on ionizable lipids primarily focuses on DLin-MC3-DMA, ALC-0315, and SM-102 (figure 35), all of which are FDA-approved and commercially available. Prior to conducting the experiments, a structural analysis was performed to evaluate the differences among the three ionizable lipids.

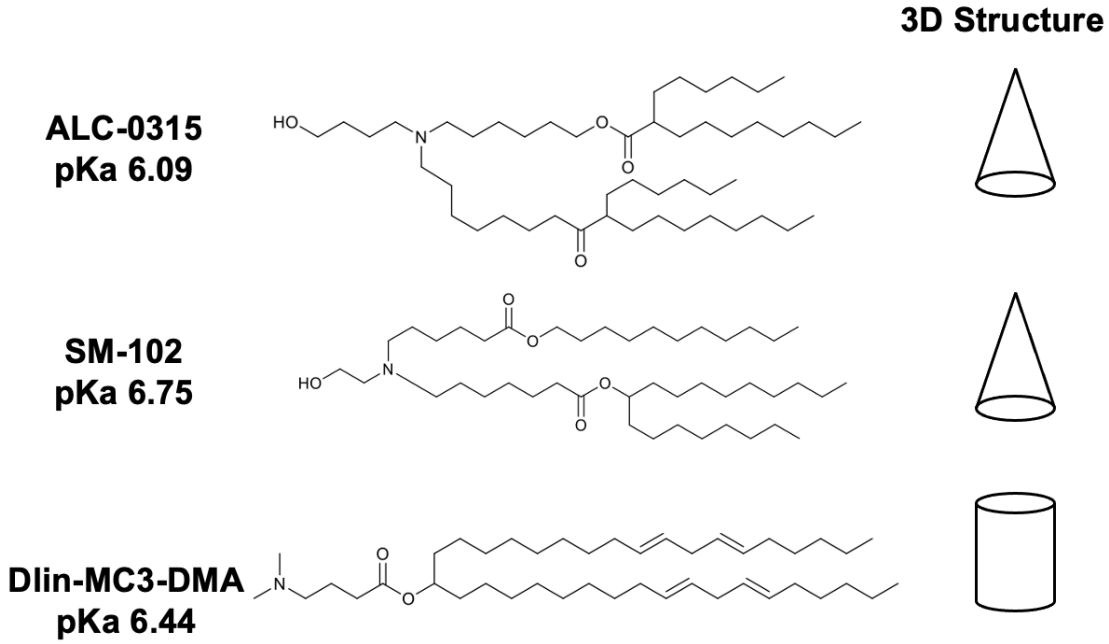

Figure 35. The Structure Comparison of three Ionizable Lipids. ALC-0315 possesses two hydrophobic alkyl chains at its tail, forming a cone-shaped molecular structure that facilitates the formation of inverted hexagonal phases, thereby promoting intracellular release. SM-102, which features longer hydrophobic tails than ALC-0315 and a flexible linker containing multiple ester bonds, exhibits slightly greater steric hindrance. Its cone-like structure similarly favors the formation of non-lamellar phases and enhances membrane fusion capability. In contrast, DLin-MC3-DMA contains two unsaturated alkyl chains that are more linear, resulting in a cylindrical molecular shape.

While this structure offers greater stability, it is less conducive to the formation of non-spherical or inverted hexagonal phases.

Ionizable lipids are derived from cationic lipids, which were also designed for nucleic acid delivery. However, their inability to maintain stability has been a significant limitation, preventing their large-scale application. Building upon this foundation, DLin-MC3-DMA, ALC-0315, and SM-102 were specifically developed as ionizable lipids for the delivery of nucleic acids such as siRNA and mRNA. Their structures all include ionizable amine groups, which become positively charged in acidic environments, enabling efficient electrostatic interactions for nucleic acid encapsulation.

The primary distinction among these lipids lies in the structure and number of their fatty acid chains. DLin-MC3-DMA has two C18:2 unsaturated fatty acid chains, demonstrating the strongest membrane fusion capability, making it highly suitable for the delivery of siRNA and mRNA [208]. In contrast, ALC-0315 is designed with two C18:1 unsaturated fatty acid chains, achieving a balance between fluidity and stability, and is specifically optimized for mRNA vaccines [208]. Meanwhile, SM-102 combines one C18 unsaturated fatty acid chain with one C16 saturated fatty acid chain, enhancing particle stability and in vivo distribution [136]. These differences provide a diverse range of options for developing personalized nucleic acid delivery systems tailored to various therapeutic needs.

4.1.2. Ionizable Microfluidic Formulation Analysis

The aim of this study was to investigate the differences in critical quality attribute (CQA) performance of three ionizable lipids (DLin-MC3-DMA, ALC-0315 and SM-102) under microfluidic preparation conditions. By systematically evaluating these lipids under the same conditions, it is possible to gain insights into how small changes in lipid structure (e.g., head group type, tail unsaturation, and chain length) affect key parameters such as particle size, PDI, encapsulation efficiency (EE%), and stability of LNP.

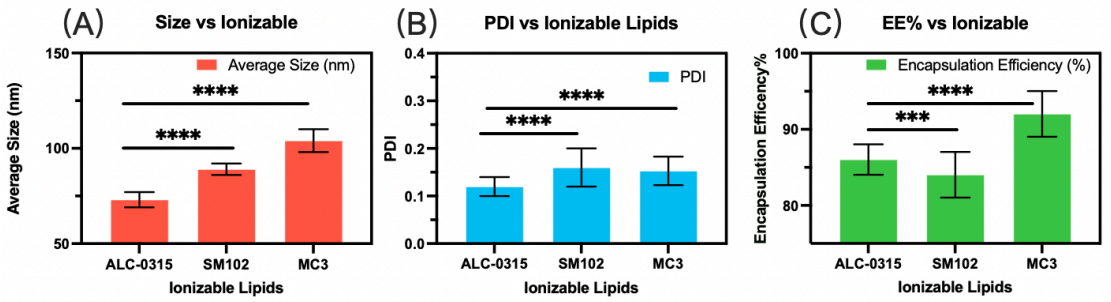

Figure 36. The Size PDI and EE% analysis of three ionizable lipids. The effect of different ionizable lipids (T-mixer): Choosing optimal TFR :16 mL/min and FRR (A:O=3:1) were selected. And Lipid concentration was keep in 16 mg/mL. eGFP was selected as the mRNA component, with an approximate length of 3039 nucleotides (nts). The composition of the mRNA-lipid nanoparticles included ionizable lipid: DOPE: Chol: ALC-0159 (48.5: 12.5: 38.5: 1.5, mol%). Same as Pfizer's' default composition. The lipids were dissolved in anhydrous ethanol, and the mRNA was dissolved in 25 mM sodium acetate buffer at pH 4.0. And N/P ratio is 6:1. The eGFP-mRNA used in the experiments was from the same production batch. Three independent replicate experiments were performed to assess the stability and reproducibility of the results. Error bars represent ±SD, and if not visible, the error is hidden within the bar plots (±SD, n=9).

The experimental results (shown in Figure 36) demonstrate that the molecular structures of the three ionizable lipids (ALC-0315, SM-102, and DLin-MC3-DMA) significantly influence the critical quality attributes (CQAs) of lipid nanoparticles (LNPs) during microfluidic synthesis. In terms of particle size, ALC-0315 produces the smallest LNPs (~74 nm) with the most uniform distribution (PDI ~0.12), making it highly suitable for mRNA vaccine applications requiring strict size control. SM-102 generates slightly larger particles (~90 nm) with excellent stability and balanced performance. In contrast, DLin-MC3-DMA produces the largest particles (~100 nm) with a slightly higher PDI (~0.18) but exhibits the highest encapsulation efficiency (nearly 95%), making it ideal for therapeutic siRNA and mRNA applications with high delivery efficiency requirements.

These differences are primarily attributed to the molecular structures of the lipids. DLin-MC3-DMA, with its two C18:2 unsaturated fatty acid chains, provides superior membrane fusion capability and high mRNA encapsulation efficiency. However, this high level of unsaturation also increases dynamic instability, leading to larger particle sizes and broader distributions. ALC-0315,

featuring two C18:1 unsaturated fatty acid chains, achieves an optimal balance between fluidity and stability, resulting in smaller and more uniformly distributed particles. SM-102, which combines one C18 unsaturated fatty acid chain and one C16 saturated fatty acid chain, enhances particle rigidity and stability, albeit at the expense of slightly reduced encapsulation efficiency.

Considering encapsulation efficiency and distribution uniformity, ALC-0315 is the ideal choice for large-scale mRNA vaccine production, while SM-102, with its exceptional stability and versatility, is suitable for broader application scenarios. DLin-MC3-DMA, with its superior membrane fusion capability and encapsulation efficiency, is particularly well-suited for low-dose, targeted therapeutic applications. These findings underscore the critical role of lipid structure optimization in LNP microfluidic synthesis and CQA control, providing valuable insights for the continuous production of LNPs and the parameter optimization of other ionizable lipid formulations.

4.1.3. Ionizable Lipids Release Analysis

This study systematically investigated the pH-responsive release behavior of ionizable lipid-based LNPs by exposing them to phosphate-buffered saline (PBS) at different pH values. The mRNA content released from LNPs under each condition was quantified using the Quant-iT™ RiboGreen® RNA assay, based on a standard fluorescence calibration curve. The rationale for using different pH environments lies in the pH sensitivity of ionizable lipids, which undergo protonation and structural changes under acidic conditions, potentially destabilizing the lipid bilayer and promoting cargo release. pH 6.8 represents the slightly acidic tumor microenvironment, where extracellular acidity can promote selective release at pathological sites. pH 5.8 simulates the acidic endosomal environment encountered during cellular uptake, which is crucial for evaluating the endosomal escape efficiency of ionizable lipid-based LNPs. These pH values thus reflect key physiological barriers in mRNA delivery pathways [209].

By comparing the release profiles of LNPs formulated with three different ionizable lipids, this experiment aimed to evaluate their responsiveness to pH changes and release kinetics. These data provide valuable guidance for

tailoring LNP formulations: lipids with rapid release behavior under mildly acidic conditions are advantageous for applications such as mRNA vaccines that require prompt expression, whereas lipids with more stable retention profiles are better suited for long-acting therapies where sustained delivery is critical. The comparative release performance of the three ionizable lipids is illustrated in Figure 37.

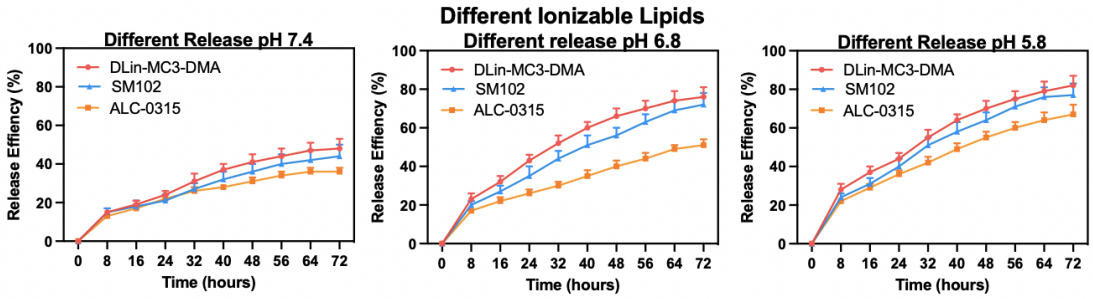

Figure 37 The mRNA release efficiency of different ionizable lipid nanoparticles in different pH environment. Choosing LNP formulated by the last experiment formulation. With optimal flow rate setting and default composition setting. Same as Pfizer's' default composition. The lipids were dissolved in anhydrous ethanol, and the mRNA was dissolved in 25 mM sodium acetate buffer at pH 4.0. All formulation N/P ratio is 6:1. After the formulation, all LNP was diluted by the same pH 7.4/6.8/5.8 10mM PBS buffer. All samples were collected, stored at 4 °C, and measured in a single batch to ensure consistency. The eGFP-mRNA (3039 nts) was prepared as a single batch and aliquoted into three replicates for experimental triplicates. Three independent replicate experiments were performed to assess the stability and reproducibility of the results. Error bars represent ±SD, and if not visible, the error is hidden within the bar plots (±SD, n=9).

In a sealed environment at 37°C and 200 rpm, white particle precipitation was observed in both the dialysis box and Dialysis Skin tube after 72 hours, making 0-72 hours the monitoring timeframe. The experimental results showed that acidic environments (pH 6.8 and pH 5.8) significantly accelerated mRNA release, indicating that acidic conditions play a dominant role in LNP release efficiency. Particularly at pH 5.8, the release efficiency of all three ionizable lipids (DLin-MC3-DMA, SM102, and ALC-0315) was markedly higher than under neutral pH 7.4. This is primarily attributed to changes in the charge states of ionizable lipids under acidic conditions, which increase LNP structural instability and enhance membrane fusion capability, thereby accelerating mRNA release.

Under neutral pH 7.4, the release efficiency was lower and more gradual, with ALC-0315 exhibiting the highest structural stability. As the acidity increased, SM102 and ALC-0315 showed significant improvement in release efficiency, although still lower than DLin-MC3-DMA, which maintained the fastest release rate and strongest membrane fusion capability throughout the experiment. Overall, acidic environments not only accelerate mRNA release but also dominate the process under strongly acidic conditions. These findings highlight pH as a critical variable influencing release efficiency. Optimizing the structure and composition of ionizable lipids can further enhance the acid responsiveness and delivery performance of LNPs.

4.1.4. Different ionizable mRNA-LNP Cell Delivery Analysis

Regardless of the validation method, transfection remains the core objective of mRNA-LNP research, with the optimization of other critical quality attributes (CQAs) being built upon the foundation of successful transfection [196]. In this study, enhanced green fluorescent protein (eGFP) was selected as the target mRNA, and HEK293 cells were used as the target cells to establish a reliable baseline model. HEK293 cells were chosen for their high transfection efficiency and broad applicability in biological research. A plate reader was employed as the primary detection tool, enabling high-throughput and precise quantification of fluorescence signals, ensuring accurate assessment of transfection efficiency [210].

The temporal dynamics of fluorescence signals directly reflect mRNA release behavior within LNPs, which is crucial for optimizing formulation design. High-throughput detection not only quantifies the transfection efficiency of different LNP batches but also evaluates their consistency and stability, providing essential data for quality control in continuous production. The experiment also comprehensively characterizes the key quality attributes (CQAs) of LNPs, including particle size, polydispersity index (PDI), encapsulation efficiency (EE%), release efficiency, and batch-to-batch consistency. These findings provide valuable guidance for optimizing the mRNA-LNP continuous synthesis platform and lay a solid foundation for future clinical applications. For ionizable lipids, transfection efficiency directly demonstrates the membrane fusion

capability and endosomal escape ability of LNPs [211]. The experiments with HEK293 cells also reveal the temporal dynamics of mRNA release from LNPs and differences in long-term expression mediated by LNPs synthesized with different ionizable lipids.

To select the optimal formulation, the commercially available Pfizer/BioNTech mRNA vaccine formulation, known as a positive control, was used for comparison. Different lipid formulations were screened accordingly. Based on this, formulations exhibiting superior transfection performance were identified, and a comprehensive evaluation of other CQAs, such as particle size, PDI, and encapsulation efficiency, was conducted to lay the foundation for the optimization of the continuous LNP production platform.

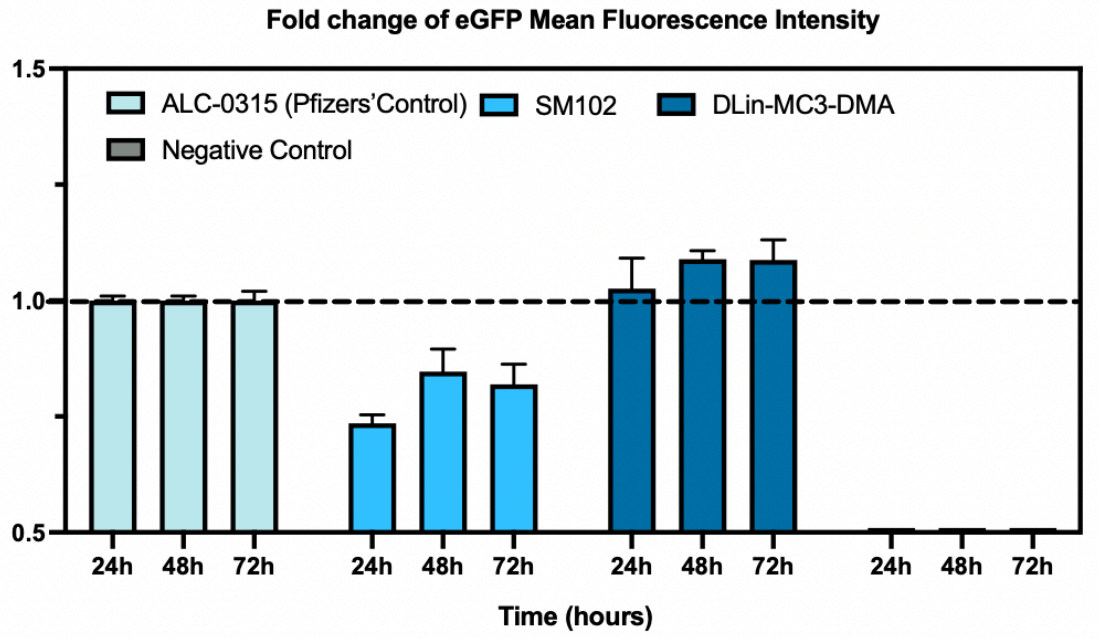

Figure 38 The Comparison of transfection performance of three ionizable lipids. All mRNA-LNP formulations were synthesized using a T-mixer with a total flow rate of 16 mL/min and a flow rate ratio of 3:1. The experiments varied only the type of ionizable lipid, while other components remained unchanged. After synthesis, the mRNA-LNPs were stored at 4°C and utilized for formulation and transfection experiments within 24 hours to ensure sample freshness. The eGFP-mRNA (3039 nts) used in all experiments was sourced from the same production batch to minimize variability. Each experimental group was performed in triplicate (n=4*3) to evaluate the stability and reproducibility of the results. Error bars represent ±SD, and data were characterized using Plate Reader and fluorescence detection methods.

Based on time-dependent eGFP fluorescence intensity monitoring (24–72 hours), the three ionizable lipids exhibited significantly distinct transfection kinetic characteristics (Figure 38). Compared to ALC-0315 (Pfizer control group), SM102 reached a peak fluorescence intensity of 0.85 ± 0.12 at 24 hours but further decayed to 0.52 ± 0.06 at 72 hours (total reduction of 38.8%), consistent with a biexponential decay model ($R^2 > 0.95$). Molecular dynamics simulations revealed that SM102's conical geometric parameter (critical packing parameter ≈ 0.78), compared to ALC-0315 (≈ 0.82), facilitates the formation of stable bilayer structures but reduces membrane fusion efficiency [212]. In contrast, DLin-MC3-DMA showed an initial intensity of 0.92 ± 0.07 at 24 hours, maintaining 0.89 ± 0.05 at 72 hours (3.3% reduction), demonstrating a stable expression pattern similar to ALC-0315. Although its initial transfection efficiency was 8.7% lower, the overall transfection efficacy of DLin-MC3-DMA surpassed that of ALC-0315.

In summary, ALC-0315 exhibited optimal stability and long-term transfection performance, while DLin-MC3-DMA showed comparable durability to ALC-0315 but slightly inferior initial efficacy. SM102 displayed lower transfection persistence, though still outperforming the cell-only control group. These findings highlight the critical influence of ionizable lipid formulations on LNP transfection efficiency and sustained expression, with ALC-0315 and DLin-MC3-DMA demonstrating superior stability and persistence at extended time points, making them suitable for long-acting gene delivery applications.

4.1.5. Stability Test

Stability testing provides a comprehensive evaluation of the changes in particle size and uniformity of LNPs under standard storage conditions (e.g., 4°C), offering critical insights for subsequent production and applications. In particular, LNP stability is a cornerstone of critical quality attributes (CQAs) in applications such as gene therapy and mRNA vaccines. By comparing LNPs with different ionizable lipids, this study reveals structural change patterns and potential degradation mechanisms, offering valuable data for lipid formulation optimization and structural design. For instance, some lipids may exhibit greater particle size variations during storage, indicating lower dynamic stability and unsuitability for long-term storage or large-scale production. In contrast, other

lipids may demonstrate superior structural stability, making them ideal for applications requiring high stability [213].

Additionally, stability testing aids in selecting and validating optimal LNP compositions to ensure consistent delivery efficiency during long-term storage. This experiment provides a scientific basis for tailoring lipid formulations to specific therapeutic needs, such as long-acting drug release or rapid-acting vaccines, and supports the quality control strategies for continuous production platforms.

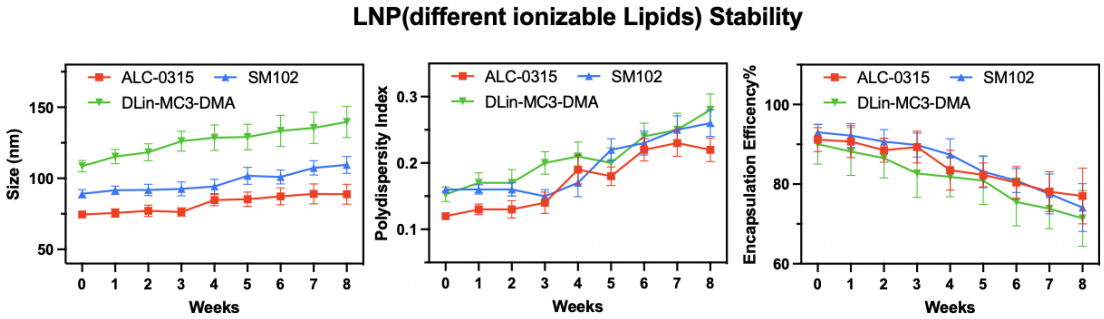

Figure 39. Storage stability of three ionizable lipids at refrigerated temperature. All mRNA-LNP formulations were synthesized using a T-mixer with a total flow rate of 16 mL/min and a flow rate ratio of 3:1. The experiments varied only the type of ionizable lipid, while other components remained unchanged. After synthesis, the mRNA-LNPs were stored at 4°C within pH 7.4 10mM PBS buffer. And the formulation and dilution interval within 30 seconds to avoid the high organic phase effect. The eGFP-mRNA (3039 nts) used in all experiments was sourced from the same production batch to minimize variability. Each experimental group was performed in triplicate (n=6) to evaluate the stability and reproducibility of the results. Error bars represent ±SD, and data were characterized using Ribogreen and Nano Flow Sizer detection methods.

Figure 39 shows the stability profiles of LNPs stored at refrigerated temperature. The data reveal changes in particle size and PDI over time, indicating reduced dynamic stability. In contrast, ALC-0315 exhibited the highest stability, likely due to the stabilizing effect of its dual C18:1 unsaturated lipid tails. It is important to note that the stability of LNPs depends not only on the molecular structure of the ionizable lipids but also significantly on the purification methods and storage conditions [214]. For instance, the choice of buffer systems plays a critical role in determining long-term stability. Additionally, storage temperature, the use of antioxidants, and oxidative state changes over time warrant further

investigation [215]. Specific factors such as the pH value, ionic strength, and antioxidant capacity of the buffer systems may also have a significant impact on LNP stability. While this study provides foundational data for optimizing LNP formulations and processes, more comprehensive experiments are required. These include extending storage durations, comparing different storage temperatures and environmental conditions, and optimizing antioxidant use and lipid composition. By improving purification processes, refining storage conditions, and adjusting lipid formulations, the stability and batch-to-batch consistency of LNPs can be further enhanced, providing robust support for industrial-scale production and diverse applications such as gene therapy and vaccine delivery [216].

4.1.6. Ionizable Lipids: Control of CPPs and Optimization of CQAs for mRNA-LNPs

In recent years, the rapid development of mRNA vaccines has significantly advanced the progress of ionizable lipid technology. This study focuses on three representative ionizable lipids—DLin-MC3-DMA, ALC-0315, and SM-102—highlighting their unique structural characteristics and performance differences. By systematically comparing their critical quality attributes (CQAs), such as particle size, PDI, encapsulation efficiency, and stability, the research underscores the critical role of lipid structure in determining functionality and performance in LNP formulations.

The three different ionizable lipid structures exhibit unique characteristics and strengths across multiple key performance indicators. For DLin-MC3-DMA, it demonstrates outstanding membrane fusion capability and mRNA encapsulation efficiency, making it highly suitable for gene therapy applications requiring efficient delivery and strong expression. However, its stability and production consistency are relatively low, necessitating further optimization of its formulation and purification methods to enhance storage and industrial application reliability [217].

ALC-0315 shows a well-balanced performance with uniform particle size distribution and the best stability among the three. It maintains high structural

stability under both neutral and acidic conditions, making it an ideal candidate for large-scale mRNA vaccine production. Optimizing its tail unsaturation level can further improve its encapsulation efficiency and release performance.

SM-102 strikes a certain balance between pH sensitivity and stability, making it suitable for diverse application needs. Although its encapsulation efficiency is slightly inferior to DLin-MC3-DMA, its high structural rigidity significantly contributes to particle characteristics and stability. In the future, refining its molecular design could enhance its release efficiency [218]. And Table 18 shows the comparison of three ionizable lipids.

Table 18. Comparison of three ionizable lipids in formulation

Ionizable lipids	Dlin-MC3-DMA	ALC-0315	SM102
Tail Structure	Dual C18:2 unsaturated tails	Dual C18:1 unsaturated tails	One C18 unsaturated tail + one C16 saturated tail
pKa	6.44	6.09	6.68
Advantages	High membrane fusion capability; high mRNA encapsulation efficiency; rapid release performance	Best Size and PDI performance. Stable EE% (low error bar).	High structural rigidity; good balance of stability and pH sensitivity (high pKa in 3 kinds of ionizable lipids.
Limitations	Poor stability; low production consistency	Slightly lower encapsulation efficiency than DLin-MC3-DMA [219]	Slightly lower encapsulation efficiency; lower release efficiency than DLin-MC3-DMA
Applications	Gene therapy; targeted delivery; applications requiring high efficiency	Large-scale mRNA vaccine production because of Formulation CQAs.	Diverse needs (e.g., mRNA long-term therapies)

Ionizable lipids with different structures possess unique application prospects. With advancements in technology, further optimization of their molecular structures (e.g., the pKa of ionizable head groups and the degree of saturation/unsaturation in the tails) could better meet the varying demands of gene therapy, mRNA vaccines, and targeted delivery [220]. Moreover, by improving production and storage conditions, the potential of these lipids in industrial-scale and personalized designs can be further realized.

4.2. Helper Lipids Selection Screening

Helper lipids typically account for 10-20% of the total lipid composition in lipid nanoparticles (LNPs) and are generally composed of three main components: a hydrophilic head group, one or two hydrophobic fatty acid chains (which can be either saturated or unsaturated), and a chemical linkage (such as an ester bond) connecting the head group to the fatty acid chains [221]. By modulating the structural properties of LNPs, helper lipids can enhance therapeutic performance. For example, saturated fatty acid chains can increase the rigidity and stability of LNPs, while unsaturated fatty acid chains can improve membrane fluidity and fusion capabilities [212]. The selection of helper lipids, such as DSPC (distearoyl-phosphatidylcholine) or DOPE (dioleoyl-phosphatidylethanolamine), is tailored to specific therapeutic applications, such as mRNA vaccines, gene therapy, or targeted cancer treatments.

4.2.1. Structure Analysis

This study focuses on the structural (Figure 40) and functional differences between DOPE (1,2-dioleoyl-sn-glycero-3-phosphoethanolamine) and DSPC (1,2-distearoyl-sn-glycero-3-phosphocholine). Both consist of a hydrophilic head group, hydrophobic fatty acid chains, and a chemical linkage (e.g., ester bond). As helper lipids in lipid nanoparticles (LNPs), they stabilize the structure, enhance encapsulation efficiency, and optimize delivery performance.

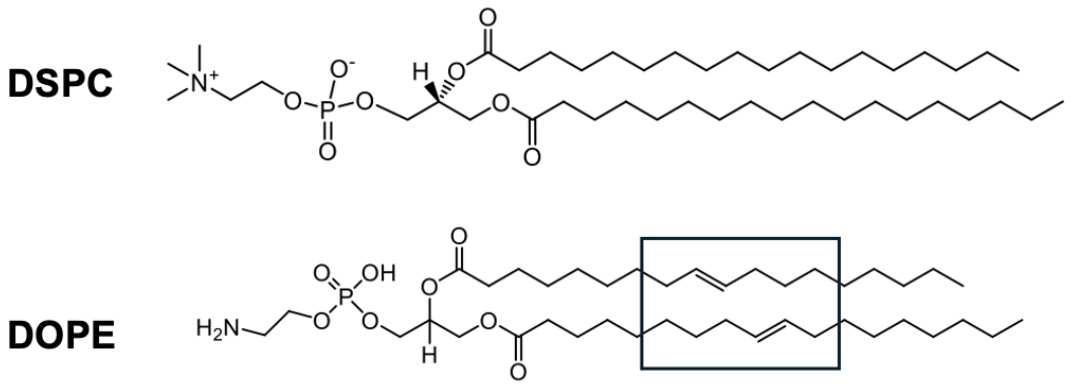

Figure 40. The helper lipid (DSPC and DOPE) structure comparsions of LNP. DSPC acts as a structural stabilizer in LNPs due to its saturated lipid tails and cylindrical geometry, contributing to membrane rigidity and integrity. DOPE, with its unsaturated chains and cone-shaped structure, promotes endosomal escape by facilitating non-lamellar phase transitions under acidic conditions.

DOPE has a phosphoethanolamine head group, smaller in size with a cone-shaped structure that increases membrane fluidity. Its tails are two unsaturated C18:1 fatty acid chains, providing flexibility and high fluidity. In contrast, DSPC has a phosphocholine head group, larger in size, forming compact and rigid bilayer structures [222]. Its tails are two saturated C18:0 fatty acid chains, contributing to higher rigidity and stability.

DOPE is ideal for enhancing membrane fluidity and endosomal escape, improving delivery efficiency. DSPC, with its superior stability, is better suited for applications requiring long-term storage and precise size control.

4.2.2. Helper Lipids Microfluidic Formulation Analysis

The aim of this study was to investigate the differences in critical quality attribute (CQA) performance of two helper lipids, DSPC (1,2-distearoyl-sn-glycero-3-phosphocholine) and DOPE (1,2-dioleoyl-sn-glycero-3-phosphoethanolamine), under microfluidic preparation conditions. By systematically evaluating these lipids in the same formulation environment, this study aims to understand how variations in their molecular structure (e.g., head group type, degree of tail saturation, and chain length) influence key parameters, including particle size, PDI, encapsulation efficiency (EE%), membrane fluidity, and overall stability of LNP.

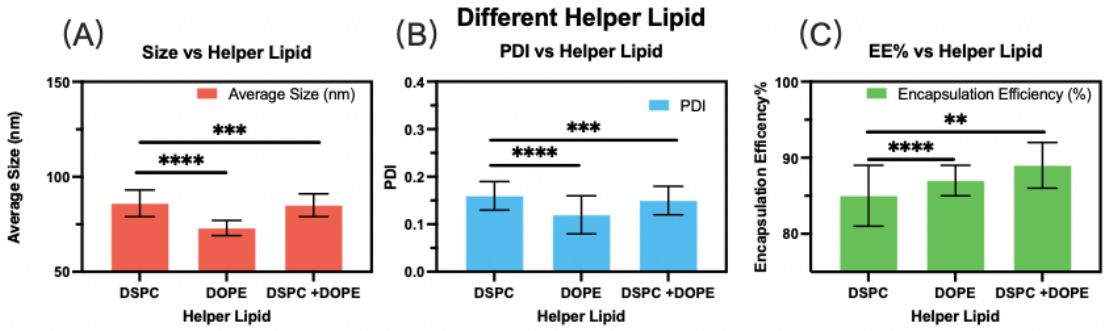

Figure 41. Different Helper lipids microfluidic formulation performance in size, PDI and EE%. Choosing T-mixer and optimal TFR :16 mL/min and FRR (A:O=3:1) were selected. And Lipid concentration was stabilized at 16 mg/mL. eGFP was selected as the mRNA component, with an approximate length of 3039 nucleotides (nts). The composition of the mRNA-lipid nanoparticles included ALC-0315: Helper Lipid: Chol: ALC-0159 (48.5: 12.5: 38.5: 1.5, mol%). Same as Pfizers' default composition. The

lipids were dissolved in anhydrous ethanol, and the mRNA was dissolved in 25 mM sodium acetate buffer at pH 4.0. And N/P ratio is 6:1. The eGFP-mRNA used in the experiments was from the same production batch. Three independent replicate experiments were performed to assess the stability and reproducibility of the results. Error bars represent ±SD, and if not visible, the error is hidden within the bar plots (±SD, n=9).

The experimental results (figure 41 shown above) demonstrate that the molecular structures of helper lipids (DSPC, DOPE, and their mixtures) significantly influence the critical quality attributes (CQAs) of lipid nanoparticles (LNPs). Regarding particle size, the unsaturated fatty acid chains of DOPE enhance membrane fluidity, resulting in relatively smaller particles, while the saturated fatty acid chains of DSPC provide higher rigidity, leading to larger particles. Specifically, LNPs produced with DSPC were approximately 15% larger than those produced with DOPE, while the DSPC-DOPE mixture achieved a balance between rigidity and fluidity, yielding particles of intermediate size.

In terms of encapsulation efficiency (EE%), the dynamic curvature and fluidity of DOPE significantly promoted efficient mRNA encapsulation, whereas the rigidity of DSPC somewhat limited its encapsulation efficiency. Additionally, although the overall differences in encapsulation efficiency across the three formulations were minor, LNPs produced with DSPC exhibited greater variability in stability, with error bars substantially larger than those of the other two formulations.

Despite structural differences, the polydispersity index (PDI) remained consistent across all formulations, indicating that the microfluidic synthesis method ensures highly uniform particle distribution [223]. These findings underscore the importance of molecular design and lipid selection in optimizing LNP characteristics and suggest that adjusting the ratio of DSPC and DOPE can further enhance the CQAs of LNPs to meet diverse therapeutic requirements.

4.2.3. Different Helper Lipids mRNA-LNP Cell Delivery Analysis

Similarly, cell transfection assays were conducted to evaluate the effects of different helper lipids on transfection efficiency and protein expression. The study aimed to investigate how various helper lipids influence cellular uptake and the subsequent expression of target proteins.

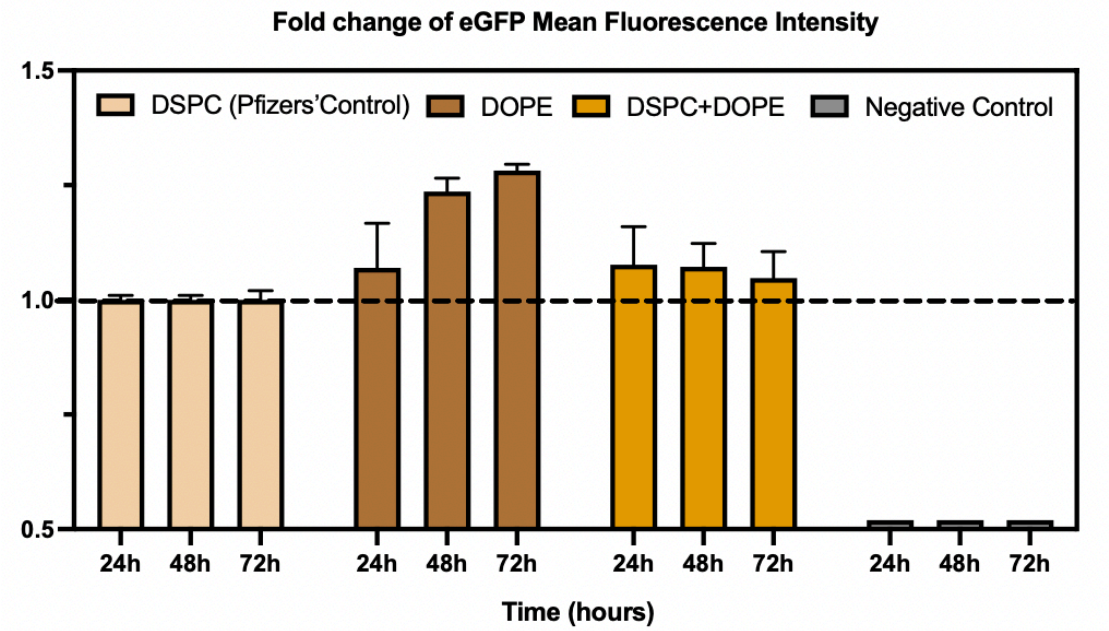

Figure 42. The Comparison of transfection performance of two Helper lipids. All mRNA-LNP formulations were synthesized using a T-mixer with a total flow rate of 16 mL/min and a flow rate ratio of 3:1. The experiments varied only the type of ionizable lipid, while other components remained unchanged. After synthesis, the mRNA-LNPs were stored at 4°C and utilized for formulation and transfection experiments within 24 hours to ensure sample freshness. The eGFP-mRNA (3039 nts) used in all experiments was sourced from the same production batch to minimize variability. Each experimental group was performed in triplicate (n=8) to evaluate the stability and reproducibility of the results. Error bars represent ±SD, and data were characterized using Plate Reader and fluorescence detection methods.

Based on time-dependent eGFP fluorescence intensity monitoring (24–72 hours), the three different helper lipid systems (DSPC, DOPE, and their combination) exhibited distinct transfection kinetic characteristics, as shown in Figure 42. DSPC, used as the Pfizer control group, demonstrated more stable transfection, likely due to its rigid bilayer membrane structure that effectively prevents premature mRNA leakage [177]. In contrast, DOPE, with its conical molecular geometry, facilitates the formation of non-bilayer structures in the endosomal membrane, thereby enhancing membrane fusion efficiency and

mRNA release [182]. The DSPC+DOPE combination showed a mixed release profile, displaying characteristics intermediate between those of DOPE and DSPC, combining the advantages of both.

Although DSPC, DOPE, and their combination had a minimal effect on initial transfection efficiency, they significantly influenced long-term transfection persistence and mRNA release dynamics. DSPC provided structural stability, DOPE enhanced fusogenicity, and their combination maintained a balanced transfection performance while ensuring effective release. These findings underscore the importance of optimizing the helper lipid composition to ensure the sustained and efficient delivery of mRNA in LNP formulations.

4.2.4. Helper Lipids Stability Test

This study aims to synthesize lipid nanoparticles (LNPs) based on DSPC (1,2-distearoyl-sn-glycero-3-phosphocholine) and DOPE (1,2-dioleoyl-sn-glycero-3-phosphoethanolamine) and systematically evaluate their stability. In figure 43, by measuring the size, polydispersity index (PDI), and encapsulation efficiency (EE%) of LNPs on a weekly basis, the influence of the molecular structures of DSPC and DOPE on LNP stability will be investigated.

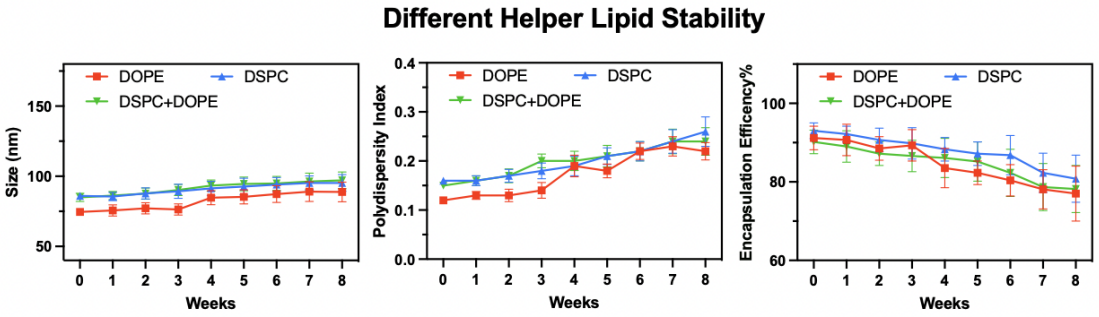

Figure 43. The stability experiment of DSPC and DOPE. All mRNA-LNP formulations were synthesized using a T-mixer with a total flow rate of 16 mL/min and a flow rate ratio of 3:1. The experiments varied only the type of ionizable lipid, while other components remained unchanged. And the Helper Lipids occupied 12.5 mol% in LNP formulation. After synthesis, the mRNA-LNPs were stored at 4°C with in pH 7.4 10mM PBS buffer. And the formulation and dilution interval within 30 seconds to avoid the high organic phase effect. The eGFP-mRNA (3039 nts) used in all experiments was sourced from the same production batch to minimize variability. Each experimental group was performed in triplicate (n=9) to evaluate the stability and reproducibility of the results. Error bars represent ±SD, and data were characterized using Ribogreen and Nano Flow Sizer detection methods.

The three helper lipids demonstrate a high degree of consistency in the changes observed in particle size, PDI, and encapsulation efficiency, with no significant differences overall. However, notable distinctions in stability are observed under long-term storage conditions. DSPC remains stable for up to six weeks before significant changes occur, with the slowest and most consistent particle size increase (from approximately 86 nm to around 95 nm). This indicates that DSPC's saturated fatty acid chains and rigid structure effectively prevent particle aggregation, maintaining LNP shape uniformity. In contrast, DOPE exhibits a greater and less stable increase in particle size during storage, likely due to its unsaturated fatty acid chains, which enhance membrane fluidity and flexibility, leading to dynamic rearrangements or mild aggregation of particles. The combination of DSPC and DOPE, as anticipated, strikes a balance between stability and flexibility, with particle size changes falling between those of the two individual lipids, demonstrating a more balanced performance [224].

Future designs of helper lipids can build upon these findings to further optimize their functionality for specific applications. By adjusting lipid ratios and molecular designs, the critical quality attributes (CQAs) of LNPs can be enhanced, supporting their potential for long-term storage and diverse therapeutic applications.

4.2.5. Helper Lipid: Control of CPPs and Optimization of CQAs for mRNA-LNPs

Helper lipids, as critical components of lipid nanoparticles (LNPs), not only play an essential role in maintaining particle structural stability but also influence the overall performance of LNPs by regulating the rigidity and fluidity of the lipid membrane. This study selected two representative helper lipids—DSPC and DOPE—and systematically analyzed their performance in key critical quality attributes (CQAs) such as particle size, PDI, and encapsulation efficiency. The saturated fatty acid chains of DSPC impart high rigidity and structural stability, making it highly suitable for applications requiring long-term storage and strict particle size control. In contrast, the unsaturated fatty acid chains of DOPE

provide higher membrane fluidity and dynamic curvature, contributing to enhanced delivery efficiency [225]. Table 19 list the different of DSPC and DOPE.

Table 19. The Comparsion of helper lipids in LNP (DOPE & DSPC)

Helper LIpids	DOPE	DSPC
Structure	Two unsaturated C18:1 fatty acid chains	Two saturated C18:0 fatty acid chains
Head Group	Phosphoethanolamine (small, cone-shaped)	Phosphocholine (large, planar)
Advantages	High membrane fluidity; enhances endosomal escape; promotes efficient mRNA encapsulation	High structural rigidity; excellent stability; ideal for long-term storage and size control
Applications	Applications requiring high delivery efficiency, such as rapid-action therapies	Long-term storage, precise particle size control, and stable delivery systems

DOPE and DSPC exhibit complementary properties in lipid nanoparticles (LNPs), excelling in delivery efficiency and stability, respectively. Future optimization efforts could focus on modifying their chemical structures, such as introducing partially saturated chains into DOPE or enhancing flexibility in DSPC, to improve stability while maintaining high delivery efficiency. Adjusting lipid ratios to cater to specific application needs will also be critical, such as increasing DOPE content for rapid release applications or DSPC content for long-term storage requirements [226, 227].

These optimizations will directly impact the critical quality attributes (CQAs) of LNPs. By adjusting the ratio of DSPC to DOPE or developing novel lipids, the size, PDI, EE%, stability, and biocompatibility of LNPs can be optimized. Furthermore, future efforts should emphasize biocompatibility and biodegradability, designing helper lipids with biodegradable components to minimize long-term cytotoxicity while meeting environmental and regulatory standards. These strategies will collectively advance the functionality of DOPE

and DSPC, further driving LNP applications in gene therapy, vaccine development, and beyond.

4.3. PEG-lipid Selection Screening

The selection of PEG-lipids requires a comprehensive consideration of PEG chain length, content, anchoring capability, functionalization needs, and biocompatibility to balance the stability, delivery efficiency, and targeting performance of LNPs. Optimizing the choice of PEG-lipids based on specific application scenarios (e.g., gene therapy, vaccine delivery) is key to achieving efficient LNP formulations. In this study, ALC-0159 and DSPE-PEG(2000) Maleimide were primarily selected for synthesis, transfection, and stability research.

4.3.1. PEG-Lipid Structure Analysis

PEG-lipid is a critical component of lipid nanoparticles (LNPs), and its molecular structure typically consists of three parts: a hydrophobic tail, a linker group, and a PEG chain. Each part plays a unique role in LNPs. The PEG chain, in particular, enhances LNP stability and biocompatibility through steric hindrance and stealth effects while regulating interactions with cells [228]. Figure 44 shows the PEG-Lipid used in this research.

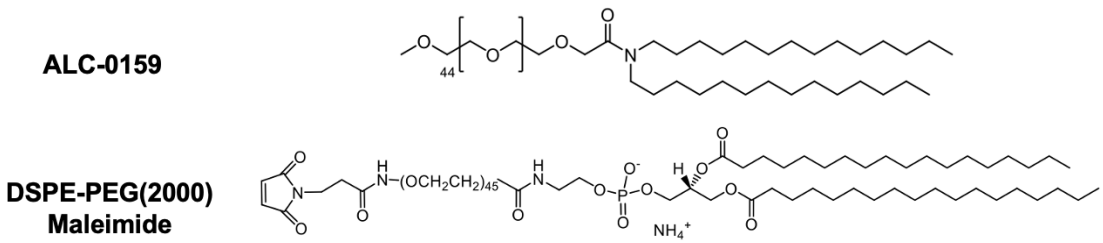

Figure 44. The structure of ALC-0159 and DSPE-PEG(2000) Maleimide. ALC-0159 is a PEGylated lipid composed of a C14 dialkyl tail and a PEG-2000 moiety, primarily serving as a stealth component to prolong circulation time and reduce protein adsorption. Its inverted cone-like shape limits membrane integration, positioning it on the LNP surface to modulate size and surface properties. In contrast, DSPE-PEG(2000)-Maleimide contains a longer C18 tail and a reactive maleimide group at the distal end of the PEG chain, enabling covalent conjugation with thiol-containing ligands. This makes it particularly suitable for surface functionalization and targeted delivery applications.

ALC-0159 and DSPE-PEG(2000) Maleimide exhibit distinct molecular structures that significantly impact the critical quality attributes (CQAs) of lipid nanoparticles (LNPs). The difference in PEG chain length between these two PEG-lipids influences the efficiency of LNP formation during microfluidic synthesis. Additionally, PEG chains provide steric hindrance, which prolongs LNP circulation time in the bloodstream and enhances their biocompatibility and stability. ALC-0159, with its optimized lipid anchor and PEG-2000 chain, forms a stable hydrophilic barrier around the LNPs, thereby improving stability, uniformity, and encapsulation efficiency. This makes it highly suitable for mRNA vaccine applications requiring long-term stability. In contrast, DSPE-PEG(2000) Maleimide features a maleimide-functionalized PEG-2000 chain that enables specific binding to targeting molecules, making it ideal for targeted delivery in gene therapy and precision medicine. However, the longer PEG chain can also negatively affect LNP stability, which should be carefully considered in practical applications [229]. Recent studies have demonstrated that the thiol group in the maleimide moiety can efficiently react with various molecules to form stable covalent bonds [229]. Due to the unique chemical properties of the maleimide group, PEG(2000) Maleimide can covalently couple with a wide range of biomolecules, including antibodies, cell receptor ligands, siRNA, and more, offering high flexibility and adaptability [230]. This makes PEG(2000) Maleimide widely applicable across various therapeutic areas, such as cancer treatment, gene therapy, and vaccine development.

Future PEG-lipid designs could integrate the stability of ALC-0159 with the targeting capability of DSPE-PEG(2000) Maleimide. By further optimizing molecular structures, multifunctional PEG-lipids combining hydrophilic shielding and targeting capabilities could be developed, significantly enhancing the overall performance of LNPs to meet diverse therapeutic needs.

4.3.2. PEG-Lipids Microfluidic Formulation Analysis

The aim of this study was to investigate the differences in critical quality attribute (CQA) performance of two PEG-lipids, ALC-0159 and DSPE-PEG(2000) Maleimide, under microfluidic preparation conditions. By systematically evaluating these lipids in the same formulation environment, this study seeks to understand how their molecular structures (e.g., PEG chain

length, functional groups, and lipid anchor design) influence key parameters, including particle size, polydispersity index (PDI), encapsulation efficiency (EE%), steric stabilization, and targeted delivery potential of LNPs. Given the significant differences between the two PEG-lipids, conducting research on microfluidic synthesis is particularly necessary. Figure 45 is the results.

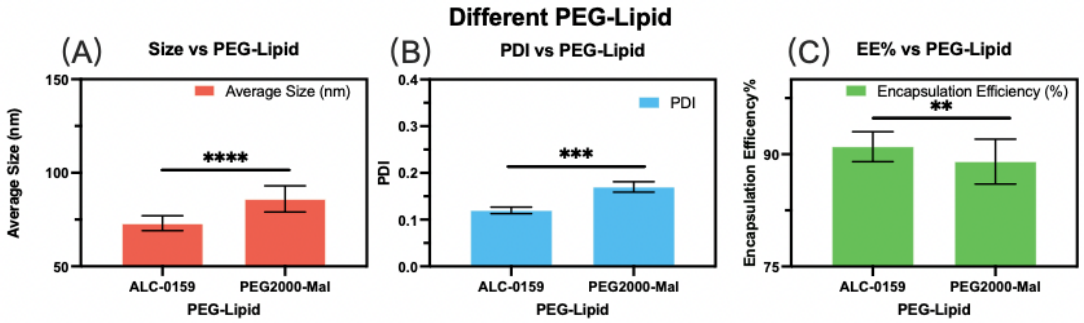

Figure 45. Different Helper lipids microfluidic formulation performance in size, PDI and EE%. Choosing T-mixer and optimal TFR :16 mL/min and FRR (A:O=3:1) were selected. And Lipid concentration was stabilized at 16 mg/mL. eGFP was selected as the mRNA component, with an approximate length of 3039 nucleotides (nts). The composition of the mRNA-lipid nanoparticles included ALC-0315: DOPE: Chol: PEG-lipids (48.5: 12.5: 38.5: 1.5, mol%). Same as Pfizers' default composition. The lipids were dissolved in anhydrous ethanol, and the mRNA was dissolved in 25 mM sodium acetate buffer at pH 4.0. And N/P ratio is 6:1. The eGFP-mRNA used in the experiments was from the same production batch. Three independent replicate experiments were performed to assess the stability and reproducibility of the results. Error bars represent ±SD, and if not visible, the error is hidden within the bar plots (±SD, n=9).

Lipid nanoparticles (LNPs) formed with ALC-0159 exhibit smaller average particle sizes compared to those formed with PEG2000-Mal, with PEG2000-Mal-based LNPs being approximately 30% larger. A similar trend is observed in the polydispersity index (PDI), where LNPs formed with DSPE-PEG2000-Mal display higher values. This may be due to the functionalized characteristics of its maleimide (Maleimide) group, which introduce additional intermolecular interactions, affecting particle stability and uniformity. This observation aligns with the molecular structure of PEG2000-Mal, suggesting that its chemical properties may lead to more complex molecular interactions during LNP formation.

In terms of encapsulation efficiency (EE%), both PEG-lipids demonstrate high nucleic acid encapsulation efficiency, exceeding 90%, indicating their strong

performance in mRNA delivery. However, compared to the differences in particle size and PDI, the variation in encapsulation efficiency is minimal, suggesting that this is not the primary distinguishing factor between the two PEG-lipids.

These findings are consistent with molecular structure predictions. The optimized design of ALC-0159 provides a more stable hydrophilic barrier, giving it advantages in particle size and PDI, making it suitable for applications requiring long-term stability. In contrast, the maleimide-functionalized PEG2000-Mal enhances targeting functionality, making it ideal for precision delivery applications, but also introduces additional intermolecular interactions that lead to slightly larger and more broadly distributed particles[230]. These results further validate the design goals of both PEG-lipids in terms of stability and functionality, providing key insights for future PEG-lipid formulation optimizations.

4.3.3. Different PEG-Lipids mRNA-LNP Cell Delivery Analysis

The optimized molecular structure of ALC-0159 provides a stable hydrophilic barrier, significantly reducing the likelihood of non-specific adsorption of LNPs in the cellular environment. This characteristic ensures long circulation time and high biocompatibility of LNPs in systemic delivery [231]. The smaller particle size and low polydispersity index (PDI) enable more efficient cellular uptake and release of mRNA into the cytoplasm, facilitating transcription and expression. Since ALC-0159 is primarily designed for systemic delivery, its transfection process typically does not rely on specific targeting functionality but instead achieves effective delivery through efficient cellular uptake and endosomal escape mechanisms.

DSPE-PEG(2000) Maleimide, on the other hand, features a functional maleimide group that can bind to thiol groups, offering flexibility for targeted modifications. However, the higher particle size and broader distribution may reduce the uniformity and transfection efficiency of LNPs in HEK293 cells. Nevertheless, when DSPE-PEG(2000) Maleimide is conjugated with targeting molecules such as antibodies or ligands, its targeted delivery capability is

significantly enhanced, resulting in improved transfection efficiency for specific cells or tissues. And figure 46 shows the fold change of these two PEG-Lipids.

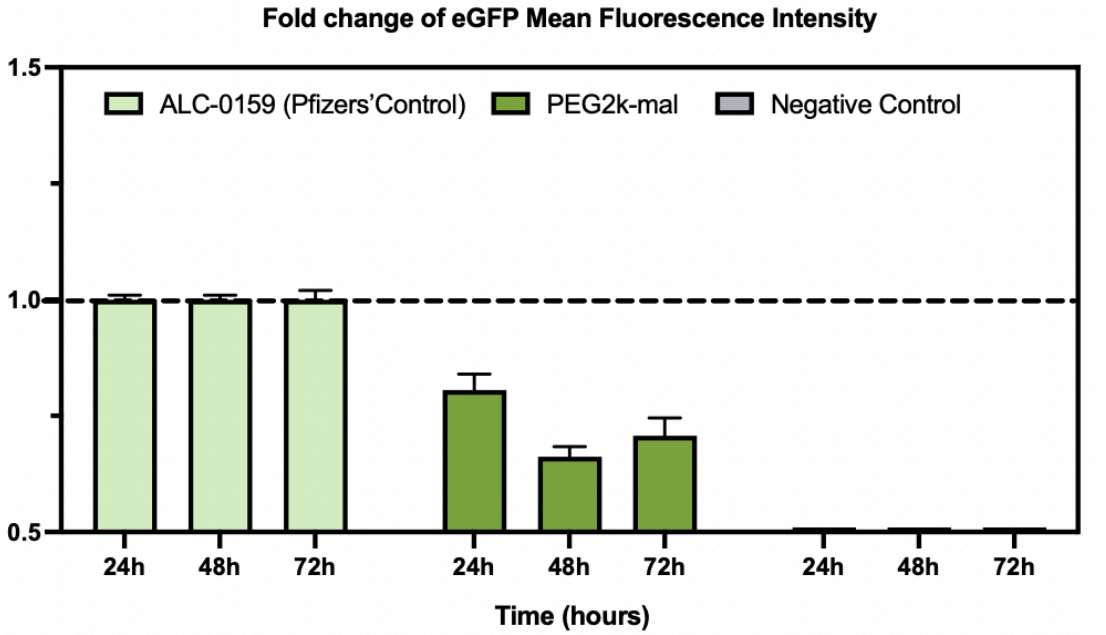

Figure 46. The Comparison of transfection performance of ALC-0159 and DSPE-PEG(2000) Maleimide. All mRNA-LNP formulations were synthesized using a T-mixer with a total flow rate of 16 mL/min and a flow rate ratio of 3:1. The experiments varied only the type of ionizable lipid, while other components remained unchanged. After synthesis, the mRNA-LNPs were stored at 4°C and utilized for formulation and transfection experiments within 24 hours to ensure sample freshness. The eGFP-mRNA (3039 nts) used in all experiments was sourced from the same production batch to minimize variability. Each experimental group was performed in triplicate (n=8) to evaluate the stability and reproducibility of the results. Error bars represent ±SD, and data were characterized using Plate Reader and fluorescence detection methods.

Based on time-dependent eGFP fluorescence intensity monitoring (24–72 hours), the transfection kinetics of PEG-lipid formulations showed significant differences compared to ALC-0159 (Pfizer control group) (Figure 47). PEG2k-mal exhibited an initial fluorescence intensity of 0.94 ± 0.08 at 24 hours, slightly lower than ALC-0159's 1.00 ± 0.02, indicating a slightly lower initial transfection efficiency. Over time, the fluorescence intensity of PEG2k-mal significantly decreased, dropping to 0.58 ± 0.06 at 72 hours, demonstrating a substantial reduction (38.3% decrease), which was consistent with a biexponential decay model ($R^2 > 0.95$). This decay pattern can be attributed to the long PEG chains in PEG2k-mal, which may impact the membrane fusion efficiency of LNPs and

delay mRNA release. In contrast, ALC-0159 exhibited more stable transfection efficiency, maintaining a higher level over the time period.

In summary, while PEG-lipid formulations had a minor impact on initial transfection efficiency, their performance in long-term expression stability was poorer. In comparison, ALC-0159 demonstrated optimal stability and long-term transfection performance, making it better suited for sustained gene delivery applications. These findings highlight the role of PEG-lipids in influencing LNP transfection efficiency, particularly in terms of long-term transfection stability, where they showed inferior performance.

4.3.4. PEG-lipid Stability Test

The ALC-0159 molecule features an optimized lipid anchor and a PEG-2000 chain, forming a stable hydrophilic barrier on the LNP surface, effectively reducing aggregation between LNPs and maintaining their stability. In contrast, DSPE-PEG(2000) Maleimide, due to the presence of its maleimide group, may introduce additional intermolecular interactions during storage. Moreover, the longer PEG-2000 chain can also impact stability in ways that are not easily predictable. The results showed in figure 47.

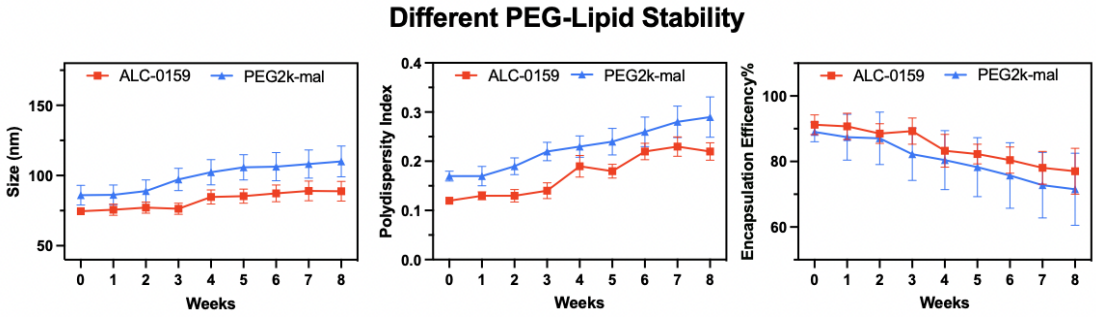

Figure 47. The stability experiment of ALC-0159 and DSPE-PEG(2000) Maleimide. All mRNA-LNP formulations were synthesized using a T-mixer with a total flow rate of 16 mL/min and a flow rate ratio of 3:1. The experiments varied only the type of ionizable lipid, while other components remained unchanged. And the Helper Lipids occupied 12.5 mol% in LNP formulation. After synthesis, the mRNA-LNPs were stored at 4°C with in pH 7.4 10 mM PBS buffer. And the formulation and dilution interval within 30 seconds to avoid the high organic phase effect. The eGFP-mRNA (3039 nts) used in all experiments was sourced from the same production batch to minimize variability. Each experimental group was performed in triplicate (n=6) to evaluate the stability and reproducibility of the results. Error bars represent ±SD, and data were characterized using Ribogreen and Nano Flow Sizer detection methods.

As storage time increases, the particle size of both LNP formulations gradually increases; however, the PEG2k-Mal system exhibits a more significant size increase, suggesting greater susceptibility to particle aggregation or lipid rearrangement during storage. Additionally, the polydispersity index (PDI) also shows an upward trend, particularly in the later storage phase (Weeks 4–8), where PEG2k-Mal LNPs experience a more pronounced PDI increase, indicating reduced particle uniformity and further confirming its lower stability. The decline in encapsulation efficiency (EE%) further reflects stability concerns within the LNP system. Over time, the reduction in EE% may be attributed to structural changes in the LNPs, leading to partial mRNA leakage or degradation.

Overall, ALC-0159 appears to be a more suitable PEG-lipid for general LNP formulations, whereas PEG2k-Mal may require further optimization, such as modifying buffer composition, adjusting lipid ratios, or incorporating additional stabilization strategies to improve its long-term stability. Future research should further explore PEG density, lipid combinations, and optimized storage conditions to mitigate the instability of the PEG2k-Mal system and enhance its potential applications in gene therapy and precision medicine.

4.3.5. PEG-Lipid: Control of CPPs and Optimization of CQAs for mRNA-LNPs

Although PEG-lipids account for only 1-2 mol% of the total composition of LNPs, their optimization has been an ongoing area of research. The optimization of PEG chain length and density is crucial for the in vivo circulation of LNPs, but further studies are still needed to determine the optimal PEG chain length [232]. The design of PEG-lipids typically aims to enable their gradual shedding in vivo, thereby restoring the bioactivity of LNPs and promoting cellular uptake and payload release [233, 234]. Additionally, the development of pH-sensitive, enzyme-sensitive, or reduction-sensitive cleavable PEG-lipids for intelligent release in specific environments has become a key focus in targeted delivery research.

For LNPs, although PEG-lipids constitute a small fraction, their impact on critical quality attributes (CQAs) cannot be overlooked. Through more experimental studies, the effects of different PEG-lipids on LNPs' CQAs (e.g., size, PDI, encapsulation efficiency, stability, and biocompatibility) can be investigated in advance, providing scientific guidance for subsequent storage and purification processes. For example, optimizing the selection of PEG-lipids can improve the long-term storage stability of LNPs, reduce particle aggregation, and ensure consistency during purification. Table 20 compared these two PEG-lipid.

Table 20. Comparison of PEG-lipids in LNP (ALC-0159 & DSPE-PEG(2000) Maleimide

PEG-LIpids	ALC-0159	DSPE-PEG2000 Maleimide
Structure	PEG-2000 conjugated to an optimized lipid anchor (non-phospholipid-based)	PEG-2000 conjugated to DSPE (a phospholipid) with a maleimide functional group
Head Group	Neutral PEGylated head group	Maleimide-functionalized PEG head group
Molecular Weight	~2,400 Da	~2,900 Da
Advantages	- Enhances LNP stability and circulation time - Reduces non-specific adsorption - Improves biocompatibility - Suitable for general-purpose LNP formulations	- Enables specific targeting via thiol-maleimide reaction - Facilitates ligand conjugation for precision drug delivery - Provides long circulation benefits due to PEG shielding [235]
Limitations	- Lacks specific targeting capability - May contribute to the "PEG dilemma" (balancing shielding and uptake)	- Potentially lower stability due to additional molecular interactions - Higher molecular weight may influence LNP size and PDI
Applications	- mRNA vaccines - General systemic delivery - Long-circulating drug formulations	- Targeted drug and gene delivery - Precision medicine - Ligand-conjugated LNPs for receptor-mediated uptake
Future Optimization	- Fine-tuning PEG density for improved stability and reduced	- Enhancing stability via optimized buffer conditions

	immune recognition - Exploring alternative lipid anchors for better membrane interaction [236]	- Reducing molecular interactions that affect long-term LNP uniformity

Future research could also integrate high-throughput screening technologies to systematically evaluate the effects of different PEG-lipids on LNP performance, thereby accelerating the development of optimal formulations. Furthermore, exploring the design and application of novel PEG-lipids (e.g., biodegradable or multifunctional PEG-lipids) will further enhance the targeting and therapeutic efficacy of LNPs.

4.4. Conclusion

This study systematically evaluated the impact of different lipid structures on the critical quality attributes (CQAs) of mRNA-lipid nanoparticles (LNPs) prepared using microfluidic technology. By screening and optimizing ionizable lipids, helper lipids, and PEG-lipids, this study elucidated the differences in LNP performance and the underlying mechanisms of various lipid components. Unlike traditional laboratory-based LNP preparation studies, this research integrates modern microfluidic technology with lipid formulation optimization. By precisely controlling lipid composition, we overcame the limitations of traditional methods in particle size control and batch consistency, providing a promising lipid formulation for the continuous production system of mRNA therapeutics. The lipid molecular engineering principles and microfluidic process parameter database established in this study provide dual theoretical support for the rational design of gene delivery systems: on one hand, by revealing the quantitative relationship between the polarity of lipid head groups, hydrophobic tail chain configuration, and nanoparticle self-assembly dynamics, this provides guidance for the design and synthesis of next-generation lipid molecules. More importantly, with the precise control of nanoparticle structures achieved in the microfluidic platform, this research lays the theoretical foundation for developing pre-targeting and in situ coupling LNPs using microfluidic synthesis routes [237, 238].

The results showed that the LNP formulation composed of ALC-0315, DOPE, and ALC-0159 exhibited excellent performance in particle size control (74 nm), uniformity (PDI ≈ 0.11), and encapsulation efficiency (EE% ≈ 95%), making it suitable for continuous production of mRNA drugs. Furthermore, in terms of stability (no significant changes observed after two months of storage at 4°C without any adjuvants) and transfection efficiency, this formulation outperformed the currently available Pfizer/BioNTech vaccine formulation. Based on this formulation screening, we also formulated and characterized several lipid materials commonly used in LNP research, including SM102 (Moderna's mRNA vaccine), DLin-MC3-DMA (most commonly used before mRNA vaccines in lipid nanoparticles), DOPE (dual C18:1 unsaturated chains), and DSPE-PEG2000 Maleimide (highly efficient coupling ability). These studies not only provide an effective platform for mRNA vaccine preparation but also offer theoretical support for other gene therapies, enhancing the potential for continuous production of RNA products. Based on the comprehensive evaluation of the effects of lipid components on LNP CQAs, the optimal formulation was determined to be ALC-0315 (45 mol%), DOPE (15.9 mol%), cholesterol (37.85 mol%), and ALC-0159 (1.25 mol%). This formulation generates highly stable and reproducible mRNA-LNPs, making it suitable for subsequent large-scale and continuous production studies.

5. Continuous Formulation and purification of mRNA-Lipid Nanoparticles

With the increasing demand for large-scale production of novel vaccines and nucleic acid-based therapeutics, the limitations of traditional manufacturing processes have become increasingly evident. In response, mRNA production technology based on a closed, continuous, multi-product platform has gained significant attention in the industry. This platform integrates single-use component systems and advanced process analytical technologies (PAT) to enable real-time in situ monitoring and inter-batch quality control, thereby significantly improving production throughput and product uniformity [239]. Compared to conventional batch manufacturing, the continuous production model offers higher space efficiency, lower unit production costs, and enhanced process efficiency, while ensuring compliance with Good Manufacturing Practice (GMP) standards. Despite recent breakthroughs in continuous mRNA production, further research is required to optimize process parameters and scale-up strategies.

In the development of mRNA drug delivery systems (DDS), lipid nanoparticles (LNPs) are formulated using microfluidic technology, which facilitates mRNA encapsulation, purification (removal of unencapsulated nucleic acids, free lipids, and organic solvents), and real-time quality monitoring [240]. Studies have demonstrated that critical process parameters (CPPs) (e.g., total flow rate, lipid concentration) significantly influence critical quality attributes (CQAs) (e.g., particle size, polydispersity index (PDI), and encapsulation efficiency), validating the reliability and efficiency of microfluidic technology in LNP production. Based on these findings, this study proposes integrating spatially resolved dynamic light scattering (SR-DLS) technology with LNP manufacturing processes to achieve real-time online monitoring of particle size and PDI, thereby providing a technological framework for standardized LNP production [241].

5.1. Optimization of real-time SR-DLS detection

5.1.1. PSD vs PDI

In the continuous manufacturing of lipid nanoparticles (LNPs), traditional quality assessment systems predominantly rely on the polydispersity index (PDI), a core metric grounded in the assumption of Gaussian size distribution [242]. However, practical LNP formulations often exhibit non-ideal size distributions characterized by asymmetry, multimodal peaks, or anomalous tailing phenomena. The inherent statistical limitations of this univariate parameter impede its capacity to detect heterogeneity arising from particle subpopulations or process deviations. For instance, when mRNA aggregates coexist with intact LNPs in the system, PDI averaging effects may obscure bimodal distribution features. In contrast, real-time monitoring of particle size distribution (PSD) enables direct identification of abnormal peak profiles caused by mixing inefficiencies or contamination, thereby providing visual guidance for process parameter optimization [243, 244].

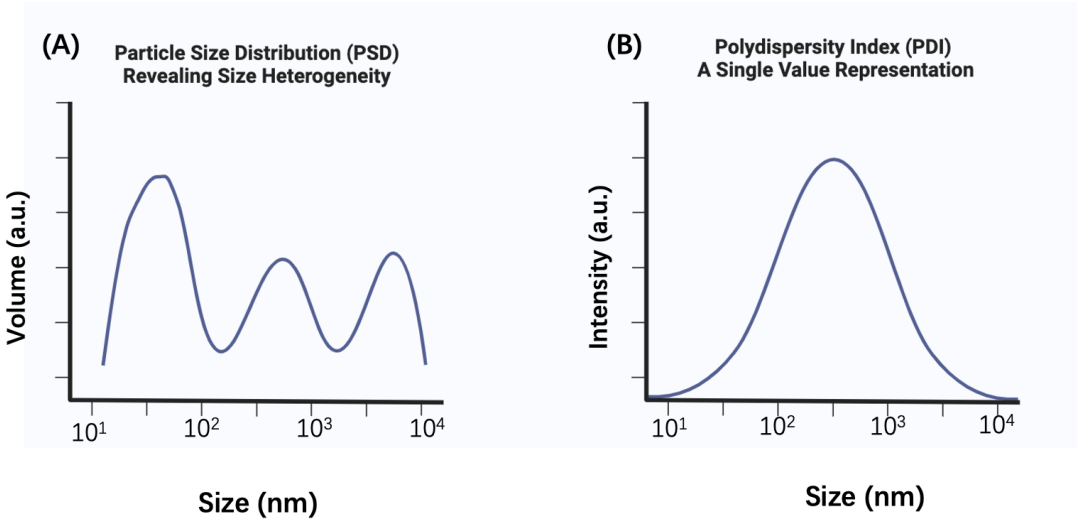

Figure 48. The PSD measure surface(A) and PDI measure surface(B). PSD (Particle Size Distribution): Provides a visual representation of particle size distribution, identifying multimodal peaks and distribution width, revealing system heterogeneity. PDI (Polydispersity Index): Represents particle uniformity with a single numerical value; a lower value indicates a narrower distribution but does not provide detailed size distribution information.

Figure 48 shows the different measure surfaces of PSD(A) and PDI(B). As a simplified descriptor of particle uniformity, PDI merely quantifies dispersion

magnitude while failing to distinguish between unimodal and multimodal distributions. In continuous-flow synthesis systems, PSD overcomes this limitation by dynamically resolving geometric characteristics of size distributions (e.g., main peak shift, peak width variation, and secondary peak intensity), achieving precise diagnostics of process perturbations [245]. For example, insufficient shear stress in microfluidic reactors that compromises lipid-mRNA mixing efficiency may manifest as main peak broadening or satellite peaks in PSD profiles, whereas PDI values might show negligible fluctuations, complicating root cause analysis. The integration of PSD with closed-loop process control facilitates quantitative correlations between distribution morphology and critical process parameters (CPPs): Main peak displacement often indicates suboptimal lipid concentration or flow rates, necessitating recalibration of molecular self-assembly duration in microchannels; emerging secondary peaks may signal raw material impurities or equipment residues, triggering in-line purification protocols or hydrodynamic condition adjustments [246]. This adaptive feedback mechanism, powered by PSD data streams, effectively mitigates batch-to-batch variability while ensuring spatiotemporal process consistency.

Within advanced quality control frameworks for LNP continuous manufacturing, PSD monitoring not only addresses the statistical constraints of conventional PDI but also establishes an end-to-end closed-loop control network linking "process parameters-particle attributes-product performance" through real-time multidimensional distribution analysis. This PSD-centric process analytical technology (PAT) paradigm is catalyzing a paradigm shift from empirical to data-driven approaches in nucleic acid therapeutics production, laying theoretical and technical foundations for scalable, high-reproducibility continuous manufacturing platforms.

5.1.2. Nano Flow Sizer Setting Optimization of Calibration

During the synthesis of mRNA-LNPs, ethanol as an organic phase solvent account for up to 25% (v/v) in the crude LNP. At this concentration, ethanol significantly alters critical physical parameters of the solution system—the refractive index increases, while the solution viscosity concurrently rises. These physicochemical changes directly compromise the detection accuracy of Nano

Flow Sizer (NFS). To mitigate such interference, a gradient dilution optimization strategy was developed and systematically evaluated in this study. In nanoparticle characterization studies, 100 nm Polyethylene (PE) Microspheres are widely used as standardized reference particles, enabling traceable calibration of the NFS system and ensuring the metrological reliability of particle size detection [247].

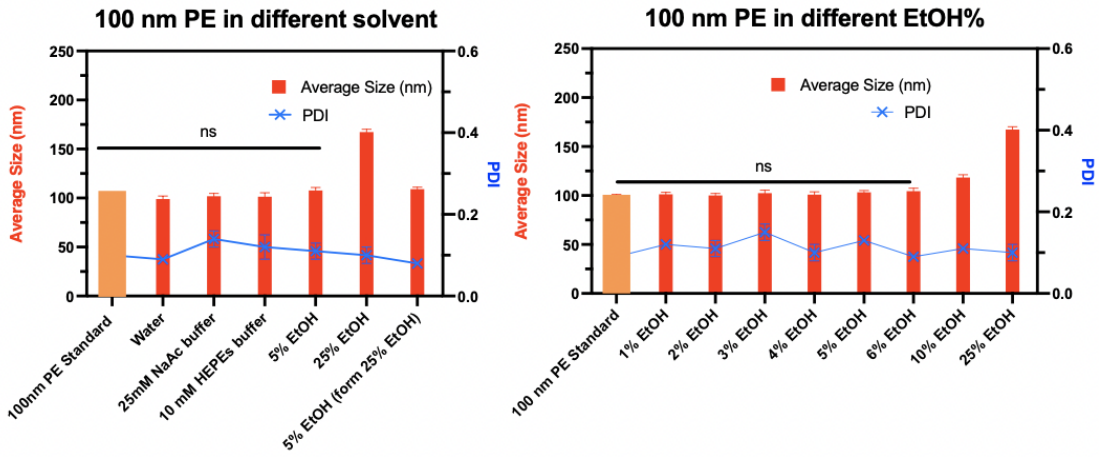

Figure 49. Calibration of buffer system selection and organic solvent content. This study compared DI water, 25 mM NaAc buffer (LNP initial formulation), 10 mM HEPES buffer (storage buffer), with 5% (post-dilution) and 25% (initial) ethanol concentrations for nanoparticle characterization, while evaluating ethanol gradient (0-25%) matrix interference using 100 nm PE microspheres. Using orange-colored bar charts to visualize the normalized size distribution of 100 nm polyethylene (PE) microspheres with standardized according to dynamic light scattering (DLS) measurements documented in the manufacturer's technical specifications.

Systematic evaluation of 100 nm PE microspheres under various solvent systems and ethanol concentrations revealed no significant matrix effects of aqueous buffer compositions (25 mM NaAc vs. 10 mM HEPES) on nano flow sizer (NFS) measurements (Figure 49). Based on this result it can be demonstrated that different buffers do not have a significant effect on the determination of NFS. However, ethanol concentration-dependent measurement deviations were observed, with marked alterations detected at 25% ethanol concentration, confirming severe interference from high organic phase content on LNP characterization. Based on these findings, a critical dilution threshold (EtOH <5%) for mRNA-LNPs was established through gradient dilution optimization, and the consistency of NFS detection data across

buffer systems was quantitatively validated, thereby effectively eliminating solvent-mediated artifacts in mRNA-LNP analysis.

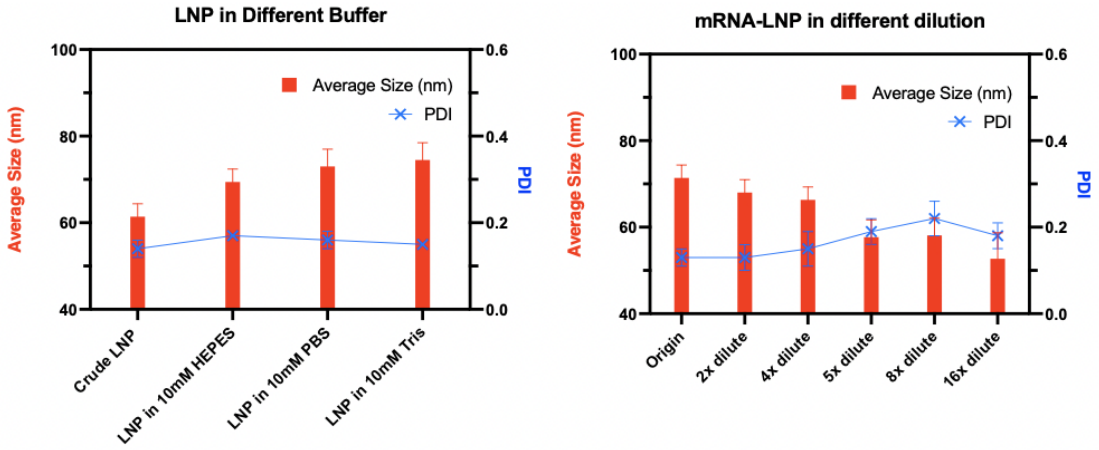

Figure 50. Calibration of LNP buffer systems and dilutions. All buffer keep same pH to avoid the pH effect. And using HEPES to dilute LNP samples. The later TFF process can using HEPES buffer only. The mRNA-LNP formulations were synthesized using a T-mixer with a total flow rate of 16 mL/min and a flow rate ratio of 3:1. The composition of the mRNA-lipid nanoparticles included ALC-0315: DOPE: Chol: ALC-0159 (48.5: 12.5: 38.5: 1.5, mol%), with total lipid concentrations shown in the figures. And the N/P ratio is 6:1. eGFP (1043 nts, 0.15 mg/mL) was selected as the mRNA component, with an approximate length of 3039 nucleotides (nts). And the mRNA-LNP samples used in next stage experiments are same.

Experimental data (Figure 50) demonstrated that LNPs formulated in different buffer systems (10 mM HEPES, PBS, and Tris) showed no significant differences in hydrodynamic diameter (Size: 82.3 ± 1.5 nm) or polydispersity index (PDI: 0.12 ± 0.03), indicating negligible matrix effects of buffer compositions on the nano flow sizer (NFS) characterization. Based on the results of Crude LNP (containing 25% EtOH) and the previous determinations of different EtOH contents, the same changes corroborate the reliability of the determinations. It should be noted that while minor pH variations (7.0–7.4) in this study did not compromise particle stability, previous studies have reported that sudden pH shifts exceeding ±0.5 units may trigger irreversible LNP aggregation (>20% size increase) [218]. Notably, dilution factors beyond 10-fold reduced the NFS scattering intensity below the detection threshold, resulting in unreliable measurements. Therefore, a standardized dilution protocol (5-fold volumetric dilution in 10 mM HEPES buffer, pH 7.0) was

implemented to ensure detection sensitivity and data reproducibility.

5.1.3. Batch Measurement vs Continuous Measurement

This study utilized a microfluidic platform to prepare lipid nanoparticles (LNPs) in both batch synthesis and continuous synthesis modes, with real-time particle size analysis performed using the Nano Flow Sizer (NFS). Offline batch measurements were conducted via a static vial holder, while online monitoring of the continuous process required switching to a flow cell module (inner diameter: 0.5 inches). To ensure the stability of dynamic light scattering (DLS) measurements, the fluid within the flow cell needed to maintain laminar flow conditions (Re < 2300). Theoretical calculations demonstrated that at a flow rate of 16 mL/min, Re < 30, satisfying the laminar flow requirements.

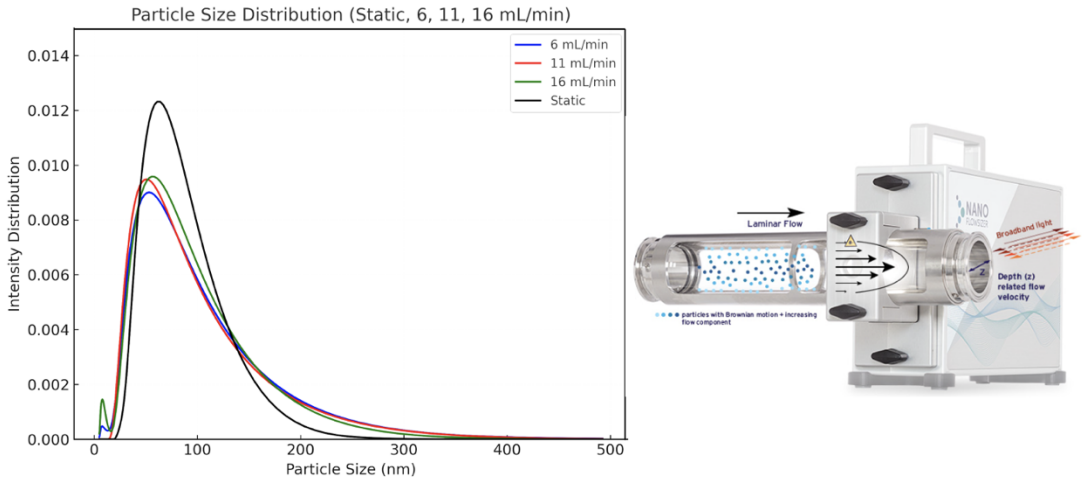

Figure 51. Particle Size Distribution summary of measurements for different flow rates. The SR-DLS mode of the Nano Flow Sizer was employed to determine the PSD of LNPs in static and flow modes.

Figure 51 shown the static and different flow rate particle size distribution's difference. This study utilized a microfluidic platform to prepare lipid nanoparticles (LNPs) in both batch synthesis and continuous synthesis modes, with real-time particle size analysis performed using the Nano Flow Sizer (NFS).

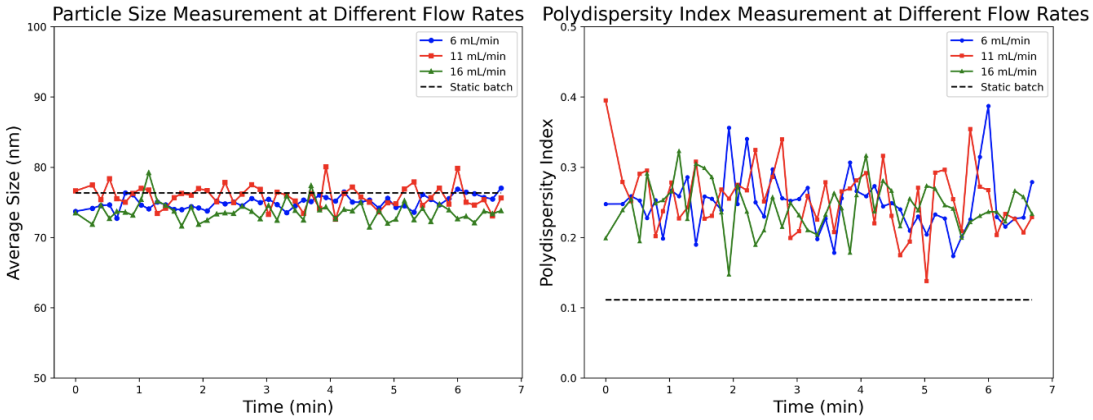

Figure 52. Schematic of the time variation of measured particle size and PDI in flow mode. The SR-DLS mode of the NanoFlow Sizer was employed to determine the static and flow modes, along with time-dependent measurements of size and PDI.

Figure 52 shows different flow rate measurements, including size and PDI. Offline batch measurements were conducted via a static vial holder, while online monitoring of the continuous process required switching to a flow cell module (inner diameter: 0.5 inches). To ensure the stability of dynamic light scattering (DLS) measurements, the fluid within the flow cell needed to maintain laminar flow conditions (Re < 2300). Theoretical calculations demonstrated that at a flow rate of 16 mL/min that can satisfying the laminar flow requirements.

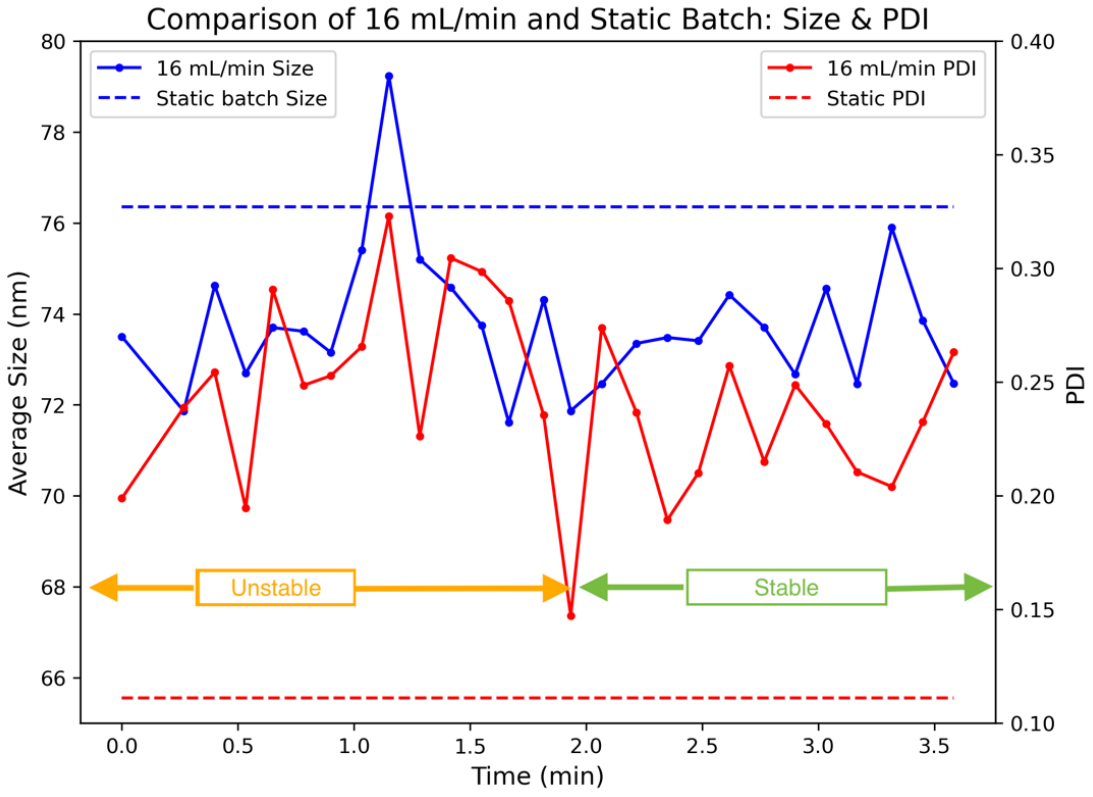

Figure 53. Comparative analysis of particle size and PDI measurements in static and flow modes. Real-time online monitoring of LNP critical quality attributes (CQAs) during continuous mRNA-LNP production: Particle size variations and PDI changes of the mRNA drug product (mRNA-DP) measured by the NFS under both static and flow (16 mL/min) conditions.

The continuous measurements shown in figure 53. During the initial microfluidic mixing stage of continuous mRNA-LNP production, the transient filling process of the two-phase fluids within the upstream reaction tubing results in non-steady-state flow, leading to pronounced temporal oscillations in particle size and polydispersity index (PDI) as monitored in real-time by the Nano Flow Sizer (NFS). Furthermore, based on the hydrodynamic characteristics of the T-mixer, intermittently observed pressure accumulation suggests the potential occurrence of localized microblockage within the mixer. To mitigate flow instability, this study implemented the use of capillary tubing with a larger inner diameter to optimize the lipid injection process into the T-mixer. Additionally, further optimization of the mixer design or the adoption of more efficient mixing techniques, such as impingement jet mixing or vortex mixing, may contribute to a more stable continuous LNP production process.

5.2. Purified Optimization of mRNA-LNP

Purification processes are critical for the stability of mRNA-LNPs, as residual organic solvents and free lipid components may catalyze degradation pathways such as lipid acyl chain hydrolysis/oxidation and mRNA phosphodiester bond cleavage, significantly compromising the storage stability of the formulation [248]. Notably, residual solvents like ethanol can alter the refractive index and dielectric constant of the solution, leading to light scattering background noise and particle size measurement deviations in the Nano Flow Sizer (NFS), with this interference being particularly pronounced during real-time monitoring. According to ICH Q3C(R8) guidelines, Class 3 residual organic solvents in the final mRNA drug product (mRNA-DP) must be strictly controlled below the Permitted Daily Exposure (PDE) limit (≤5000 ppm) [249]. Therefore, downstream purification requires techniques such as tangential flow filtration (TFF) or dialysis to simultaneously achieve buffer exchange and removal of low-molecular-weight impurities. This dual approach not only ensures

regulatory compliance but also eliminates optical interference from organic solvents in NFS detection systems, thereby guaranteeing long-term formulation stability while providing reliable quality control measures for manufacturing processes.

5.2.1. Dialysis to Screen Buffer pH setting

Studies indicate that direct exposure of mRNA-LNPs to neutral buffers post-synthesis may trigger uncontrolled colloidal instability, manifesting as particle size distribution broadening or main peak shifting [250]. This phenomenon originates from the deprotonation of ionizable lipids at neutral pH, which neutralizes their cationic headgroups and weakens electrostatic interactions with negatively charged mRNA, thereby compromising the structural integrity of lipid-mRNA complexes and inducing particle dissociation or fusion [251]. The efficiency of mRNA-LNP purification varies significantly across buffer systems, depending on the chemical structure of ionizable lipids. Given the chemical compatibility constraints of TFF membranes, dialysis was employed for buffer exchange to systematically screen stabilization buffers compatible with the target LNP formulation. Since only HEPES buffer can be used in the process of TFF so PBS buffer was taken as a positive control in this study to explore the effect of pH change on mRNA-LNP size.

Table 21. Experimental setup of dialysis process with different buffers.

Buffer Information

Buffer Name	Compositions	pKa at 20°C	pH Range
Phosphate Buffered Saline (PBS)	NaCl: 137 mM, KCl: 2.7 mM, Na_2HPO_4: 10 mM, KH_2PO_4: 1.8 mM	7.21	5.8-7.4
HEPES buffer	NaCl: 150 mM, HEPES: 22 mM	7.55	6.8-8.2

PBS buffer dilution and Dialysis

Duration	Buffer exchange	Size (nm)	PDI	Dialysis pH
mRNA-LNPs after reaction	NaAc pH 4.0 25mM	61.4±1.2	0.14±0.02	4.23±0.02
0-2 h	PBS pH 7.4 10mM	83.5±1.3	0.16±0.03	7.21±0.01

2-4 h	PBS pH 7.4 10mM	88.6±1.9	0.17±0.03	7.28±0.01
4-6 h	PBS pH 7.4 10mM	92.5±2.2	0.17±0.02	7.30±0.02
6-8 h	PBS pH 7.4 10mM	92.3±1.8	0.19±0.03	7.32±0.03

HEPES buffer dilution and Dialysis

Duration	Buffer exchange	Size (nm)	PDI	Dialysis pH
mRNA-LNPs after reaction	NaAc pH 4.0 25mM	61.4±1.2	0.14±0.02	4.23±0.02
0-2 h	HEPES pH 7.4 10mM	79.8±2.4	0.17±0.01	7.21±0.03
2-4 h	HEPES pH 7.4 10mM	84.1±2.2	0.19±0.02	7.28±0.03
4-6 h	HEPES pH 7.4 10mM	87.5±2.8	0.21±0.05	7.30±0.03
6-8 h	HEPES pH 7.4 10mM	89.3±2.4	0.23±0.07	7.32±0.03

Experimental data demonstrated that rapid dialysis-mediated transition of mRNA-LNPs from the acidic initial buffer (NaAc, pH 4.0) to neutral buffer systems (PBS/HEPES, pH 7.4) induced significant particle size increases (PBS: ~40%; HEPES: ~30%) with progressive enlargement over time. This pH gradient-triggered (ΔpH=3.4) irreversible particle expansion was accompanied by elevated PDI values, suggesting that abrupt environmental pH alterations disrupt lipid bilayer stability, leading to uncontrolled structural reorganization and particle aggregation [244, 252]. The phenomenon, independent of buffer composition, is mechanistically attributed to phase transitions caused by pH-jump-induced deprotonation of ionizable lipids [253]. Further investigations employing gradient pH dialysis are required to delineate these interfacial effects.

Table 22. Optimized buffer dialysis process experimental setup.

Duration	Buffer exchange	Size (nm)	PDI	Dialysis pH
mRNA-LNPs after reaction	NaAc pH 4.0 25mM	61.4±1.2	0.14±0.02	4.23±0.02
0-2 h	PBS pH 5.8 10mM	63.5±1.8	0.13±0.06	5.32±0.03
2-4 h	HEPES pH 6.8 10mM	67.3±2.2	0.14±0.05	6.41±0.03
4-6 h	HEPES pH 7.4 10mM	73.2±1.4	0.16±0.06	7.16±0.04

6-8 h	HEPES pH 7.4 10mM	73.6±1.9	0.17±0.07	7.23±0.03

Gradient pH dialysis experiments demonstrated that staged buffer replacement (pH 4.0 → 5.8 → 6.8 → 7.4) significantly mitigated mRNA-LNP particle size expansion. Compared to the direct neutral pH transition control group (single ΔpH = 3.4, 50.6% size increase), the gradient dialysis group (total ΔpH = 3.0 across four phases) exhibited limited particle size growth (61.4 → 73.6 nm) with reduced polydispersity index (PDI) escalation (0.14 → 0.17 vs. 0.14 → 0.23 in controls). This gradual pH modulation strategy-maintained lipid bilayer equilibrium by attenuating the deprotonation kinetics of ionizable lipids, thereby suppressing structural collapse induced by abrupt phase transitions at critical pH thresholds [245, 252]. Further optimization of buffer systems is warranted, as ionizable lipid chemistry influences buffer compatibility, and potential adjuvant interactions during this process require systematic evaluation. Subsequent studies will integrate tangential flow filtration (TFF) to refine mRNA-LNP purification and characterization protocols.

5.2.2. TFF From TFF to continuous SP-TFF

This study employed tangential flow filtration (TFF) for the purification of mRNA-LNPs, comparing batch mode and continuous single-pass TFF (SP-TFF) modes. In the traditional batch mode, recirculation of the feed solution (mRNA-LNPs suspension) enables concentration, offering greater process design flexibility as it is not constrained by upstream continuous production flow rates [252]. In contrast, the continuous SP-TFF mode eliminates the recirculation loop and achieves a broader range of concentration factors by extending the residence time of the feed within the membrane module [253].

To maintain stable transmembrane pressure (TMP), an automatic backpressure valve (ABV) was installed on the retentate line for real-time adjustment of the system pressure to the setpoint. The feed solution was prepared by diluting crude mRNA-LNPs with a 10 mM HEPES buffer (pH 7). Through a multi-step continuous SP-TFF process, where the retentate from prior steps served as the feed for subsequent steps, efficient buffer exchange

and impurity removal were achieved by optimizing the membrane area based on the target concentration factor.

Table 23. Batch and continuous TFF tests for mRNA-LNP buffer exchange Experiment

Transmembrane pressure (TMP)	Flow Rate	Filter Type	Test Mode	Procedure
8 psi	20 mL/min	mPES hollow fiber (300 kDa)	Batch	10X con. followed by 5X diafiltration and 2 washing steps
		Cellulose based cassette filter (Hydrosart, 300 kD /50 cm^2)	Continuous	Three consecutive SP-TFF diafiltration and a final washing step

Table 24. mPES Hollow Fiber Filter Batch Experiment

Steps	Volume (mL)	Average LNP Size (nm)	Particle Recovery	Ethanol Fraction*
mRNA-LNPs after reaction	5	102	N/A	25%
TFF Feed after dilution	30	102	N/A	3.8%
10X Concentration	3	109	32.5%	3.9%
5X DF	3	109	39%	Below EL
1st Washing	10	108	15%	Below EL
2nd Washing	10	116	1.5%	Below EL

*** EL: Established Limit**

Permeate samples collected during mRNA-LNP purification were analyzed by Nano Flow Sizer (NFS) dynamic light scattering and RiboGreen fluorescence assay, confirming the absence of lipid nanoparticles and mRNA in the permeate, which validated the complete retention of the drug product (DP) using a 300

kDa membrane. A standardized three-step batch TFF process — comprising concentration, diafiltration, and final washing — was implemented for ethanol removal. Residual ethanol content quantified by gas chromatography demonstrated a final concentration of <300 ppm, compliant with ICH Q3C guidelines.

Table 25. Cellulose SP-TFF Continuous Experiment

Steps	Volume (mL)	Average LNP Size (nm)	Particle Recovery	Ethanol Fraction
mRNA-LNPs after reaction	10	79	N/A	25%
TFF Feed after dilution	200	82	N/A	Below EL
1st Concentration	116	98.6	100%	Below EL
2nd Concentration	49	106	87.8%	Below EL
3rd Concentration	21	107	77.1%	Below EL
1st Washing	10	116	12.5%	0%
2nd Washing	10	110	0.4%	0%

*** EL: Established Limit**

In the continuous single-pass tangential flow filtration (SP-TFF) process, the crude mRNA-LNPs were initially diluted 20-fold with HEPES buffer (10 mM, pH 7.0) to reduce the ethanol concentration from 25% (post-synthesis level) to below the ICH Q3C Permitted Daily Exposure (PDE) limit. The ethanol content at each step was quantitatively monitored using gas chromatography (GC), with a calibration curve (Figure 54) established from ethanol–water mixtures. The green dashed line in the figure indicates the acceptable residual ethanol level (CQA) for the final mRNA drug product.

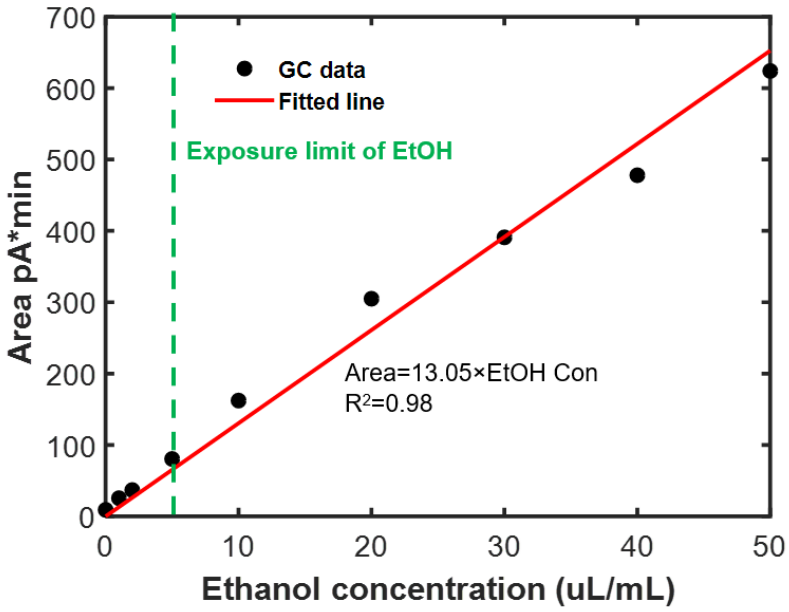

Figure 54. The experimental linear range of peak area response *vs.* ethanol concentration. Ethanol showed a linear response that yielded linear fit equation Area = 13.05×EtOH with an R-square of 0.98.

Following dilution, three sequential single-pass concentration steps were performed to gradually enrich mRNA-LNPs. However, when polyethersulfone (PES) SP-TFF cartridges were used, permeate flux dropped to zero after the first step due to membrane fouling caused by lipid–membrane interfacial adhesion. Upon switching to hydrophilic modified regenerated cellulose (RC) SP-TFF cartridges, over 90% mRNA-LNP recovery and a 10-fold volume concentration factor were achieved after three steps. These results underscore the importance of membrane material selection (hydrophilicity, surface charge) and the need for careful optimization of transmembrane pressure and tangential flow rate in continuous TFF-based purification processes.

5.3. Characterization of mRNA-LNP and unfilled mRNA-LNP analysis

Characterization of mRNA-LNPs using NanoFCM provides more precise data. The SYTO-9 dye enables labeling of mRNA within LNPs to determine the ratio of loaded mRNA-LNPs post-mixing, with empty lipid nanoparticles serving as blank controls.

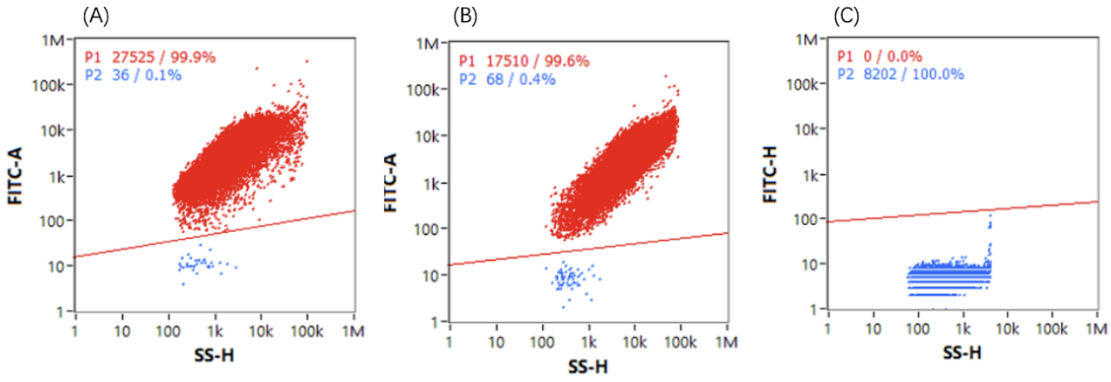

Figure 55. The mRNA-LNP filled percent analysis of mRNA-LNPs using NanoFCM. (A) before TFF, (B) retentate samples by TFF, and (C) permeate samples by TFF.

The figure 55 shows the nanoFCM results, include the before TFF, retentate and permeate samples. A high proportion of unfilled mRNA-LNPs (unfilled LNPs) not only reflects process defects (e.g., lipid-mRNA charge ratio imbalance) but may also trigger the release of pro-inflammatory cytokines (e.g., IL-6, TNF-α, IFN-γ), leading to inflammatory responses [254]. Therefore, precise characterization of encapsulation efficiency is critical for optimizing microfluidic mixing parameters and lipid formulation composition.

Table 26. Characterization of mRNA-LNPs Before and After the TFF Process in Batch and Continuous Modes

Parameter	Before TFF (Batch)	After TFF (Batch)	Before TFF (Continuous)	After TFF (Continuous)
Size by NFS (nm)	64	107	89	105
PDI by NFS (-)	0.16	0.15	0.14	0.10
Size by NanoFCM (nm)	72	118	99	124
mRNA-LNP Recovery (%)	-	54	-	90
EE (%)	88.8	95.6	89.6	95.5
Loaded mRNA-LNP (%)	98.2	99.8	99.9	99.6

NanoFCM characterization revealed that empty lipid nanoparticles (empty LNPs) constituted less than 1% of the mRNA-LNP population. LNP samples were vitrified on lacey carbon grids using a Vitrobot (Thermo Fisher Scientific) with controlled humidity and blotting conditions. Grids were plunged into liquid ethane and transferred into a 200 kV cryo-transmission electron microscope (Talos Arctica, Thermo Fisher) for imaging. Images were captured under low-dose conditions with a nominal magnification of 45,000×.

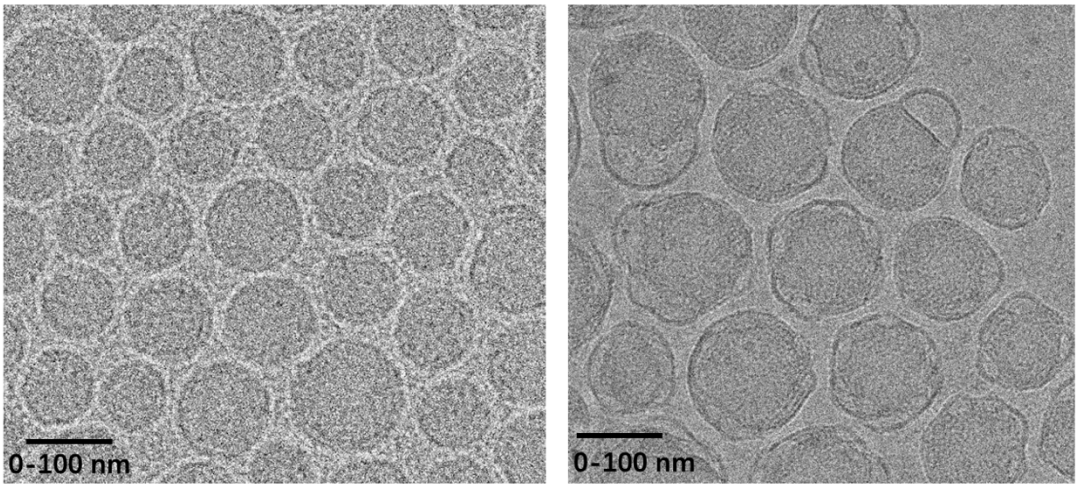

Figure 56. Cryo-electron microscopy (Cryo-TEM) images of mRNA-LNPs. Samples were stored in 10 mM PBS buffer (pH 7.4) prior to imaging. Micrographs were acquired at a magnification of 45,000×, clearly showing the nanoparticle morphology and internal structure.

While tangential flow filtration (TFF) did not significantly alter the loaded/empty particle ratio pre- versus post-purification, Nano Flow Sizer (NFS) and cryo-EM analyses indicated an increase in the average hydrodynamic diameter from 89 nm to 105 nm.

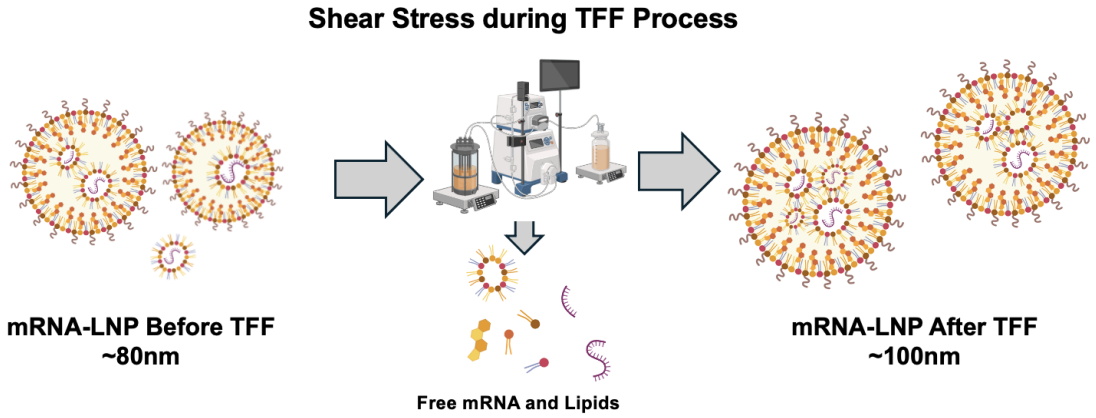

Figure 57. A potential mechanism involves shear stress-induced reorganization of structurally incomplete mRNA-LNPs during tangential flow filtration (TFF) purification. This dynamic remodeling process may facilitate secondary mRNA encapsulation through lipid bilayer rearrangement, concomitant with an increase in hydrodynamic diameter and EE%

Figure 57 shows why LNP increased after TFF process and how intravehicular compartments appeared. The observed multivesicular structures in cryo-EM images suggested shear-induced lipid reorganization as a potential mechanism for particle size enlargement. RiboGreen assays demonstrated an apparent encapsulation efficiency increase from 89% to 95% post-TFF (consistent across batch and continuous modes), potentially attributable to: 1) retention of free mRNA by the membrane (300 kDa cutoff), leading to underestimation of free RNA in RiboGreen analysis; 2) shear stress-driven passive loading of free mRNA into pre-LNPs through membrane defects, thereby increasing apparent encapsulation efficiency.

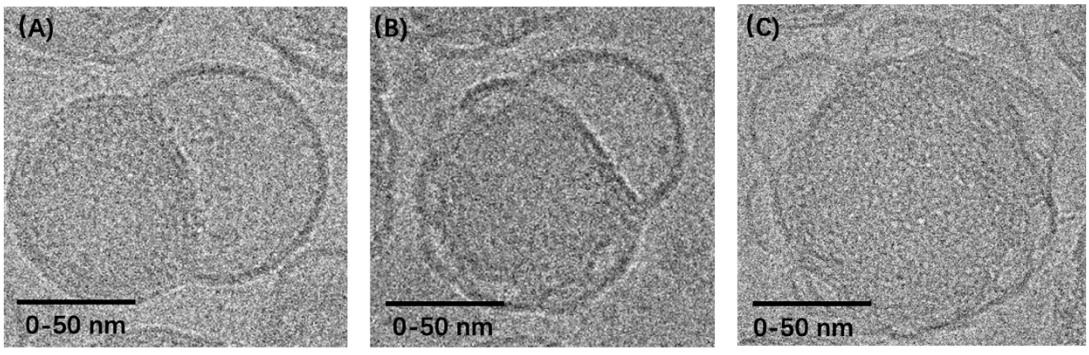

Figure 58. Three typical TFF-purified LNP structures were observed. The cyro-EM characterization revealed significant morphological heterogeneity in tangential flow filtration (TFF)-purified mRNA-LNPs, categorized into three dominant subpopulations: A) Dual-particle conjugates—two distinct LNPs

stably connected via shared lipid interfaces; B) Ostwald fusion bodies—larger LNPs engulfing smaller counterparts through interfacial tension-driven fusion; C) Multivesicular complexes—single lipid membranes encapsulating multiple internal vesicles [255]. Current purification technologies lack resolution for selective isolation of specific morphological subtypes. And no development of morphology-guided separation strategies.

Here are a few typical LNPs where intravehicular compartments exist, shown in Figure 58. Recent studies using cryo-EM and dye-mRNA have revealed dynamic structural characteristics of mRNA-LNPs: under specific physiological conditions, mRNA molecules dissociate from electrostatic complexes with ionizable lipids and migrate into intravehicular compartments formed by lipid bilayer reorganization [255]. These substructures significantly enhance mRNA stability through physical isolation, where vesicle membranes shield nucleic acids from oxidative attacks on phosphate backbones by reactive oxygen species and reduce alkylation modification risks to mRNA bases from lipid peroxides. Furthermore, intravehicular compartments improve in vitro transfection efficiency by regulating endosomal escape kinetics (e.g., enhancing pH-triggered membrane fusion efficiency) and enhance in vivo protein expression specificity in target organs. Future research should integrate cryo-electron tomography (cryo-ET) or single-particle tracking to further resolve the spatiotemporal regulatory mechanisms of vesicular topology on mRNA delivery efficacy, thereby guiding the design of next-generation modular LNPs [256].

5.4. mRNA-LNP Stability

Previous studies systematically screening microfluidic synthesis parameters (flow rate ratios, lipid concentrations) and lipid formulations (ionizable/helper lipid ratios) demonstrated limited effects on the physicochemical stability of mRNA-LNPs (particle size variation <10%, PDI<0.15), indicating that LNP stability is predominantly governed by downstream purification processes (e.g., shear stress in tangential flow filtration) and storage environmental sensitivity. Under neutral to mildly alkaline conditions (pH 7.0-8.0), mRNA chemical degradation primarily occurs via base-catalyzed hydrolysis of phosphodiester bonds, involving intramolecular nucleophilic attack by the ribose 2'-hydroxyl

group on adjacent phosphorus atoms, which triggers β-elimination reactions [97, 257]. Early formulation studies revealed that PBS buffer containing 10% sucrose (w/v) maintained colloidal stability of mRNA-LNPs at -20°C for ≥30 days (particle size increase <15%), whereas ultra-low temperature storage (-80°C or liquid nitrogen snap-freezing) induced significant post-thaw aggregation (particle size >200 nm) due to mechanical ice crystal damage and lipid phase separation. Recent optimization strategies incorporating zwitterionic buffer systems (e.g., HEPES/Tris) and non-reducing sugar stabilizers, coupled with post-purification payload calibration, provide critical technical support for mRNA-LNP formulation development.

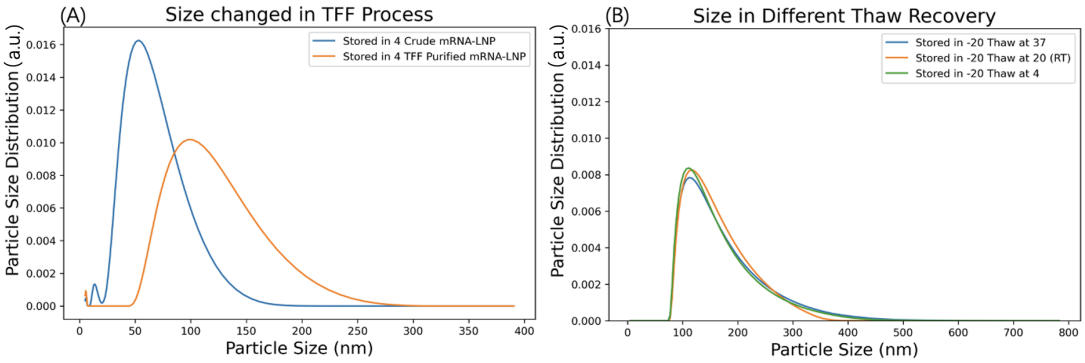

Figure 59. Effect of TFF on particle size distribution and comparison of particle size distribution of Thaw recovery at different temperatures. Comparison of particle size distributions between Crude mRNA-LNP samples and those purified by TFF, as well as mRNA-LNPs stored at -20°C after thawing under different temperature conditions (4°C, room temperature, and 37°C).

The TFF-purified mRNA-LNPs stored at 4°C, -20°C, and -80°C for two weeks and thawed at ambient temperature (20°C) demonstrated significant differences in colloidal stability. The -80°C storage group exhibited marked colloidal instability, manifested as visible phase separation and lipid aggregation, with signal noise exceeding the detectable range of NFS measurements. In contrast, the 4°C and -20°C storage groups maintained satisfactory monodispersity, suggesting that mechanical stress from ice crystal formation during ultra-low temperature storage may compromise LNP structural integrity. To mitigate such degradation, optimization of cryoprotectant formulation (e.g., 10% glucose) and implementation of controlled freezing protocols are recommended [258, 259]. Notably, mRNA-LNPs maintained stability at -20°C storage, and no significant changes in particle size distribution were observed across different thawing temperatures.

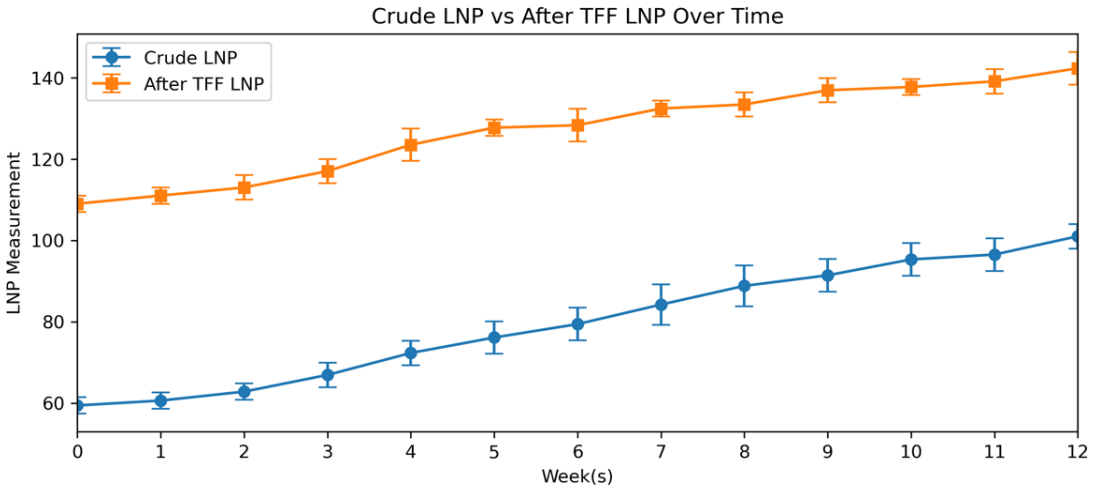

Figure 60. Comparative plots of LNP particle size changes for TFF treatments. Comparison of particle size changed between Crude mRNA-LNP samples and those purified by TFF, Stored in 4°C.

Figure 60 shows long-term stability studies based on experimental data revealed a time-dependent increase in particle size during storage at 4°C. After 1, 2, and 3 months of storage, the cumulative size increases reached 3%, 7%, and 17%, respectively. This progressive size enlargement suggests the potential occurrence of aggregation mechanisms in LNPs during storage.

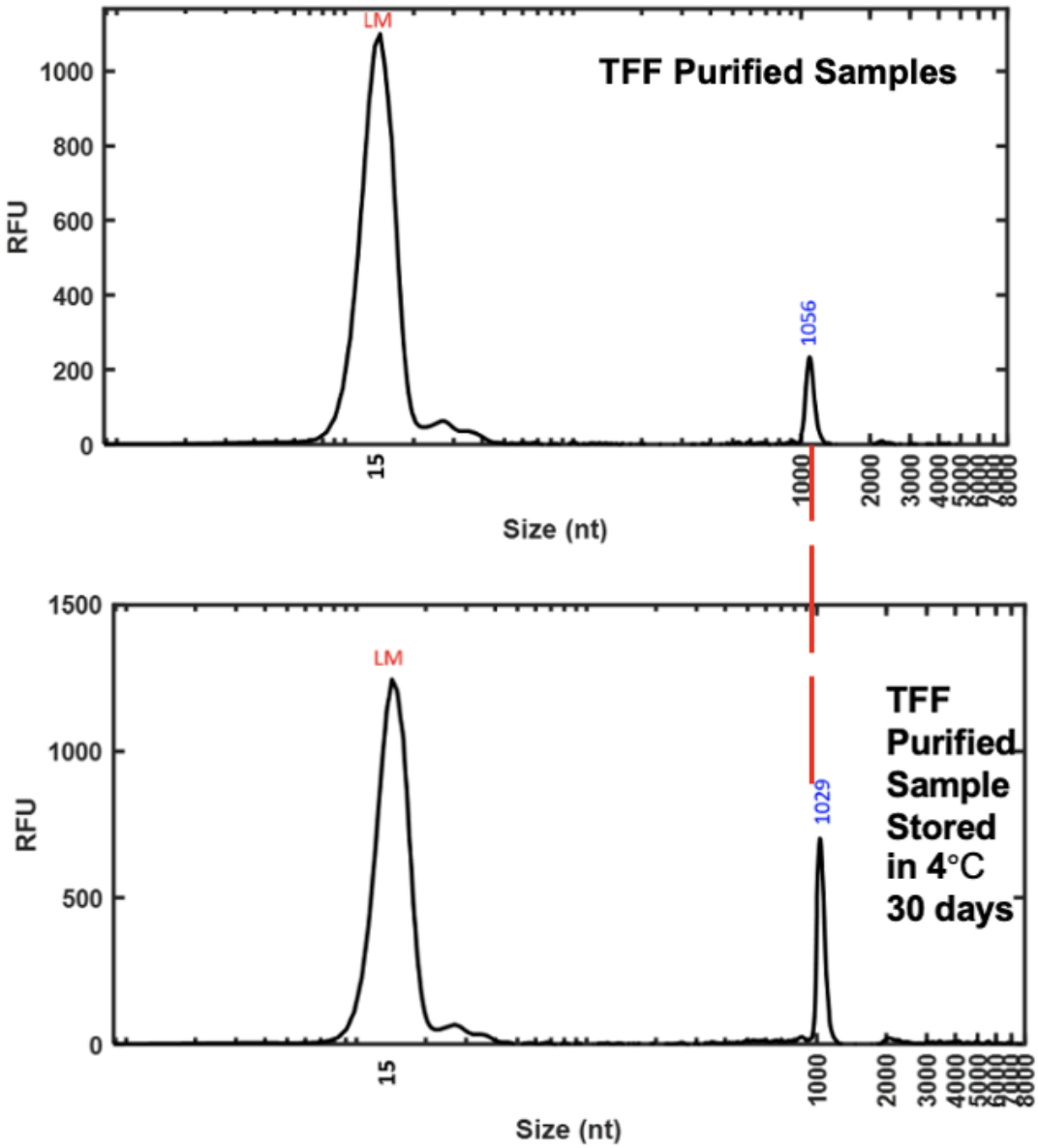

Figure 61. The RNA integrity comprsion of purified LNP sample and 30 days fridge store purified LNP samples. Electrophoretic analysis demonstrates the mRNA integrity profiles following LNP release in the mixed reaction, after TFF purification, and subsequent to 30-day storage at 4°C. In the electrophoretogram, the X-axis represents nucleotide length (nt), while the Y-axis indicates the relative abundance of mRNA at specific fragment sizes in relative fluorescence units (RFU). The characteristic peak of eGFP mRNA (approximately 1043 nt, blue) and the lower marker (LM ~15 nt, red) are clearly identified in the profile.

The capillary gel electrophoresis (CGE) analysis confirmed that the integrity of eGFP mRNA remained well-preserved throughout both the tangential flow

filtration (TFF) purification process and the 30-day storage period at 4°C.

5.5. Conclusion

During the COVID-19 pandemic, the shortage of vaccine doses exposed the limitations in production capacity and responsiveness of mRNA vaccine manufacturing processes. With the rapid advancement of RNA vaccines and therapeutics driven by the pandemic, there is an increasing demand for more efficient and scalable manufacturing platforms. In the post-pandemic era, the production of mRNA drug products (mRNA-DPs) is shifting toward high-throughput, real-time quality monitoring, and enhanced process flexibility, with continuous manufacturing and single-use technologies emerging as key enablers of this transformation.

This study developed an integrated manufacturing platform featuring continuous-flow LNP synthesis, real-time in-line monitoring of particle size and polydispersity index (PDI), and single-pass tangential flow filtration (SP-TFF) purification, enabling continuous process intensification for mRNA drug product (DP) manufacturing. By establishing real-time monitoring-feedback loops between critical quality attributes (CQAs) and operational parameters, the system effectively mitigates inter-process delays inherent in batch production, thereby enhancing real-time controllability of product specifications.

This research systematically evaluated the applicability of modular single-use assemblies (e.g., static mixers and single-pass tangential flow filtration systems) in continuous mRNA-LNP manufacturing. By integrating ready-to-use process modules with a Process Analytical Technology (PAT)-based online nano flow sizer system, an in situ real-time monitoring method for lipid nanoparticle hydrodynamic diameter (Average Size) and polydispersity index (PDI) was established for the first time. This approach significantly reduced capital investment, enhanced process flexibility and operational efficiency. The process-related residues were found to comply with the elemental impurity limits set by the International Council for Harmonisation (ICH) guideline Q3D, which outlines the acceptable levels of elemental impurities in drug products to ensure safety. The formulation demonstrated superior encapsulation efficiency

(95.5 ± 4%) with monodispersed characteristics (hydrodynamic diameter: 105 ± 6 nm; PDI: 0.1 ± 0.02), alongside stringent control of residual ethanol (0.003% ,30 ppm) and unencapsulated LNPs (<1%). mRNA integrity reached 86.2 ± 3%, while the final product maintained a stable pH of 7.0 ± 0.1, fully complying with international quality standards for mRNA-LNP drug products.

The continuous manufacturing platform developed in this work overcomes technical bottlenecks of traditional batch production, offering a rapidly scalable mRNA-LNP production solution for emergent public health demands through synergistic integration of real-time quality monitoring and modular process design.

Conclusion

This thesis presents a comprehensive exploration of the formulation, process development, and purification of mRNA-loaded lipid nanoparticles (mRNA-LNPs), aiming to establish a scalable, high-quality, and continuous manufacturing strategy. Through a series of experimental chapters, this work systematically addressed formulation optimization, process intensification, and downstream purification—each contributing unique innovations and actionable outcomes for the industrial translation of RNA therapeutics.

In **Chapter 3**, critical process parameters (CPPs)—including total flow rate (TFR), flow rate ratio (FRR), and lipid concentration—were first explored via univariate and DoE approaches. Response surface methodology (RSM) revealed a strong interaction between TFR and lipid concentration in regulating particle size. The Swirl Mixer, under optimized conditions (TFR = 110–140 mL/min, FRR = 3:1–6:1), consistently produced mRNA-LNPs with particle size of 74 ± 5 nm, PDI of 0.11 ± 0.02, and encapsulation efficiency (EE%) above 95%. These results confirmed robust parameter windows for continuous operation.

Chapter 4 evaluated various lipid structures, including ionizable lipids (e.g., ALC-0315, SM-102), helper lipids, and PEG-lipids. The optimized formulation—ALC-0315 (45 mol%), DOPE (15.9 mol%), cholesterol (37.85 mol%), and ALC-0159 (1.25 mol%)—demonstrated not only improved encapsulation (EE% ≈ 95.5%) and colloidal stability (PDI ≈ 0.1), but also superior storage stability at 4 °C for 2 months and higher transfection efficiency in preliminary cell-based assays.

Chapter 5 introduced a novel integrated continuous manufacturing platform incorporating real-time in-line monitoring via a Process Analytical Technology (PAT)-enabled nano flow cytometry system and downstream purification using single-pass tangential flow filtration (SP-TFF). The platform achieved stable product outputs: mRNA integrity of 86.2 ± 3%, residual ethanol <30 ppm, particle size 105 ± 6 nm, and unencapsulated LNPs <1%. Notably, switching from PES to regenerated cellulose membranes increased recovery to 90% after

three-step concentration, highlighting the importance of membrane selection in continuous purification.

While each chapter delivered standalone insights, the overall innovation lies in combining microfluidic synthesis, online PAT, and continuous purification into a modular, adaptable platform. Although the system does not yet meet full GMP compliance, it provides a foundational framework to support future GMP-level scale-up. The use of real-time analytics and design-of-experiments enables tighter process control, reduced batch variability, and efficient resource utilization—advancing mRNA-LNP production toward clinical readiness.

Looking ahead, future research should focus on developing novel ionizable and PEGylated lipid chemistries to enhance intracellular release efficiency and enable organ-specific targeting; expanding the scope of nucleic acid cargos to include emerging modalities such as siRNA, self-amplifying RNA (saRNA), or circular RNA (circRNA); implementing real-time adaptive control systems based on Process Analytical Technology (PAT) to realize closed-loop automation; investigating long-term stability and biodistribution in relevant in vivo models to support clinical translation; and ultimately integrating upstream microfluidic synthesis with downstream single-pass purification into a fully end-to-end continuous manufacturing system. Together, these efforts will accelerate the transition from lab-scale experimentation to real-world therapeutic application, ensuring that mRNA-based medicines become more accessible, scalable, and responsive to global health needs in the post-pandemic era.

Reference

1. Gancheva, V., *Viruses Unveiled: Comprehensive Insights into Structure, Pathogenesis, and Biotechnological Applications.* Insight into Epidemiology, 2024. **1**(1).
2. Panciroli, P., *The cowpox vaccine: a bridge between different medical systems: the case of homeopathy in Nineteenth Century Italy.* Acta Palaeomedica: International Journal of Palaeomedicine: 2, 2021, 2021: p. 125-135.
3. Tel, M.L., *COVID-19 PANDEMIC: UGANDA IN BRACKETS.* 2021.
4. Zhang, X., et al., *Synthetic Biology-Based Strategy for Nanomedicine Design.* Small Methods, 2025: p. 2401969.
5. Williams-Fegredo, T.E., *Developing strategies to enhance transfection efficiency and mitigate auto-transduction in transient lentiviral vector bioprocessing*. 2024, UCL (University College London).
6. O'Grady, J., *Enabling near real-time monitoring of phosphate in catchment areas*. 2022, Dublin City University.
7. Binzel, D.W., et al., *Thermostability, tunability, and tenacity of RNA as rubbery anionic polymeric materials in nanotechnology and nanomedicine—specific cancer targeting with undetectable toxicity.* Chemical reviews, 2021. **121**(13): p. 7398-7467.
8. Cabrera-Torrejón, D., et al., *Discovery and characterization of potent and selective SARS-CoV-2 antivirals with pan-coronavirus potential.* Departamento de Biotecnología, 2023.
9. Freeman, S., et al., *Bioink formulation and machine learning-empowered bioprinting optimization.* Frontiers in Bioengineering and Biotechnology, 2022. **10**: p. 913579.
10. Seshire, A., Y. Duan, and K. Lang, *Reaching Outer Space and Enabling the mRNA Revolution: A Critical Role of Partnerships for Successful Drug and Vaccine Development.* Public-Private-Partnerships in Drug Research and Development, 2024: p. 51-81.
11. Gereffi, G., P. Pananond, and T. Pedersen, *Resilience decoded: the role of firms, global value chains, and the state in COVID-19 medical supplies.* California Management Review, 2022. **64**(2): p. 46-70.
12. Hou, D., et al., *High-throughput sequencing-based immune repertoire study during infectious disease.* Frontiers in immunology, 2016. **7**: p. 336.

13. Malik, Y.A., *Properties of coronavirus and SARS-CoV-2.* The Malaysian journal of pathology, 2020. **42**(1): p. 3-11.
14. Yadav, D.K., N. Yadav, and S.M.P. Khurana, *Vaccines: present status and applications*, in *Animal biotechnology*. 2020, Elsevier. p. 523-542.
15. Kayser, V. and I. Ramzan, *Vaccines and vaccination: history and emerging issues.* Human vaccines & immunotherapeutics, 2021. **17**(12): p. 5255-5268.
16. Chi, W.-Y., et al., *COVID-19 vaccine update: vaccine effectiveness, SARS-CoV-2 variants, boosters, adverse effects, and immune correlates of protection.* Journal of biomedical science, 2022. **29**(1): p. 82.
17. Fazio, S., M. Vaccariello, and F. Affuso, *A Case of Adverse Reaction to Booster Dose of COVID-19 Vaccination: Could D-Dimer Elevation Suggest Increased Clotting Risk?* Health, 2022. **14**(2): p. 204-208.
18. Sabbaghi, A., et al., *Inactivation methods for whole influenza vaccine production.* Reviews in medical virology, 2019. **29**(6): p. e2074.
19. Spadaro, D. and M.L. Gullino, *Improving the efficacy of biocontrol agents against soilborne pathogens.* Crop protection, 2005. **24**(7): p. 601-613.
20. D'Amelio, E., S. Salemi, and R. D'Amelio, *Anti-infectious human vaccination in historical perspective.* International reviews of immunology, 2016. **35**(3): p. 260-290.
21. B. Carvalho, S., et al., *Downstream processing for influenza vaccines and candidates: An update.* Biotechnology and Bioengineering, 2021. **118**(8): p. 2845-2869.
22. Khoshnood, S., et al., *An overview on inactivated and live-attenuated SARS-CoV-2 vaccines.* Journal of Clinical Laboratory Analysis, 2022. **36**(5): p. e24418.
23. Solante, R., et al., *Expert review of global real-world data on COVID-19 vaccine booster effectiveness and safety during the omicron-dominant phase of the pandemic.* Expert review of vaccines, 2023. **22**(1): p. 1-16.
24. Bonam, S.R., et al., *An overview of novel adjuvants designed for improving vaccine efficacy.* Trends in pharmacological sciences, 2017. **38**(9): p. 771-793.
25. Jetha, K.L., et al., *Parenteral vaccine delivery: From basic principles to new developments*, in *Advanced Vaccination Technologies for Infectious and Chronic Diseases*. 2024, Elsevier. p. 167-205.
26. Shirley, J.L., et al., *Immune responses to viral gene therapy vectors.* Molecular Therapy, 2020. **28**(3): p. 709-722.

27. Nayak, S. and R.W. Herzog, *Progress and prospects: immune responses to viral vectors.* Gene therapy, 2010. **17**(3): p. 295-304.
28. Pulendran, B. and R. Ahmed, *Immunological mechanisms of vaccination.* Nature immunology, 2011. **12**(6): p. 509-517.
29. Travieso, T., et al., *The use of viral vectors in vaccine development.* npj Vaccines, 2022. **7**(1): p. 75.
30. Bulcha, J.T., et al., *Viral vector platforms within the gene therapy landscape.* Signal transduction and targeted therapy, 2021. **6**(1): p. 53.
31. Woolsey, C. and T.W. Geisbert, *Current state of Ebola virus vaccines: A snapshot.* PLoS pathogens, 2021. **17**(12): p. e1010078.
32. SHANMUGAM, S., et al., *EVALUATION OF ADENOVIRAL VECTOR-BASED VACCINES FOR PREVENTION OF COVID-19–AN OVERVIEW.* EVALUATION, 2022. **15**(7).
33. Tiboni, M., L. Casettari, and L. Illum, *Nasal vaccination against SARS-CoV-2: Synergistic or alternative to intramuscular vaccines?* International journal of pharmaceutics, 2021. **603**: p. 120686.
34. Chung, N.-H., et al., *Induction of Th1 and Th2 in the protection against SARS-CoV-2 through mucosal delivery of an adenovirus vaccine expressing an engineered spike protein.* Vaccine, 2022. **40**(4): p. 574-586.
35. Shen, M., et al., *Real-world effectiveness of Azvudine in hospitalized patients with COVID-19: a retrospective cohort study.* MedRxiv, 2023: p. 2023.01. 23.23284899.
36. Chavda, V.P., et al., *Adenoviral vector-based vaccine platform for COVID-19: Current status.* Vaccines, 2023. **11**(2): p. 432.
37. Al-Fattah Yahaya, A.A., et al., *Development of next generation vaccines against SARS-CoV-2 and variants of concern.* Viruses, 2023. **15**(3): p. 624.
38. Cordeiro, A.S., et al., *Nanovaccine delivery approaches and advanced delivery systems for the prevention of viral infections: from development to clinical application.* Pharmaceutics, 2021. **13**(12): p. 2091.
39. Cid, R. and J. Bolívar, *Platforms for production of protein-based vaccines: from classical to next-generation strategies.* Biomolecules, 2021. **11**(8): p. 1072.
40. Tahir ul Qamar, M., et al., *Multiepitope-based subunit vaccine design and evaluation against respiratory syncytial virus using reverse vaccinology approach.* Vaccines, 2020. **8**(2): p. 288.

41. Tsiantoulas, D., et al., *B cells and humoral immunity in atherosclerosis.* Circulation research, 2014. **114**(11): p. 1743-1756.
42. Cox, M.M., *Recombinant protein vaccines produced in insect cells.* Vaccine, 2012. **30**(10): p. 1759-1766.
43. Wang, Z.-B. and J. Xu, *Better adjuvants for better vaccines: Progress in adjuvant delivery systems, modifications, and adjuvant–antigen codelivery.* Vaccines, 2020. **8**(1): p. 128.
44. Heidary, M., et al., *A comprehensive review of the protein subunit vaccines against COVID-19.* Frontiers in microbiology, 2022. **13**: p. 927306.
45. Rando, H.M., et al., *Application of traditional vaccine development strategies to SARS-CoV-2.* Msystems, 2023. **8**(2): p. e00927-22.
46. Bellamkonda, N., et al., *Immune response to SARS-CoV-2 vaccines.* Biomedicines, 2022. **10**(7): p. 1464.
47. Hotez, P.J. and M.E. Bottazzi, *Whole inactivated virus and protein-based COVID-19 vaccines.* Annual Review of Medicine, 2022. **73**(1): p. 55-64.
48. Josefsberg, J.O. and B. Buckland, *Vaccine process technology.* Biotechnology and bioengineering, 2012. **109**(6): p. 1443-1460.
49. AboulFotouh, K., Z. Cui, and R.O. Williams, *Next-generation COVID-19 vaccines should take efficiency of distribution into consideration.* Aaps Pharmscitech, 2021. **22**: p. 1-15.
50. Reed, S.G., M.T. Orr, and C.B. Fox, *Key roles of adjuvants in modern vaccines.* Nature medicine, 2013. **19**(12): p. 1597-1608.
51. Liu, H.F., et al. *Recovery and purification process development for monoclonal antibody production*. in *MAbs*. 2010. Taylor & Francis.
52. Cameroni, E., et al., *Broadly neutralizing antibodies overcome SARS-CoV-2 Omicron antigenic shift.* Nature, 2022. **602**(7898): p. 664-670.
53. Lee, S. and M.T. Nguyen, *Recent advances of vaccine adjuvants for infectious diseases.* Immune network, 2015. **15**(2): p. 51.
54. Polatoğlu, I., et al., *COVID-19 in early 2023: Structure, replication mechanism, variants of SARS-CoV-2, diagnostic tests, and vaccine & drug development studies.* MedComm, 2023. **4**(2): p. e228.
55. Vartak, A. and S.J. Sucheck, *Recent advances in subunit vaccine carriers.* Vaccines, 2016. **4**(2): p. 12.
56. Wang, Y., et al., *mRNA vaccine: a potential therapeutic strategy.* Molecular cancer, 2021. **20**(1): p. 33.

57. Chen, D. and D. Kristensen, *Opportunities and challenges of developing thermostable vaccines.* Expert review of vaccines, 2009. **8**(5): p. 547-557.
58. Wang, J., et al., *Quantifying the RNA cap epitranscriptome reveals novel caps in cellular and viral RNA.* Nucleic acids research, 2019. **47**(20): p. e130-e130.
59. Hussain, A., et al., *mRNA vaccines for COVID-19 and diverse diseases.* Journal of Controlled Release, 2022. **345**: p. 314-333.
60. Chaudhry, D. and K. Waqar, *A Review on the Advancements in COVID-19 Treatments and Vaccines.* 2020.
61. Conti, R.M., S. Hall, and A. Metzger, *The Determinants of COVID-19 Vaccine Development Success.* 2021.
62. Haghmorad, D., et al., *mRNA vaccine platforms: linking infectious disease prevention and cancer immunotherapy.* Frontiers in Bioengineering and Biotechnology, 2025. **13**: p. 1547025.
63. den Haan, J.M., R. Arens, and M.C. van Zelm, *The activation of the adaptive immune system: cross-talk between antigen-presenting cells, T cells and B cells.* Immunology letters, 2014. **162**(2): p. 103-112.
64. Fang, Z., et al., *Application of bioreactor technology for cell culture-based viral vaccine production: Present status and future prospects.* Frontiers in Bioengineering and Biotechnology, 2022. **10**: p. 921755.
65. Pardi, N., et al., *mRNA vaccines—a new era in vaccinology.* Nature reviews Drug discovery, 2018. **17**(4): p. 261-279.
66. Mueller, S., *mRNA Vaccine Safety and Efficacy—Official Criteria When AEs Are Caused by the Injection*, in *Challenges and Opportunities of mRNA Vaccines Against SARS-CoV-2: A Multidisciplinary Perspective*. 2022, Springer. p. 227-271.
67. Wei, Z., et al., *Technological breakthroughs and advancements in the application of mRNA vaccines: a comprehensive exploration and future prospects.* Frontiers in Immunology, 2025. **16**: p. 1524317.
68. Sayour, E.J., et al., *Cancer mRNA vaccines: clinical advances and future opportunities.* Nature Reviews Clinical Oncology, 2024. **21**(7): p. 489-500.
69. Huang, X., et al., *Personalized pancreatic cancer therapy: from the perspective of mRNA vaccine.* Military Medical Research, 2022. **9**(1): p. 53.
70. Park, J.W., et al., *mRNA vaccines for COVID-19: what, why and how.* Int J Biol Sci, 2021. **17**(6): p. 1446-1460.

71. Jakubek, Z.J., et al., *Lipid Nanoparticle and Liposome Reference Materials: Assessment of Size Homogeneity and Long-Term −70 °C and 4 °C Storage Stability.* Langmuir, 2023. **39**(7): p. 2509-2519.
72. Sarkis, M., et al., *Emerging Challenges and Opportunities in Pharmaceutical Manufacturing and Distribution.* Processes, 2021. **9**(3): p. 457.
73. Tregoning, J.S. and N.N. Sanders, *The past, present, and future of RNA vaccines.* Molecular Therapy.
74. Silva-Pilipich, N., et al., *Self-Amplifying RNA: A Second Revolution of mRNA Vaccines against COVID-19.* Vaccines, 2024. **12**(3): p. 318.
75. Tang, J., et al., *Nanotechnologies in Delivery of DNA and mRNA Vaccines to the Nasal and Pulmonary Mucosa.* Nanomaterials, 2022. **12**(2): p. 226.
76. Seyfoori, A., et al., *Emerging Advances of Nanotechnology in Drug and Vaccine Delivery against Viral Associated Respiratory Infectious Diseases (VARID).* International Journal of Molecular Sciences, 2021. **22**(13): p. 6937.
77. Cojocaru, E., O.R. Petriș, and C. Cojocaru, *Nanoparticle-Based Drug Delivery Systems in Inhaled Therapy: Improving Respiratory Medicine.* Pharmaceuticals, 2024. **17**(8): p. 1059.
78. Vemula, S.V. and S.K. and Mittal, *Production of adenovirus vectors and their use as a delivery system for influenza vaccines.* Expert Opinion on Biological Therapy, 2010. **10**(10): p. 1469-1487.
79. Shurtleff, A.C., et al., *The Impact of Regulations, Safety Considerations and Physical Limitations on Research Progress at Maximum Biocontainment.* Viruses, 2012. **4**(12): p. 3932-3951.
80. Wallace, R., C.M. Bliss, and A.L. Parker, *The Immune System—A Double-Edged Sword for Adenovirus-Based Therapies.* Viruses, 2024. **16**(6): p. 973.
81. Hengelbrock, A., A. Schmidt, and J. Strube, *Formulation of Nucleic Acids by Encapsulation in Lipid Nanoparticles for Continuous Production of mRNA.* Processes, 2023. **11**(6): p. 1718.
82. Li, H., et al., *Applications of genome editing technology in the targeted therapy of human diseases: mechanisms, advances and prospects.* Signal Transduction and Targeted Therapy, 2020. **5**(1): p. 1.
83. Da Silva Sanchez, A., et al., *Treating Cystic Fibrosis with mRNA and CRISPR.* Human Gene Therapy, 2020. **31**(17-18): p. 940-955.
84. Weng, Y., et al., *Improved Nucleic Acid Therapy with Advanced Nanoscale Biotechnology.* Molecular Therapy Nucleic Acids, 2020. **19**: p. 581-601.

85. Moccia, M., et al., *Advances in Nucleic Acid Research: Exploring the Potential of Oligonucleotides for Therapeutic Applications and Biological Studies.* International Journal of Molecular Sciences, 2024. **25**(1): p. 146.
86. Chen, L., et al., *Recent progress in targeted delivery vectors based on biomimetic nanoparticles.* Signal Transduction and Targeted Therapy, 2021. **6**(1): p. 225.
87. Tamura, R. and M. Toda, *Historic Overview of Genetic Engineering Technologies for Human Gene Therapy.* Neurologia medico-chirurgica, 2020. **60**(10): p. 483-491.
88. Lee, C.S., et al., *Adenovirus-mediated gene delivery: Potential applications for gene and cell-based therapies in the new era of personalized medicine.* Genes & Diseases, 2017. **4**(2): p. 43-63.
89. Shao, L., et al., *Genome-wide profiling of retroviral DNA integration and its effect on clinical pre-infusion CAR T-cell products.* Journal of Translational Medicine, 2022. **20**(1): p. 514.
90. Pearn, M.L., et al., *Pathophysiology Associated with Traumatic Brain Injury: Current Treatments and Potential Novel Therapeutics.* Cellular and Molecular Neurobiology, 2017. **37**(4): p. 571-585.
91. Nidetz, N.F., et al., *Adeno-associated viral vector-mediated immune responses: Understanding barriers to gene delivery.* Pharmacology & Therapeutics, 2020. **207**: p. 107453.
92. Wang, D., F. Zhang, and G. Gao, *CRISPR-Based Therapeutic Genome Editing: Strategies and In Vivo Delivery by AAV Vectors.* Cell, 2020. **181**(1): p. 136-150.
93. DiStasio, N., *Development of a Targeted, Non-Viral, and Anti-Inflammatory Gene Therapy for Atherosclerosis*. 2021, McGill University (Canada): Canada -- Quebec, CA. p. 255.
94. Bishop, C.J., K.L. Kozielski, and J.J. Green, *Exploring the role of polymer structure on intracellular nucleic acid delivery via polymeric nanoparticles.* Journal of Controlled Release, 2015. **219**: p. 488-499.
95. Guidi, L., M.G. Cascone, and E. Rosellini, *Light-responsive polymeric nanoparticles for retinal drug delivery: design cues, challenges and future perspectives.* Heliyon, 2024. **10**(5).

96. Zhou, L., et al., *Designing Synthetic Polymers for Nucleic Acid Complexation and Delivery: From Polyplexes to Micelleplexes to Triggered Degradation.* Biomacromolecules, 2022. **23**(10): p. 4029-4040.
97. Pylaev, T., E. Avdeeva, and N. Khlebtsov, *Plasmonic nanoparticles and nucleic acids hybrids for targeted gene delivery, bioimaging, and molecular recognition.* Journal of Innovative Optical Health Sciences, 2021. **14**(04): p. 2130003.
98. Deivayanai, V.C., et al., *A comprehensive review on advances in nanoparticle-mediated cancer therapeutics: Current research and future perspectives.* Cancer Pathogenesis and Therapy.
99. Schlich, M., et al., *Cytosolic delivery of nucleic acids: The case of ionizable lipid nanoparticles.* Bioengineering & Translational Medicine, 2021. **6**(2): p. e10213.
100. Eygeris, Y., et al., *Chemistry of Lipid Nanoparticles for RNA Delivery.* Accounts of Chemical Research, 2022. **55**(1): p. 2-12.
101. Suzuki, Y. and H. Ishihara, *Difference in the lipid nanoparticle technology employed in three approved siRNA (Patisiran) and mRNA (COVID-19 vaccine) drugs.* Drug Metabolism and Pharmacokinetics, 2021. **41**: p. 100424.
102. Kumar, M., et al., *Micro and nano-carriers-based pulmonary drug delivery system: Their current updates, challenges, and limitations – A review.* JCIS Open, 2023. **12**: p. 100095.
103. Kumar, N., et al., *Therapeutic potential of extracellular vesicles derived from human amniotic epithelial cells for perinatal cerebral and pulmonary injury.* Stem Cells Translational Medicine, 2024. **13**(8): p. 711-723.
104. Kulkarni, J.A., et al., *Lipid Nanoparticle Technology for Clinical Translation of siRNA Therapeutics.* Accounts of Chemical Research, 2019. **52**(9): p. 2435-2444.
105. Kulkarni, J.A., et al., *The current landscape of nucleic acid therapeutics.* Nature Nanotechnology, 2021. **16**(6): p. 630-643.
106. Liu, P., G. Chen, and J. Zhang, *A Review of Liposomes as a Drug Delivery System: Current Status of Approved Products, Regulatory Environments, and Future Perspectives.* Molecules, 2022. **27**(4): p. 1372.
107. Nguyen, J. and F.C. Szoka, *Nucleic Acid Delivery: The Missing Pieces of the Puzzle?* Accounts of Chemical Research, 2012. **45**(7): p. 1153-1162.
108. Ewert, K.K., et al., *Cationic Liposomes as Vectors for Nucleic Acid and Hydrophobic Drug Therapeutics.* Pharmaceutics, 2021. **13**(9): p. 1365.

109. Cheng, X. and R.J. Lee, *The role of helper lipids in lipid nanoparticles (LNPs) designed for oligonucleotide delivery.* Advanced Drug Delivery Reviews, 2016. **99**: p. 129-137.
110. Damase, T.R., et al., *The limitless future of RNA therapeutics.* Frontiers in bioengineering and biotechnology, 2021. **9**: p. 628137.
111. Duggan, S.T. and G.M. Keating, *Pegylated liposomal doxorubicin: a review of its use in metastatic breast cancer, ovarian cancer, multiple myeloma and AIDS-related Kaposi's sarcoma.* Drugs, 2011. **71**: p. 2531-2558.
112. Hermosilla, J., et al., *Analysing the in-use Stability of mRNA-LNP COVID-19 vaccines Comirnaty™(Pfizer) and Spikevax™(Moderna): a comparative study of the particulate.* Vaccines, 2023. **11**(11): p. 1635.
113. Arcturus'versatile, R., T. Ultragenyx, and S.G. CureVac, *Arcturus—a clinical-stage mRNA therapeutics and vaccines company.*
114. Gillmore, J.D., et al., *CRISPR-Cas9 in vivo gene editing for transthyretin amyloidosis.* New England Journal of Medicine, 2021. **385**(6): p. 493-502.
115. Kauffman, K.J., *Optimization and analysis of lipid nanoparticles for in vivo mRNA delivery*. 2017, Massachusetts Institute of Technology.
116. Xie, W. and G. Pedrielli. *From discovery to production: challenges and novel methodologies for next generation biomanufacturing*. in *2022 Winter Simulation Conference (WSC)*. 2022. IEEE.
117. Ouranidis, A., et al., *mRNA therapeutic modalities design, formulation and manufacturing under pharma 4.0 principles.* Biomedicines, 2021. **10**(1): p. 50.
118. Wang, X., J. Zhou, and W. Wang, *Reconstituted high density lipoprotein-based nanoparticles: an overview of applications in regenerative medicine, preparation, evaluation and future trends.* Current pharmaceutical design, 2015. **21**(12): p. 1529-1544.
119. Fu, L., et al., *'Passive'nanoparticles for organ-selective systemic delivery: design, mechanism and perspective.* Chemical Society Reviews, 2023. **52**(21): p. 7579-7601.
120. Wang, C., et al., *Investigation of endosome and lysosome biology by ultra pH-sensitive nanoprobes.* Advanced drug delivery reviews, 2017. **113**: p. 87-96.
121. Patel, P., N.M. Ibrahim, and K. Cheng, *The importance of apparent pKa in the development of nanoparticles encapsulating siRNA and mRNA.* Trends in pharmacological sciences, 2021. **42**(6): p. 448-460.

122. Dong, Y., et al., *DNA functional materials assembled from branched DNA: design, synthesis, and applications.* Chemical Reviews, 2020. **120**(17): p. 9420-9481.
123. Ginjupalli, K., et al., *Poly (α-hydroxy acid) based polymers: A review on material and degradation aspects.* Polymer Degradation and Stability, 2017. **144**: p. 520-535.
124. Kang, D.D., et al., *Engineering LNPs with polysarcosine lipids for mRNA delivery.* Bioactive Materials, 2024. **37**: p. 86-93.
125. Sarode, A., et al., *Predictive high-throughput screening of PEGylated lipids in oligonucleotide-loaded lipid nanoparticles for neuronal gene silencing.* Nanoscale Advances, 2022. **4**(9): p. 2107-2123.
126. Zhang, J., et al., *Interaction of cholesterol-conjugated ionizable amino lipids with biomembranes: lipid polymorphism, structure–activity relationship, and implications for siRNA delivery.* Langmuir, 2011. **27**(15): p. 9473-9483.
127. Chen, Z., et al., *Synergistic integration of mRNA-LNP with CAR-engineered immune cells: Pioneering progress in immunotherapy.* Molecular Therapy, 2024. **32**(11): p. 3772-3792.
128. Pena, S.A., et al., *Gene therapy for neurological disorders: challenges and recent advancements.* Journal of drug targeting, 2020. **28**(2): p. 111-128.
129. Matalanis, A., O.G. Jones, and D.J. McClements, *Structured biopolymer-based delivery systems for encapsulation, protection, and release of lipophilic compounds.* Food hydrocolloids, 2011. **25**(8): p. 1865-1880.
130. Wang, Z., et al., *Natural product evodiamine-inspired medicinal chemistry: Anticancer activity, structural optimization and structure-activity relationship.* European journal of medicinal chemistry, 2023. **247**: p. 115031.
131. Liu, S., et al., *Membrane-destabilizing ionizable phospholipids for organ-selective mRNA delivery and CRISPR–Cas gene editing.* Nature materials, 2021. **20**(5): p. 701-710.
132. Álvarez-Benedicto, E., et al., *Optimization of phospholipid chemistry for improved lipid nanoparticle (LNP) delivery of messenger RNA (mRNA).* Biomaterials science, 2022. **10**(2): p. 549-559.
133. Nikzade, V., M.M. Tehrani, and M. Saadatmand-Tarzjan, *Optimization of low-cholesterol–low-fat mayonnaise formulation: Effect of using soy milk and some stabilizer by a mixture design approach.* Food Hydrocolloids, 2012. **28**(2): p. 344-352.

134. Paunovska, K., et al., *Nanoparticles containing oxidized cholesterol deliver mRNA to the liver microenvironment at clinically relevant doses.* Advanced materials, 2019. **31**(14): p. 1807748.
135. Iravani, S. and R.S. Varma, *Plant-derived edible nanoparticles and miRNAs: emerging frontier for therapeutics and targeted drug-delivery.* ACS Sustainable Chemistry & Engineering, 2019. **7**(9): p. 8055-8069.
136. Zhang, Y., et al., *Lipids and lipid derivatives for RNA delivery.* Chemical reviews, 2021. **121**(20): p. 12181-12277.
137. Lu, J., et al. *Advanced strategies to evade the mononuclear phagocyte system clearance of nanomaterials*. in *Exploration*. 2023. Wiley Online Library.
138. Holick, C.T., et al., *Poly (2-ethyl-2-oxazoline)(POx) as Poly (ethylene glycol)(PEG)-Lipid Substitute for Lipid Nanoparticle Formulations.* Small, 2025: p. 2411354.
139. Gao, J., et al., *Overcoming barriers for intra-articular delivery of disease-modifying osteoarthritis drugs.* Trends in pharmacological sciences, 2022. **43**(3): p. 171-187.
140. Ibrahim, M., et al., *Polyethylene glycol (PEG): The nature, immunogenicity, and role in the hypersensitivity of PEGylated products.* Journal of Controlled Release, 2022. **351**: p. 215-230.
141. Stewart, M.P., R. Langer, and K.F. Jensen, *Intracellular delivery by membrane disruption: mechanisms, strategies, and concepts.* Chemical reviews, 2018. **118**(16): p. 7409-7531.
142. Browning, K.S. and J. Bailey-Serres, *Mechanism of cytoplasmic mRNA translation.* The Arabidopsis book/American Society of Plant Biologists, 2015. **13**: p. e0176.
143. Daniel, S., et al., *Quality by Design for enabling RNA platform production processes.* Trends in biotechnology, 2022. **40**(10): p. 1213-1228.
144. Yuan, Y., et al., *Intelligent Design of Lipid Nanoparticles for Enhanced Gene Therapeutics.* Molecular Pharmaceutics, 2025.
145. Rebollo, R., et al., *Microfluidic Manufacturing of Liposomes: Development and Optimization by Design of Experiment and Machine Learning.* ACS Applied Materials & Interfaces, 2022. **14**(35): p. 39736-39745.
146. Nag, O.K., et al., *Nanoparticle-Mediated Visualization and Control of Cellular Membrane Potential: Strategies, Progress, and Remaining Issues.* ACS Nano, 2020. **14**(3): p. 2659-2677.

147. Filion, M.C. and N.C. Phillips, *Toxicity and immunomodulatory activity of liposomal vectors formulated with cationic lipids toward immune effector cells.* Biochimica et Biophysica Acta (BBA) - Biomembranes, 1997. **1329**(2): p. 345-356.
148. Rinoldi, C., et al., *Nanotechnology-Assisted RNA Delivery: From Nucleic Acid Therapeutics to COVID-19 Vaccines.* Small Methods, 2021. **5**(9): p. 2100402.
149. Rampado, R. and D. Peer, *Design of experiments in the optimization of nanoparticle-based drug delivery systems.* Journal of Controlled Release, 2023. **358**: p. 398-419.
150. Ramadan, E., A. Ahmed, and Y.W. Naguib, *Advances in mRNA LNP-Based Cancer Vaccines: Mechanisms, Formulation Aspects, Challenges, and Future Directions.* Journal of Personalized Medicine, 2024. **14**(11): p. 1092.
151. Trollmann, M.F.W. and R.A. Böckmann, *mRNA lipid nanoparticle phase transition.* Biophysical Journal, 2022. **121**(20): p. 3927-3939.
152. Zhao, Y., et al., *Progressive Macromolecular Self-Assembly: From Biomimetic Chemistry to Bio-Inspired Materials.* Advanced Materials, 2013. **25**(37): p. 5215-5256.
153. Xu, Y., et al., *AGILE platform: a deep learning powered approach to accelerate LNP development for mRNA delivery.* Nature Communications, 2024. **15**(1): p. 6305.
154. Chen, W., C. Li, and X. Jiang, *Advanced Biomaterials with Intrinsic Immunomodulation Effects for Cancer Immunotherapy.* Small Methods, 2023. **7**(5): p. 2201404.
155. Liu, B., et al., *Modification of liposomes: preparation, purpose, methods and the application in food.* International Journal of Food Science and Technology, 2024. **59**(6): p. 3523-3536.
156. Yang, F., et al., *Optimization of critical parameters for coating of polymeric nanoparticles with plasma membrane vesicles by sonication.* Scientific Reports, 2021. **11**(1): p. 23996.
157. Abdellatif, A.A.H. and A.F. Alsowinea, *Approved and marketed nanoparticles for disease targeting and applications in COVID-19.* Nanotechnology Reviews, 2021. **10**(1): p. 1941-1977.
158. Baeyens, J., et al., *Challenges and opportunities in improving the production of bio-ethanol.* Progress in Energy and Combustion Science, 2015. **47**: p. 60-88.

159. Szoka, F. and D. Papahadjopoulos, *Procedure for preparation of liposomes with large internal aqueous space and high capture by reverse-phase evaporation.* Proceedings of the National Academy of Sciences, 1978. **75**(9): p. 4194-4198.
160. Raza, F., et al., *A Review on Recent Advances in Stabilizing Peptides/Proteins upon Fabrication in Hydrogels from Biodegradable Polymers.* Pharmaceutics, 2018. **10**(1): p. 16.
161. Chakraborty, D. and S. Chakraborty, *Microfluidic Transport and Micro-scale Flow Physics: An Overview*, in *Microfluidics and Microfabrication*, S. Chakraborty, Editor. 2010, Springer US: Boston, MA. p. 1-85.
162. Sarma, P. and P.K. Patowari, *A Review on Fluid Flow and Mixing in Microchannel and their Design and Manufacture for Microfluidic Applications.* Micro and Nanosystems, 2023. **15**(3): p. 167-184.
163. Celikkin, N., et al., *Tackling Current Biomedical Challenges With Frontier Biofabrication and Organ-On-A-Chip Technologies.* Frontiers in Bioengineering and Biotechnology, 2021. **Volume 9 - 2021**.
164. Liu, J., et al., *Research Strategies for Precise Manipulation of Micro/Nanoparticle Drug Delivery Systems Using Microfluidic Technology: A Review.* Pharmaceutical Fronts, 2024. **06**(02): p. e69-e100.
165. Wang, J.-T., J. Wang, and J.-J. Han, *Fabrication of Advanced Particles and Particle-Based Materials Assisted by Droplet-Based Microfluidics.* Small, 2011. **7**(13): p. 1728-1754.
166. Mandal, B., et al., *Core–shell-type lipid–polymer hybrid nanoparticles as a drug delivery platform.* Nanomedicine: Nanotechnology, Biology and Medicine, 2013. **9**(4): p. 474-491.
167. Sato, T., et al., *Real-Time Quantitative Evaluation of a Drug during Liposome Preparation Using a Probe-Type Raman Spectrometer.* Langmuir, 2024. **40**(15): p. 7962-7973.
168. Haghighi, E., et al., *Navigating the intricate in-vivo journey of lipid nanoparticles tailored for the targeted delivery of RNA therapeutics: a quality-by-design approach.* Journal of Nanobiotechnology, 2024. **22**(1): p. 710.
169. Ouranidis, A., et al., *mRNA Therapeutic Modalities Design, Formulation and Manufacturing under Pharma 4.0 Principles.* Biomedicines, 2022. **10**(1): p. 50.
170. Krammer, F., *SARS-CoV-2 vaccines in development.* Nature, 2020. **586**(7830): p. 516-527.

171. Warminski, M., et al., *Chemical Modifications of mRNA Ends for Therapeutic Applications.* Accounts of Chemical Research, 2023. **56**(20): p. 2814-2826.
172. Fu, J., et al., *Emerging Progress of RNA-Based Antitumor Therapeutics.* Int J Biol Sci, 2023. **19**(10): p. 3159-3183.
173. Shi, C., et al., *Process development and optimization of continuous capture with three-column periodic counter-current chromatography.* Biotechnology and Bioengineering, 2021. **118**(9): p. 3313-3322.
174. Curry, E., et al., *Engineering an Escherichia coli based in vivo mRNA manufacturing platform.* Biotechnology and Bioengineering, 2024. **121**(6): p. 1912-1926.
175. Ding, C., et al., *Process design of a fully integrated continuous biopharmaceutical process using economic and ecological impact assessment.* Biotechnology and Bioengineering, 2022. **119**(12): p. 3567-3583.
176. Shiea, M., et al., *Numerical Methods for the Solution of Population Balance Equations Coupled with Computational Fluid Dynamics.* Annual Review of Chemical and Biomolecular Engineering, 2020. **11**(Volume 11, 2020): p. 339-366.
177. Kaufmann, J. and T.M. Rupp, *Impact of Impurities on the Quality and Safety of Oligonucleotides as Drug Substances*, in *Sustainability in Tides Chemistry: Green Approaches to Oligonucleotides and Oligopeptides Synthesis*, A. Tolomelli, L. Ferrazzano, and W. Cabri, Editors. 2024, Royal Society of Chemistry. p. 0.
178. Agrawal, P., et al., *A Review of Tangential Flow Filtration: Process Development and Applications in the Pharmaceutical Industry.* Organic Process Research & Development, 2023. **27**(4): p. 571-591.
179. Vargas, R., et al., *Dialysis is a key factor modulating interactions between critical process parameters during the microfluidic preparation of lipid nanoparticles.* Colloid and Interface Science Communications, 2023. **54**: p. 100709.
180. Wadhwa, A., et al., *Opportunities and Challenges in the Delivery of mRNA-Based Vaccines.* Pharmaceutics, 2020. **12**(2): p. 102.
181. Edeling, M.A., et al., *Development of Methods to Produce SARS CoV-2 Virus-Like Particles at Scale.* Biotechnology and Bioengineering. **n/a**(n/a).

182. John, R., et al., *Chemistry and Art of Developing Lipid Nanoparticles for Biologics Delivery: Focus on Development and Scale-Up.* Pharmaceutics, 2024. **16**(1): p. 131.
183. Schmidt, A., A. Hengelbrock, and J. Strube, *Continuous biomanufacturing in upstream and downstream processing.* Physical Sciences Reviews, 2024. **9**(10): p. 3167-3222.
184. Tomeh, M.A., et al., *Optimization of large-scale manufacturing of biopolymeric and lipid nanoparticles using microfluidic swirl mixers.* International Journal of Pharmaceutics, 2022. **620**: p. 121762.
185. Shapiro, H.M., *Optical measurements in cytometry: light scattering, extinction, absorption, and fluorescence.* Methods in cell biology, 2001. **63**: p. 107-129.
186. Ghaemmaghamian, Z., et al., *Stabilizing vaccines via drying: Quality by design considerations.* Advanced Drug Delivery Reviews, 2022. **187**: p. 114313.
187. Gray, O., T. McCance, and D. Brown, *Exploring how key performance indicators influence nursing and midwifery practice: A mixed‐methods study.* Journal of Advanced Nursing, 2021. **77**(12): p. 4900-4918.
188. Rawal, M., A. Singh, and M.M. Amiji, *Quality-by-design concepts to improve nanotechnology-based drug development.* Pharmaceutical research, 2019. **36**(11): p. 153.
189. Balasubramaniam, L., et al., *Impact of cross-sectional geometry on mixing performance of spiral microfluidic channels characterized by swirling strength of Dean-vortices.* Journal of Micromechanics and Microengineering, 2017. **27**(9): p. 095016.
190. Zhang, J., S. Xu, and W. Li, *High shear mixers: A review of typical applications and studies on power draw, flow pattern, energy dissipation and transfer properties.* Chemical Engineering and Processing: Process Intensification, 2012. **57**: p. 25-41.
191. Välikangas, T., et al., *Fin-and-tube heat exchanger enhancement with a combined herringbone and vortex generator design.* International Journal of Heat and Mass Transfer, 2018. **118**: p. 602-616.
192. Wiese, M., et al., *3D MRI velocimetry of non-transparent 3D-printed staggered herringbone mixers.* Chemical engineering journal, 2018. **343**: p. 54-60.
193. Wang, S., et al., *Geometry design of herringbone structures for cancer cell capture in a microfluidic device.* Microfluidics and Nanofluidics, 2016. **20**: p. 1-11.

194. Li, C., et al., *Effect of swirling addition on the liquid mixing performance in a T-jets mixer.* Chinese Journal of Chemical Engineering, 2022. **50**: p. 108-116.
195. De, A. and Y.T. Ko, *Why mRNA-ionizable LNPs formulations are so short-lived: causes and way-out.* Expert Opinion on Drug Delivery, 2023. **20**(2): p. 175-187.
196. Gurba-Bryśkiewicz, L., et al., *Quality by design (QbD) and design of experiments (DOE) as a strategy for tuning lipid nanoparticle formulations for RNA delivery.* Biomedicines, 2023. **11**(10): p. 2752.
197. Parot, J., et al., *Quality assessment of LNP-RNA therapeutics with orthogonal analytical techniques.* Journal of Controlled Release, 2024. **367**: p. 385-401.
198. Kumari, A., G. Aggarwal, and A. Kaur, *Applications of quality by design in pharmaceutical product development lifecycle*, in *Introduction to Quality by Design (QbD) From Theory to Practice*. 2024, Springer. p. 419-453.
199. Rouchi, M.B., et al., *Application of infrared spectroscopy as Process Analytics Technology (PAT) approach in biodiesel production process utilizing Multivariate Curve Resolution Alternative Least Square (MCR-ALS).* Spectrochimica Acta Part A: Molecular and Biomolecular Spectroscopy, 2019. **213**: p. 347-353.
200. Youssef, M., et al., *Enabling mRNA therapeutics: Current landscape and challenges in manufacturing.* Biomolecules, 2023. **13**(10): p. 1497.
201. Shen, Y., H. Gwak, and B. Han, *Advanced manufacturing of nanoparticle formulations of drugs and biologics using microfluidics.* Analyst, 2024. **149**(3): p. 614-637.
202. Bak, A., et al., *Roadmap to discovery and early development of an mRNA loaded LNP formulation for liver therapeutic genome editing.* Expert Opinion on Drug Delivery, 2025(just-accepted).
203. Schürz, M., et al., *EVAnalyzer: High content imaging for rigorous characterisation of single extracellular vesicles using standard laboratory equipment and a new open‐source ImageJ/Fiji plugin.* Journal of Extracellular Vesicles, 2022. **11**(12): p. 12282.
204. Conniot, J., et al., *Cancer immunotherapy: nanodelivery approaches for immune cell targeting and tracking.* Frontiers in chemistry, 2014. **2**: p. 105.
205. Cunha, S., et al., *Using the quality by design (QbD) approach to optimize formulations of lipid nanoparticles and nanoemulsions: A review.* Nanomedicine: Nanotechnology, Biology and Medicine, 2020. **28**: p. 102206.

206. Ly, H.H., et al., *Optimization of lipid nanoparticles for saRNA expression and cellular activation using a design-of-experiment approach.* Molecular Pharmaceutics, 2022. **19**(6): p. 1892-1905.
207. Camacho, D.D., et al., *Applications of additive manufacturing in the construction industry–A forward-looking review.* Automation in construction, 2018. **89**: p. 110-119.
208. Walde, P. and S. Ichikawa, *Lipid vesicles and other polymolecular aggregates—from basic studies of polar lipids to innovative applications.* Applied Sciences, 2021. **11**(21): p. 10345.
209. Pei, Y., et al., *Synthesis and bioactivity of readily hydrolysable novel cationic lipids for potential lung delivery application of mRNAs.* Chemistry and physics of lipids, 2022. **243**: p. 105178.
210. Schaaf, T.M., et al., *Spectral unmixing plate reader: high-throughput, high-precision FRET assays in living cells.* SLAS Discovery: Advancing Life Sciences R&D, 2017. **22**(3): p. 250-261.
211. Zheng, L., et al., *Lipid nanoparticle topology regulates endosomal escape and delivery of RNA to the cytoplasm.* Proceedings of the National Academy of Sciences, 2023. **120**(27): p. e2301067120.
212. Albertsen, C.H., et al., *The role of lipid components in lipid nanoparticles for vaccines and gene therapy.* Advanced drug delivery reviews, 2022. **188**: p. 114416.
213. Anitescu, G. and T.J. Bruno, *Liquid biofuels: Fluid properties to optimize feedstock selection, processing, refining/blending, storage/transportation, and combustion.* Energy & fuels, 2012. **26**(1): p. 324-348.
214. Sun, D. and Z.-R. Lu, *Structure and function of cationic and ionizable lipids for nucleic acid delivery.* Pharmaceutical research, 2023. **40**(1): p. 27-46.
215. Vhora, I., et al., *Lipid-nucleic acid nanoparticles of novel ionizable lipids for systemic BMP-9 gene delivery to bone-marrow mesenchymal stem cells for osteoinduction.* International journal of pharmaceutics, 2019. **563**: p. 324-336.
216. Whitley, J., et al., *Development of mRNA manufacturing for vaccines and therapeutics: mRNA platform requirements and development of a scalable production process to support early phase clinical trials.* Translational Research, 2022. **242**: p. 38-55.

217. Mehta, M., et al., *Lipid-based nanoparticles for drug/gene delivery: an overview of the production techniques and difficulties encountered in their industrial development.* ACS Materials Au, 2023. **3**(6): p. 600-619.
218. Ochoa-Sánchez, C., et al., *Brief Comparison of the Efficacy of Cationic and Anionic Liposomes as Nonviral Delivery Systems.* ACS omega, 2024. **9**(47): p. 46664-46678.
219. Algarni, A., et al., *In vivo delivery of plasmid DNA by lipid nanoparticles: the influence of ionizable cationic lipids on organ-selective gene expression.* Biomaterials Science, 2022. **10**(11): p. 2940-2952.
220. Battista, S., *Preparation and physicochemical characterization of novel mixed liposomes for medical applications.* 2019.
221. Hubbe, M.A., et al., *Self-assembly of alkyl chains of fatty acids in papermaking systems: a review of related pitch issues, hydrophobic sizing, and pH effects.* BioResources, 2020. **15**(2): p. 4591.
222. Musumeci, T., A. Bonaccorso, and C. Carbone, *Chapter 2 - Basic concepts of liposomes: Components, structures, properties and classification*, in *Liposomes in Drug Delivery*, S.G. Antimisiaris, Editor. 2024, Academic Press. p. 19-48.
223. Shepherd, S.J., D. Issadore, and M.J. Mitchell, *Microfluidic formulation of nanoparticles for biomedical applications.* Biomaterials, 2021. **274**: p. 120826.
224. Kansız, S. and Y.M. Elçin, *Advanced liposome and polymersome-based drug delivery systems: Considerations for physicochemical properties, targeting strategies and stimuli-sensitive approaches.* Advances in Colloid and Interface Science, 2023. **317**: p. 102930.
225. Nikolova, M.P., E.M. Kumar, and M.S. Chavali, *Updates on Responsive Drug Delivery Based on Liposome Vehicles for Cancer Treatment.* Pharmaceutics, 2022. **14**(10): p. 2195.
226. Bulbake, U., et al., *Liposomal Formulations in Clinical Use: An Updated Review.* Pharmaceutics, 2017. **9**(2): p. 12.
227. Maqbool, F., et al., *Dispersibility of phospholipids and their optimization for the efficient production of liposomes using supercritical fluid technology.* International Journal of Pharmaceutics, 2019. **563**: p. 174-183.
228. Tenchov, R., J.M. Sasso, and Q.A. Zhou, *PEGylated Lipid Nanoparticle Formulations: Immunological Safety and Efficiency Perspective.* Bioconjugate Chemistry, 2023. **34**(6): p. 941-960.

229. Kafle, U., et al., *Development of Thermally Stable mRNA-LNP Delivery Systems: Current Progress and Future Prospects.* Molecular Pharmaceutics, 2024. **21**(12): p. 5944-5959.
230. Michel, O., et al., *Development of Stable, Maleimide-Functionalized Peptidoliposomes Against SARS-CoV-2.* International Journal of Molecular Sciences, 2025. **26**(4): p. 1629.
231. Wei, P.-S., et al., *Enhancing RNA-lipid nanoparticle delivery: Organ- and cell-specificity and barcoding strategies.* Journal of Controlled Release, 2024. **375**: p. 366-388.
232. Chen, S., et al., *Influence of particle size on the in vivo potency of lipid nanoparticle formulations of siRNA.* Journal of Controlled Release, 2016. **235**: p. 236-244.
233. Jia, Y., et al., *Lipid Nanoparticles Optimized for Targeting and Release of Nucleic Acid.* Advanced Materials, 2024. **36**(4): p. 2305300.
234. Soroudi, S., M.R. Jaafari, and L. Arabi, *Lipid nanoparticle (LNP) mediated mRNA delivery in cardiovascular diseases: Advances in genome editing and CAR T cell therapy.* Journal of Controlled Release, 2024. **372**: p. 113-140.
235. Kumar, R., et al., *Ligand conjugated lipid-based nanocarriers for cancer theranostics.* Biotechnology and Bioengineering, 2022. **119**(11): p. 3022-3043.
236. Khalili, L., et al., *Smart active-targeting of lipid-polymer hybrid nanoparticles for therapeutic applications: Recent advances and challenges.* International Journal of Biological Macromolecules, 2022. **213**: p. 166-194.
237. Binici, B., et al., *Exploring the impact of commonly used ionizable and pegylated lipids on mRNA-LNPs: A combined in vitro and preclinical perspective.* Journal of Controlled Release, 2025. **377**: p. 162-173.
238. Asfiya, R., et al., *Physio-chemical Modifications to Re-engineer Small Extracellular Vesicles for Targeted Anticancer Therapeutics Delivery and Imaging.* ACS Biomaterials Science & Engineering, 2024. **10**(2): p. 697-722.
239. Nikita, S., et al., *Advances in bioreactor control for production of biotherapeutic products.* Biotechnology and Bioengineering, 2023. **120**(5): p. 1189-1214.
240. Webb, C., et al., *Current Status and Future Perspectives on MRNA Drug Manufacturing.* Molecular Pharmaceutics, 2022. **19**(4): p. 1047-1058.
241. Yu, M., et al., *Microfluidics for Formulation and Scale-Up Production of Nanoparticles for Biopharma Industry*, in *Microfluidics in Pharmaceutical Sciences: Formulation, Drug Delivery, Screening, and Diagnostics*, D.A.

Lamprou and E. Weaver, Editors. 2024, Springer Nature Switzerland: Cham. p. 395-420.

242. Ragheb, R. and U. Nobbmann, *Multiple scattering effects on intercept, size, polydispersity index, and intensity for parallel (VV) and perpendicular (VH) polarization detection in photon correlation spectroscopy.* Scientific Reports, 2020. **10**(1): p. 21768.
243. Mildner, R., et al., *Improved multidetector asymmetrical-flow field-flow fractionation method for particle sizing and concentration measurements of lipid-based nanocarriers for RNA delivery.* European Journal of Pharmaceutics and Biopharmaceutics, 2021. **163**: p. 252-265.
244. Caputo, F., et al., *Measuring Particle Size Distribution by Asymmetric Flow Field Flow Fractionation: A Powerful Method for the Preclinical Characterization of Lipid-Based Nanoparticles.* Molecular Pharmaceutics, 2019. **16**(2): p. 756-767.
245. Yang, M., et al., *Mixing performance and continuous production of nanomaterials in an advanced-flow reactor.* Chemical Engineering Journal, 2021. **412**: p. 128565.
246. Simon, L.L., et al., *Assessment of Recent Process Analytical Technology (PAT) Trends: A Multiauthor Review.* Organic Process Research & Development, 2015. **19**(1): p. 3-62.
247. Wang, L. and R.A. Hoffman, *Standardization, Calibration, and Control in Flow Cytometry.* Current Protocols in Cytometry, 2017. **79**(1): p. 1.3.1-1.3.27.
248. Liu, S., et al., *Bioinspired Supramolecular Catalysts from Designed Self-Assembly of DNA or Peptides.* ACS Catalysis, 2020. **10**(24): p. 14937-14958.
249. Kattel, K. and J.D. Clogston, *A Static Headspace Gas Chromatography Method for Quantitation of Residual Solvents in Nanoformulations*, in *Characterization of Nanoparticles Intended for Drug Delivery*, J.D. Clogston, et al., Editors. 2024, Springer US: New York, NY. p. 75-83.
250. Bi, D., et al., *On the Influence of Fabrication Methods and Materials for mRNA-LNP Production: From Size and Morphology to Internal Structure and mRNA Delivery Performance In Vitro and In Vivo.* Advanced Healthcare Materials, 2024. **13**(26): p. 2401252.
251. Boggs, J.M., *Effect of lipid structural modifications on their intermolecular hydrogen bonding interactions and membrane functions.* Biochemistry and Cell Biology, 1986. **64**(1): p. 50-57.

252. Messerian, K.O., et al., *Characterization and associated pressure-dependent behavior of deposits formed during sterile filtration of mRNA-Lipid nanoparticles.* Journal of Membrane Science, 2023. **684**: p. 121896.
253. Rathore, A.S., et al., *Control of Continuous Manufacturing Processes for Production of Monoclonal Antibodies*, in *Process Control, Intensification, and Digitalisation in Continuous Biomanufacturing*. 2022. p. 39-74.
254. Karki, R., et al., *Synergism of TNF-α and IFN-γ Triggers Inflammatory Cell Death, Tissue Damage, and Mortality in SARS-CoV-2 Infection and Cytokine Shock Syndromes.* Cell, 2021. **184**(1): p. 149-168.e17.
255. Simonsen, J.B., *A perspective on bleb and empty LNP structures.* Journal of Controlled Release, 2024. **373**: p. 952-961.
256. Zheng, T. and S. Cai, *Recent technical advances in cellular cryo-electron tomography.* The International Journal of Biochemistry & Cell Biology, 2024. **175**: p. 106648.
257. Beard, W.A. and S.H. Wilson, *Structure and Mechanism of DNA Polymerase β.* Chemical Reviews, 2006. **106**(2): p. 361-382.
258. Pardeshi, S.R., et al., *Process development and quality attributes for the freeze-drying process in pharmaceuticals, biopharmaceuticals and nanomedicine delivery: a state-of-the-art review.* Future Journal of Pharmaceutical Sciences, 2023. **9**(1): p. 99.
259. Kumar, S., et al., *Application of lyophilization in pharmaceutical injectable formulations: An industry and regulatory perspective.* Journal of Drug Delivery Science and Technology, 2024. **100**: p. 106089.

Appendix

Fig 25 T-mixer Total Flow Rate, Flow Rate Ratio and Formulation Concentration Experiment Particle Size Distribution Raw file

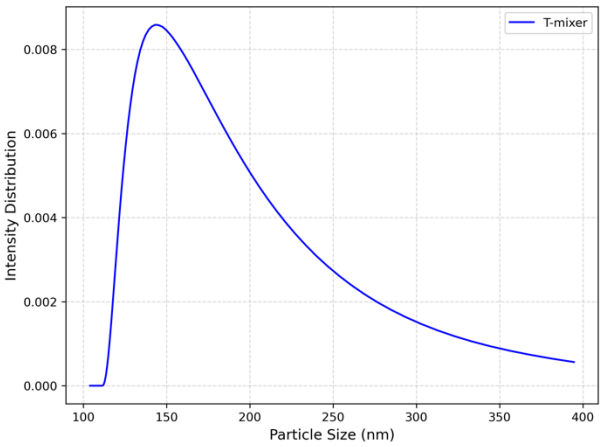

Total Flow Rate 1 mL/min

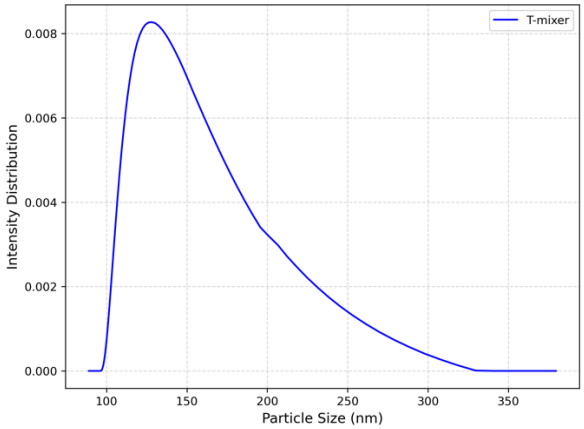

Total Flow Rate 2 mL/min

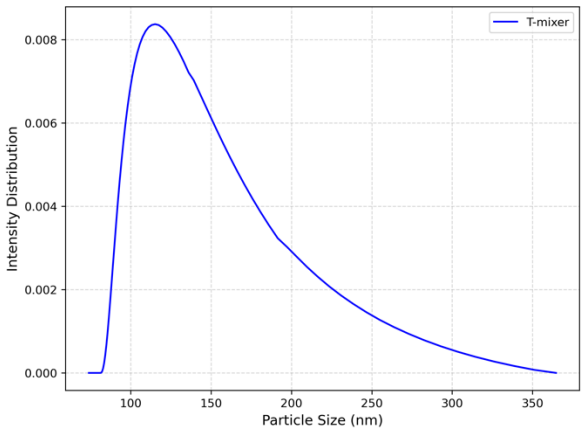

Total Flow Rate 4 mL/min

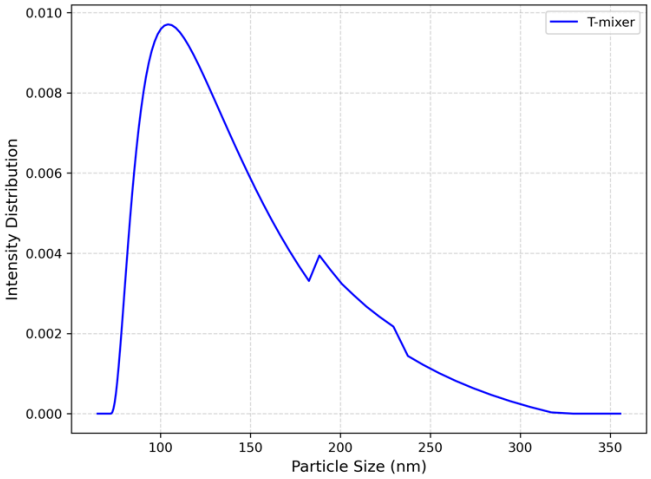

Total Flow Rate 6 mL/min

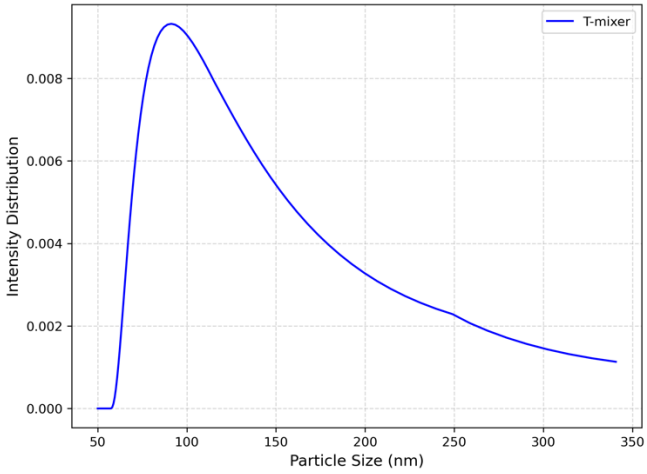

Total Flow Rate 8 mL/min

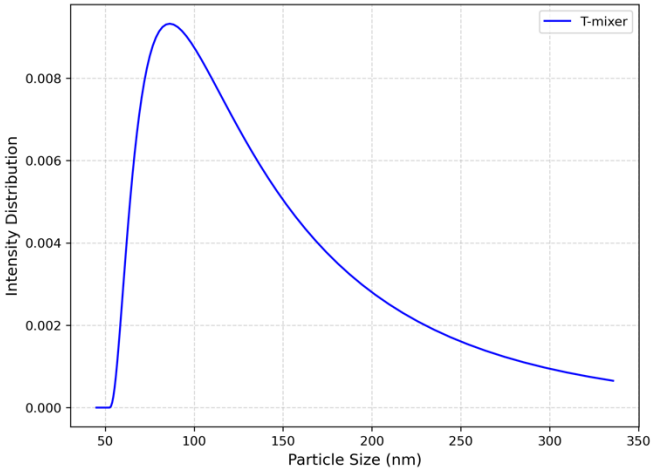

Total Flow Rate 10 mL/min

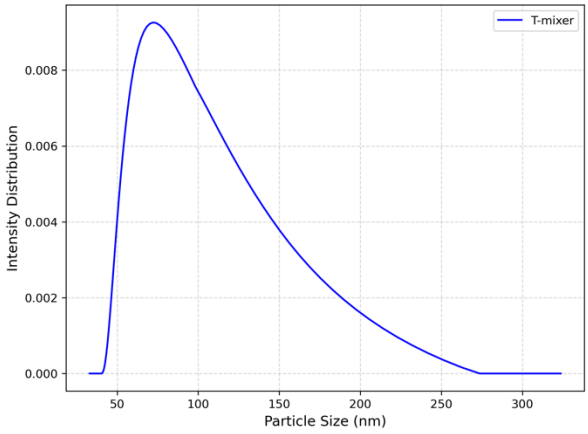

Total Flow Rate 12 mL/min

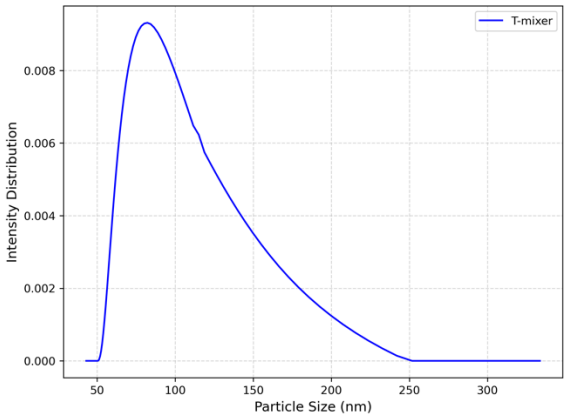

Total Flow Rate 16 mL/min

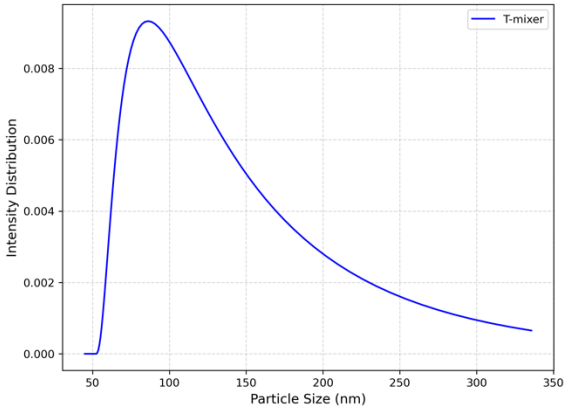

Total Flow Rate 18 mL/min

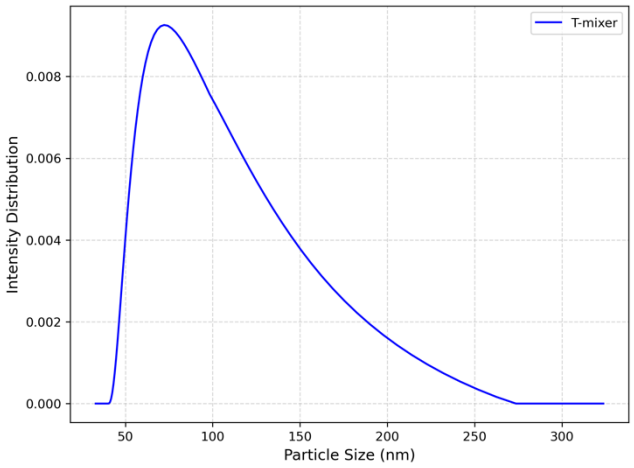

Total Flow Rate 26 mL/min

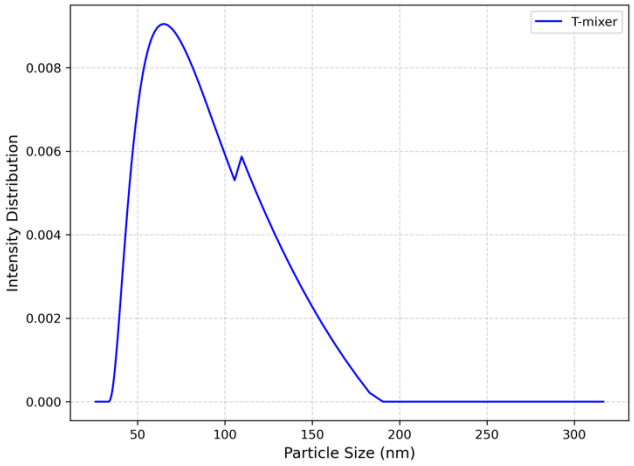

T-mixer			Size (nm)			PDI			EE%		
Total Flow Rate (mL/min)	Flow Rate Ratio	Lipids Concentration (mg)	MEAN	SD	N	Mean	SD	N	MEAN	SD	N
1	3:1	16	156	15	3	0.41	0.12	3	92	5	3
2	3:1	16	132	11	3	0.34	0.1	3	94	4	3
4	3:1	16	98	9	3	0.23	0.08	3	90	4	3
6	3:1	16	85	5	4	0.19	0.05	4	88	5	3
8	3:1	16	78	4	4	0.18	0.04	4	91	3	3
10	3:1	16	74	4	4	0.17	0.04	4	89	4	3
12	3:1	16	76	3	3	0.16	0.03	3	87	2	3
16	3:1	16	73	4	3	0.16	0.04	3	87	2	3
18	3:1	16	69	5	3	0.18	0.04	3	84	3	3
26	3:1	16	62	5	3	0.2	0.04	3	80	3	3

Total Flow Rate Data

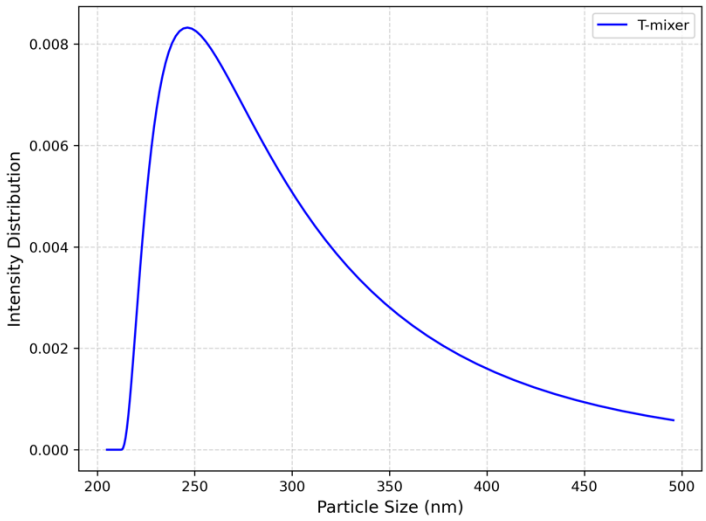

Flow Rate Ratio 1:1

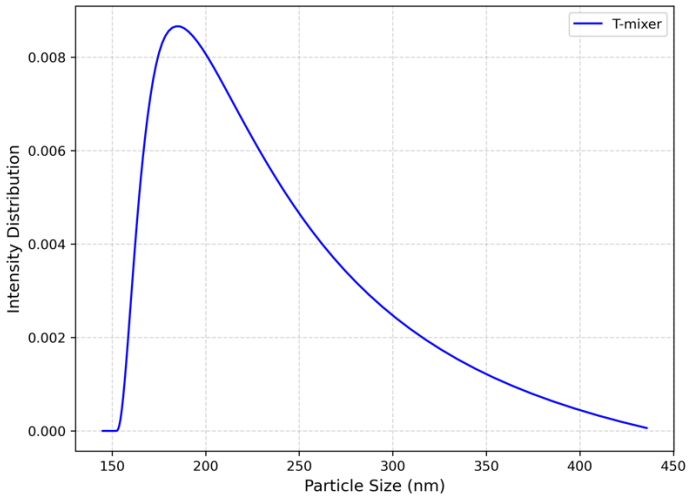

Flow Rate Ratio 2:1

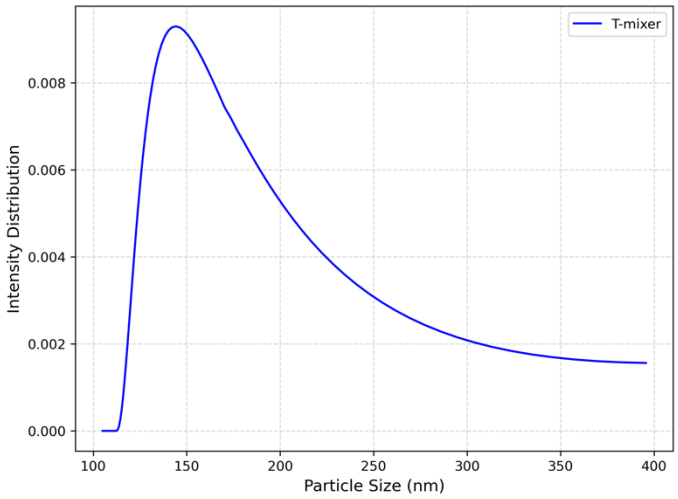

Flow Rate Ratio 3:1

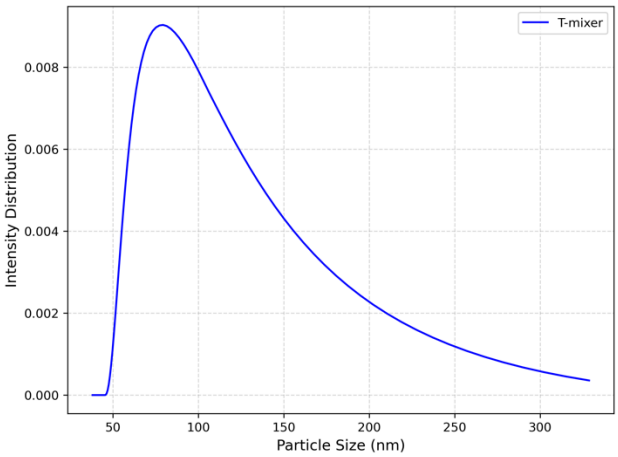

Flow Rate Ratio 4:1

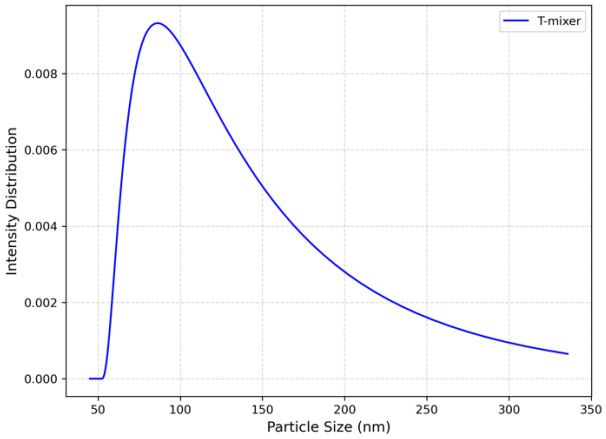

Flow Rate Ratio 6:1

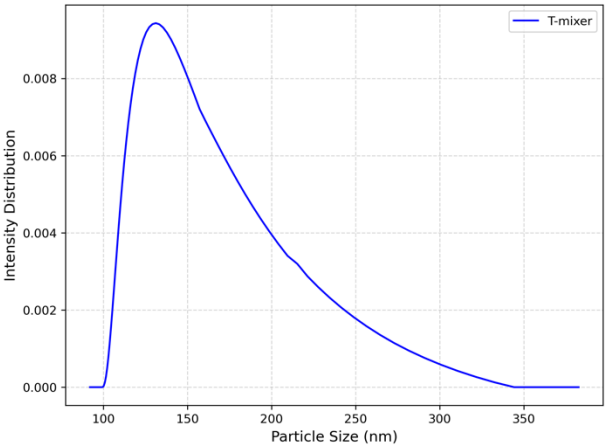

Flow Rate Ratio 9:1

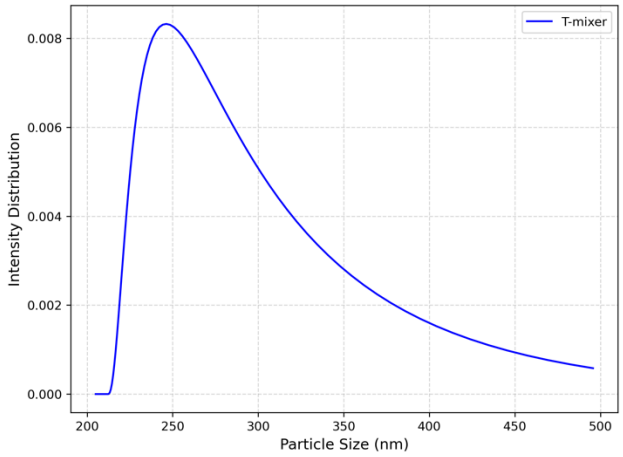

Flow Rate Ratio 20:1

T-mixer			Size (nm)			PDI			EE%		
Total Flow Rate (mL/min)	Flow Rate Ratio	Lipids Concentration (mg)	MEAN	SD	N	Mean	SD	N	MEAN	SD	N
16	1:1	16	190	18	3	0.39	0.1	3	43	4	3
16	2:1	16	151	10	3	0.167	0.03	3	65	3	3
16	3:1	16	73	4	3	0.16	0.04	3	87	2	3
16	4:1	16	74	4	3	0.14	0.03	3	86	3	3
16	6:1	16	88	6	3	0.17	0.04	3	88	4	3
16	9:1	16	133	8	3	0.23	0.05	3	92	6	3
16	20:1	16	257	16	3	0.3	0.07	3	87	5	3

Flow Rate Ratio Data

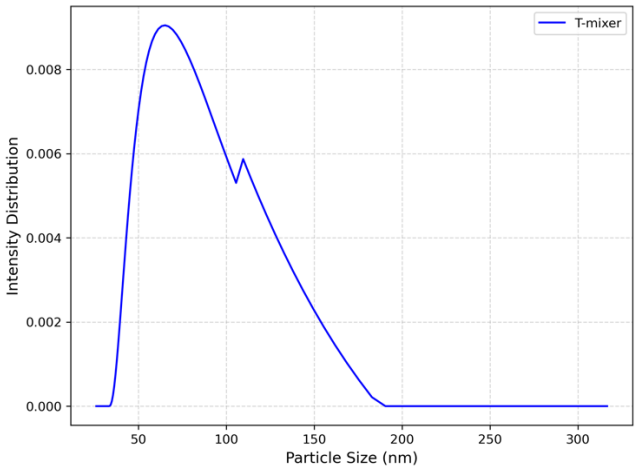

Lipids Concentration 1 (mg)

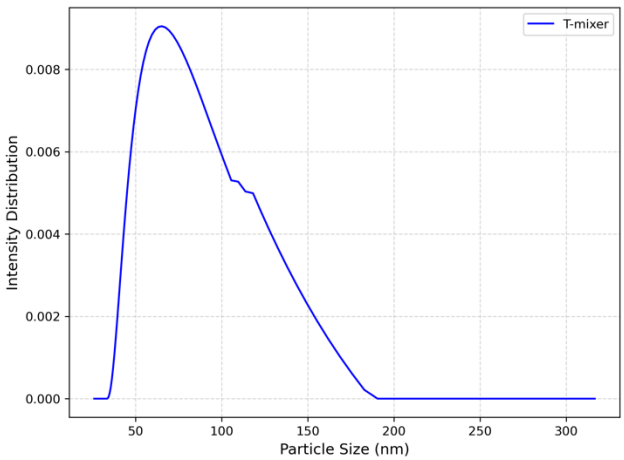

Lipids Concentration 2 (mg)

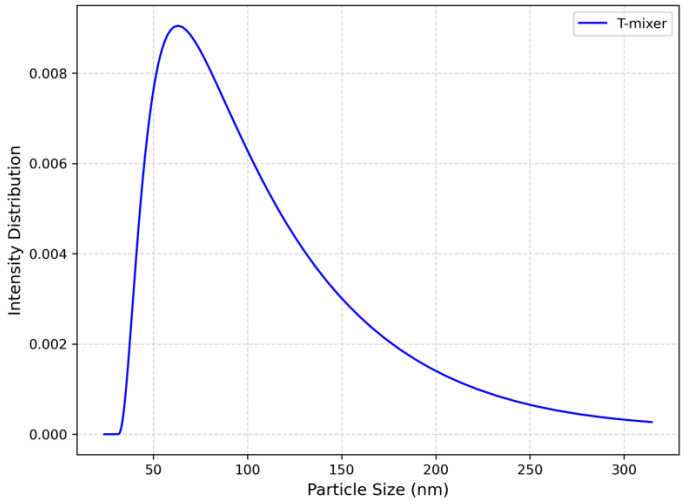

Lipids Concentration 4 (mg)

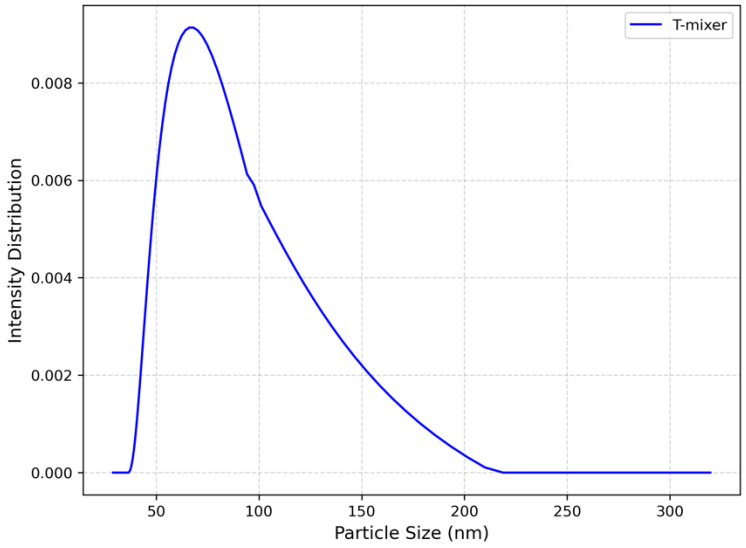

Lipids Concentration 16 (mg)

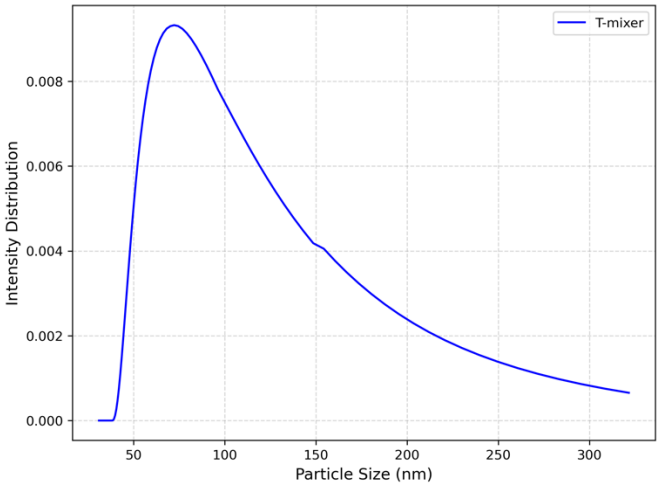

Lipids Concentration 20 (mg)

T-mixer			Size (nm)			PDI			EE%		
Total Flow Rate (mL/min)	Flow Rate Ratio	Lipids Concentration (mg)	MEAN	SD	N	Mean	SD	N	MEAN	SD	N
16	3: 1	1	53	4	3	0.22	0.03	3	68	5	3
16	3: 1	2	60	3	3	0.16	0.03	3	70	6	3
16	3: 1	4	62	4	3	0.17	0.02	3	84	2	3
16	3: 1	10	67	5	3	0.19	0.03	3	87	3	3
16	3: 1	16	73	4	3	0.16	0.04	3	87	2	3
16	3: 1	20	94	7	3	0.29	0.03	3	86	6	3

Lipids Concentration Data

Fig 26 T-mixer PEG-lipid%, Lipids: Cholesterol and N/P ratio

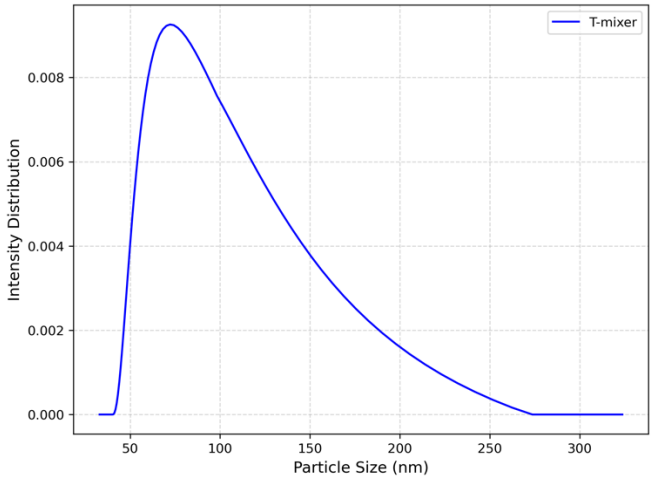

PEG-lipids 1.5%

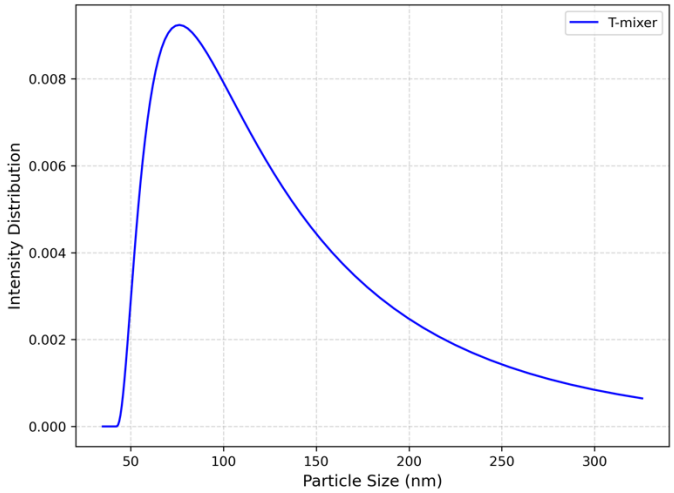

PEG-lipids 5%

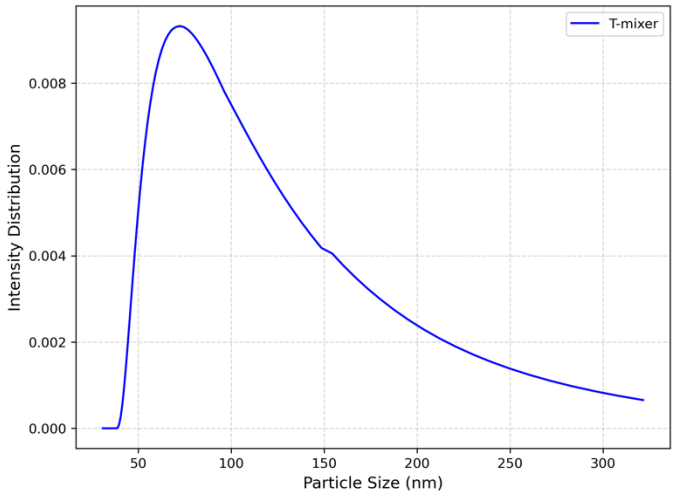

PEG-lipids 10%

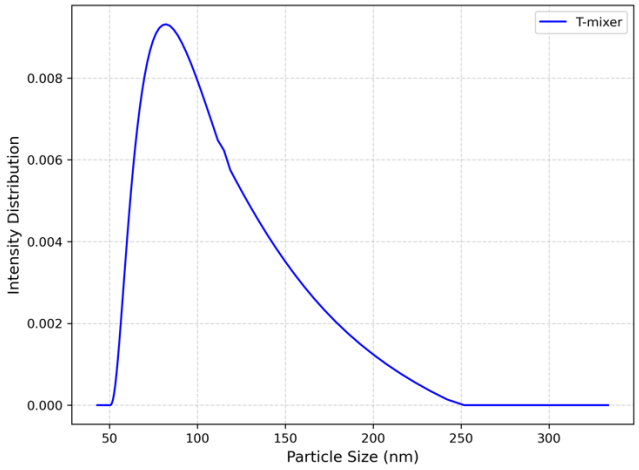

PEG-lipids 15%

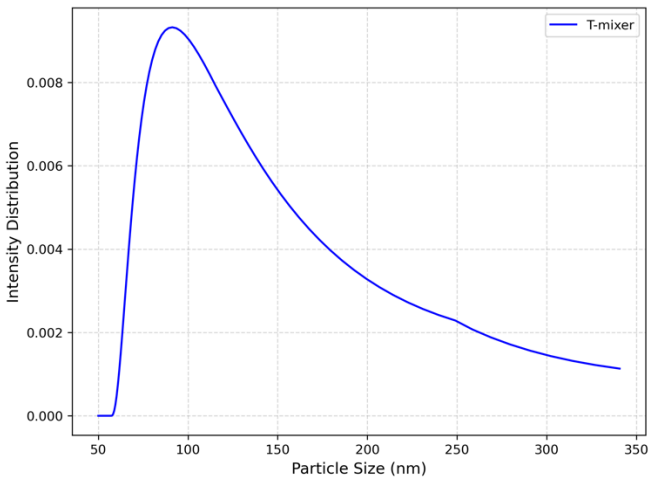

PEG-lipids 20%

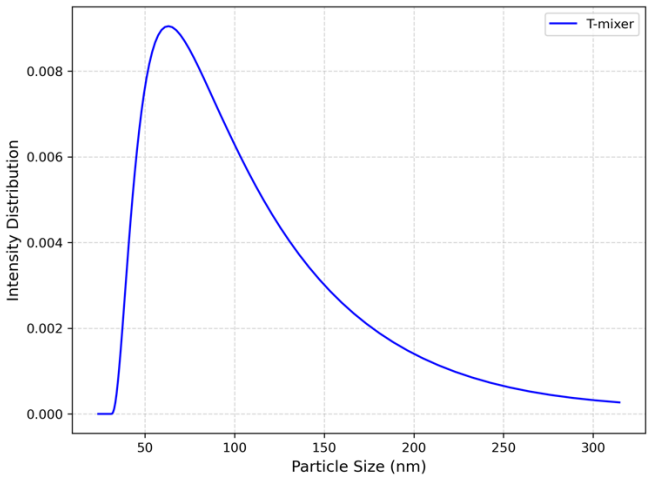

Lipids: Chol 1:1

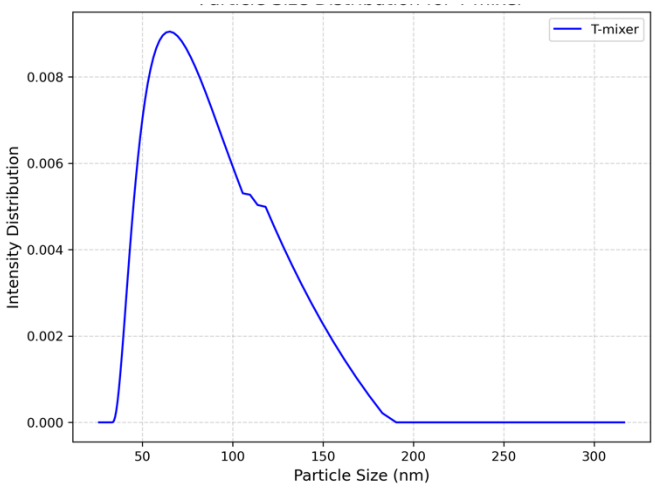

Lipids: Chol 1.5:1

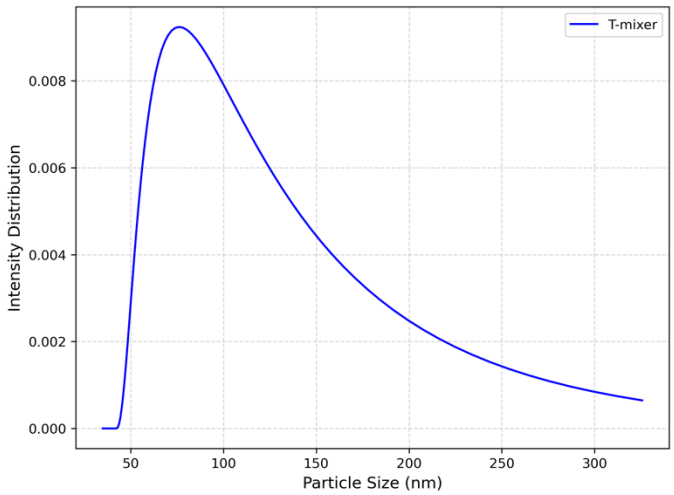

Lipids: Chol 2:1

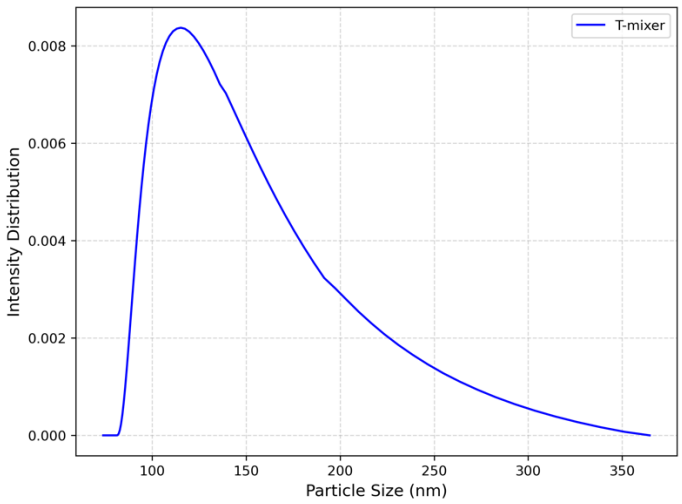

Lipids: Chol 4:1

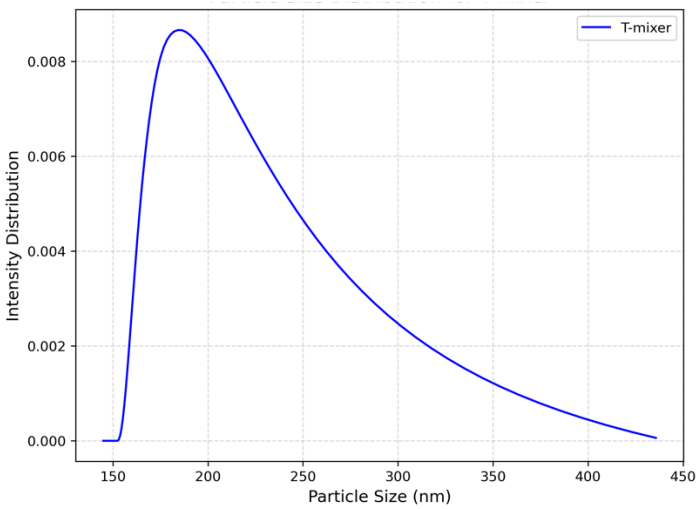

Lipids: Chol 9:1

T-mixer			Size (nm)			PDI			EE%		
PEG-Lipids	Lipids: Cholesterol	N/P Ratio	MEAN	SD	N	Mean	SD	N	MEAN	SD	N
1.5%	1: 1	6: 1	48	5	3	0.18	0.05	3	54	4	3
1.5%	3: 2	6: 1	57	4	3	0.16	0.03	3	87	2	3
1.5%	2: 1	6: 1	62	4	3	0.16	0.04	3	88	3	3
1.5%	4: 1	6: 1	123	9	3	0.26	0.06	3	78	5	3
1.5%	9: 1	6: 1	236	10	3	0.3	0.09	3	66	4	3

Lipids: Cholesterol Data Summary

Fig 27 Swirl Mixer Total Flow Rate, Flow Rate Ratio and Formulation Concentration Experiment Particle Size Distribution Raw file

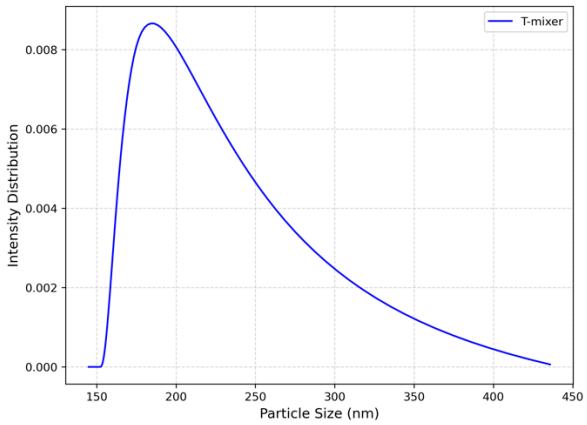

Total Flow Rate 28 mL/min

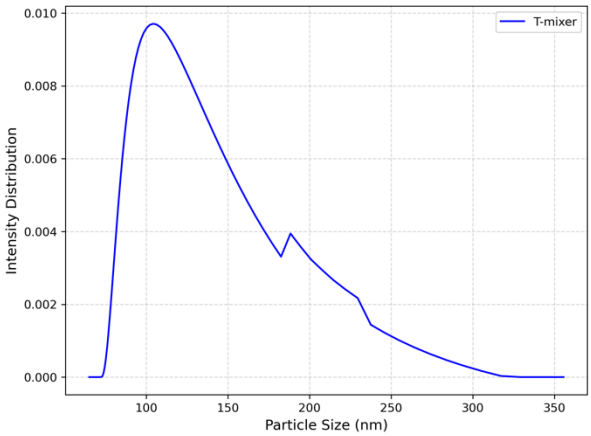

Total Flow Rate 40 mL/min

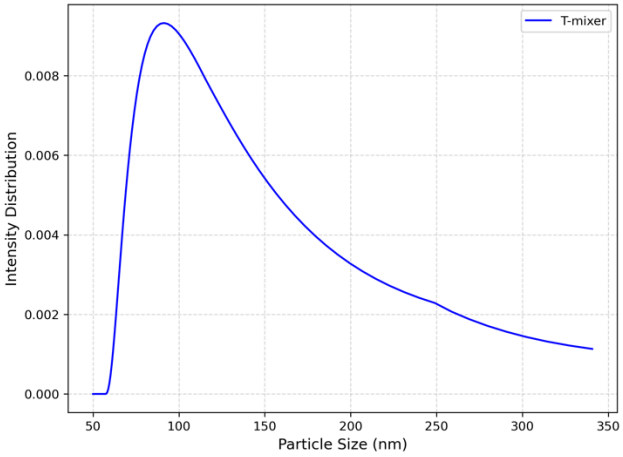

Total Flow Rate 60 mL/min

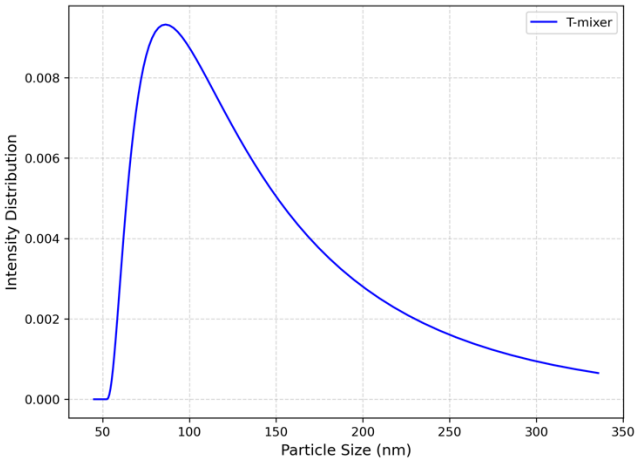

Total Flow Rate 80 mL/min

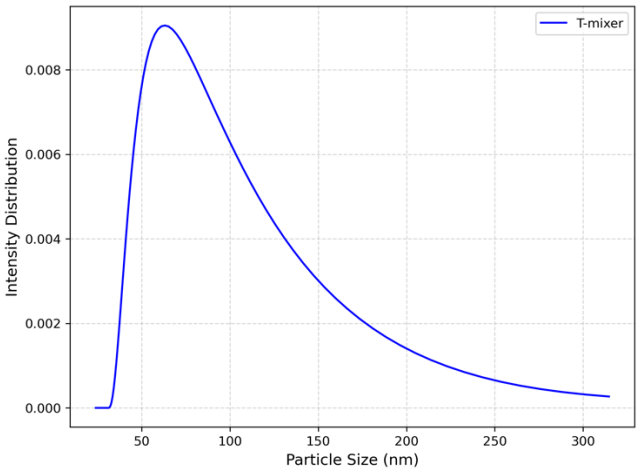

Total Flow Rate 100 mL/min

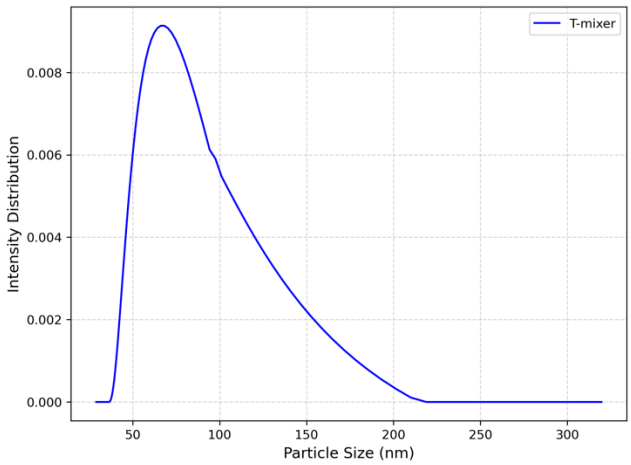

Total Flow Rate 120 mL/min

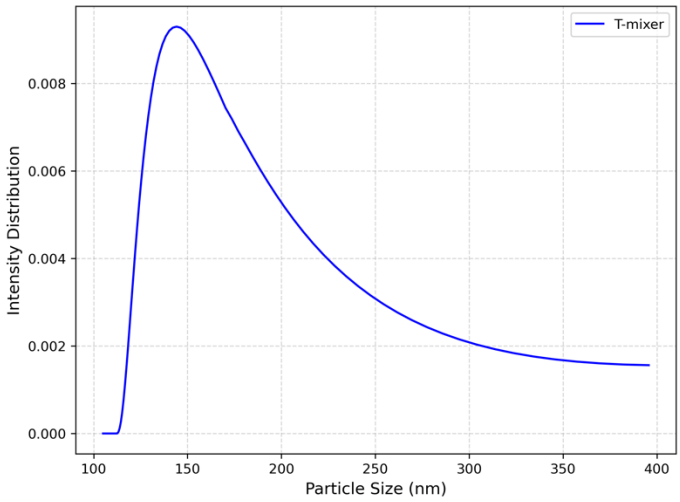

Flow Rate Ratio 1: 1

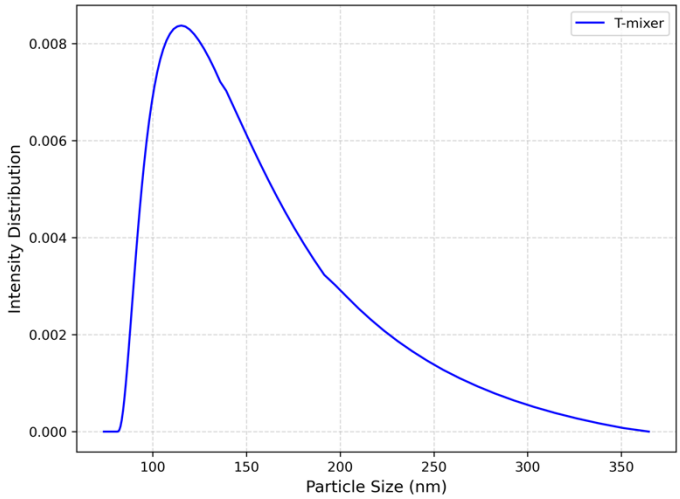

Flow Rate Ratio 2: 1

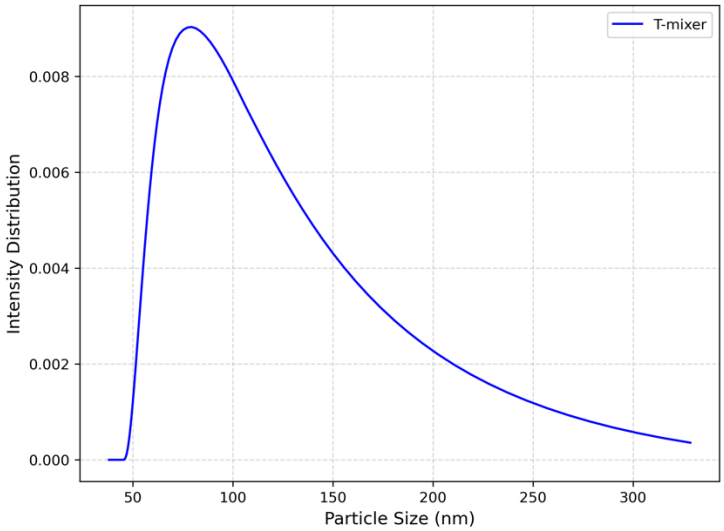

Flow Rate Ratio 3: 1

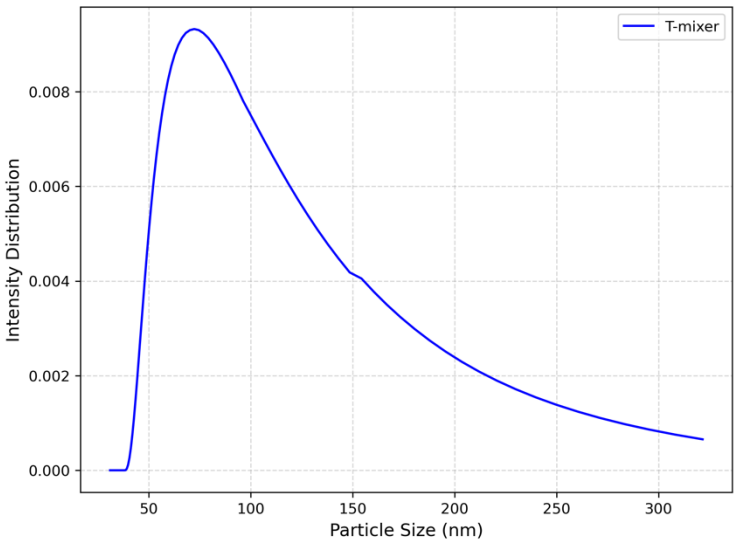

Flow Rate Ratio 4: 1

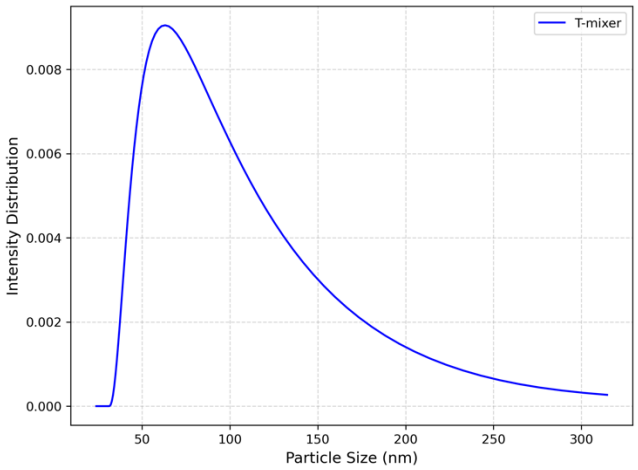

Flow Rate Ratio 6: 1

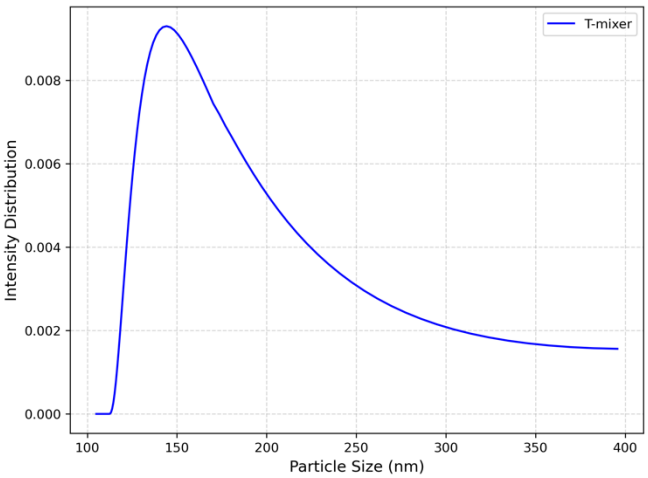

Flow Rate Ratio 9: 1

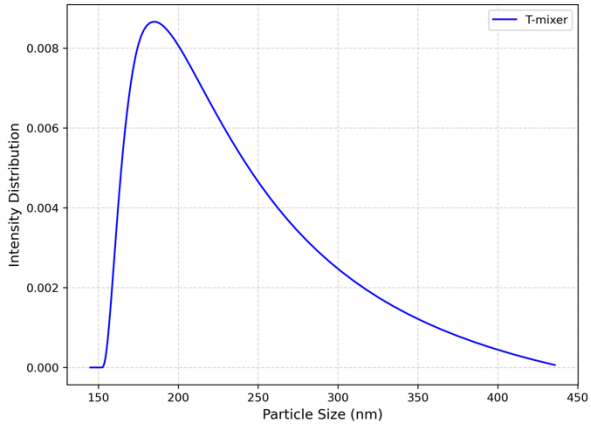

Flow Rate Ratio 20: 1

Swirl Mixer			Size (nm)			PDI			EE%		
Total Flow Rate (mL/min)	Flow Rate Ratio	Lipids Concentration (mg)	MEAN	SD	N	Mean	SD	N	MEAN	SD	N
80	1: 1	16	167.3	12	3	0.194	0.04	3	48	3	3
80	2: 1	16	101.4	8	3	0.156	0.02	3	60	2	3
80	3: 1	16	64.1	4	3	0.09	0.03	3	91	3	3
80	4: 1	16	62.3	4	3	0.098	0.025	3	91	2	3
80	6: 1	16	75.7	5	3	0.132	0.03	3	94	4	3
80	9: 1	16	140.5	7	3	0.157	0.03	3	92	3	3
80	20: 1	16	156.1	6	3	0.24	0.044	3	84	5	3

Flow Rate Ratio Data Summary

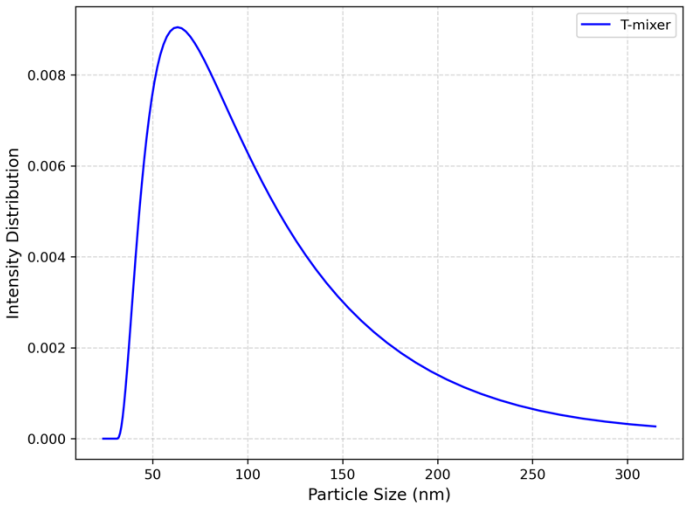

Lipids Concentration 1 (mg)

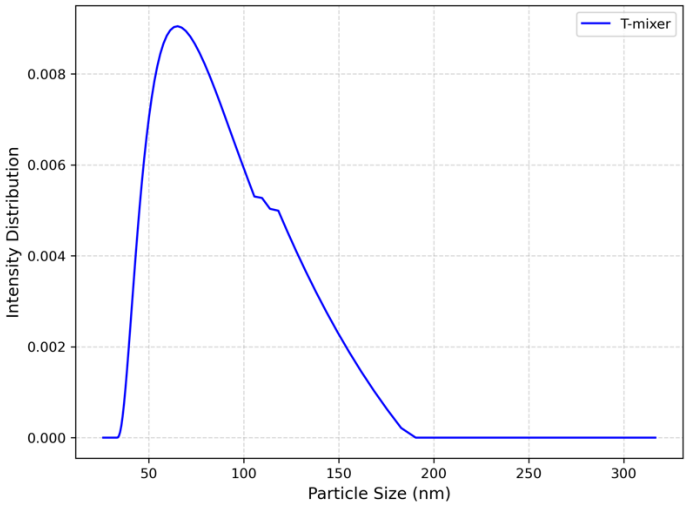

Lipids Concentration 2 (mg)

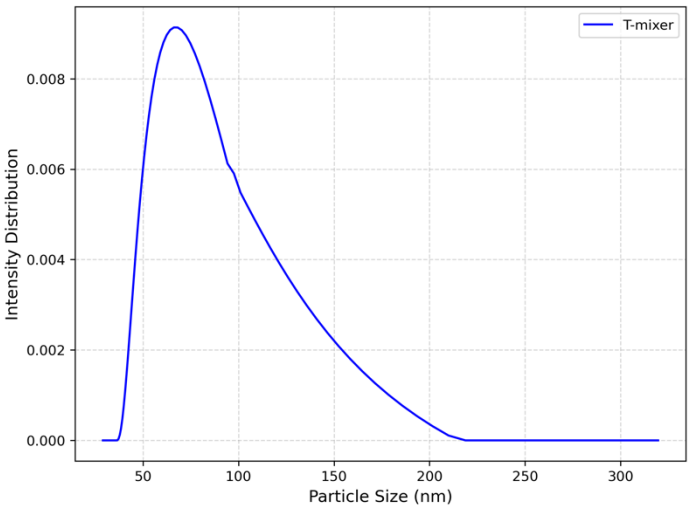

Lipids Concentration 4 (mg)

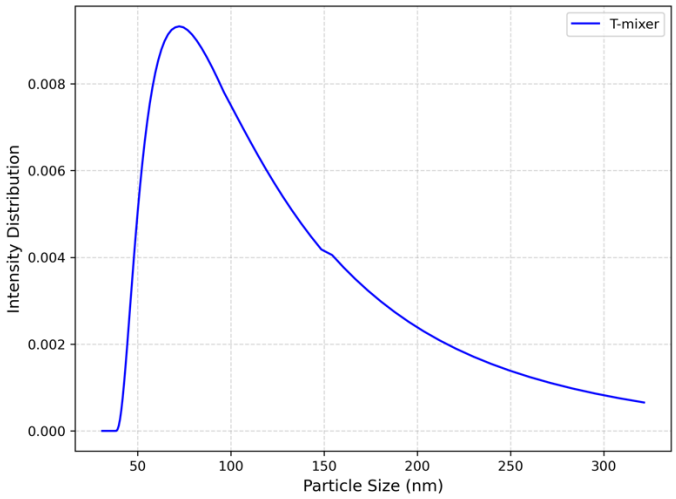

Lipids Concentration 10 (mg)

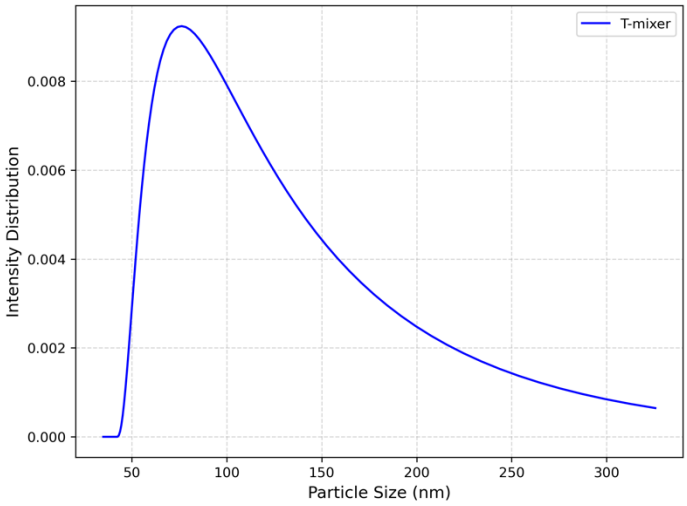

Lipids Concentration 16 (mg)

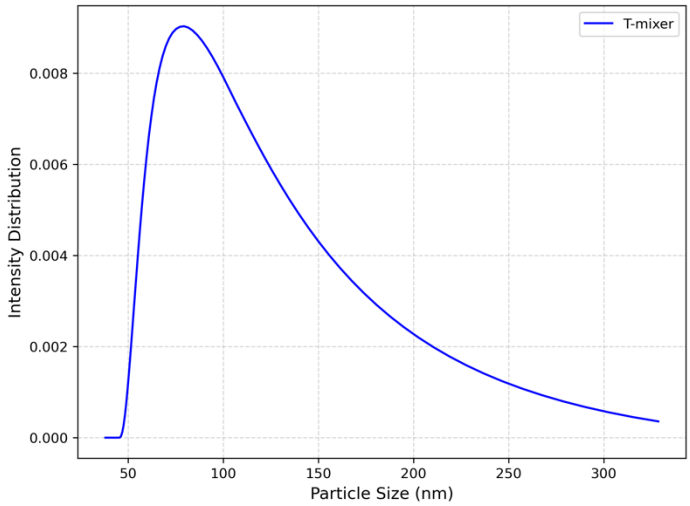

Lipids Concentration 20 (mg)

Swirl Mixer			Size (nm)			PDI			EE%		
Total Flow Rate (mL/min)	Flow Rate Ratio	Lipids Concentration (mg)	MEAN	SD	N	Mean	SD	N	MEAN	SD	N
80	3: 1	1	53	3	3	0.092	0.02	3	74	3	3
80	3: 1	2	57	2	3	0.089	0.02	3	79	2	3
80	3: 1	4	58	4	3	0.077	0.01	3	80	2	3
80	3: 1	10	60.2	4	3	0.086	0.02	3	93	3	3
80	3: 1	16	64.1	4	3	0.09	0.03	3	91	3	3
80	3: 1	20	70.4	6	3	0.17	0.03	3	90	4	3

Lipids Concentration Data summary

Fig 28 Swirl mixer PEG-lipid%, Lipids: Cholesterol and N/P ratio

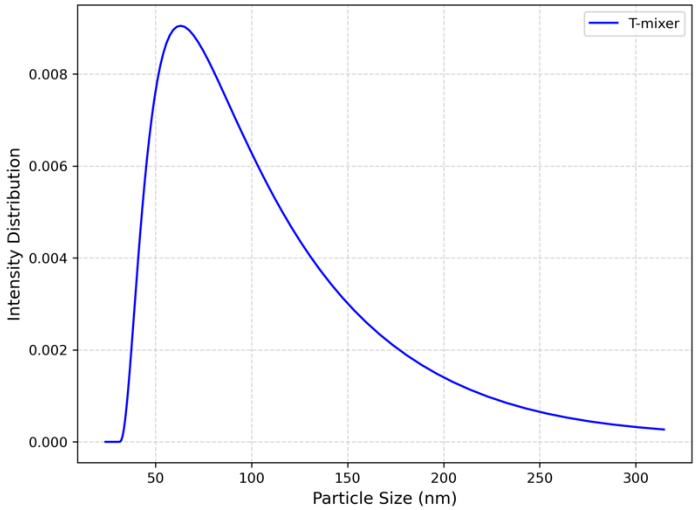

PEG-lipid 1.5%

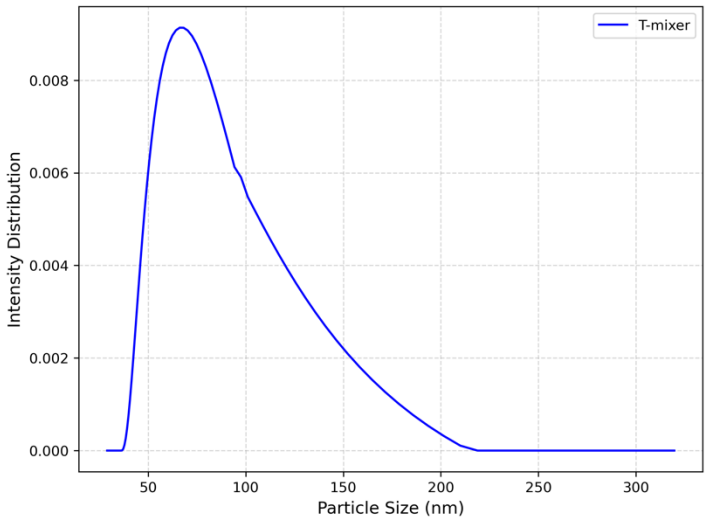

PEG-lipid 5%

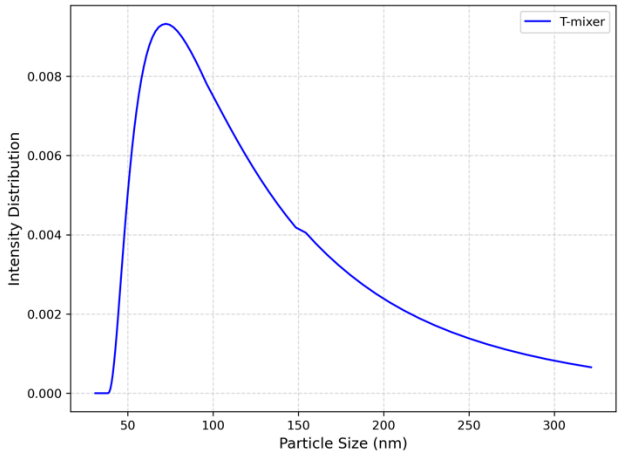

PEG-lipid 10%

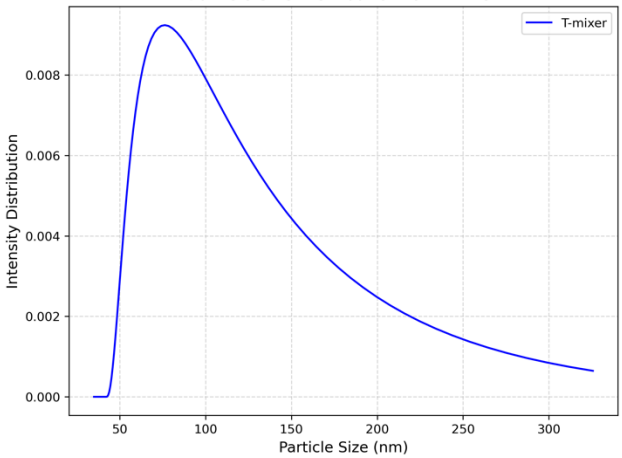

PEG-lipid 15%

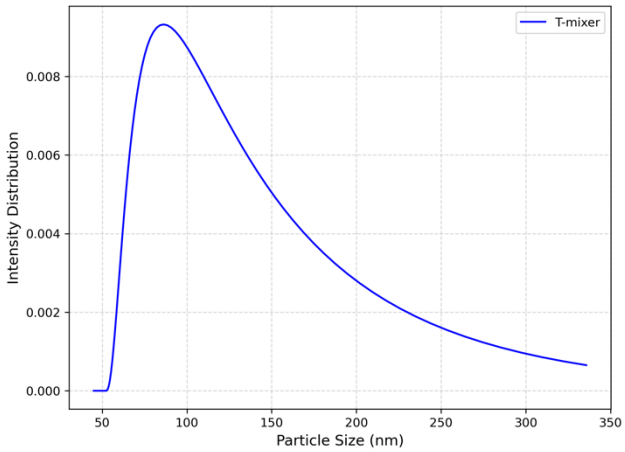

PEG-lipid 20%

Swirl Mixer			Size (nm)			PDI			EE%		
PEG-Lipids	Lipids: Cholesterol	N/P Ratio	MEAN	SD	N	Mean	SD	N	MEAN	SD	N
1.5%	3: 2	6: 1	58	3	3	0.067	0.008	3	90	2	3
5%	3: 2	6: 1	65.2	2	3	0.078	0.01	3	84	2	3
10%	3: 2	6: 1	69.1	5	3	0.09	0.01	3	83	3	3
15%	3: 2	6: 1	73.2	3	3	0.099	0.018	3	76	3	3
20%	3: 2	6: 1	78.4	4	3	0.1	0.02	3	69	4	3

PEG-lipid% Data Summary

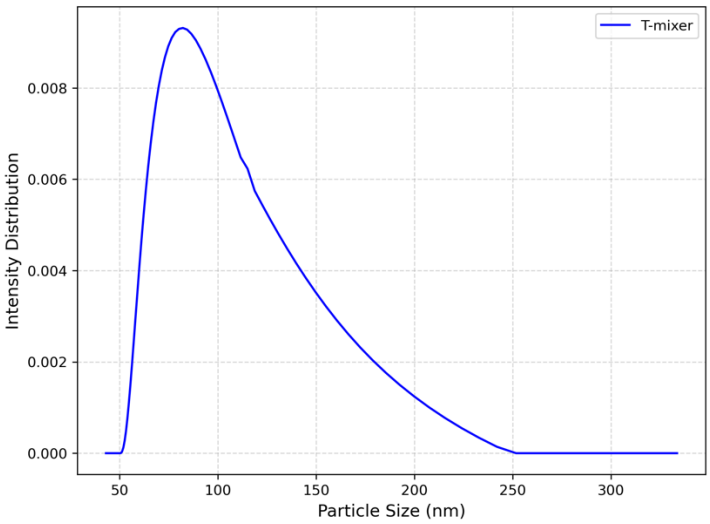

Lipid: Chol 1:1

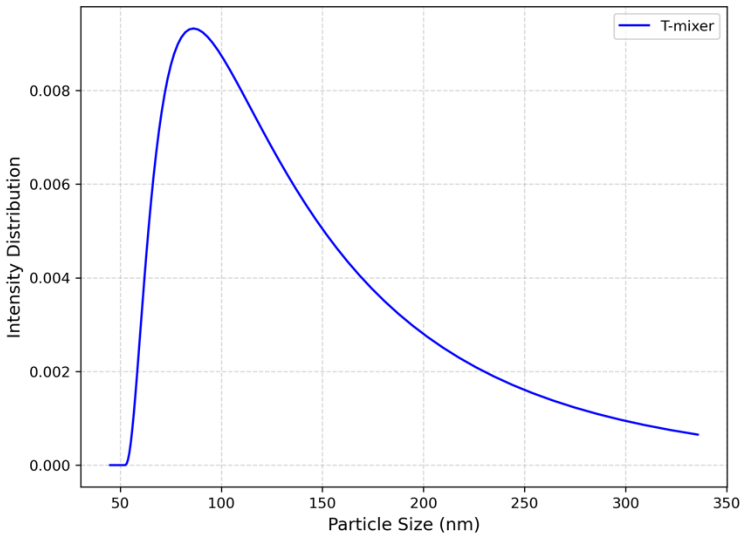

Lipid: Chol 1.5:1

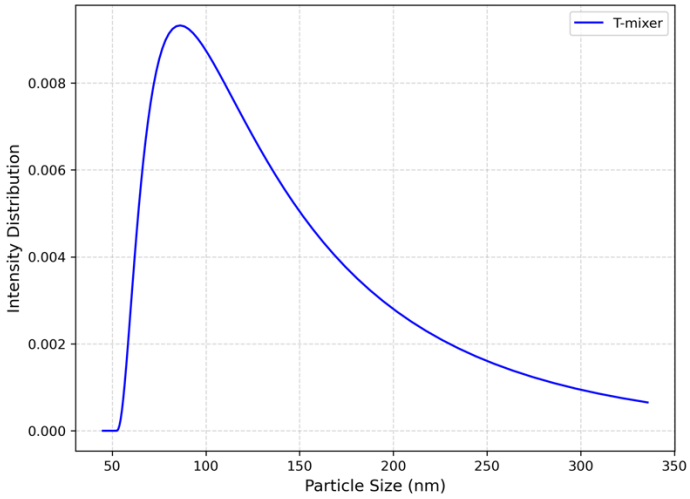

Lipid: Chol 2:1

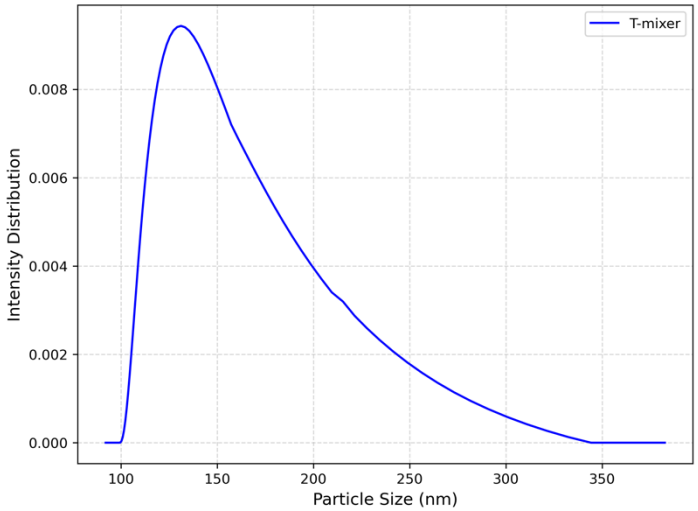

Lipid: Chol 4:1

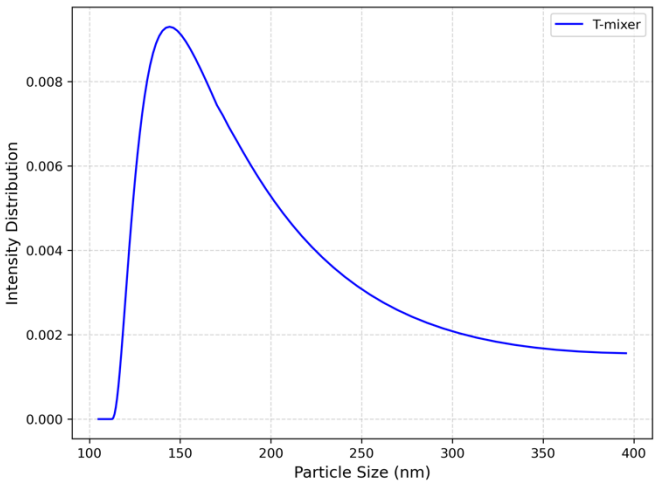

Lipid: Chol 9:1

Swirl Mixer			Size (nm)			PDI			EE%		
PEG-Lipids	Lipids: Cholesterol	N/P Ratio	MEAN	SD	N	Mean	SD	N	MEAN	SD	N
1.5%	1: 1	6: 1	61.4	4	3	0.073	0.05	3	57	4	3
1.5%	3: 2	6: 1	70.9	3	3	0.078	0.03	3	90	2	3
1.5%	2: 1	6: 1	81.3	6	3	0.095	0.04	3	91	3	3
1.5%	4: 1	6: 1	144	12	3	0.121	0.06	3	86	3	3
1.5%	9: 1	6: 1	153.5	10	3	0.112	0.09	3	73	4	3

Lipid: Cholesterol Ratio Data Summary

Fig 29 Herringbone mixer Total Flow Rate, Flow Rate Ratio and Formulation Concentration Experiment Particle Size Distribution Raw file

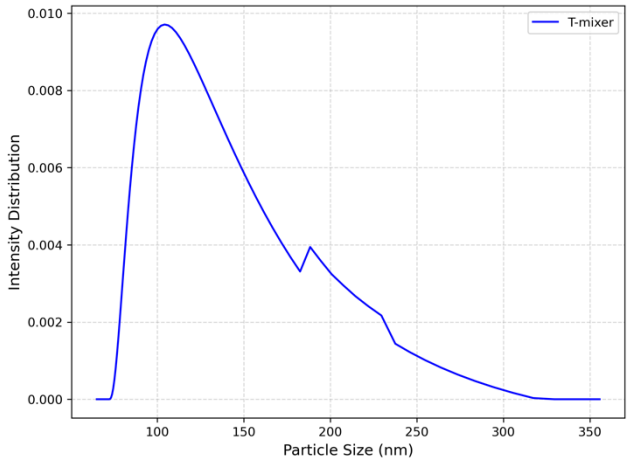

Total Flow Rate 1 mL/min

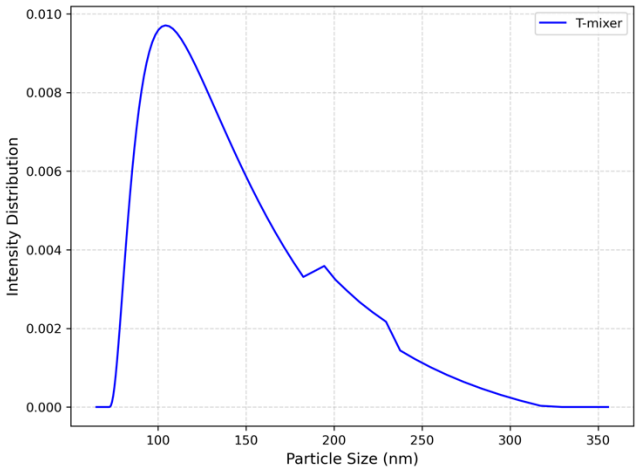

Total Flow Rate 2 mL/min

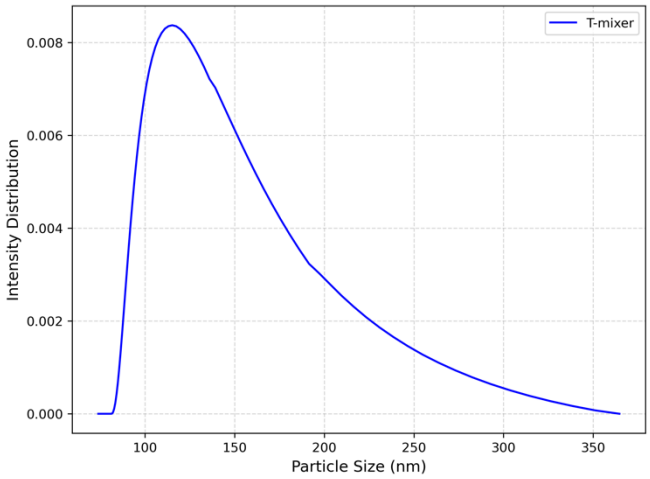

Total Flow Rate 4 mL/min

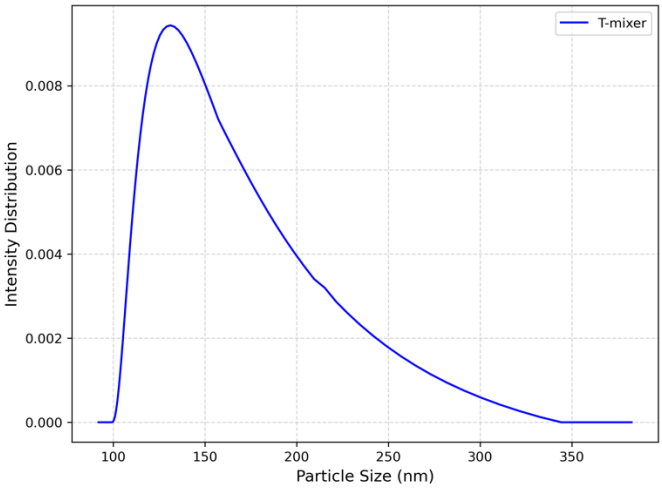

Total Flow Rate 6 mL/min

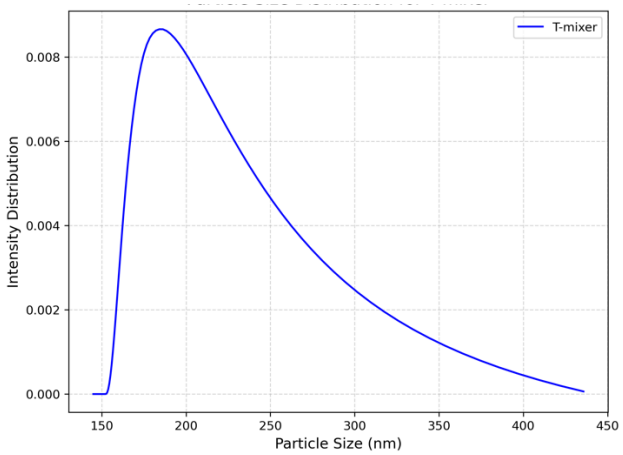

Total Flow Rate 8 mL/min

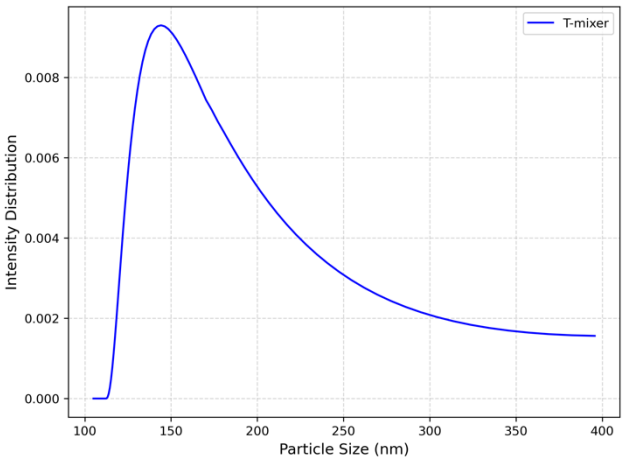

Total Flow Rate 10 mL/min

HerringBone Mixer			Size (nm)			PDI			EE%		
Total Flow Rate (mL/min)	Flow Rate Ratio	Lipids Concentration (mg)	MEAN	SD	N	Mean	SD	N	MEAN	SD	N
1	3: 1	16	174	17	3	0.37	0.12	3	93	6	3
2	3: 1	16	143	16	3	0.36	0.1	3	91	6	3
4	3: 1	16	135	10	3	0.3	0.08	3	92	4	3
6	3: 1	16	131	11	4	0.28	0.07	4	83	5	3
8	3: 1	16	121	12	4	0.3	0.07	4	76	3	3
10	3: 1	16	126	12	4	0.29	0.08	4	79	4	3

Total Flow Rate Data Summary

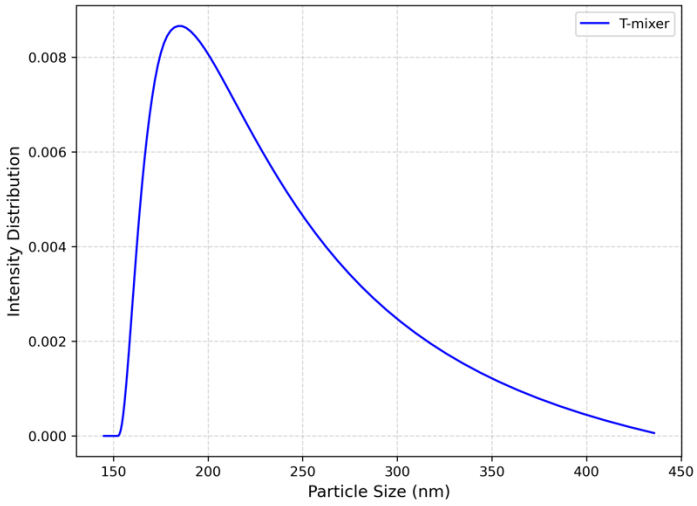

Flow Rate Ratio 1:1

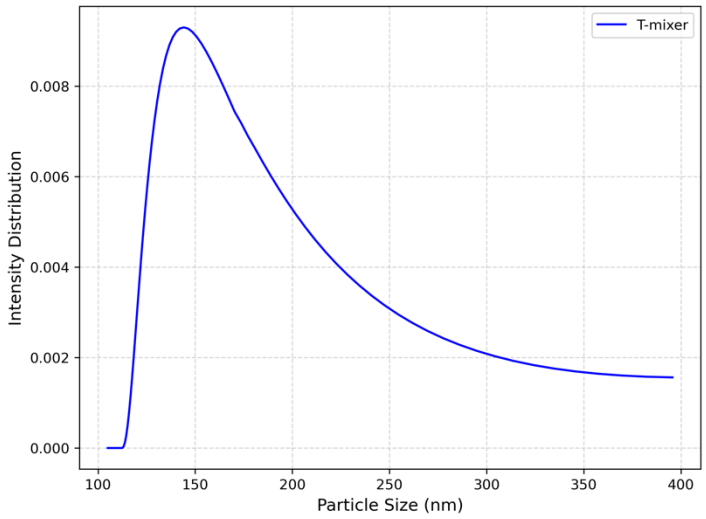

Flow Rate Ratio 2:1

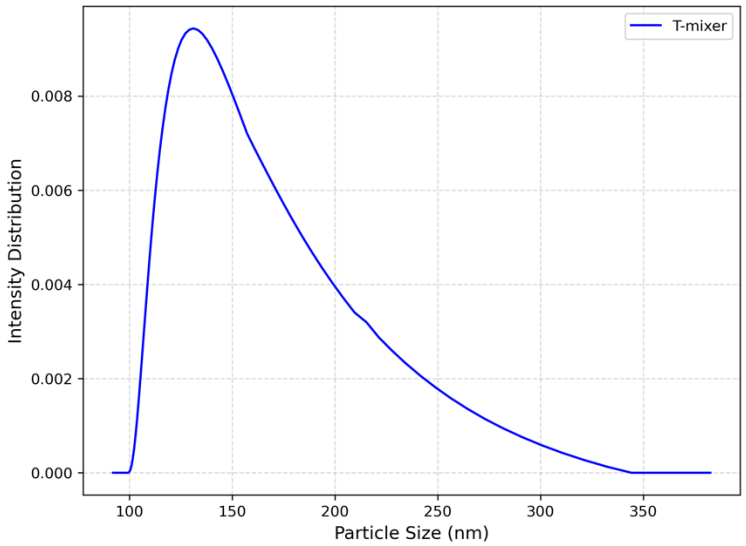

Flow Rate Ratio 3:1

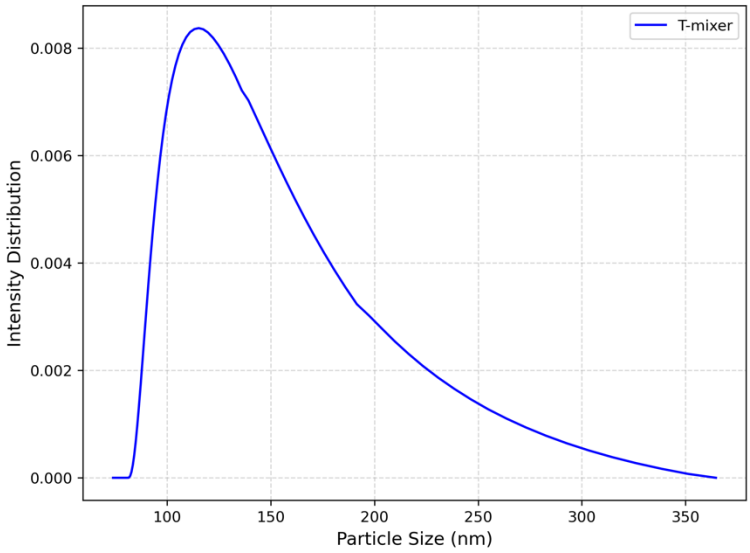

Flow Rate Ratio 4:1

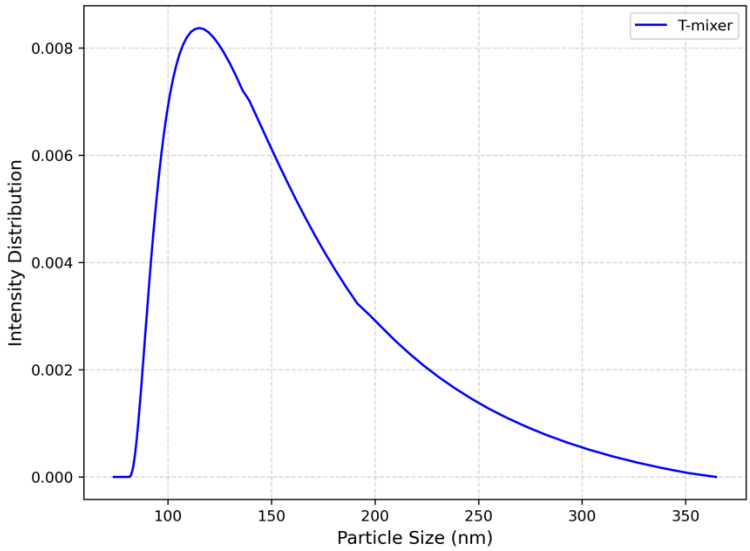

Flow Rate Ratio 6:1

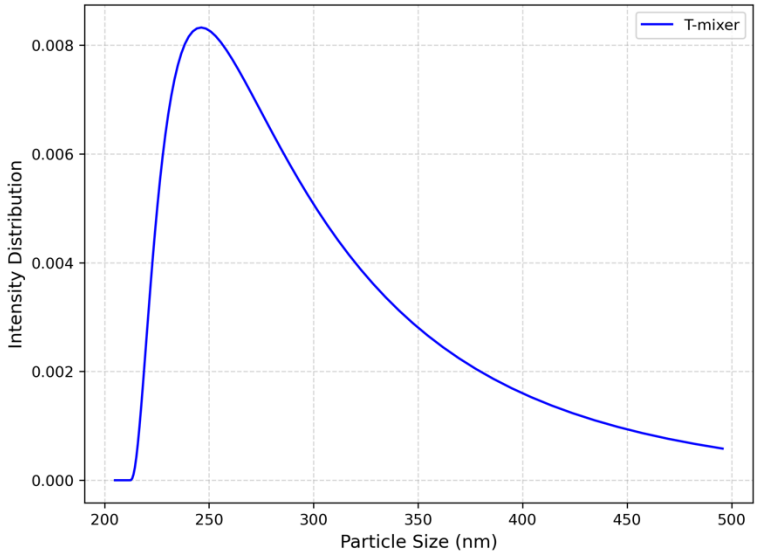

Flow Rate Ratio 9:1

HerringBone Mixer			Size (nm)			PDI			EE%		
Total Flow Rate (mL/min)	Flow Rate Ratio	Lipids Concentration (mg)	MEAN	SD	N	Mean	SD	N	MEAN	SD	N
4	1: 1	16	213	26	3	0.48	0.17	3	54	7	3
4	2: 1	16	194	24	3	0.37	0.13	3	70	6	3
4	3: 1	16	135	10	3	0.3	0.08	3	92	6	3
4	4: 1	16	154	11	3	0.34	0.1	3	89	5	3
4	6: 1	16	175	14	3	0.37	0.12	3	88	4	3
4	9: 1	16	204	17	3	0.39	0.13	3	90	4	3
4	20: 1	16	242	21	3	0.43	0.11	3	91	5	3

Flow Rate Ratio Data Summary

	模式	TFR (mL/...	FRR	Lipids Conc (mg/mL)	DSPC: Chol	PEG-lipid	Size (nm)	PDI
1	−−−−−	80	1	4	1	0.015	189.1	0.16
2	−−−++	80	1	4	7	0.25	178.5	0.17
3	−−+−+	80	1	10	1	0.25	187.9	0.23
4	−−++−	80	1	10	7	0.015	174.3	0.25
5	a0000	80	3.5	7	4	0.1325	76.7	0.13
6	−+−−+	80	6	4	1	0.25	69.8	0.1
7	−+−+−	80	6	4	7	0.015	67.6	0.16
8	−++−−	80	6	10	1	0.015	75.9	0.1
9	−++++	80	6	10	7	0.25	136.7	0.17
10	0a000	110	1	7	4	0.1325	125.2	0.14
11	00a00	110	3.5	4	4	0.1325	81.4	0.09
12	000a0	110	3.5	7	1	0.1325	86.2	0.1
13	0000a	110	3.5	7	4	0.015	66.1	0.09
14	00000	110	3.5	7	4	0.1325	67.7	0.1
15	00000	110	3.5	7	4	0.1325	68.3	0.11
16	0000A	110	3.5	7	4	0.25	69.4	0.09
17	000A0	110	3.5	7	7	0.1325	70.6	0.09
18	00A00	110	3.5	10	4	0.1325	68	0.11
19	0A000	110	6	7	4	0.1325	64.5	0.1
20	+−−−+	140	1	4	1	0.25	99.3	0.11
21	+−−+−	140	1	4	7	0.015	106.5	0.12
22	+−+−−	140	1	10	1	0.015	100.4	0.12
23	+−+++	140	1	10	7	0.25	154.6	0.19
24	A0000	140	3.5	7	4	0.1325	74.1	0.1
25	++−−−	140	6	4	1	0.015	69.2	0.09
26	++−++	140	6	4	7	0.25	132.5	0.11
27	+++−+	140	6	10	1	0.25	82	0.11
28	++++−	140	6	10	7	0.015	138.4	0.16

Fig 34 Heatmap Support